Mechano-chemical feedbacks during deformation and hydration of peridotites

Claire Olga Maryse Aupart

Main supervisor: Bjørn Jamtveit

Co-supervisors: Håkon Austheim & Anders Malthe-Sørenssen

PhD Defense on the 13th November 2020

Committee:

Administrator:

Valérie Maupin
Centre for Earth Evolution and Dynamics, University of Oslo

Opponents:

Javier Escartin
École Normale Supérieure de Paris

José Alberto Padrón-Navarta
Géosciences Montpellier, University of Montpellier

Series of dissertations submitted to the
Faculty of Mathematics and Natural Sciences, University of Oslo
No. 2319

ISSN 1501-7710

Cover: Hanne Baadsgaard Utigard.
Print production: Reprosentralen, University of Oslo.

Acknowledgments

These have been almost five full years on many aspects! Of course, I learned a lot about my research subject, on what it is to work in research, I learned to use new tools and techniques, I improved (I hope) some previous skills, and I gained (a little bit) of confidence and maturity in my work and in my ideas. But what made these years invaluable is everything that went around that and everyone I met in Oslo and elsewhere.

I should first thank Bjørn for giving me the opportunity to do this PhD at PGP, in such a nice environment, for sending me all over the globe to learn, meet other researchers and students, describe beautiful serpentine cores full of veins, dykes and unidentifiable minerals and structures. Thank you also for always being available when I needed it, for your advices, for giving me liberty in my work but never letting me down. Next on the list would be François, the first person I met from the lab before I even came in Oslo. Thank you for your cheerfulness, for coming say bye and ask for news almost every evening, for the French dinners, for Blesle. Thank you also for your advices and for sometimes acting as an unofficial supervisor.

I had the luck to have a group of perfect officemates. Kristina, Xiaojiao, Arianne and Neelima; our girl group formed very quickly and naturally, it has been a real pleasure to share offices with you. Thank you for the nice working environments, the cookie breaks, the concerts, museums, and discussions. Thanks for the few dinners we managed to have together. I have been missing you during this pandemic period. Thanks to my few other office mates, even though we did not spend much time together. Thank you, Xin, for the evening discussions. Thank you, Monem, for welcoming me into your office in the very beginning of my PhD and helping me feeling not too lost in this new environment. Thank you, of course, to everyone past and present at PGP and in the Njord (and friends) group. Thank you for the lunch times, for the seminars, for the Christmas and summer parties, for the paper club, for the few afternoon coffee breaks I managed to participate to. Thank you for putting some life into the fourth floor and making it such a good place to work at. John, I am really grateful you decided to come over to my desk and talk about my cat. A special thanks to Siri, Muriel and Berit for your help and insight at the SEM and at the microprobe.

I have never been travelling as much as the last few years and each trip has been a great adventure. I met so many great people on those trips. Some of them I will probably never see again, some that I will meet occasionally and others that will become lifelong friends. Whatever the outcome I cherish any of these encounters as these trips would have not been the same without them. Thank you, Ingrid, you are such a kind person. I will never forget your support during this week in England. Thank you, Manue, for the time in Bremerhaven and at the Christmas market in Bremen. Thank you also Vera and Florian for your warm welcome at the AWI. Thank you, Benoît and Fabrice, for welcoming me at Geosciences

Montpellier and introducing me to the Crystal probe and EBSD technique. Thank you, Margot, for popping into my life every once in a while. That is always a pleasure to talk and work with you.

I want to give a huge thank to everyone in the Oman DP. Being part of this project has been one of the greatest experiences in my life. Thank you for Ibra, thank you for the Chikyu, thank you for the wavy waxy green veins and the 143 samples. We worked hard in Oman to get the cores curated, labelled, photographed, sketched, described, and put into boxes. In the hard work we also had a lot of fun and some nice sightseeing (thanks Ole Ivar for the drives!). While I thought the days were pretty busy on the drilling site (and they were!), it was nothing compared to our days (or rather nights for our night shift group) on the Chikyu. At the end of the first day, I remember feeling discouraged when realizing the amount of work we had to accomplish. But in these hardest times also come the best memories: our daily sunrise breaks, the noon meetings, Katsu’s cheerfulness every very early morning, the weekly drill exercises (once seeing dolphins!), the birthdays on board, the day we decided to embellish Samuel’s desk, and so much more. An extra thanks for Lotta and Ben for the fun we had and still have.

Living in a foreign country has also been a very enriching experience. I have discovered the joys of Norway the snow (that I love), the ice (that tricked me several times), the endless days and early nights depending on the season. I always received very warm welcomes wherever I went. In Norwegian classes, in ballet classes or at the music school. Thanks to everyone I met there and who made me feel more at home.

And finally, I want to thank my family for having been so patient. You were what I missed the most during the past years. My stays in France were never long enough but you have always been supportive and respected my decisions. Thank you all.

Table of content

1 Introduction

Ultra-mafic rocks are silica-poor rocks (less than 45 wt% SiO_2) composed of ferromagnesian minerals, in particular olivine, orthopyroxene and clinopyroxene (Figure 1-1). Olivine-rich rocks, peridotites, are the major component of the upper Earth's mantle. As such, they represent one of the Earth's most common rock types. When peridotites are emplaced to shallower depths by tectonic activity, they interact with crustal fluids. These interactions have significant consequences regarding the global cycles of a range of volatile components. Understanding the processes behind them are crucial to constrain exchanges between surface-near environments and the deep Earth. It is particularly relevant with respect to global warming as these interactions involve major greenhouse gases such as H_2O, CO_2 and CH_4.

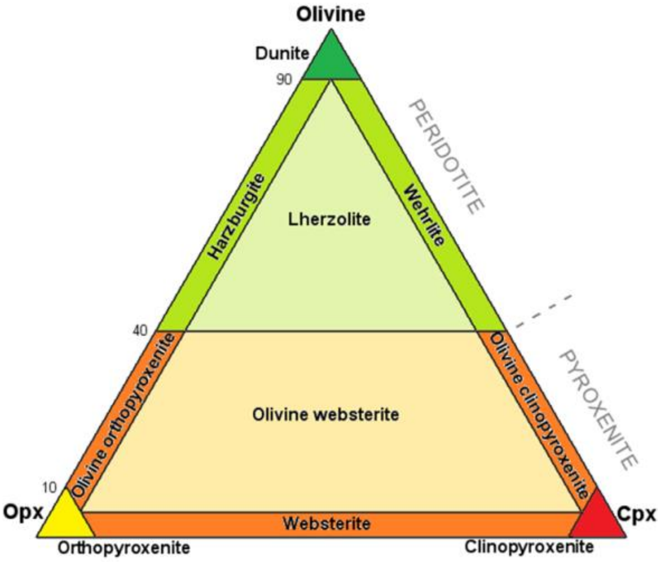

Figure 1-1: *Ternary diagram showing the classification of ultra-mafic rocks depending their main mineralogy.*

This work mainly focuses on serpentinization, the main process by which peridotite is hydrated to produce a serpentine dominated rock, serpentinite. This rock type is found on every continent, in every ocean (Guillot & Hattori, 2013) and even on other planets (Ehlmann et al., 2010). In addition to be one of the most important process for the transfer of volatiles from the hydrosphere to the lithosphere and deep mantle (e.g. Alt et al., 2013; Deschamps et al., 2011; Hattori & Guillot, 2007), serpentinization is believed to be intimately linked with the origin of life (e.g. Schulte et al., 2006; McCollom & Seewald, 2013) and serpentinites play a major role in some of the Earth main tectonic and magmatic processes (e.g. Guillot & Hattori, 2013; Hattori & Guillot, 2003; Hirth & Guillot, 2013). Fluid-induced retrograde metamorphisms, including serpentinization, are processes that require fluid supply to the reactive rock. Pristine peridotite has a very low permeability and consequently serpentinization requires permeability generation both to be initiated and sustained (Figure 1-2). This is usually associated with fracturing. The main causes of fracturing during serpentinization are tectonic stress and associated faulting (e.g. Bayrakci et al., 2016), thermal contraction (e.g. DeMartin et al., 2004; Rouméjon & Cannat, 2014) and reaction-driven fracturing associated with the volume increase induced by serpentinization (e.g. O'Hanley, 1992; Jamtveit et al., 2008). These fracturing processes enable migration of fluids to the reactive rock surface, leading to more serpentinization and potentially more fracturing. However, the volume increase associated with serpentinization can also lead to clogging of available porosity and stop further reaction (Hövelmann et al., 2012). Significant rock weakening after only a few percent of serpentinization (Escartin et al., 1997; Escartin et al., 2001) makes the relation between the reaction of serpentinization and tectonics highly complex.

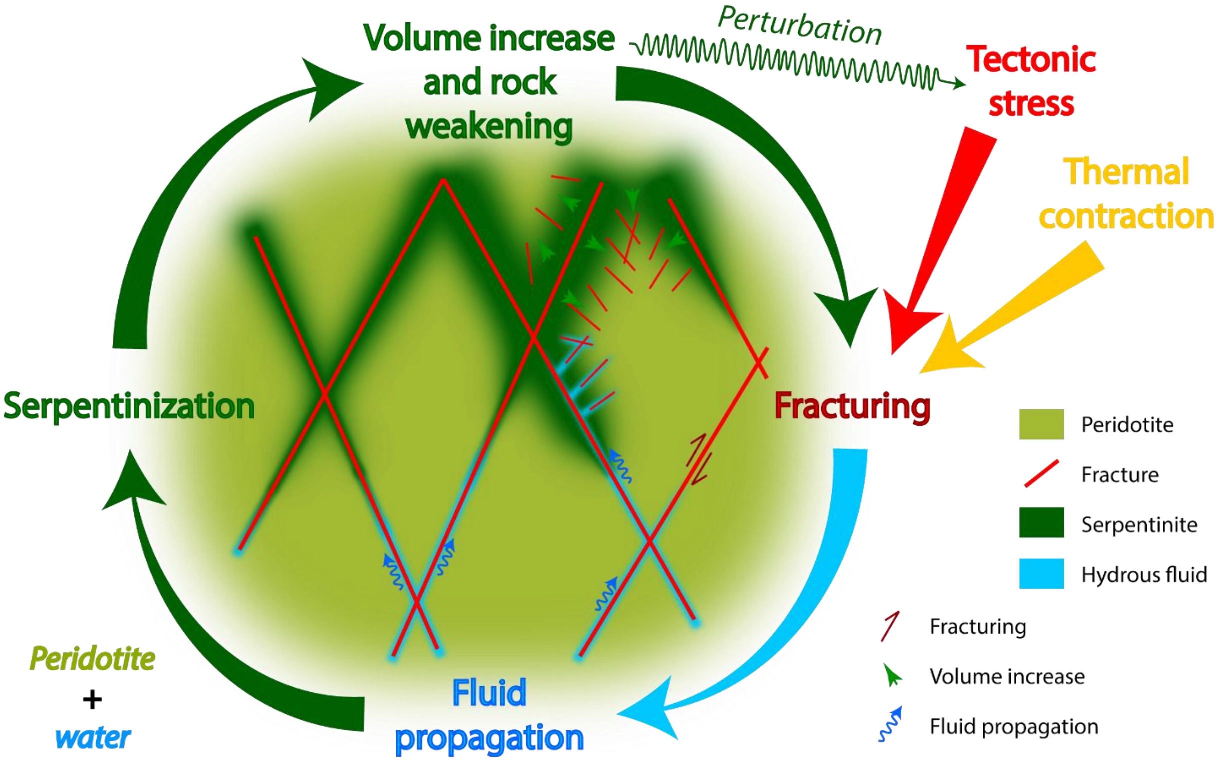

Figure 1-2: *Schematic representation of the interactions between serpentinization and tectonics.*

This thesis aims at getting a better understanding of the mechano-chemical couplings during serpentinization. It was planned to be based mostly on data from the Oman Drilling Project (Oman DP), combining the study of recovered core samples with geophysical data acquired in and around the boreholes. However, because of delays of this international project, the cores were only drilled during the third year of my PhD and some of the geophysical data I was supposed to study are not yet available. I could start working on samples from Oman only by the end of my fourth year of PhD and hence had to focus on data from other locations and sources in the meantime. The first project I started to work on was a study of deformation microstructures in peridotites that experienced high stress conditions during tectonic loading. Even if this project did not involve serpentinization directly, understanding how the mantle is deformed is of crucial importance for the propagation of water within it and thus, for serpentinization. For the second project, I had the opportunity to work on seismic data from the South West Indian Ridge recovered by Vera Schlindwein. The aim of this project was to study the impact of seismic activity on the progress of serpentinization along an ultra-slow spreading ridge. Each project led to the writing of an article for a scientific journal. The work done on the samples from the Oman DP led to the writing of a third article based on the study of a family of faults and cataclasites formed during the early stages of serpentinization.

The unfortunate delay on the Oman DP, finally led to the widening of the initial field of study of my PhD project, working with rocks and data from very diverse origins or geological context, with scales from micrometer up to several tens of kilometers, with a wide variety of techniques, and with researchers from very different fields of geosciences. This results in a thesis manuscript divided into five chapters including this introduction (chapter 1):

- Chapter 2 presents the global context within which this work is embedded based on the literature I read during my PhD. This chapter first introduces the reaction of serpentinization: its chemistry, the main mineral phases involved and the typical associated textures. It then focuses on the main environments where serpentinization can occur, notably the mid-oceanic ridge axes and the subduction zones. The emphasis is mostly put on the mid-oceanic ridges as most of the work I did during my PhD is related to them. The last part of chapter 1 introduces the intimate relation between tectonic deformation and fluid-induced metamorphism. A special focus is put on the case of serpentinization.
- Chapter 3 summarize the main findings and innovative aspects developed in each manuscript included in chapter 4 and discusses their impact on current research.
- Chapter 4 is composed of the three articles written during my PhD that represent the core of this PhD thesis. Each manuscript is preceded by a detailed description of my personal contributions.
- Chapter 5 is an outlook paragraph summarizing the main findings associated with this thesis work and discussing the perspectives it opens.

2 Scientific background

2.1 Serpentinization

The hydration of peridotite leads to the formation of a lower density, sheet silicate, serpentine, at the expense of olivine and pyroxene. This process is widely spread on earth and particularly affects the oceanic lithosphere. It is of particular importance as this reaction causes important changes in mantle rheology (e.g. Raleigh & Paterson, 1965; Escartin et al., 2001) and physical properties (e.g. Miller & Christensen, 1997; Oufi et al., 2002), has major consequences of volatiles deep cycles (e.g. Früh-Green et al., 2004; Alt et al., 2013; Debret et al., 2013) and is intimately linked to seafloor hydrothermal (e.g. Holm & Charlou, 2001; Lowell & Rona, 2002) and biological (e.g. Früh-Green et al., 2004; Schrenk et al., 2013) activities.

2.1.1 Chemistry of serpentinization

Serpentinization involves hydration of olivine, orthopyroxene, and to a lesser extent clinopyroxene. The onset of serpentinization is mainly controlled by temperature, but a variety of other factors also play a role, including the composition of the fluid, the composition of the primary peridotite, the redox state, etc. The reaction is often considered mostly isochemical but is often associated with an increase in the concentration of specific elements easily incorporated in serpentine minerals and associated phases. The isotopic signatures in serpentinites can give valuable information about the serpentinizing fluids and the conditions of serpentinization.

2.1.1.1 Conditions of serpentinization

Natural serpentinization leads to an uptake of water that may represent up to 10-15 % of the serpentinized peridotites (Dungan, 1979; Mével, 2003). It occurs under a large range of temperatures, starting below 100°C and extend up to more than 500°C (Mével, 2003; Malvoisin, 2015). Experimental studies have shown that maximum reactions rates are obtained around 300°C for olivine and 400°C for orthopyroxene hydration (Martin & Fyfe, 1970; Malvoisin et al., 2012; Wegner & Ernst, 1983). Pressure is not a limiting factor for serpentine stability in most natural settings. However, a decrease in temperature and/or pressure will favor serpentine nucleation and growth from a reactive fluid as it reduces silica solubility (Andreani et al., 2007). Serpentinization is often considered to produce reducing conditions. This is in general verified in closed system and rock dominated conditions. However, in open systems, with abundant fluids, the reaction can be associated with oxidizing conditions. It is common to associate early stages of serpentinization with closed system conditions and more advanced stages with open system conditions (e.g. Alt & Shanks, 2002; Andreani et al., 2007; Bach et al., 2006; Rouméjon et al., 2015). The reaction is extremely fast on geologic time scale (Martin & Fyfe, 1970; Malvoisin et al., 2012). Under near-equilibrium conditions, the kinetics of serpentinization are related to the size of the available reactive surface area (grain size). It Implies that the dissolution rates of primary minerals are controlling the kinetics of the reaction, the precipitation of serpentine being a faster process (Malvoisin et al., 2012). Open-system serpentinization is often reported to occur out of equilibrium (e.g. Allen & Seyfried, 2003; Andreani et al. 2007). Common phases formed during serpentinization apart from serpentine are magnetite, brucite, talc, chlorite, tremolite, H_2 and CH_4. Serpentinization is also often associated with carbonation (e.g. Kelemen et al., 2011) thus being a relevant process in the deep carbon cycle.

Olivine as the most common phase is the first to react, in particular its magnesian end-member with associated formation of brucite and serpentine (Bach et al., 2006; Klein et al., 2013; Miura et al., 2011; Pens et al., 2016; Rouméjon et al., 2015):

$$\begin{gathered} 2Mg_2SiO_4 + 3H_2O = Mg(OH)_2 + Mg_3Si_2O_5(OH)_4 \\ Olivine + water = brucite + serpentine \end{gathered} \tag{R1}$$

The serpentinization of pyroxene, and particularly orthopyroxene, leads to the release of silica in the reactive fluid (Bach et al., 2006; Malvoisin, 2015; Rouméjon et al., 2015, 2019; Seyfried et al., 2007):

$$\begin{gathered} 3MgSiO_3 + 2H_2O = SiO_{2(\mathrm{aq})} + Mg_3Si_2O_5(OH)_4 \\ Orthopyroxene + water = aqueous\ silica + serpentine \end{gathered} \tag{R2}$$

This silica can react further with olivine to form serpentine:

$$\begin{gathered} 3Mg_2SiO_4 + SiO_{2(\mathrm{aq})} + 4H_2O = 2Mg_3Si_2O_5(OH)_4 \\ Olivine + aqueous\ silica + water = serpentine \end{gathered} \tag{R3}$$

As serpentinization progresses the ratio of altered pyroxene compared to olivine will increase leading to more intense Si-metasomatism (Klein & Le Roux, 2020; Seyfried et al., 2007). Si-metasomatism leads to the dissolution of brucite (Bach et al., 2004; Bach et al., 2006; Klein et al., 2009; Malvoisin, 2015), causing a depletion in magnesium (Malvoisin, 2015), and may lead to the formation of talc (Klein et al., 2013). Talc can also form directly from the alteration of pyroxene above 400˚C (Martin & Fyfe, 1970).The amount of Si-metasomatism has in consequence a significant control over the mineralogy of the serpentinite (Bach et al., 2004; Klein et al., 2009) and , through the relative amount of brucite (stable until ca. 300 ˚C) and/or talc (stable until ca. 750 ˚C), on its thermal stability (Malvoisin, 2015). The timing between the serpentinization of olivine and pyroxene also has its importance. Indeed, while asynchronous serpentinization will favor local compositional heterogeneities, their concomitant reaction will redistribute Si in the rock and limit brucite and talc formation (Klein et al., 2013).

The alteration of the iron end-member of olivine and pyroxene often leads to the formation of magnetite (Allen & Seyfried, 2003):

$$3Fe_2SiO_4 + 2H_2O = SiO_{2(\mathrm{aq})} + 2Fe_3O_4 + 2H_2 \tag{R4}$$

$$Olivine\ +\ water\ =\ aqueous\ silica +\ magnetite + dihydrogene$$

$$3FeSiO_3 + H_2O = 3SiO_{2(\mathrm{aq})} + Fe_3O_4 + H_2 \tag{R5}$$

$$Orthopyroxene\ +\ water\ =\ aqueous\ silica +\ magnetite + dihydrogen$$

These reactions also lead to the release of aqueous silica, contributing to the Si-metasomatism, and hydrogen (Bach et al., 2006; Allen & Seyfried, 2003). However, the amount of magnetite observed in serpentinites is highly variable (Klein et al., 2014). This is mainly caused by two factors: the diffusion rate of Mg (Evans, 2010) and the speciation of Fe in the different phases (Klein et al., 2009; Klein et al., 2014). Olivine and orthopyroxene behave slightly differently as serpentine formed after orthopyroxene tends to conserve Mg-Fe ratio and Fe^{2+}- Fe^{3+} proportions, while serpentine formed after olivine is more prone to changes (Klein et al., 2013). These disparities are homogenized by the simultaneous hydration of olivine and orthopyroxene (Klein et al., 2013).

During the hydration of olivine, magnesium preferentially migrates towards the reaction front. Above ca. 500 °C, this process is fast enough, and a limited amount of Fe is involved in the serpentinization reaction, leading to limited or no magnetite and hydrogen formation and the enrichment of olivine in iron. Below ca. 500°C, or if the reaction is enhanced by intense fluid flux, the migration of Mg is too slow, and Fe is involved in the hydration process. Olivine then preserves its Mg-Fe ratio. This invariably leads to the oxidation of Fe^{2+} into Fe^{3+} and reduced fluid conditions through the production of hydrogen (Klein et al, 2013; Klein et al, 2014) but magnetite is not necessarily formed. The occurrence of significant magnetite in serpentinites is either associated with temperatures above 200°C (Klein et al., 2009) or high degrees of serpentinization with a peak at >70% serpentinization regardless of temperature (Bach et al., 2006; Oufi et al., 2002). In the case of low-temperature serpentinization (<200˚C), if the system is closed, Fe^{3+} is taken up in brucite and serpentine by Mg-Fe substitutions (Klein et al., 2013; McCollom et al., 2016; Seyfried et al., 2007); if the system is open, iron is easily leached out (Dungan, 1979). A peak of hydrogen production has been identified in association with the magnetite production peak around 300-330˚C (Klein et al., 2009; McCollom & Bach, 2009). Hydrogen production and iron oxidation are enhanced in open system by the intense fluid circulation continuously removing hydrogen from the reaction front (Klein et al., 2013).

The alteration of orthopyroxene occasionally leads to the formation of chlorite due to its higher capacity, compared to serpentine, to store elements other than magnesium in its crystalline structure. The alteration of clinopyroxene, more resistant to alteration, commonly leads to tremolite formation. While Fe and Si concentrations are conserved during serpentinization, Ca (mostly contained in clinopyroxene) is exchanged with Mg from the serpentinizing fluid (Allen and Seyfried, 2003; Klein & Le Roux, 2020).

Serpentinization is most of the time associated with oceanic settings where seawater can interact with carbonates and store dissolved carbon dioxide. This carbon dioxide can further interact with the peridotite or serpentinite to precipitate new carbonates and serpentine minerals (Kelemen et al., 2011). The dissolution of the magnesium end-member of olivine or orthopyroxene will lead to the precipitation of magnesium rich carbonates, while the presence of dilute calcium, from sedimentary carbonates or from clinopyroxene dissolution will lead to the precipitation of calcium-rich carbonates. These carbonates occur either as veins or in the bulk rock. Carbonate minerals progressively incorporate magnesium and calcium; this leads to the progressive increase in silica of the concomitantly formed silicates, first serpentine, then talc, then quartz. Dissolved carbon can also interact with the hydrogen formed during serpentinization to form methane and other organic compounds (McCollom & Seewald, 2007; McCollom, 2013).

2.1.1.2 Transport of elements

Serpentinization is often not associated with major leaching of elements (Bach et al., 2006; Mével, 2003; Rouméjon et al., 2015). However, the involvement of fluids in the reaction is intimately linked to transport of elements and local metasomatism. The intensity of fluid circulation dictates the importance of element transport and which elements are transported. Previous interactions of the fluid will modify its composition and influence the changes in the composition of the serpentinized peridotite.

The composition of the serpentinizing fluid is of crucial importance for the composition of the serpentinite. While concentration of most elements with low solubility are similar in serpentinites and peridotite, Fluid Mobile Elements (FME; e.g. Li, B, F, Cl, As, Sr, Pb, Sb, Cs, Ba, U) are characteristically enriched within serpentinites (Deschamps et al., 2011; Deschamps et al., 2013; Hattori & Guillot, 2003; Peters et al., 2017). Hence these elements are useful to trace the extent of interaction between peridotite and seawater as their concentration in serpentinites will increase with the amount of fluid migrating through the rock. Among FME, B is particularly enriched (e.g. Deschamps et al., 2011; Kodolányi et al., 2012; Peters et al., 2017). Other FME enrichments vary depending on the lithologies the fluid has been interacting with and can thus inform us on the context of serpentinization (Peters et al., 2017). Enrichments in W have been noticed in correlation with FME enrichments in low temperature environments (Peters et al., 2017). Serpentinized peridotites are described as a sink for S, forming all kinds of sulfides (Alt & Shanks, 2002). Enrichments in sulfates are rarer and in general associated with shallow fluid-rock interactions.

The composition of the fluid can also have consequences on the serpentinization reaction itself. For example, the presence of alumina in the fluid has a critical effect on the serpentinization rate. While it enhances the reaction with olivine, it slows down it with orthopyroxene (Pens et al., 2016). Interaction of water with gabbroic rocks is known to additionally enrich the fluid in Light Rare Earth Elements (LREE; Nb, Y, Th, Ta; e.g. Rouméjon et al., 2018a), S (e.g. Alt & Shanks, 2002; Andreani et al., 2007) and Si (e.g. Rouméjon et al., 2019). Serpentinites formed after interactions with such fluids are consequently enriched in these elements.

Another aspect of element transport during serpentinization is the transport of elements away from the serpentinization zone. As mentioned earlier, local Si-metasomatism is associated with the serpentinization of pyroxene and iron end-member of olivine. Brucite formed during the serpentinization of the magnesian end-member of olivine is easily dissolved (Malvoisin, 2015) leading to Mg enrichment of the serpentinizing fluid. High fluid fluxes can cause depletion of the Ca, Al, Cr and Ni contained in the original peridotite (Rouméjon et al., 2015). Iron may also be depleted in systems characterized by high water-rock ratios (Gahlan et al., 2006).

2.1.1.3 Isotopic signature

Exchanges between the rock and the serpentinizing fluid leads to specific isotopic signatures in serpentinites. The study of this isotopic signature can help tracing origin of the serpentinizing fluid and conditions of serpentinization. The most commonly used isotopes are the oxygen stable isotopes, but other stable isotopes such as those of hydrogen, chlorine or sulfur can also be used (e.g. Alt & Shanks, 2002; Barnes et al., 2009; Bonifacie et al., 2008). Carbon isotopes are also commonly used when carbon phases are present (e.g. Charlou et al., 2002).

Research on stable isotopes relies on the study of the variations of the ratio of the concentrations of a rare isotope to a more common one. To be comparable from one sample to another, the isotopes ratio is normalized to the value of a standard. As variations are very small, a delta notation is used. For example, the delta notation for the oxygen stable isotopes is:

$$\delta^{18}\mathrm{O} = \left(\frac{(\frac{^{18}\mathrm{O}}{^{16}\mathrm{O}})_{\mathrm{sample}}}{(\frac{^{18}\mathrm{O}}{^{16}\mathrm{O}})_{\mathrm{standard}}} - 1 \right) \cdot 1000‰$$

An increase of the $\delta^{18}\mathrm{O}$ means an increase in the concentration of $^{18}\mathrm{O}$ in the studied phase. In the case of oxygen, the standard usually used is seawater (standard mean ocean water – SMOW).

Three main factors influence the $\delta^{18}\mathrm{O}$ of serpentinized peridotite: the temperature of serpentinization, the amount of interaction between the serpentinizing fluid and the rock represented by the water-rock ratio, and the $\delta^{18}\mathrm{O}$ of the serpentinizing fluid. $\delta^{18}\mathrm{O}$ in peridotite has been measured to be around 5.5‰ (Mattey et al., 1994). The value in serpentinizing fluids is estimated to vary between 0‰ (seawater) and 2.4‰ (hydrothermal fluid after interaction with magmatic rocks; Campbell et al., 1988). Repartition of the oxygen isotopes between water and serpentine is controlled by a fractionation coefficient expressed as $\alpha^{^{18}\mathrm{O}-^{16}\mathrm{O}}_{\mathrm{serpentine-water}}$. A fractionation coefficient higher than 1 will lead to serpentine being enriched in ^{18}O compared to the fluid while a coefficient smaller than 1 will lead to ^{18}O being enriched in the fluid. $\alpha^{^{18}O-^{16}O}_{serpentine-water}$ depends strongly on the temperature of serpentinization. Models show that it has high values at low temperatures and values smaller than 1 above 300-350˚C (Früh-Green et al., 1996; Saccocia et al., 2009; Zheng, 1993). The more interaction between the fluid and the rock, the closest the $\delta^{18}O$ in serpentine will be from an equilibrium value dictated by $\alpha^{^{18}O-^{16}O}_{serpentine-water}$, the composition of the fluid and temperature in closed system (cf. curves in Figure 2.1-1) or from the fluid $\delta^{18}O$-value in open system. $\delta^{18}O$ values in natural serpentinized peridotites have been reported between 0‰ and more than 12‰ (Mével, 2003). Most of these values are smaller than 5.5‰ as expected for peridotite serpentinized from seawater or hydrothermal fluids at optimal serpentinization temperatures. The range of $\delta^{18}O$ can be interpreted as serpentine being formed over a large range of temperature from seafloor temperatures up to 500˚C (Agrinier & Cannat, 1997; Früh-Green et al., 1996; Mével, 2003).

The study of oxygen isotopes is useful to help constrain the temperature of serpentinization, water-rock ratios and the source of the serpentinizing fluid. However, the combination of these three factor to obtain a given $\delta^{18}O$ in serpentine is not unique and $\delta^{18}O$ analyses have to be completed with a petrological study, the measurement of trace elements concentration, or the analysis of supplementary isotopes.

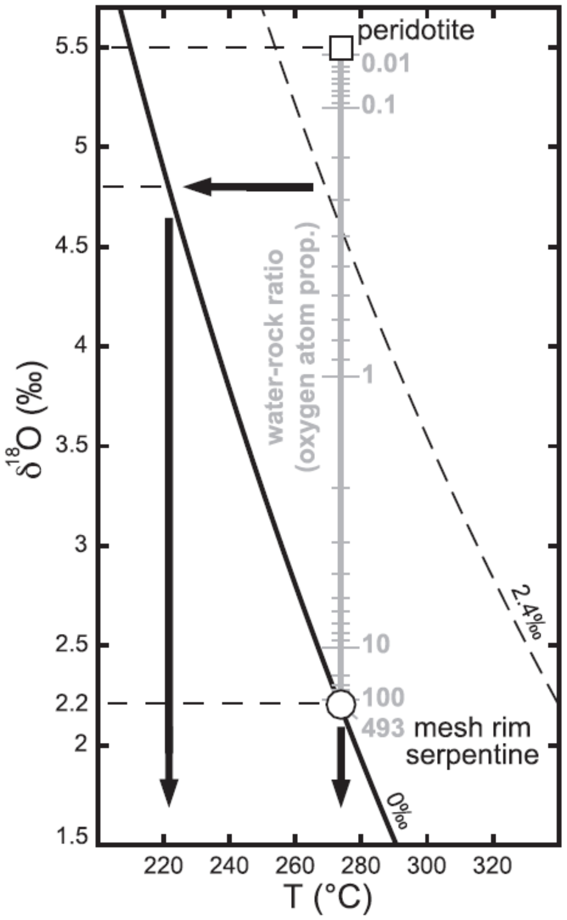

Figure 2.1-1: *Evolution of the $\delta^{18}O$ in serpentine depending on temperature, water-rock ratio and $\delta^{18}O$ in the fluid. The two curves show the evolution of the equilibrium $\delta^{18}O$ in serpentine by interaction with a fluid with a $\delta^{18}O$ of 0‰ or of 2.4‰. The example on the figure show the result of the interaction of seawater (0‰) with a peridotite (5.5‰) at 275° and different water-rock ratios. For a high water-rock ratio, the $\delta^{18}O$ in serpentine reaches the equilibrium value and the temperature of serpentinization can be estimated from it. For a low water-rock ratio, the $\delta^{18}O$ in serpentine is higher than the equilibrium value and the temperature estimated from it in underestimated. (from Rouméjon et al., 2018b)*

2.1.2 The different types of serpentine

Formation of serpentine at the expense of olivine and pyroxene leads to a radical change in density and mineral structure. The density decreases from ~3.3 to ~2.6, and the 3D-structure of olivine and pyroxene is replaced by a layered structure. Serpentine minerals are phyllosilicates. They are composed of alternating tetrahedral (T layers: Si_2O_5) and octahedral (O layers: $Mg_3O_2(OH)_4$) sheets (Figure 2.1-2). T and O layers share oxygen atoms that hold the layers together and each TO group of layers is bounded to other TO groups by hydrogen bounds. However, T and O sheets present a slight geometric misfit that can be accommodated in various ways giving rise to different types of serpentine. The various types of serpentine are not easily differentiated using optical microscopy and other techniques are often required to formally identify them (i.e. XRD, Raman spectroscopy, TEM).

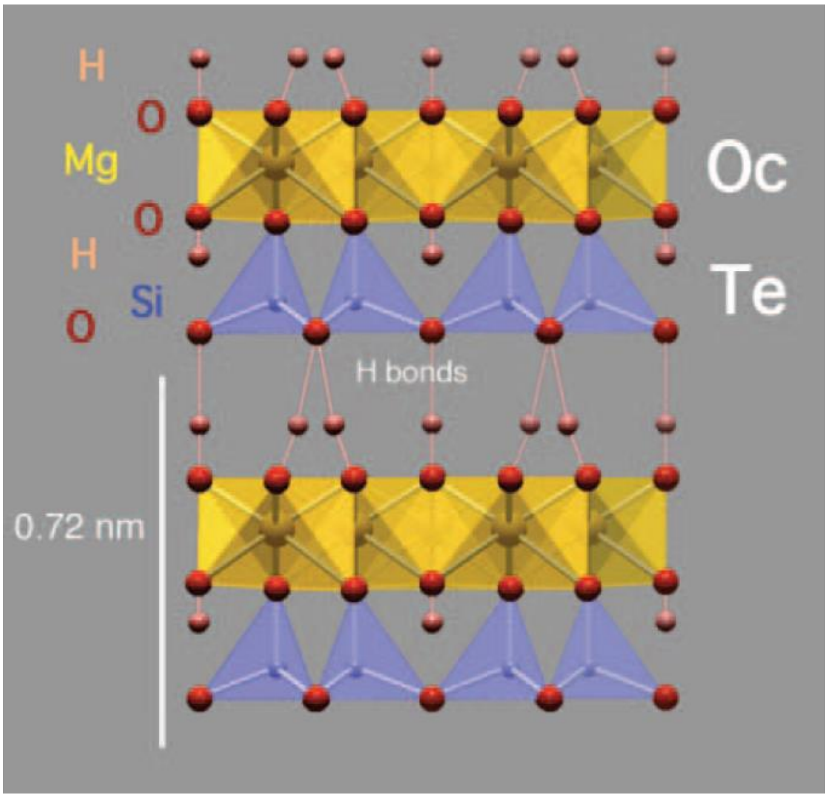

Figure 2.1-2: *Serpentine crystallographic structure, example of the lizardite structure accommodating the misfit between T and O layers by a rotation of the silica tetrahedrons. (from Evans et al., 2013)*

2.1.2.1 Lizardite and polyhedral serpentine

Lizardite is the low-temperature and low-pressure form of serpentine, favored in rock-dominated environments (Evans 2004; Mével, 2003). It is the most thermodynamically stable form below 300°C and is one of the most common types of serpentine. Its structure compensates for the misfit between T and O sheets by a slight rotation of the SiO_4 tetrahedra in the T layer (Figures 2.1-2 & 2.1-3). This keeps layers flat and promotes the hydrogen bonding between each TO group of layers. The misfit can be further compensated by substitutions of Si^{4+} and Mg^{2+} by cations like Al^{3+} and Fe^{3+} stabilizing the whole structure (Dungan, 1979; Evans, 2013). The occurrence of alumina, chromium and iron in pyroxene makes lizardite the favored serpentine form replacing pyroxene (Dungan, 1979; Evans, 2004). The replacement is most of the time topotaxial for pyroxene while it is rarer for olivine. This is linked to the structure of pyroxene that is closer to the structure of lizardite than olivine leading to easier topotactic replacement.

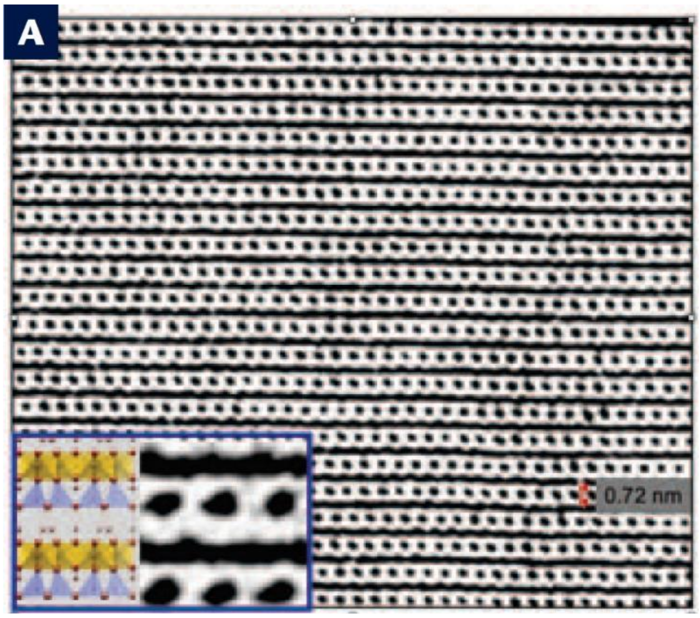

Figure 2.1-3: *Structure of lizardite under high-resolution Transmission Electronic Microscope (TEM). Each dot is a silica tetrahedron within the T layers and black lines are O layers. (from Evans et al. 2013)*

Lizardite is typically well crystalized into elongated pyramidal sectors with triangular sections (Viti & Mellini, 1998; Figure 2.1-4). These sectors organize themselves somehow parallel to each other to form a lamellar texture. Lizardite's flat layers enable it to grow in all directions without constraints, helping its thermodynamic stability. However, lizardite formation can be sluggish. For this reason, it is favored under stable thermodynamic conditions and closed systems (Evans, 2004).

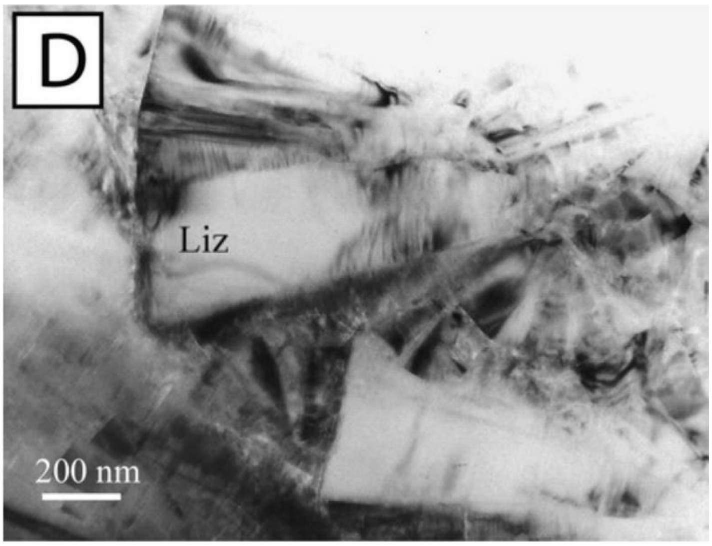

Figure 2.1-4: *Typical triangular sections of lizardite crystals under a TEM. (Andreani et al., 2008)*

Pyramidal shaped lizardite sectors can sometimes arrange radially to form another, less common serpentine type: the polyhedral serpentine (Figure 2.1-5; Andreani et al., 2008). This serpentine type is favored by open spaces, low temperatures and the occurrence of trivalent cations like Fe^{3+} and Al^{3+}. It forms from a gel precursor and grows by addition of layers around the spherical shape. Polygonal serpentine has a typical cross extinction under crossed polarized light with no grain size sorting. The interspace between the spheres is usually filled with fibrous serpentine or poorly crystalline material.

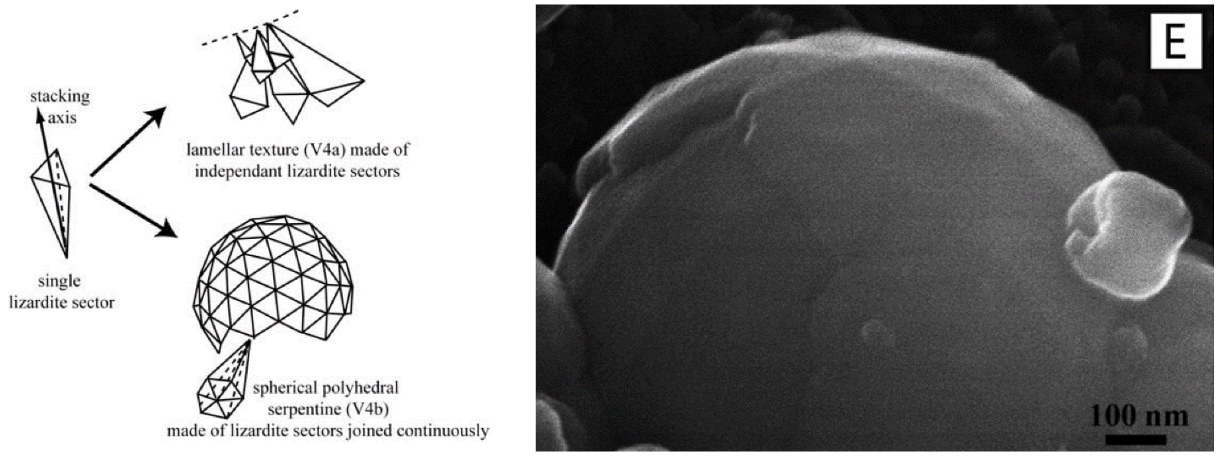

Figure 2.1-5: *On the left, difference between classical lizardite and polyhedral serpentine (from Andreani et al., 2007). On the right, TEM image of a sphere of polyhedral serpentine (from Andreani et al., 2008).*

2.1.2.2 *Chrysotile and polygonal serpentine*

Chrysotile is a polymorph of lizardite encountered in the same pressure-temperature range but that may be stable at slightly higher temperatures. Lizardite is the most stable form thermodynamically. However, the formation chrysotile can be favored by kinetics (Evans, 2004). The misfit between the T and O sheets in chrysotile is accommodated by the curvature of the TO layers (Figure 2.1-6). Chrysotile crystals can thus have a tubular or conical shape (Andreani et al., 2007; Figure 2.1-7), forming a fibrous texture.

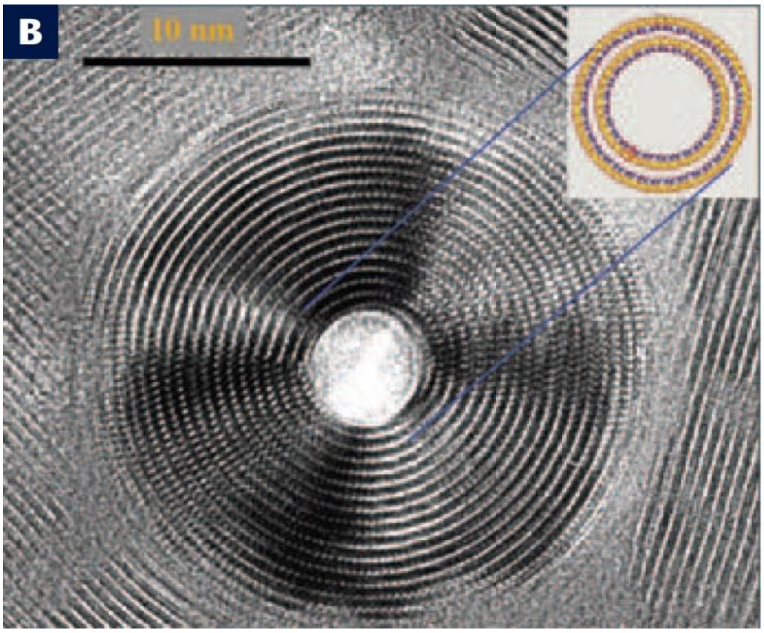

Figure 2.1-6: *Cross section of a chrysotile fiber under high resolution TEM. (from Evans et al., 2013)*

Chrysotile growth can happen either by addition of layers or increase of the fibers' length. The radial growth is limited by the curvature of the layers that must stay within a certain range to accommodate properly the T-O layers misfit. The radius of the chrysotile layers is thus comprised between 35 and 150 Å with an optimal radius of 188 Å (Evans, 2004). As radial growth is limited, the preferred growth mechanism is by elongation of the fibers. This growth makes that chrysotile fibers have a high surface energy compared to lizardite crystals and explain that it is thermodynamically less stable. However, high fluid supersaturation, open spaces and high water-rock ratios seem to favor chrysotile nucleation and growth (Evans, 2004; Normand et al., 2002). Chrysotile is thus typically encountered in open-systems. It is also favored in the replacement of small grains sizes when the dissolution of the original mineral does not limit the reaction (Malvoisin et al., 2012). The difference in terms of favored growth environment between lizardite and chrysotile lead to their common conjoint and contemporaneous occurrence in natural rocks.

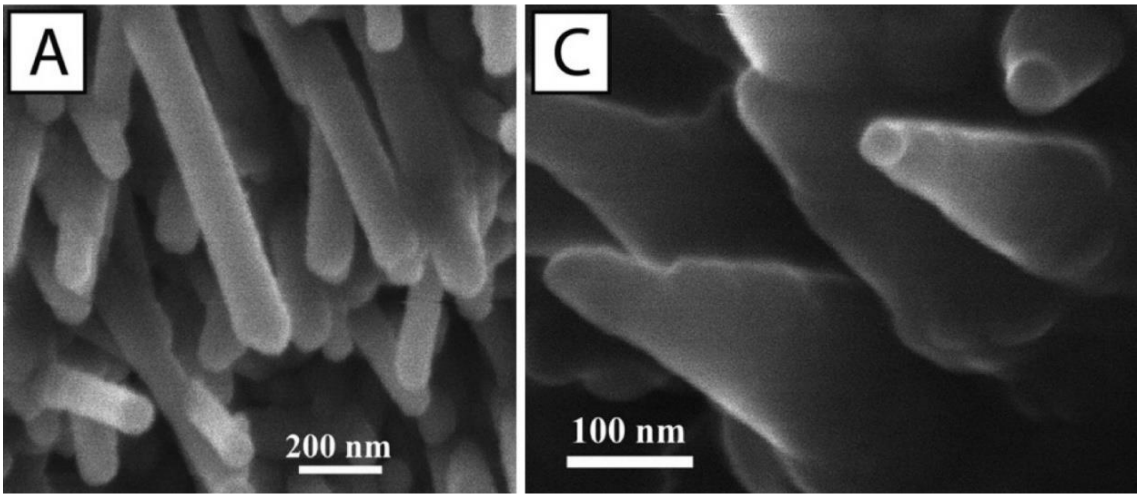

Figure 2.1-7: *TEM images of the two types of chrysotile fibers. On the left the cylindrical fibers and on the right the conical fibers. (from Andreani et al., 2008)*

If conditions are particularly favorable to its growth, it is possible for chrysotile fibers to growth to a larger radius than allowed by its layers' curvature. In this case, the core of the fiber is composed of normal chrysotile while the external part is made of sections of lizardite (Middleton & Whittaker, 1976; Morandi & Felice, 1979). This specific type of serpentine is called polygonal serpentine as its external lizardite composition gives the fibers a polygonal outer shape (Figure 2.1-8; Evans 2004).

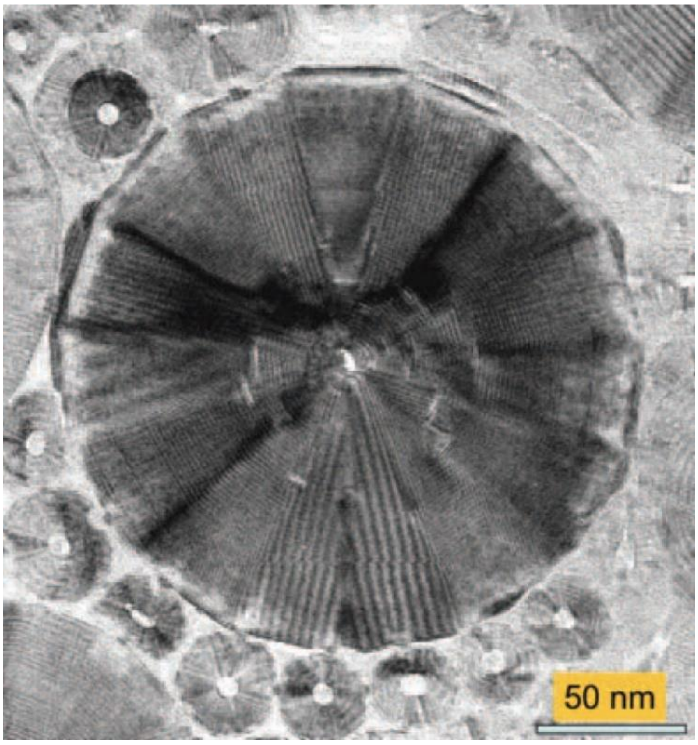

Figure 2.1-8: *Cross section of a polygonal serpentine fiber under high resolution TEM. (from Evans et al., 2013)*

2.1.2.3 Antigorite

The last major type of serpentine, antigorite, is not strictly a polymorph. Its exact chemical formula is: $Mg_{48}Si_{34}O_{85}(OH)_{62}$ making it slightly more silica rich (Si/Mg ~ 0.71 vs ~ 0.67 for lizardite or chrysotile) and slightly less hydrated (OH/(Si+Mg) ~ 0.76 vs ~ 0.8 for lizardite or chrysotile). Its structure is wavy, the misfit between the T and O sheets being compensated by regular inversion of the side of the silica tetrahedrons of the T sheet compared to the O sheet (Figure 2.1-9). Each wave has a radius of approximately 63 Å and an inversion occurs each 16 or 32 Å. The fact that the T layer side compared to the O layer is regularly inverted make the structure stronger than other serpentine types as all the layers are linked by Si-O bonds. This peculiar structure makes antigorite the high pressure and high temperature phase of serpentine. As between each T layer inversion it has a structure similar to lizardite, the two serpentine types share some similarities (Evans, 2013). As lizardite, antigorite tends to form well crystallized crystals and has sluggish nucleation and growth kinetics (Evans, 2004). Its slow kinetics can also arise from its complex structure and are one of the reasons antigorite is favored by high temperatures. It can also accept some Al^{3+} and Fe^{3+} substitutions but to a lesser extent than lizardite (Dungan, 1979). Antigorite often occurs in replacement of chrysotile or lizardite after transitions to high temperature and high-pressure metamorphism or in places of moderate Si-metasomatism (Evans, 2004; Rouméjon et al., 2015; Rouméjon et al., 2019). It can also form directly from olivine hydration in relatively high-temperature and high pressure conditions (e.g. Smith, 2010;

Murata et al. 2009). Antigorite is characterized by a lower affinity with Cl, B and Sr compared to lizardite or chrysotile (Kodolányi & Pettke, 2011).

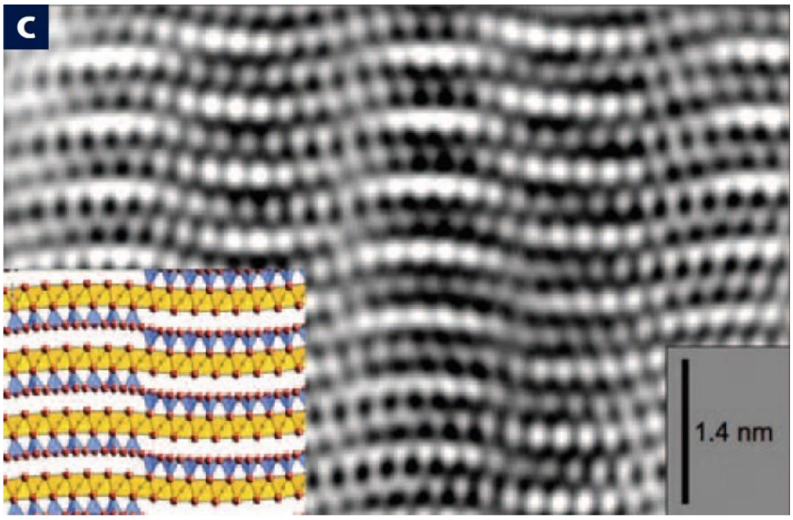

Figure 2.1-9: *Structure of antigorite under high-resolution TEM. (from Evans et al., 2013)*

2.1.3 Microstructures of serpentine

Serpentinization is associated with specific microstructures. The most common is the mesh texture, replacing olivine during pervasive alteration. It is associated with the formation of bastite which is the most common replacement of pyroxene. Mesh texture and bastite are considered as pseudomorphic structures and preserve the shape of the original minerals. Serpentine veins are also an important part of serpentinization. These are often associated with stages of open-system serpentinization. Recrystallization textures, also referred to as non-pseudomorphic textures, are the least common but can occurs in specific settings.

2.1.3.1 Mesh texture and bastite

Mesh texture is the most common microstructure formed during serpentinization. It is composed of a network of serpentine veins delimiting cores (Figure 2.1-10). The mesh veins are usually composed of lizardite, but chrysotile or antigorite have occasionally been reported (e.g. Rouméjon et al., 2015; Wicks and Whittaker, 1977; Boudier et al., 2010). The composition of the cores is more variable, it can be olivine relics, any serpentine mineral or mixture of serpentine mineral. It can also contain brucite, carbonates, iron oxides, and their texture can vary for topotaxial replacement of olivine to fibrous or isotropic. The chemistry of the cores tends to be more diverse than the mesh rims (Rouméjon et al., 2015). The mesh texture is pseudomorphic.

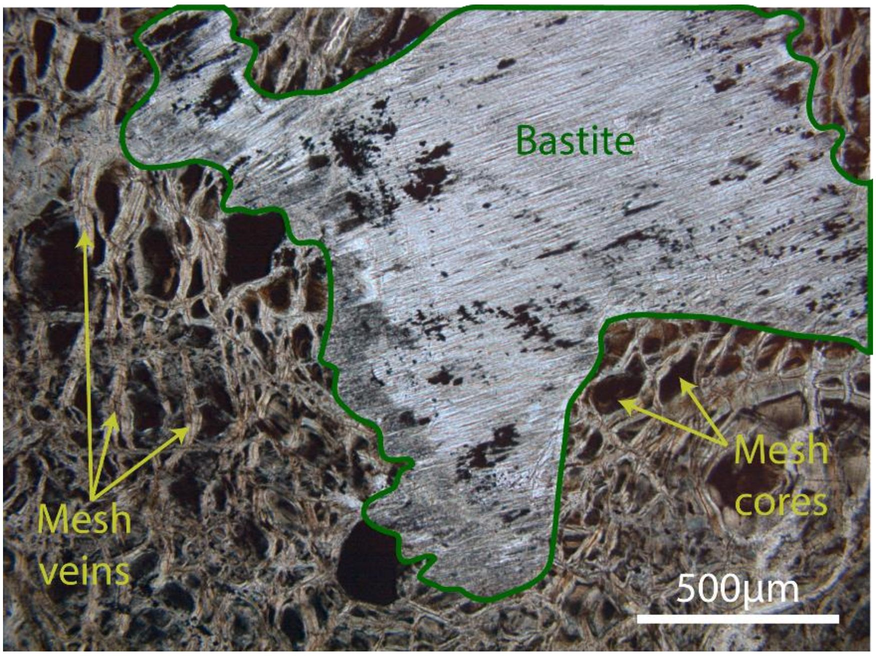

Figure 2.1-10: *Optical picture of mesh texture and a bastite in a fully serpentinized peridotite. Here mesh veins appear in a beige color and mesh cores are dark brown. The bastite is colorless with a marked fibrous texture. Black dots in the bastite are magnetite grains.*

The mesh veins are formed before the replacement of the cores by serpentine (Viti & Mellini, 1998). They formed after the progressive dissolution of olivine by the serpentinizing fluid. Their texture is usually fibrous perpendicular to the dissolution front. In the most common case of lizardite composing the veins, the fibers are composed of characteristic pyramidal sections all pointing towards the core of the mesh (Figure 2.1-11; Andreani et al., 2007; Evans, 2004; Viti & Mellini, 1998). This behavior of lizardite is sometimes referred to as columnar lizardite (Rumori et al., 2004; Boudier et al., 2010). The veins become larger with the progression of the dissolution front; the external parts of the veins are thus younger than their cores. However, the center of the vein is also a fluid pathway, water accessing the serpentinization front by diffusion through the already serpentinized part. It sometimes concentrates magnetite (e.g. Rumori et al., 2004; Oufi et al., 2002). In some cases, the mesh veins develop until no olivine is left, this leads to the hourglass texture (Figure 2.1-11; Evans, 2004; Wicks and Whittaker, 1977). This texture is not encountered often though, most of the time cores are visible, either composed of olivine relics or alteration phases (Figure 2.1-11). The formation of the mesh veins is often considered to form under low water-rock ratio, in closed system, and under static, thermodynamically controlled conditions (Andreani et al., 2007; Mével, 2003; Viti & Mellini, 1998). If the mesh cores are serpentinized, they display a wide diversity of textures and compositions depending on the origin of the studied sample, indicating a large variety of possible conditions of formation. There is a consensus that mesh core form at high water-rock ratio and under kinetically controlled conditions, likely during open system phases of alteration (Viti & Mellini, 1998).

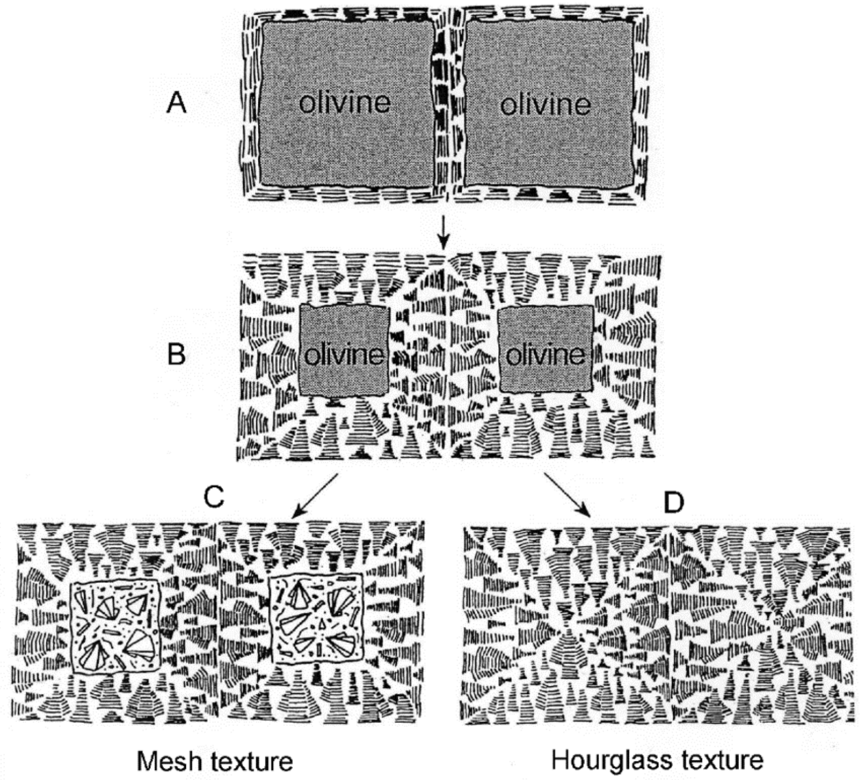

Figure 2.1-11: *Schematic representation of the formation of the mesh and hourglass textures. (from Evans, 2004)*

Bastite is the texture obtained after pyroxene during serpentinization (Figure 2.1-10). When composed of serpentine, its favored polymorph is lizardite (Dungan, 1979; Evans, 2004). This is mostly due to the presence of Al in the pyroxene that increase the thermal stability of lizardite (Caruso & Chernosky, 1979; Dungan, 1979). However, it can also be composed of other fibrous minerals associated with serpentinization such as chlorite or talc. The replacement of pyroxene is pseudomorphic and in general topotaxial. Mesh texture and bastite tend to retain the chemical signature of the original mineralogy they replace (Andreani et al., 2007; Dungan, 1979; Viti & Mellini, 1998).

2.1.3.2 Veins

Serpentine veins are common during serpentinization and display a variety of shapes and textures. They are concentrated in domains of high fluid flow and high degree of serpentinization (Rouméjon et al., 2015) but are also common elsewhere.

Veins are healed fractures implying that they represent former pathways for fluids. As fracturing may be associated with a local decrease in fluid pressure, vein opening favors serpentine growth by decreasing the solubility of SiO_2 (Andreani et al., 2007). It favors kinetic nucleation and growth explaining why chrysotile is favored in veins (Evans et al., 2004; Mével, 2003; Wicks & Whittaker, 1977). The composition of the veins gives direct information on the fluid they formed from. The veins wall morphology and internal texture are indicative of the opening mechanism of the vein (e.g. Andreani et al., 2007; Wicks & Whittaker, 1977). Matching walls indicate an opening by brittle deformation, irregular, non-matching walls indicate a dissolution of the wall-rock by the serpentinizing fluids (Figure 2.1-12a). Textures inside the veins may vary depending on the timing between opening and filling of the vein (Andreani et al., 2007). For example, fibrous veins that are banded parallel to the vein walls (Figure 2.1-12b) are typical for a faster vein opening than the crystallization rate with a repeated crack and seal mechanism (Andreani et al., 2004; Ramsay, 1980). The bandings are typically made of repeated sequences of poorly crystalline serpentine (sometimes called proto-serpentine), chrysotile and polygonal serpentine. Fibrous veins with fibers perpendicular to the veins walls (Figure 2.1-12c) are typical of veins opening in a single event and at constant rates similar or slower than the fibers growth. Veins that have isotropic or close to isotropic textures (Figure 2.1-12d) are indicative of rapid filling of the vein open space. These veins are filled by metastable proto-serpentine or silica gels that can evolve with time into more stable phases. Other textures exist such as columnar, spherulitic, botryoidal textures (Wicks & Whittaker, 1977). If grains are visible, they can give information about nucleation and growth rates. Deformation features are sometimes observed in veins, particularly in fibrous ones. Fibrous veins are generally made of chrysotile or polygonal serpentine (e.g. Morandi & Felice, 1979; Wicks & Whittaker, 1977). Veins that are not fibrous often have a waxy or milky macroscopic aspect (e.g. Wicks & Whittaker, 1977).

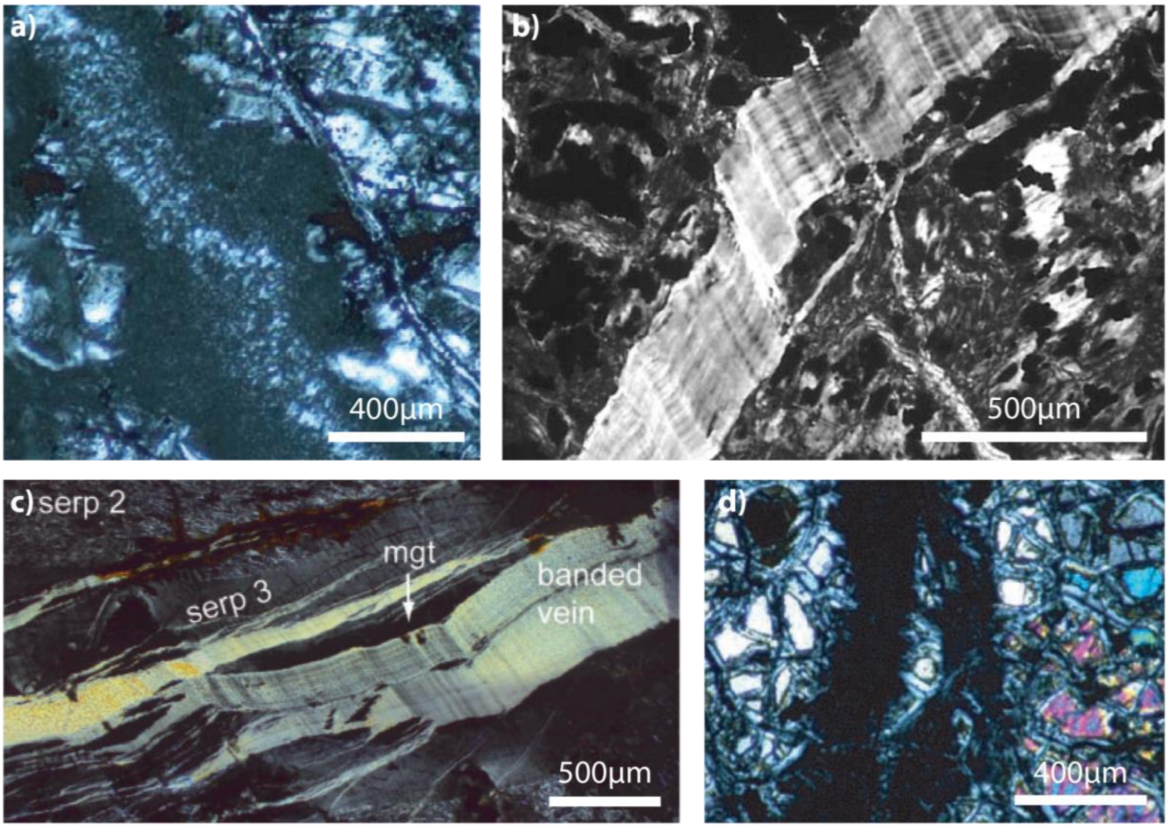

Figure 2.1-12: *Examples of serpentine veins textures under the optical microscope. All the pictures are taken with crossed polarizers. a) Vein with irregular walls (from Andreani et al., 2007). b) Fibrous vein with a banded texture parallel to the vein walls (from Andreani et al., 2004). c) Fibrous vein with a*

banded texture perpendicular to the vein walls (from Rouméjon et al., 2015). d) Amorphous vein (from Andreani et al., 2007).

2.1.3.3 Recrystallization processes

Recrystallization textures in serpentinites are also referred to as non-pseudomorphic texture in contrast to mesh texture and bastite that are pseudomorphic textures. Two mains textures are described for recrystallization: interpenetrating and interlocking textures (Figure 2.1-13; Wicks & Whittaker, 1977). Recrystallization is often associated with antigorite, particularly in rocks that have undergone high temperature or pressure metamorphism. The transition to antigorite occurs around 300°C (Evans, 2004). Recrystallization textures are otherwise present in main fluid pathways and rare elsewhere. Recrystallization processes tend to homogenize the rock chemistry where they occur (Rouméjon et al., 2015) and can lead to the loss of some FME depending on the differences in affinity between the former and new mineralogy (e.g. Kodolányi & Pettke, 2011).

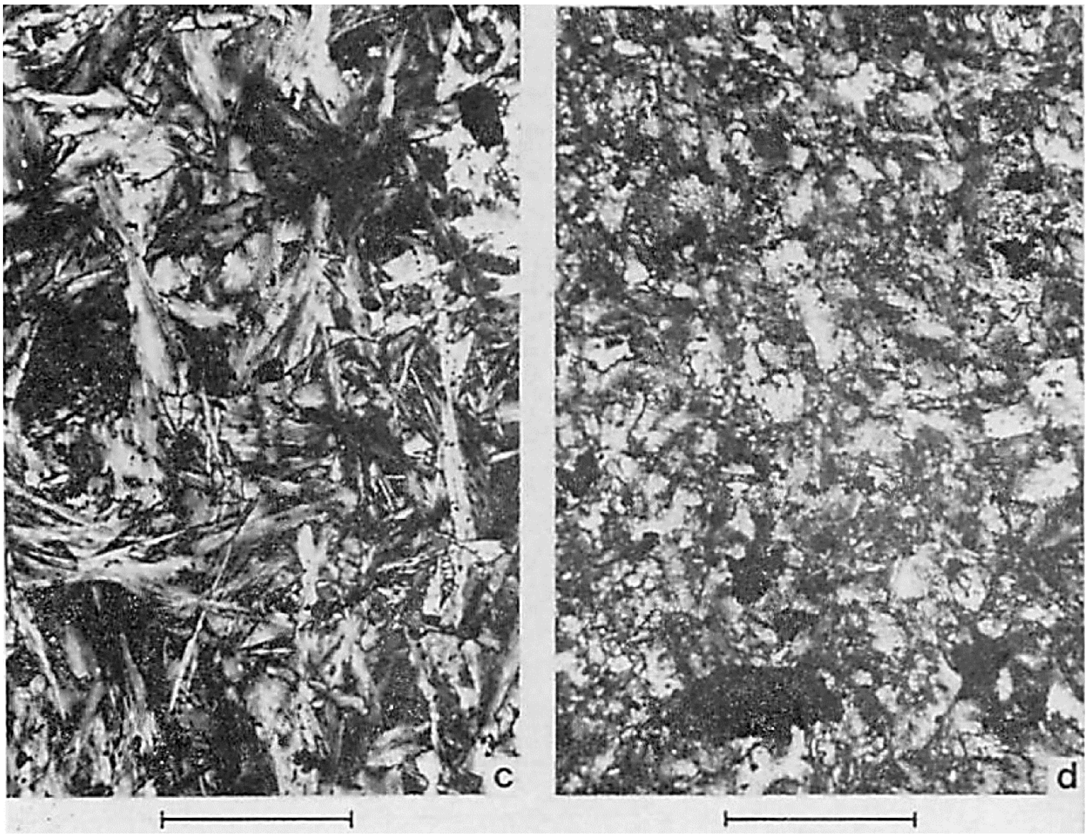

Figure 2.1-13: *Recrystallization textures. On the left the interpenetrating texture and on the right the interlocking texture. Both pictures show antigorite. The bars represent 200 µm. (Wicks & Whittaker, 1977)*

2.2 Geological settings of serpentinization

The two ingredients required for serpentinization to occur are water and peridotite. However, mantle peridotite is separated from surface water reservoirs by the Earth crust. Water thus needs pathways to access peridotite. These pathways are mainly represented by faults. While faults cutting through the entire continental crust are rare or non-existent, faults cutting the thin oceanic crust (6 km in average; Chen, 1992) are more common. In addition, the oceanic crust is in permanent contact with the largest surface water reservoir on Earth. Tectonically active zones such as mid-oceanic ridges and subduction zones are therefore loci of extensive serpentinization (Figure 2.2-1).

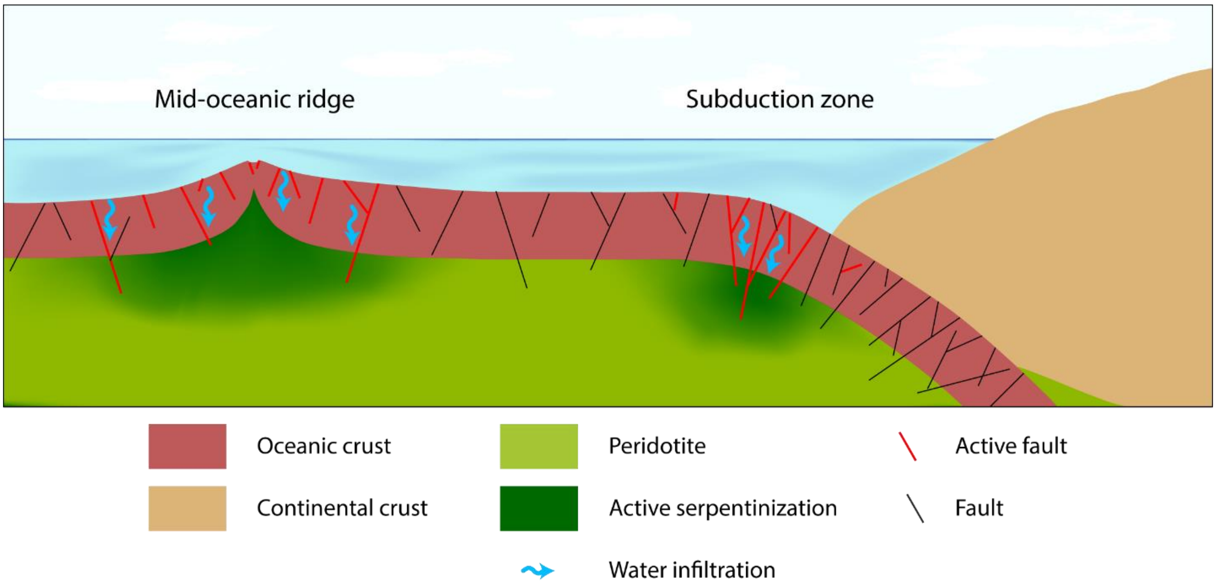

Figure 2.2-1: *Schematic representation of the preferential zones of serpentinization.*

Significant serpentinization also occurs along passive or magma-poor continental margins (e.g. Bayrakci et al., 2016; Lundin & Doré, 2011; Pérez-Gussinyé & Reston, 2001) where similar conditions as along oceanic ridges are gathered (thin crust, tectonic extension, and extensive amount of water). In addition, minor serpentinization occurs during the weathering of continental ultramafic bodies. These two settings will however not be treated in this part.

2.2.1 The oceanic lithosphere

The oceanic lithosphere covers the two thirds of the Earth surface. It forms along mid-oceanic ridges where variations in thermal regime lead to different types of lithosphere. While getting older, the oceanic lithosphere is pushed away from the ridge and becomes thicker and stronger due to conductive cooling (Richardson et al., 1995). It will eventually reach a subduction zone and be recycled into the mantle. During its life, the oceanic lithosphere interacts with seawater leading to its hydration and the production of hydrothermal activity.

2.2.1.1 Types of oceanic lithosphere

The oceanic lithosphere is formed along the mid-oceanic ridge axes, also called spreading centers. Extension of lithosphere happens within 2 km around the ridge axis (Morgan et al., 1987) by a combination of tectonic and magmatic activity. The relative contribution of these processes is controlled by the thermal regime of the ridge and leads to different types of oceanic lithospheric sections. Thermal gradient along ridges range from almost purely controlled by conductive cooling to the very steep gradients controlled by pronounced upwelling of the warm mantle.

The study of the composition and structure of the oceanic lithosphere is made through a combination of geophysical and petrographic studies. While geophysical studies can be tricky but are generally feasible *in situ*, samples from the current oceanic lithosphere are limited and sometimes impossible to obtain. A way to avoid this problem is to study ophiolitic bodies. These bodies are mostly composed of basalt, gabbro and peridotite with various degrees of metamorphism and deformation and are easy to access as they are emplaced on the continental crust. Comparisons between geophysical data and rock samples form current oceanic lithosphere have permitted identification of ophiolites as pieces of former oceanic lithosphere. Studies of ophiolites provide valuable sources of information to understand contemporary processes within the oceanic lithosphere, in particular within the lithospheric mantle.

Magmatic activity has a major role in the formation of new lithosphere. Melting at ridge axis occurs because of adiabatic upwelling of the mantle (Figure 2.2-2). Shallow (warm) mantle under ridge axes induce a steep thermal gradient. The decompression of peridotite at normal mantle temperatures allows it to partially melt. The primitive mantle has a lherzolitic composition (Bickle et al., 1976; Maaløe & Steel, 1980) with olivine, orthopyroxene and clinopyroxene as its main minerals. Partial melting leads to preferential melting of clinopyroxene, progressively modifying the remaining depleted peridotite composition to harzburgitic with olivine and orthopyroxene as its main minerals. The melt produced has a basaltic composition.

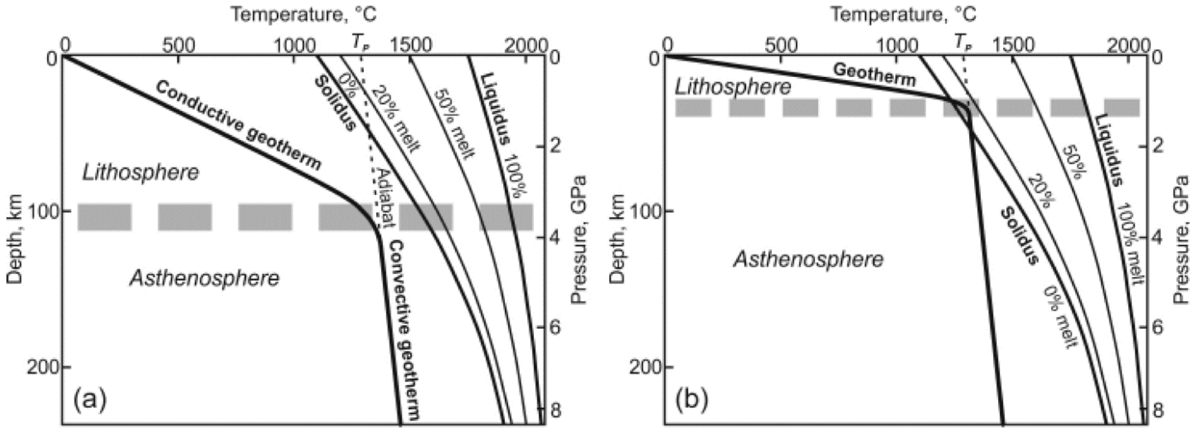

Figure 2.2-2: *Oceanic geotherm and peridotite solidus away from any ridge axis (a), and at a ridge axis (b). The adiabatic upwelling of the mantle at the ridge axis steepens the lithospheric thermal gradient and enables the oceanic geotherm to cross the peridotite solidus inducing the partial melting of the upper mantle. (from Gill, 2010)*

Where the mantle upwelling is most pronounced, magmatic activity produces large quantities of melt that form the oceanic crust. This crust is ca. 6 km thick and composed from top to bottom of pillow lavas, formed by the quenching of the melt by cold sea water, basaltic vertical (sheeted) dykes and massive gabbros. These three layers are referred to layers 2A, 2B and 3 respectively in seismic studies (e.g. Christensen & Salisbury, 1975; Mutter & Mutter, 1993; Talwani et al., 1971). Below this crust is the lithospheric mantle. The Moho transition zone (MTZ) is mainly composed of dunite with residual harzburgite below (Figure 2.2-3). The dunite is formed by interaction of harzburgite with the basaltic melt through preferential dissolution of the orthopyroxene (Kelemen et al., 1995), leaving only olivine as the main mineral. The MTZ is interpreted as a zone of melt stagnation (Boudier & Nicolas, 1995). This “complete” oceanic lithospheric section is referred to as the Penrose model (Anonymous, 1972).

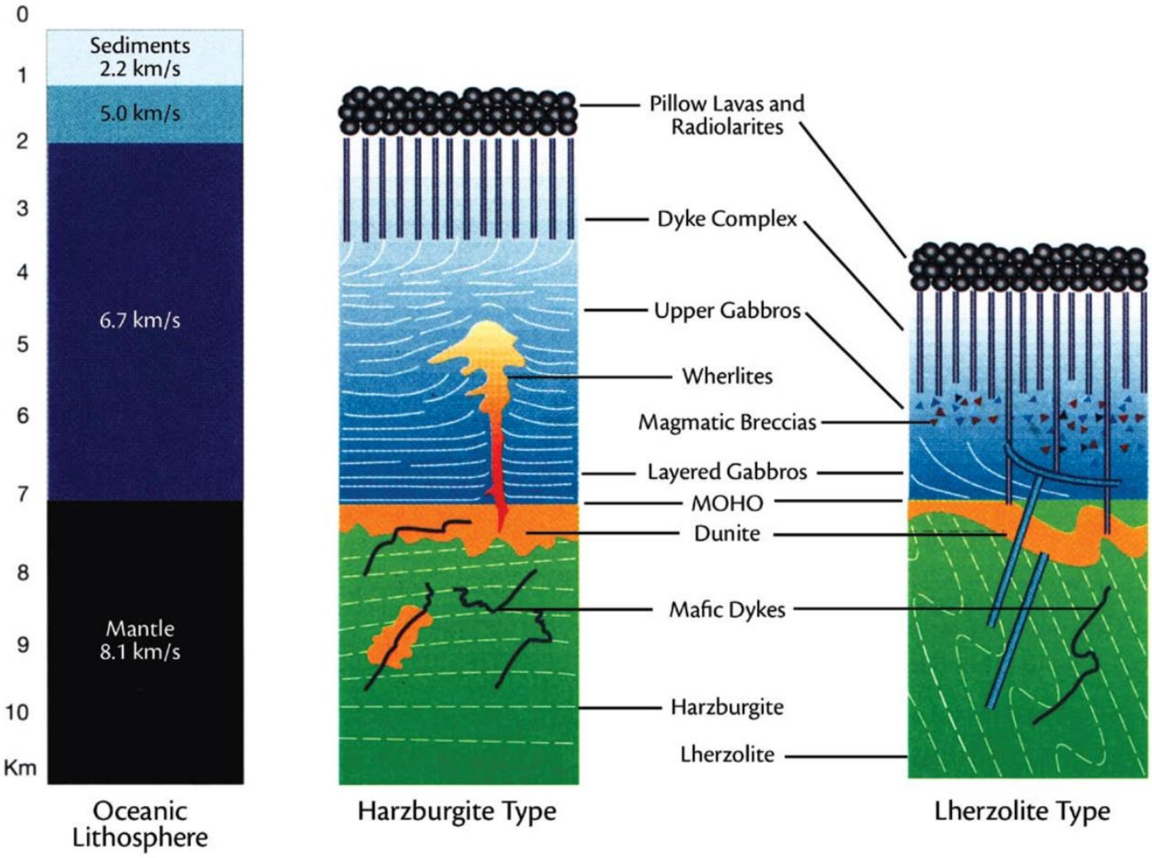

Figure 2.2-3: *Models of oceanic lithospheric sections (after Boudier & Nicolas, 1985). The left column shows the P-waves velocities in the different layers of the lithospheric section. The central column shows the typical oceanic lithospheric section after the Penrose model as observed in ophiolites with an harzburgitic mantle composition. The right column shows a variation of this model in reduced magmatism settings as observed in ophiolites with a lherzolitic mantle composition. (from Snow & Edmonds, 2007)*

In places where the intensity of mantle upwelling is reduced, the melt production is also reduced, and the composition of the residual mantle is less modified by partial melting. It stays closer to its original lherzolitic mantle composition (Figure 2.2-3). Less melt implies that the magmatic crust is thin. The gabbro layer is the most affected. As the lithosphere is colder, the magma has more difficulty to reach shallower levels. Instead of forming a continuous layer on the surface, some of it is trapped within the peridotite in the form of gabbroic plutons (Figure 2.2-4). The crust is then made up of a basaltic layer on top of a mixture of peridotite and gabbro plutons at depth (Cannat, 1993; Hess, 1962). This model is known as the “plum-pudding” lithosphere (Cannat 1996). In the most extreme cases, if the lithosphere is too cold, very little melt reaches the seafloor, only forming a thin, discontinuous basaltic layer, with peridotite directly exposed at the ocean floor (Sauter et al., 2004).

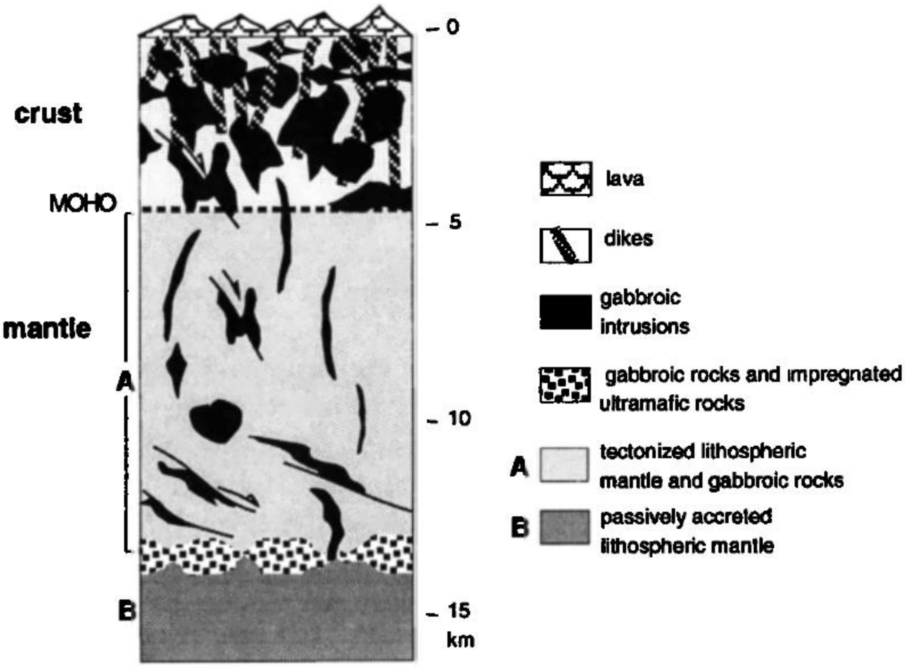

Figure 2.2-4: *Plum-pudding model. (from Cannat 1996)*

Once formed, the oceanic lithosphere is pushed away of the ridge axis. It progressively cools down by conductive cooling. This causes a deepening of the brittle-ductile transition in the mantle peridotite and consequently thickens the lithosphere. A steady thickness (ca. 100 km) is reach after 70-80 My when the thermal structure of the oceanic lithosphere has reached a steady state (Parson & Sclater, 1977; Richardson et al., 1995; Stein & Stein, 1992).

2.2.1.2 Hydrothermal activity

Circulation of seawater within the oceanic lithosphere leads to the onset of hydrothermal activity at the seafloor. Cold water infiltrates the lithosphere through the porosity of the crust and through faults. It is warmed up by a heat source at depth and the associated reduction in density leads to its return towards the ocean floor. During its passage through the lithosphere, the seawater interacts with the surrounding rocks leading to the fluid compositional evolution and rock alteration. The composition of the hydrothermally evolved fluid exiting through the hydrothermal vents help put constraints on the rock and alteration types at depth.

Hydrothermal activity is mostly found in relatively young lithosphere (less than ca. 65 Ma on average; Stein & Stein 1994). Mid-oceanic ridges, that represent a major source of heat in the oceans (Chapman & Pollack 1975; Davies & Davies, 2010; Sclater et al., 1980), concentrate approximately 30% of the hydrothermal activity in their vicinity (within 1 Ma; Stein & Stein 1994). Seawater circulation in hydrothermal conductive cells help dissipate the heat transferred from the Earth’s interior. The cooling of the lithosphere and the closure of the crust porosity (Crawford et al., 1999) as the lithosphere ages are major factors leading to the reduction in hydrothermal activity. This leads to the age of the lithosphere being the main parameter controlling the intensity of the hydrothermal activity (Stein & Stein 1994).

Two end-members of oceanic hydrothermal systems have been observed: the black smokers and the white smokers. The white smokers are low temperature vents (≈40-75°C). Their heat source is inferred to be associated with the exothermic nature of serpentinization (Kelley et al., 2001). Low temperature hydrothermal fluids typically have a high pH (e.g. Kelley et al., 2001). White smokers are associated with brucite and carbonates deposition that can form high chimneys (Kelley et al., 2001). The black smokers are high temperature vents (>300°C). Although serpentinization may contribute heat to drive hydrothermal activity, it is not sufficient to produce such high temperature. Black smokers require magmatic heat and hence occur exclusively along mid-ocean ridges. The hydrothermal fluids emitted by black smokers typically have a low pH (e.g. Charlou et al., 2002; Douville et al., 2002). Their black color is due to their high sulfur and metals contents (Fouquet et al., 1994; Fouquet, 1997). In many cases, hydrothermal systems (black or white smokers), host intense biological life, in particular where serpentinization is involved (Ohara et al., 2012; Schrenk et al., 2013). Hydrothermal systems associated with serpentinization may even be the site for the origin of life on Earth (Schulte et al., 2006; McCollom & Seewald, 2007; McCollom & Seewald, 2013).

A major factor controlling hydrothermal fluids composition is the composition of the rock hosting the hydrothermal system. Basalt-hosted systems are characterized by moderate dissolved SiO_2 concentrations and low H_2 emissions, while peridotite-hosted systems and characterized by low dissolved SiO_2 concentrations and important H_2 emissions (Wetzel & Shock, 2000). Peridotite-hosted hydrothermal systems are associated with intense serpentinization and are consequently characterized by high H2 and CH4 emissions (Kelley et al., 2001; Charlou et al., 2002; Douville et al., 2002). Mg-Ca exchanges between the fluid and the rock during serpentinization (Klein & Le Roux, 2020) lead to the enrichment of Ca in fluids emitted by peridotite-hosted hydrothermal systems (Seyfried et al., 2015). Experiments and thermodynamic models show that the temperature of serpentinization further controls the SiO_2 and H_2 concentrations and the pH of the hydrothermal fluids (e.g. Berndt et al., 1996; Allen & Seyfried, 2003; McCollom & Bach, 2009; Klein et al., 2013). Low temperatures being associated with lower SiO2 contents, more H_2 emissions and higher pH. The SiO_2 metasomatism associated with hydrothermal activity is characteristic of seafloor serpentinization and is responsible for the rare appearance of brucite in abyssal serpentinized peridotite (Peters et al., 2020).

Other factors can influence the temperature and composition of the hydrothermal fluid such as the distance to their heat source, or a specific geological context. For example, hydrothermal vents located right above the ridge axis have higher temperatures than those that are off-axis (Haymon et al., 1991; Toomey et al., 2007); the emissions of black smokers vary in time with the intensity of the volcanic activity associated with their magmatic source (Fouquet et al., 1994); hydrothermal activity from ridge axes located in the back arc of subduction zones have a specific elemental signature (Fouquet et al., 1991).

2.2.2 Mid-ocean ridges

Ocean spreading centers represent ca. 55 000 km of variably active volcanic chains (Solomon, 1989) located in the middle of the oceans at the junction between divergent tectonic plates (Figure 2.2-5). Extension along mid-oceanic ridges is accommodated by a combination of magmatic and tectonic processes. As seen in the previous section, the intensity of the magmatic activity determines the composition of the lithospheric section. The magmatic activity along mid-oceanic ridges is also one of the major processes by which heat is released from the Earth's interior (Chapman & Pollack 1975; Davies & Davies, 2010; Sclater et al., 1980). The tectonic activity controlling the structure of the seafloor is closely associated with seismic activity. Mid-oceanic ridges have characteristic spreading rates describing the speed of the oceanic extension. This number correlates with the thermal regime of the ridges and is used to classify them. Three main mid-ocean ridge types have been defined: fast ridges for spreading rates above 80 mm/yr, slow ridges for spreading rates between 20 and 55 mm/yr and ultra-slow ridges for spreading rates below 12 mm/yr. There are two supplementary mixed types corresponding to mid-ocean ridges with spreading rates between 55 and 80 mm/yr (intermediate spreading ridges) showing characteristics of fast and slow spreading ridges, and ridges with spreading rates between 12 and 20 mm/yr showing characteristics of slow and ultra-slow ridges.

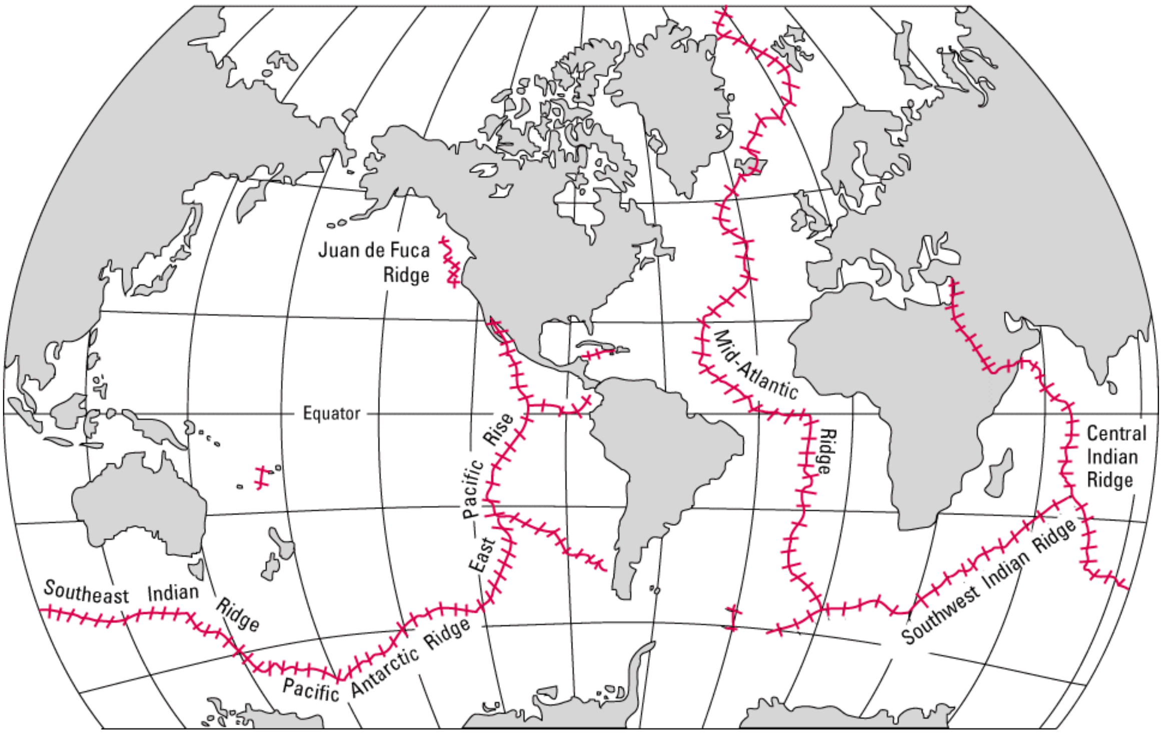

Figure 2.2-5: *Location of the mid-oceanic ridges (red hatched lines). (source: USGS, U.S Geological Survey)*

2.2.2.1 Fast spreading ridges

Fast ridges represent 16% of the ridges and produce 40% of the oceanic crust (Solomon, 1989). They are primarily defined by active magmatic and volcanic activity. The fastest ridge in the world is the East-Pacific Rise (130-150 mm/yr; DeMets et al., 1990 & 1994). Fast ridges are characterized by intense magmatic and volcanic activity taking up most of the oceanic extension. They are associated with the ideal Penrose model of lithospheric section (Figure 2.2-3; Anonymous, 1972). Their high temperatures are not favorable for tectonic extension, limited to small normal faults parallel to the ridge axis.

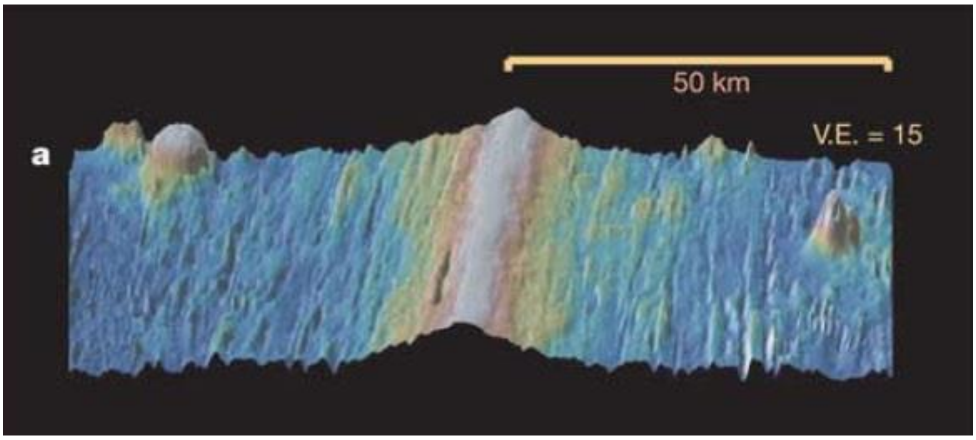

Figure 2.2-6: *Topography of a fast spreading ridge (EPR). The small axial graben is not visible at the scale of this picture. The seafloor is relatively smooth, the small-scale wrinkles are due to normal faulting. (from Buck et al., 2005)*

The topography of the seafloor is symmetrical relative to the ridge axis and rather smooth. It is characterized by an axial thermal uplift with a small axial graben (up to 50 meters deep and a few hundred meters wide) where volcanic activity is intense (Figure 2.2-6; Bourgault et al., 1993). Fast ridges are cut into ten to hundreds of kilometers long segments by transform faults that offset the different ridge segments relative to each other. They represent several kilometers deep troughs perpendicular to the ridge axis and are one of the rare places along fast spreading ridges where mantle rocks can be exposed at the seafloor and extensive serpentinization observed (e.g. Rupke & Hansclever, 2017). While shearing due to ridge extension occurs between the offset ridge segments, the external parts of the transform fault only represent a discontinuity in the age of the lithosphere on each side of the fault (Figure 2.2-7). The high temperatures of fast spreading ridges prevents any major seismicity. Faulting is only expressed by small normal faults parallel to the ridge axis and by transform faults, the latest concentrating most of the seismic activity (Stein and Woods 1989).

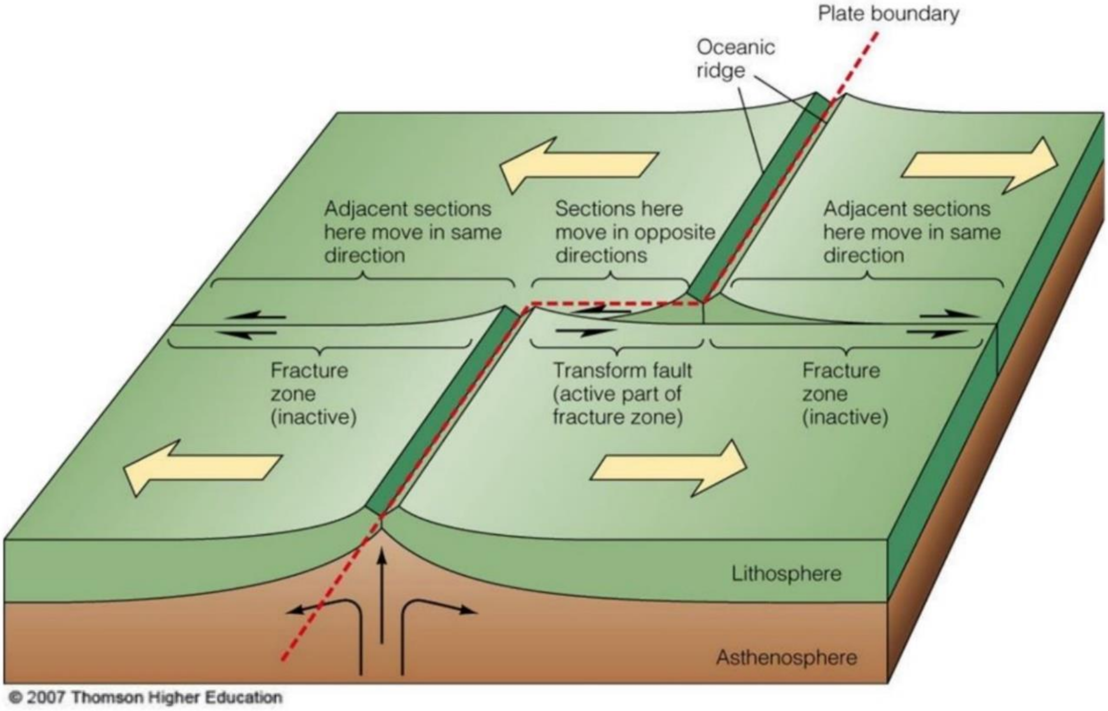

Figure 2.2-7: *Schematic representation of a transform fault zone.*

Magmatic and volcanic activities along mid-oceanic ridge are fed by the melting of the asthenospheric mantle. The complete melting zone extend to at least 100 km depth within the asthenosphere and is several hundreds of kilometers wide (Forsyth et al., 1998). Most of the magmatic activity is located at the ridge axis. However, some volcanic activity has also been reported off-axis, a few kilometers from the ridge (Canales et al., 2012). Along fast spreading ridges, below the ridge axis, the magmatic chamber feeding magmatic and volcanic activities is composed of at least two melt lenses located at different depths and linked to each other by partially molten rocks (2.5-18 % of melt) (Crawford et al., 1999) and/or multiple melt lenses (Marjanovic et al, 2014). The upper lens is located ca. 4 km depth, within the magmatic crust and is ca. 1 km wide. It is not completely continuous along axis, alternating 2-4 km long melt lenses with 15-20 km long mush lenses (Singh et al., 1998). The lower mesh lens, located at the base of the crust, is much larger and extend ca. 10 km off-axis (Crawford et al., 1999). It also shows some variations in melt percentage with zones of more intense melt concentration ≈ 25 km-spaced (Toomey et al., 2007). The composition of the oceanic crust between the upper and lower melt lenses is still debated. Two end-member models have been proposed (Figure 2.2-8). The gabbro glacier model (Quick & Denlinger, 1993; Figure 2.2-8a) implies that all the melt gathered in the lower magmatic crust is transported directly to the upper magmatic chamber. The heat generated by the presence of the melt leads to the formation of a zone of mush. The second model is the sheeted sill model (Kelemen et al., 1997; Figure 2.2-8b). In this second model, the melt is transported from the lower melt lens to the upper melt lens through a succession of other melt lenses. As diverse arguments support one or the other of these models (e.g. Cherkaoui et al., 2003; Marjanovic et al, 2014; Perk et al., 2007;

VanTongeren et al., 2015), it may be that the actual composition and structure of the oceanic crust below the ridge axis is intermediate between the gabbro glacier and the sheeted sill models (e.g. Boudier et al., 1996; Buck, 2000; MacLeod & Yaouancq, 2000).

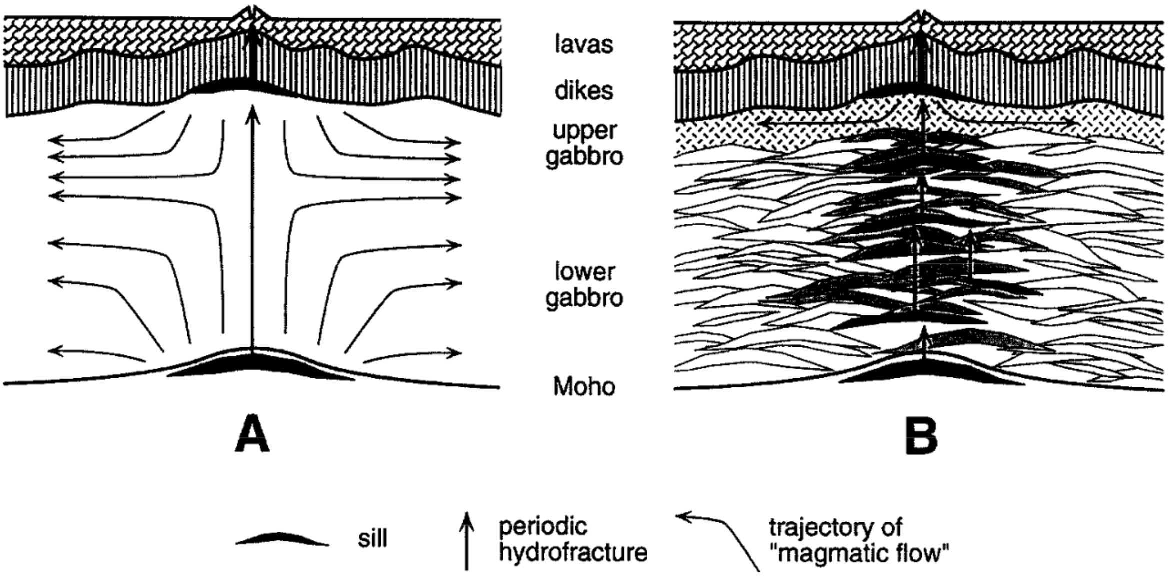

Figure 2.2-8: *Model end-members of the formation of the lower oceanic crust: the gabbro glacier model (A) and the sheeted sill model (B). (from Kelemen et al., 1997)*

Fast spreading ridges are characterized by intense high temperature hydrothermal activity close the axial high (Bourgault et al., 1993), in association with its magmatic and volcanic activity. It is favored within 1 km of the ridge axis due to high porosity that is closed as the lithosphere is pushed away (Crawford et al., 1999). Numerical models estimate that serpentinization along fast spreading ridges (not considering transform fault zones) is likely only local (Iyer et al. 2010). Extensive serpentinization along fast spreading ridges is thus only expected at transform faults.

2.2.2.2 Slow spreading ridges

Slow spreading ridges are the most common ridges together with intermediate spreading ridges. They represent 41% and 23% of the ridges respectively and produce 26% and 29% of the oceanic crust respectively (Solomon, 1989). A typical slow ridge is the Mid-Atlantic Ridge (MAR; 25 mm/yr on average; DeMets et al., 1990 & 1994); a typical intermediate spreading ridge is the South-East Indian ridge (69-75 mm/yr; Sempéré et al., 1997; DeMets et al., 1990 & 1994). These two ridge types are characterized by reduced magmatic activity with significant variations in intensity between segment centers and segment ends, close to transform faults (Figure 2.2-9). The typical lithospheric section varies from the Penrose model to the “plumb-pudding” model.

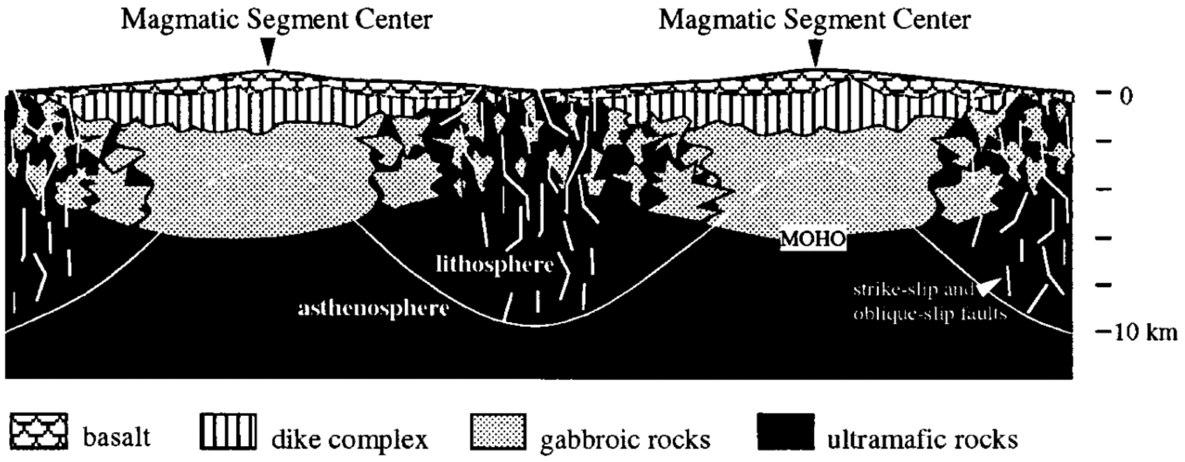

Figure 2.2-9: *Schematic view of the variations in magmatic activity along a slow-spreading ridge (from Cannat et al., 1995)*

The topography of the sea-floor at slow ridges and intermediate ridges is rough and the ridge axis is defined by a large and deep rift (a few kilometers depth and up to several tens of kilometers wide; Bourgault et al., 1993; Mutter & Karson, 1992). Thermal uplift is considerably weaker than along the fast spreading ridges if not absent. In sections where magmatism is still the dominant extensional process, the ridge profile is symmetrical (Figure 2.2-10a & upper part of Figure 2.2-11); in the slowest parts, tectonic extension becomes the main extensional process and leads to the formation of long-lived detachments and asymmetrical ridge profile (Figure 2.2-10b-c & lower part of Figure 2.2-11). Asymmetric extension represents half of the slow ridges (Escartin et al., 2008) and likely a lesser percentage of intermediate ridges.

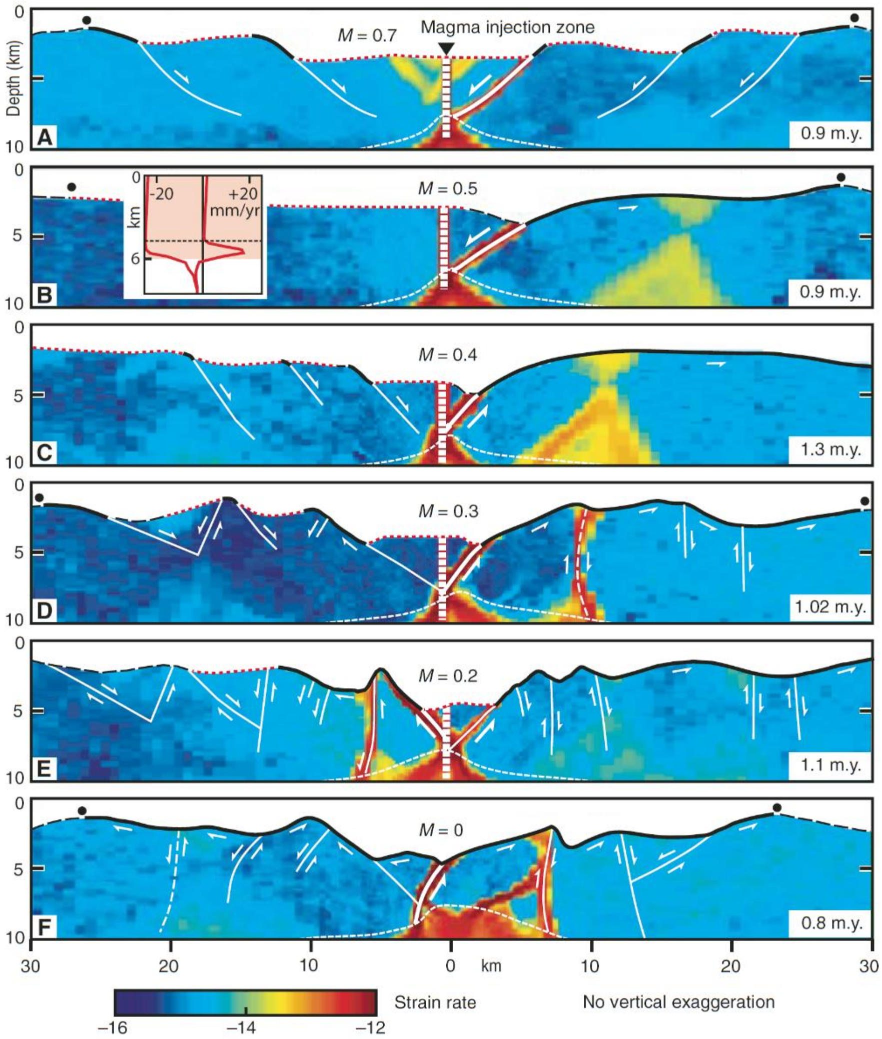

Figure 2.2-10: *Numerical modelling of the seafloor deformation depending on the relative contribution of magmatic vs tectonic extension (M = 1 purely magmatic, M = 0 purely tectonic). (from Tucholke et al., 2008)*

The globally colder thermal gradient along slow and intermediate spreading ridges compared to fast spreading ridges leads to more active tectonics. Normal faulting is more developed and is responsible for the rough topography of the seafloor (Mutter & Karson, 1992). Transform faults are similar to those of fast ridges. They expose peridotite, are the loci of extensive serpentinization, and cut ridges into segments. Slow ridges are characterized by important variations in the proportion of magmatic vs tectonic extension, especially between segments' centers and ends, the segments ends being colder than the segment centers. Segment centers are typically controlled by magmatic extension with similarities with fast spreading ridges. The topographic profile is symmetrical, the lithospheric section is close to the Penrose model and the volcanic activity, mostly confined to the large axial valley, is constant. Segment ends are typically controlled by tectonic extension with an asymmetric topography and magmatic activity is limited to short lived magmatic bodies (Mutter & Karson, 1992), leading to a "plum-pudding" type of lithosphere (Cannat et al., 1996). Colder ridge portions are associated with lower degrees of partial melting and deeper melt sources (Escartin et al., 2008).

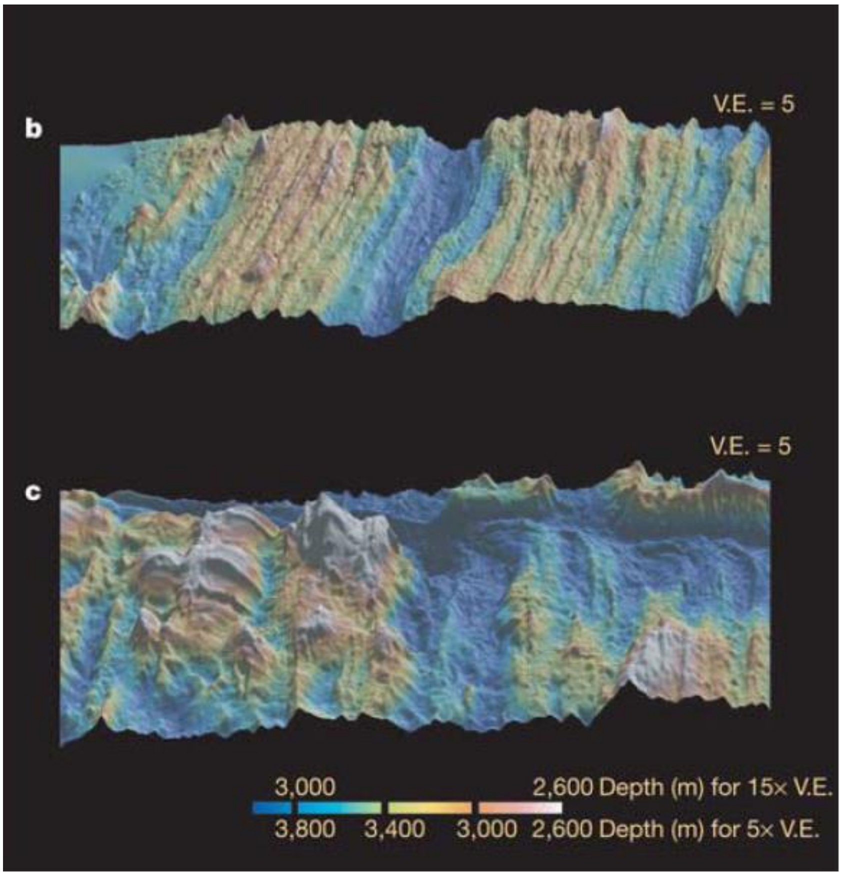

Figure 2.2-11: *Intermediate and slow spreading ridges topography. The upper figure has been made based on data from the South-East Indian ridge and is typical of sections where magmatic extension is still dominant. The lower figure is based from data form the MAR and is typical of melt depleted ridge portions such as segment ends. (from Buck et al., 2005)*

Like tectonic activity, seismic activity is noticeably increased along intermediate and especially along slow ridges compared to fast spreading ridges. Seismic activity is no more confined to transform faults but is recorded all along the ridge axes in a nearly continuous way (Stein and Woods 1989; Mutter & Karson, 1992). It is more active in association with segments ends (Kong et al., 1992; Grevemeyer et al., 2013) and especially with asymmetrical extension (Escartin et al., 2008). It is both linked to the natural tendency for long-lived detachments to generate more seismic activity (Olive & Escartin, 2016) and because of the colder regime of the lithosphere increasing the depth of stiff lithosphere and, consequently, of the seismic zone. In general, ridges with slower spreading rates tend to increase the depth of their seismic activity (Huang and Solomon, 1987; Grevemeyer et al., 2019)

The most characteristic structures of slow spreading ridges are Oceanic Core Complexes (OCC), also called megamullions. They are the 1-2 km high dome-shaped structures that form by asymmetrical extension (Tucholke et al., 1998). They form when magmatic activity is moderate, and tectonics accommodate 50% to 70% of the ridge spreading (Figure 2.2-10b; Tucholke et al., 2008). Their surface is corrugated perpendicular to the ridge axis with amplitudes of tens to several hundred meters (Tucholke et al., 1998). They develop by the flexural rotation of a long-lived detachment fault (up to 4 My; Michibayashi et al., 2014; Tucholke et al., 1998) parallel to the ridge axis. They occur only on one side, in general the ridge's inside corners if next to a transform fault (Mutter & Karson, 1992). On the other side of the ridge, extension is accommodated by magmatic activity and normal faulting, similarly to more magmatic regions. The detachment faults forming the OCCs are rooted between 8 and 12 km depth (Mutter & Karson, 1992; Tucholke et al., 1998) and temperatures of 700-900°C (Hansen et al., 2013; Michibayashi et al., 2014) likely near the brittle-ductile transition zone (Tucholke et al., 2008). The formation of the OCCs requires some magmatic activity and the onset or termination of their development is intimately linked to changes in the magmatic activity at depth (Tucholke et al., 2008). For example, the occurrence of a new gabbroic body at depth may stop the development of the former detachment and the onset of a new one. Formation of OCCs leads to the exposure of several kilometers of lower crustal gabbros and upper mantle peridotites to the seafloor (Mutter & Karson, 1992; Tucholke et al., 1998). Two end-members have been identified depending on the abundance of gabbroic bodies they host (Figure 2.2-12; Miranda & Dilek, 2010).

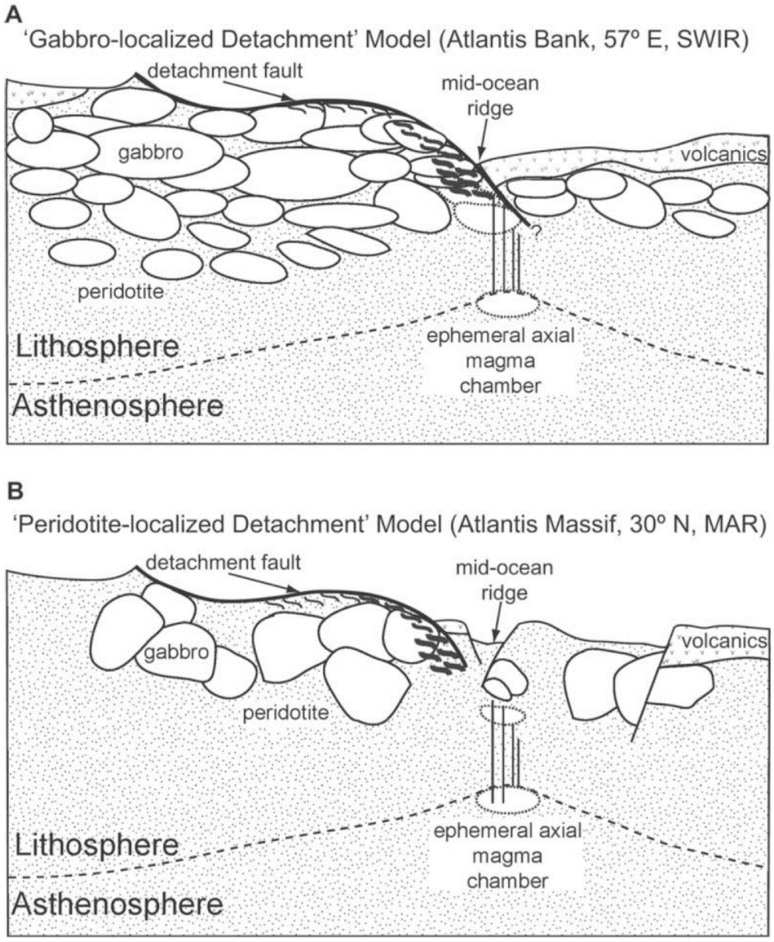

Figure 2.2-12: *Schematic representation of the two types of OCC. (from Miranda & Dilek, 2010)*

Hydrothermal activity along slow and intermediate spreading ridges is similar to what is observed along fast spreading ridges with high temperature black smoker occurring close to the ridge axial valley. However, supplementary hydrothermal activity is associated with the exposure and alteration of ultramafic rocks by OCCs (Bourgault et al., 1993; Escartin et al., 2008). This hydrothermal activity is characterized by important CH_4 output associated with serpentinization (Bourgault et al., 1993). Serpentinization is favored by the exposure of peridotites at the seafloor that is up to 20-25% of the oceanic lithosphere formed at slow spreading ridges (Cannat et al., 2010) and by intense fracturing. Water can infiltrate lower levels using normal faults and the large detachment faults that form the OCCs. Serpentinization is in consequence favored along slow spreading ridges and could reach up to 4 km depth (Cannat et al., 2010; Iyer et al., 2010). The alteration of ultramafic rocks into serpentine in turn can help OCC formation by lubricating the detachment (Bourgault et al., 1993; Ildefonse et al., 2007).

2.2.2.3 Ultra-slow ridges

Only 1% of the global ocean ridge length is represented by ultra-slow ridges. Together with very-slow ridges, they represent 19% of the ridges, but produce only 5% of the oceanic crust (Solomon, 1989). The only ultra-slow ridge is the Gakkel ridge in the Artic (spreading rates between 6 and 12.7 mm/yr; DeMets et al., 1990 & 1994), but some segments of the very-slow South-West Indian ridge (~14 mm/yr; Sauter & Cannat, 2010) are also ultra-slow. These ridges are characterized by very low melt production leading to extreme variations in magmatic activity.

Ultra-slow and very-slow spreading ridges are composed of alternating magmatic and amagmatic segments. These are referred to as super-segments as they can be several hundreds of kilometers long (Dick et al., 2003). Magmatic super-segments share similarities with slow ridges with a symmetrical ridge opening perpendicular to the ridge axis, a rough seafloor topography and the occurrence of a large and deep axial rift with relatively constant volcanic activity. The lithospheric section is covered by a continuous but thinned magmatic crust due to low melt supply. Amagmatic super-segments have, as their name indicates, a very low melt supply. In contrast to other ridge sections and because of their low thermal gradient, these super-segments are subject to conductive cooling even along the ridge axis. This leads to tectonics being the main contributor to the oceanic extension. The magmatic part of the seafloor is reduced to a thin discontinuous basaltic crust. Interestingly, amagmatic super-segments contains some of the largest on-axis volcanoes. They represent zones of melt focus and are regularly spaced 100-200 km apart (Sauter and Cannat 2010). Due to the cold lithosphere, these volcanoes have a deep source of melt (Dick et al., 2003). In their vicinity, more magmatic sections can occurs fed by the main volcano and the magmatic crust is locally thickened (Schmid et al., 2017). Transform faults are absent along ultra-slow ridges, their role in releasing shear stress is taken up by oblique extension along amagmatic super-segments (Dick et al., 2003).

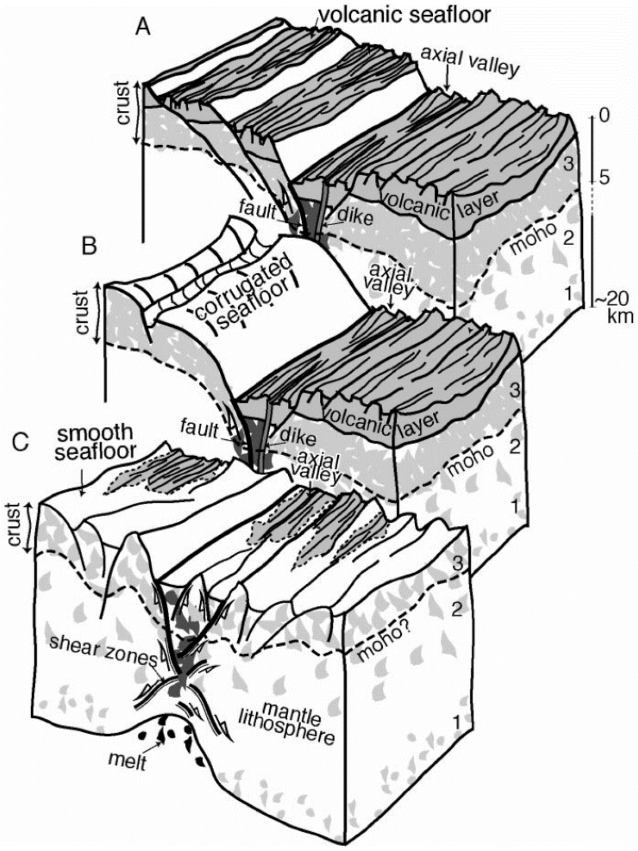

Figure 2.2-13: *Types of seafloor encountered along ultra-slow spreading ridges. Peridotite is represented in white, gabbroic rocks in light grey, basaltic rocks in medium grey and melt in black and dark grey. (from Cannat et al., 2006)*

Three types of seafloor topographies have been identified along ultra-slow and very-slow spreading ridges (Figure 2.2-13; Cannat et al., 2006). Rough seafloor, similar to what is observed along slow spreading ridges is associated with volcanic and magmatic activity taking up more than 50% of the oceanic extension (Figure 2.2-10a). Corrugated surfaces are associated with the occurrence of OCCs and magmatic extension representing 50-30% of the total ridge spreading (Figure 2.2-10b-c). The last seafloor type is a smooth type of seafloor specific for amagmatic sections of ultra-slow ridges and associated with continuous exposure of mantle rocks by tectonic extension. In this case, magmatic extension is reduced to less than 30% of total oceanic extension (Figure 2.2-10d-f). Smooth seafloors are formed by successive low angle detachments. These detachments can be compared to the ones that lead to the formation of OCC. The main difference between the two structures is the lack of magmatic activity in the case of the smooth seafloor which shortens the detachment’s life and prevents the formation of the dome-shaped structure of the OCCs. Detachments then follows one after the other, continuously expositing deeper lithospheric levels i.e. mantle peridotites (Figure 2.2-14). This model of seafloor formation has been named the “flip-flop” model (Sauter et al., 2013).

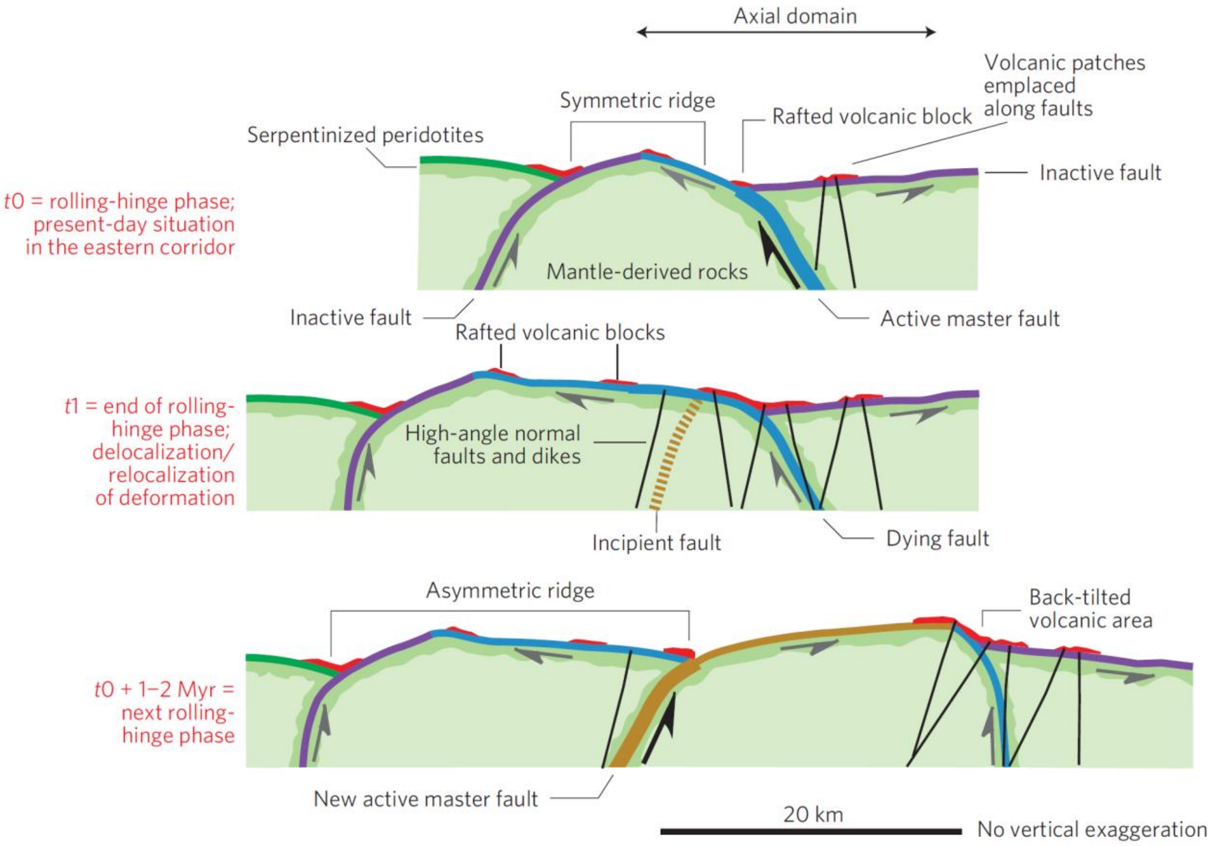

Figure 2.2-14: *Flip-flop model for amagmatic lithospheric extension. (from Sauter et al., 2013)*

As the most tectonically active ridge types, ultra-slow and very-slow ridges are also the most seismically active. The amagmatic parts present the deepest seismicity along ridge axes (Grevemeyer et al., 2019; Schlindwein & Schmid, 2016; Schmid & Schlindwein, 2016) and have the largest proportion of high magnitudes earthquakes (Bayrak et al., 2002). The abundant peridotite exposure at the seafloor in amagmatic sections, or relatively thin magmatic crust (due to low melt supply) in magmatic sections, in association with the active tectonic activity, makes ultra-slow ridges a favorable environment for serpentinization. It has been proposed that the 500°C isotherm, corresponding roughly to the onset of serpentinization based on observations on natural serpentinites, could be a hydration boundary along slower ridge types (Hess, 1962). This hypothesis is supported by seismic activity (Schlindwein & Schmid, 2016; Schmid & Schlindwein, 2016), and may imply that serpentinites represent a major component of the oceanic lithosphere in a similar way as gabbros.

2.2.3 Subduction zones

After its formation and alteration along mid-ocean ridges, the oceanic lithosphere is recycled back into the upper mantle by subduction. Subduction zones are the counterpart of mid-oceanic ridge and lead to the closure of oceans. They are characterized by a deep trench where the oceanic lithospheric plate is bent and plunges below another lithospheric plate. The bending of the subducted lithosphere leads to extensional stress on its upper part, parallel to the subduction zone, and consequently to the generation of faults. Faults created by bending of the subducted lithosphere are generally deep enough to reach mantle rocks and enable a second step of extensive serpentinization (Figure 2.2-15; Ranero et al., 2003).

The amount and depth of serpentinization during this phase is controlled by several parameters. A first parameter is the age of the lithosphere that also determine its thickness and thermal regime (Iyer et al., 2012). An old lithosphere will tend to be thick and cold. It will bend with more difficulty than a younger lithosphere, but its bending will produce more and deeper faults. A second parameter is the orientation of the subduction zone, that determines the orientation of the bend-faults, relative to structures already present in the lithosphere such as faults formed at the ride axis. Regarding this parameter, two studies return opposite results. Shillington et al. (2015), working on the Alaskan subduction zone, observe that an orientation of the subduction zone parallel to previous faults lead to a deeper hydration of the mantle. They conclude that the subduction zone being parallel to previous faults facilitate the bending of the subducting slab, leading to deeper faulting thus deeper hydration. Kita & Ferrand (2018), working on the Japanese subduction zone, observe a more intense seismic activity attributed to the dehydration of the subducting lithosphere when the orientation of the subduction zone is oblique compared to previous faults. They attribute this phenomenon to the production of a more connected fracture network by non-parallel faults, favorable to more fluid infiltration and more hydration of the subducting lithosphere. While apparently contradictory, these two studies may actually be complementary. Indeed, the subducted slab in Alaska is much younger than the Japanese one. While deeper faults are beneficial in the case of a thin young plate that tends to produce shallower bending faults, they may not be as beneficial for a thick old plate that already tends to produce deep bending faults. Moreover, it should be considered is that serpentinization does not necessarily reach the maximum depth of the faults. It is limited by the depth at which the stress due to the bending shifts from tensile to compressive (Lefeldt et al., 2012) as compressive stress will expel any fluid phase. Finally, the amount of serpentinization is dependent of the subduction rate. Slower rates will give more time for serpentinization to happen while faster rates will limit the time available for interaction between the rocks and seawater (Iyer et al., 2012).

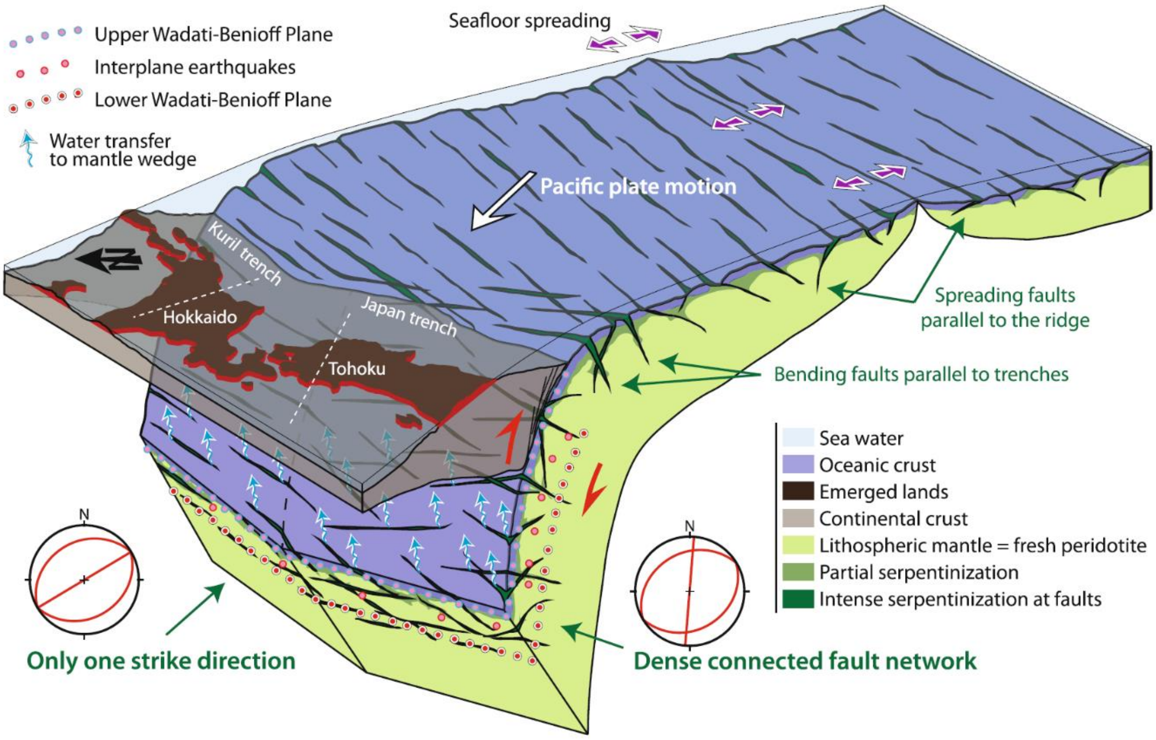

Figure 2.2.15: *Schematic view of the bend-faulting. (Modified from Kita & Ferrand, 2018)*

As the subducted lithosphere penetrates deeper into the upper mantle, it is subject to higher pressures and recrystallization of previously formed lizardite and chrysotile to antigorite occurs. The temperature also increases and ultimately exceeds the thermal stability of the serpentine (~610-650°C; Malvoisin, 2015) leading to dehydration of the serpentinites and regeneration of peridotite. This process produces seismicity and releases large quantities of fluid into the overriding lithospheric plate (Chollet et al., 2011; Dobson et al., 2002; Yamasaki & Seno, 2003). Depending on the depth at which they are released, these fluids can lead to the melting of the overriding plate and participate arc magmatism (Guillot & Hattori, 2013; Hattori & Guillot, 2003; Evans et al., 2013), and/or participate, with fluids release from upper layers of the lithosphere, to the serpentinization of the overriding lithospheric mantle (Guillot & Hattori, 2013; Schmidt & Poli, 2003) (Figure 2.2-16). During this new serpentinization step, due to the high pressure and relatively high temperature, antigorite is the preferred serpentine form. This time antigorite forms directly from olivine. The high temperature makes that a limited amount of magnetite is formed, and olivine relics are enriched in iron (Evans, 2010). This contrasts with the recrystallization from lizardite and chrysotile to antigorite that occurs in the subducting slab where previously formed magnetite (if any) is preserved in association with antigorite and olivine relics tend to preserve their mantellic Mg-Fe ratio (Evans, 2010).

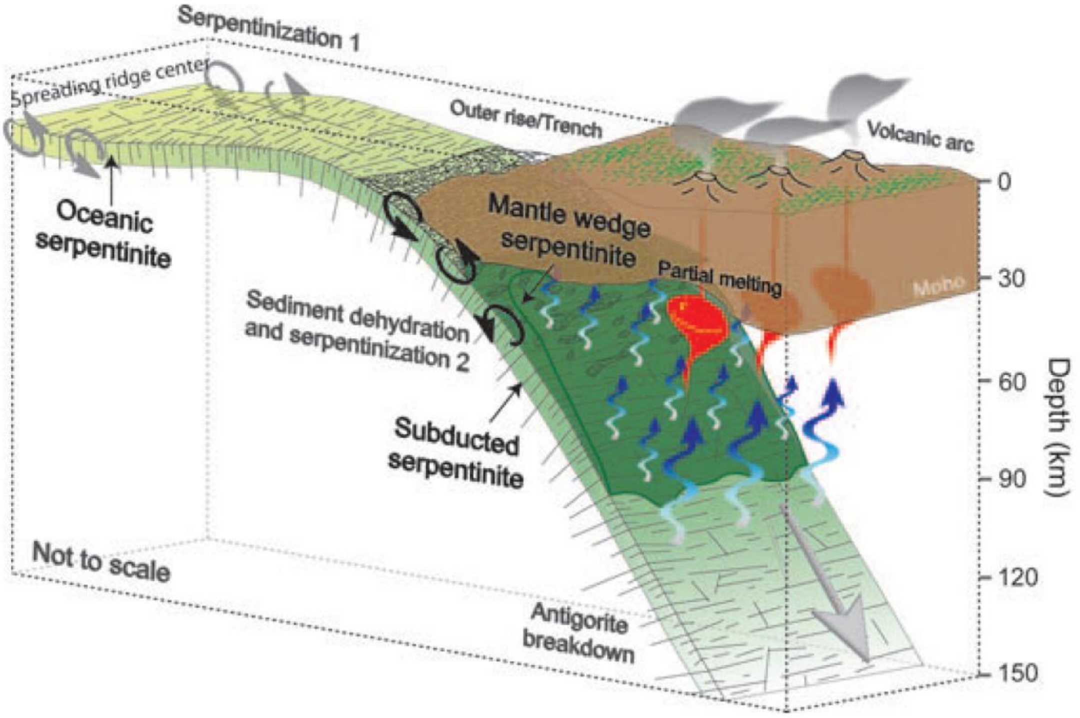

Figure 2.2.16: *Schematic view of forearc mantle serpentinization and arc magmatism production at a subduction zone. (from Deschamps et al., 2013)*

2.3 Making pathways for fluids

Deformation zones, in particular faults, are major vectors for fluids. Although in general correlation between fluid driven retrograde metamorphism and fracturing is well recognized, their detailed coupling is not completely understood. The case of serpentinization is particularly complex as the reaction itself leads to important rheological changes and to a significant volume increase that can contribute to fracturing and associated permeability increase, but also to the closure of pore space and permeability reduction.

2.3.1 Deformation and fluids

Hydration zones in association with tectonic structures are reported in a variety of geological settings. However, the detailed relation between faulting and hydration is not always simple, mainly because hydration can overprint some of the deformation features that led to fluid infiltration. The thorough study and understanding of grain scale deformation is then essential to recognized deformation processes even after rock hydration.

2.3.1.1 Interaction with tectonics

Faults have long been recognized as conduits leading fluids to a reactive rock (Figure 2.3-1), and hydration is often directly observed in association with a deformed or faulted zone (Figure 2.3-2). This process was for a long time believed to occur mainly in the upper parts of the crust, and only locally deeper in association with very large fault zones. However, an increasing number of evidences suggest that faults permit the downward progression of water much deeper than previously thought, even into the lower crust and upper mantle (Connolly & Podladchikov, 1998; Jamtveit et al., 2018; Sibson, 2000).

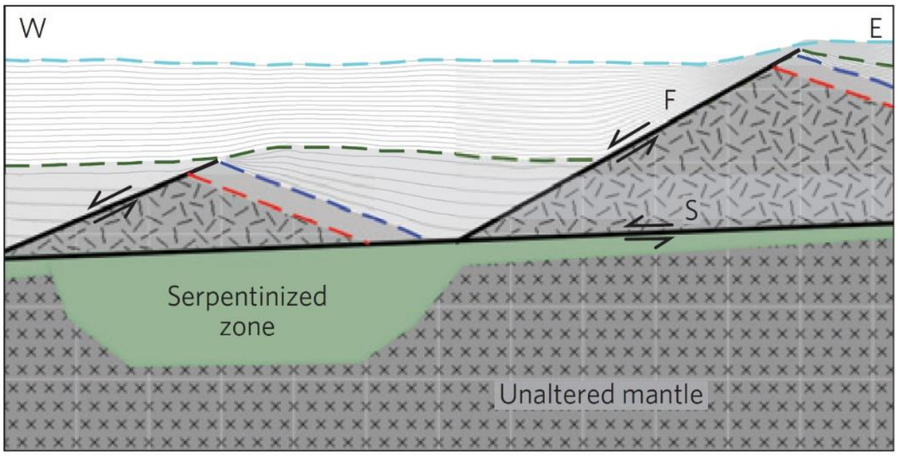

Figure 2.3-1: *Schematic representation of the preferential serpentinization in the prolongation of normal faults in a passive margin context. (from Bayrakci et al., 2016)*

Fluid migration through faults is far more complex than a simple Darcyan flow through an open crack. Some faults are filled with a low permeability gouge (Faulkner et al., 2010) or by frictional melt (Wenk 1978) that prevent or slows down the fluid migration. When the permeability inside the fault zone is limited, fluid can also progress through the damaged wall-rock (e.g. Sibson, 2000). Slower migration increases the interaction time between the wall-rock and water, leading to fluid consumption and reduced flow. The timing of faulting and availability of fluids is important. If water is available when the faulting or deformation occurs, it will be more likely to interact with the rock. For example, during seismic faulting and formation of pseudotachylytes, the immediate availability of fluid results in wall-rock alteration in the wake of the associated earthquake (Petley-Ragan et al., 2018).

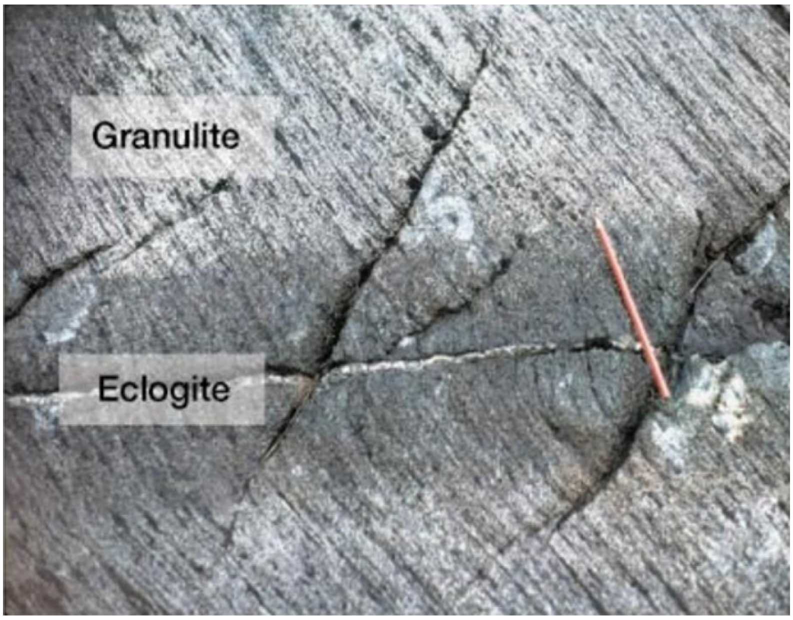

Figure 2.3-2: *Reaction zone around a fault. Here the wall-rock is a dry granulite that is hydrated into eclogite around a fault. (from Jamtveit et al., 2000)*

The stress state of the rock is an important parameter to consider while studying fluid circulation within a rock. It can prevent fluid progression by closing the faults as observed at subduction zones (Lefeldt et al., 2012) or enhance its reaction with the wall-rock (Jamtveit et al., 2000). The presence of a fluid within a fault also leads to changes in the rock stress state and modifies its rupture conditions (Sibson, 2000).

2.3.1.2 Grain scale deformation

The migration of water within faults and damaged wall-rocks is controlled by many parameters. A way to better understand the interaction between them is to study the textures and structures in hydrated samples. However, hydration can significantly overprint the rock deformation structures that led to the hydration. It is thus essential also to study rock deformation structures in their pristine state to be able to recognize them in altered samples.

Deformation of peridotites at the grain scale is mainly controlled by dislocation creeps. Dislocations are defects in the crystals lattice. They accumulate during deformation, increasing the internal energy of the grains. The release of this internal energy may drive a reorganization of the dislocations to form new grain boundaries through recrystallization and recovery processes that repair the lattice and reduce the dislocation density. Active processes vary mainly with temperature, strain rate and sometimes grain size. The presence of water could also play a role (Jung & Karato, 2001a,b; Hirth & Tullis, 1992). The final shape, size and preferred orientations of the grains are controlled by the active recrystallization processes and the relative rates of dislocation formation versus recovery processes.

The movements of dislocations through the crystal lattice are eased by high temperatures. At low temperature, the migration of dislocations is limited and deformation leads to the accumulation of dislocation eventually causing the rupture of the rock. Brittle deformation can also occur for high strain rates when deformation is too fast for recrystallization processes to accommodate it. Fragmentation processes, leading to power law distributions of the fragment, are commonly associated with brittle deformation (e.g. Sammis et al., 1987; Steacy & Sammis, 1991). If the faulting forms fragments that can move freely within the deformation zone, their crystallographic orientation tends to be random. These fragments have shapes varying from angular to rounded depending on the amount of comminution they experienced. Large grains have a tendency to break more easily than smalls ones. Healing processes are extremely slow at low temperatures. Their efficiency increases with temperature.

At temperatures typical for the lower lithosphere, recrystallization processes are effective. Dislocation creep processes are divided into two subtypes of recrystallization processes: dynamic recrystallization, occurring as the rock is deformed, and static recrystallization occurring at low strain rates or without any strain. Grain sizes associated with recrystallization processes are expected to follow a lognormal distribution when they reach steady state (Feltham, 1957; Kile et al., 2000). Dynamic recrystallization processes lead to strong crystallographic preferred orientations. Grains shapes are very dependent on the active recrystallization process. Three main processes of dynamic recrystallization have been identified: bulging, sub-grain rotation and grain boundary migration (Stipp et al., 2002). Bulging is active at relatively low temperature and for high stresses. New grains form at the border of the original grains by small scale migration of the grain boundary. This leads to a rock texture with large original grains surrounded by small grains in between the grains where the stress (and dislocations) accumulates more (Figure 2.3-3a). Sub-grain rotation is most effective at intermediate temperatures. This is the typical deformation texture found in mantle rocks. New grains are formed by the progressive rotation of parts of the original grains (sub-grains). The crystallographic orientation of the sub-grain is progressively modified by rotating until it becomes a separate grain (Figure 2.3-3b). Grain boundary migration is a process active at high temperature and low stress. It is enhanced by the presence of a fluid (Jung & Karato, 2001a) and affects the microstructure on a larger scale than bulging, often leading to characteristic amoeboid grain shapes (Figure 2.3-3c). Static recrystallization reduces the surface energy. It is characterized by 120° grain boundaries and tends to make rounded grain shapes.

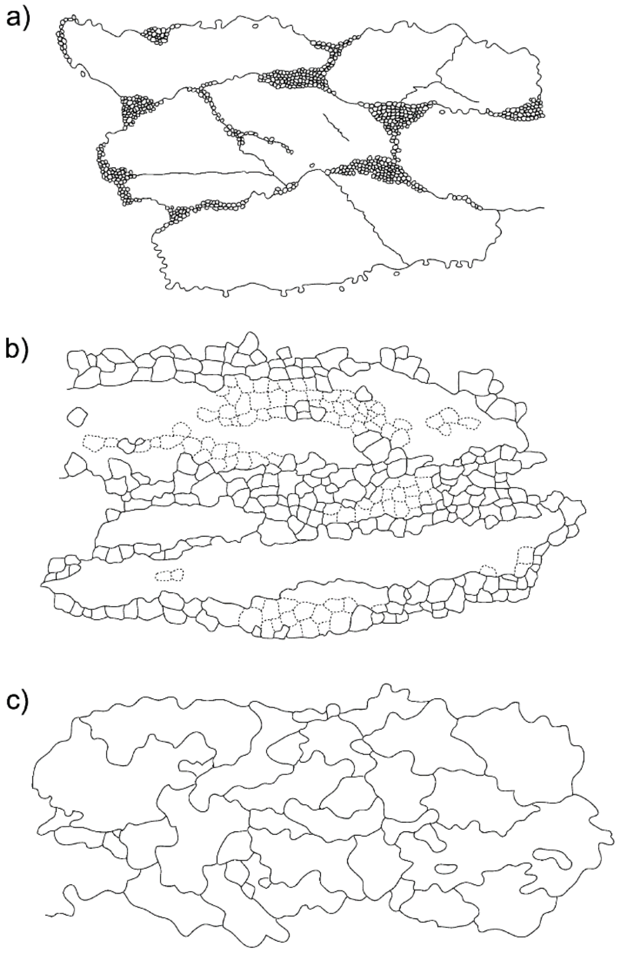

Figure 2.3-3: *Examples of texture obtained by dynamic recrystallization. a) bulging, b) sub-grain rotation and c) boundary migration (from Stipp et al., 2002)*

At very high temperatures (i.e. near melting point), dislocation can move freely by diffusion within the crystal lattice. This category of recrystallization is called diffusion creep. Its efficiency varies with grain size and it is particularly active in small grains. It is possible to have large grains deforming by dislocation creep and small grains deforming by diffusion creep. It usually leads to weak to random CPO (Fliervoet et al., 1999)

2.3.2 Serpentinization

Serpentinization represents a complex case of fluid induced metamorphism. The rheology and volume changes it induces have major consequences on the rock behavior and cause a significant mechano-chemical coupling. The processes triggering the onset of serpentinization are likely very different from the processes controlling its maintenance.

2.3.2.1 Rheological changes

Serpentinization induces radical changes in peridotite rheology. Only a few percent of serpentine may cause significant weakening of the peridotite (Figure 2.3-4; Escartin et al., 1997; Escartin et al., 2001). This weakening is mostly linked to the change in mineral structure from the 3D crystallographic structure of olivine to the layered serpentine. This rheological change has tremendous consequences for serpentinized peridotite's response to stress. It confers a ductile behavior to serpentinized rocks and concentrates deformation. It also facilitates displacements along detachment faults, such as those observed along mid-oceanic ridges (Bourgault et al., 1993; Ildefonse et al., 2007), or even at plates interfaces, such as subduction zones (Gorczyk et al., 2007; Hirth & Guillot, 2013).

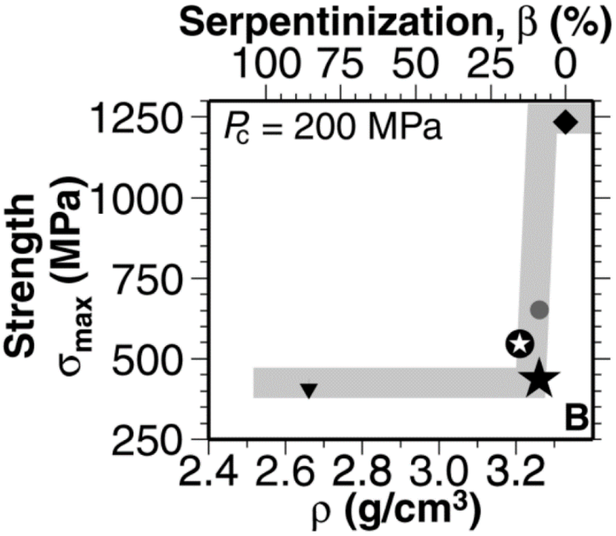

Figure 2.3-4: *Strength of peridotite depending on its degree of serpentinization, density and P-wave velocity. (from Escartin et al., 2001)*

A second major change is the decrease in density from ca. 3.3 for peridotite to ca. 2.5-2.6 for serpentine (O'Hanley, 1992; Mével, 2003). This change in density induces a number of modifications of the rock properties such as reducing its seismic speeds (Christensen, 1972) and conferring it a buoyant behavior (Gorczyk et al., 2007). The seismic velocities are widely used to identify serpentinized peridotites at depth, especially at the seafloor (e.g, Momoh et al., 2017; Shillington et al., 2015). The buoyant behavior of serpentine is responsible for the formation of serpentine diapirs and the ascension of subducted material in the forearc of subduction zones (e.g. Gorczyk et al., 2007; Guillot et al., 2009). The decrease in density is also responsible for a volume increase that can exceed 40% (Klein & Le Roux, 2020). The amplitude of the volume increase varies depending on the opening of the system. A closed system will tend to favor large volume changes, while an open system with an intense fluid circulation will tend to temperate the volume change by leaching some elements out. However, exchanges between Mg and Ca do not have a major influence on the volume change (Klein & Le Roux, 2020) The intensity of the volume change is an important aspect regarding the storage of water in serpentinites since a larger volume of serpentine means a larger amount of water. The volume increase is a source of stress, perturbing the local tectonic stress field (e.g. Schmid & Schlindwein, 2016) and may cause fracturing of the surrounding rocks and thereby, increase its permeability to facilitate fluid propagation (O'Hanley, 1992; Figure 2.3-5). In contrast, this volume increase may also lead to clogging of initial pore space, inhibiting any further alteration (Hövelmann et al., 2012).

Seismic speeds, buoyancy

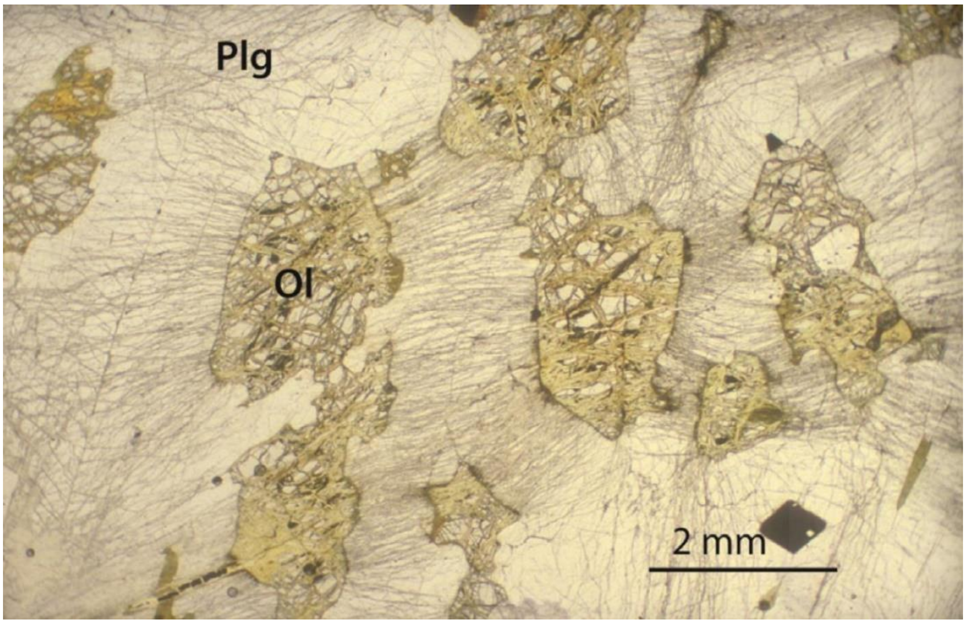

Figure 2.3-5: *Partially serpentinized olivine grains ins a plagioclase matrix from the Duluth gabbro. The volume increase induced by serpentinization led to the formation of cracks in the surrounding plagioclase. (from Jamtveit et al., 2016)*

2.3.2.2 Initiation of serpentinization

The formation of the mesh texture in serpentinites, in particular the formation of mesh veins, is often attributed to early stages of serpentinization (e.g. Andreani et al., 2007; Rouméjon & Cannat, 2014). Understanding its formation should consequently help understand how serpentinization is initiated.

Thermal cracking has been proposed as a mechanism creating a fine network of cracks along which water can circulate forming the mesh texture veins (Boudier et al., 2010). Rouméjon & Cannat (2014) proposed that the orientation of the crack network could be influenced by tectonics. In a slow-ridge setting, thermal cracking of olivine has been estimated to produce up to 3% porosity within the upper 4-6 kilometers below the seafloor (DeMartin et al., 2004). This is consistent with the estimated depth of serpentinization.

Another mechanism causing formation of mesh textures may involve self-induced propagation of cracks (Plümper et al., 2012). Hierarchical fracture patterns, similar to the mesh texture, have been observed in rocks fractured by volume increasing reactions (Figure 2.3-6; Iyer et al., 2008; Zheng et al., 2018). These fracturing processes do not invalidate the contribution of thermal cracking during initiation of serpentinization, but highlight that other processes might be involved. Moreover, the major role of tectonics highlighted by the preferential serpentinization in the vicinity of faults is not represented by these models and is still poorly understood.

Figure 2.3-6: *Hierarchical fracturation pattern in a dyke squeezed by volume increase in the surrounding serpentinized peridotite. (Iyer et al., 2008)*

2.3.2.3 Sustaining serpentinization

In abyssal peridotites, the progress of serpentinization may reach 100% (Mével, 2003). This means serpentinization is sustained by the supply of water. A recent study (Horning et al., 2018), was able to record low magnitude seismicity in an inactive OCC. This seismic activity has been interpreted as being produced by serpentinization. This may indicate that serpentinization is able to produce fractures to help sustaining reaction progress as suggested by some recent experiments (Zheng et al., 2019). However, serpentinization in natural abyssal peridotites in not homogeneous. It is focused along preferential pathways with high degrees of serpentinization spaced by 100m to 1 km (e.g. Rouméjon et al., 2015 & 2018a). These pathways are loci for open system serpentinization. In between, rocks are also serpentinized but to a lesser extent probably experiencing more close system conditions.

The most obvious way serpentinization can sustain itself is by fracturing induced by volume change. However, in an open system, volume increase will not necessarily take place. High water-rock ratios may lead to mass transport out of the system and result in volume conservation (Evans, 2004). Moreover, rock cracking due to volume increase has been estimated to occur mostly within the first 20% of serpentinization (Rouméjon & Cannat, 2014). Thus, reaction driven cracking may only concern the early close-system stages of serpentinization. It is likely that volumes undergoing closed system serpentinization develop a mesh texture, their mesh veins growing slowing as the fluid diffuses through the nanoporosity of already serpentinized parts (Tutolo et al., 2016) inducing self-induced cracking (Plümper et al., 2012). This may operate until ca. 20% of serpentinization (Rouméjon & Cannat, 2014).

After that, the leftover porosity is filled and serpentinization stopped (Hövelmann et al., 2012), unless the serpentinized zone ends up as an open system, for example near a fault zone, and mesh textured cores may be replaced by alteration phases.

References

Agrinier, P., and M., Cannat. 1997. “Oxygen isotopic constraints on serpentinization processes in ultramafic rocks from the Mid-Atlantic Ridge (23°N) in the MARK area.” In *Proceedings of the Ocean Drilling Program, Scientific Results, Vol. 153*, edited by J.A., Karson, M., Cannat, D.J., Miller, and D., Elthon, 381-388. https://doi.org/10.2973/odp.proc.sr.153.033.1997

Allen, D. E., and W.E., Seyfried. 2003. “Compositional Controls on Vent Fluids from Ultramafic-Hosted Hydrothermal Systems at Mid-Ocean Ridges: An Experimental Study at 400°C, 500 Bars.” *Geochimica et Cosmochimica Acta*, 67 (8): 1531–1542. https://doi.org/10.1016/S0016-7037(02)01173-0

Alt, J. C., E. M., Schwarzenbach, G. L., Früh-Green, W. C., Shanks, S. M., Bernasconi, C. J., Garrido, L., Crispini, L., Gaggero, J. A., Padrón-Navarta, and C., Marchesi. 2013. “The Role of Serpentinites in Cycling of Carbon and Sulfur: Seafloor Serpentinization and Subduction Metamorphism.” *Lithos*, 178 (September): 40–54. https://doi.org/10.1016/j.lithos.2012.12.006

Alt, J. C., and W. C., Shanks. 2003. “Serpentinization of Abyssal Peridotites from the MARK Area, Mid-Atlantic Ridge: Sulfur Geochemistry and Reaction Modeling.” *Geochimica et Cosmochimica Acta*, 67 (4): 641–653. https://doi.org/10.1016/S0016-7037(02)01142-0

Andreani, M., C., Mével, A.-M., Boullier, and J., Escartín. 2007. “Dynamic Control on Serpentine Crystallization in Veins: Constraints on Hydration Processes in Oceanic Peridotites: Serpentine crystallization.” *Geochemistry, Geophysics, Geosystems*, 8 (2). https://doi.org/10.1029/2006GC001373

Andreani, M., A., Baronnet, A. M., Boullier, and J. P., Gratier. 2004. “A Microstructural Study of a ‘Crack-Seal’ Type Serpentine Vein Using SEM and TEM Techniques.” *European Journal of Mineralogy*, 16 (4): 585–595. https://doi.org/10.1127/0935-1221/2004/0016-0585

Andreani, M., O., Grauby, A., Baronnet, and M., Muñoz. 2008. “Occurrence, Composition and Growth of Polyhedral Serpentine.” *European Journal of Mineralogy*, 20 (2): 159–171. https://doi.org/10.1127/0935-1221/2008/0020-1801

Anonymous. 1972. Penrose field conference on ophiolites. *Geotimes*, 17: 24-25.

Bach, W., C. J., Garrido, H., Paulick, J., Harvey, and M., Rosner. 2004. “Seawater-peridotite interactions: First insights from ODP Leg 209, MAR 15° N.” *Geochemistry, Geophysics, Geosystems*, 5. https://doi.org/10.1029/2004GC000744

Bach, W., H. Paulick, C. J., Garrido, B., Ildefonse, W. P., Meurer, and S. E., Humphris. 2006. “Unraveling the Sequence of Serpentinization Reactions: Petrography, Mineral Chemistry, and Petrophysics of Serpentinites from MAR 15°N (ODP Leg 209, Site 1274).” *Geophysical Research Letters*, 33 (13). https://doi.org/10.1029/2006GL025681

Barnes, J. D., H., Paulick, Z. D., Sharp, W., Bach, and G., Beaudoin. 2009. “Stable Isotope (δ^{18}O, δD, δ^{37}Cl) Evidence for Multiple Fluid Histories in Mid-Atlantic Abyssal Peridotites (ODP Leg 209).” *Lithos*, 110 (1–4): 83–94. https://doi.org/10.1016/j.lithos.2008.12.004

Bayrak, Y., A., Yılmaztürk, and S., Öztürk. 2002. “Lateral Variations of the Modal (a/b) Values for the Different Regions of the World.” *Journal of Geodynamics*, 34 (5): 653–666.

Bayrakci, G., T. A., Minshull, D. S., Sawyer, T. J., Reston, D., Klaeschen, C., Papenberg, C., Ranero, J. M., Bull, R. G., Davy, D. J., Shillington, M., Pérez-Gussinyé, and J. K., Morgan. 2016. “Fault-Controlled Hydration of the Upper Mantle during Continental Rifting.” *Nature Geoscience*, 9 (5): 384–388. https://doi.org/10.1038/ngeo2671

Berndt, M. E., R. R., Seal, W. C., Shanks, and W. E., Seyfried. 1996. “Hydrogen isotope systematics of phase separation in submarine hydrothermal systems: Experimental calibration and theoretical models." *Geochimica et Cosmochimica Acta*, 60 (9): 1595-1604. https://doi.org/10.1016/0016-7037(96)00033-6

Bickle, M., C., Hawkesworth, A., Martin, E. G., Nisbet, and R. K., O'Nions. 1976. "Mantle composition derived from the chemistry of ultramafic lavas." *Nature*, 263**:** 577–580. https://doi.org/10.1038/263577a0

Bonifacie, M., V., Busigny, C., Mével, P., Philippot, P., Agrinier, N., Jendrzejewski, M., Scambelluri, and M., Javoy. 2008. "Chlorine isotopic composition in seafloor serpentinites and high-pressure metaperidotites. Insights into oceanic serpentinization and subduction processes." *Geochimica et Cosmochimica Acta*, 72 (1), 126-139. https://doi.org/10.1016/j.gca.2007.10.010

Boudier, F., and A., Nicolas. 1985. "Harzburgite and Lherzolite Subtypes in Ophiolitic and Oceanic Environments." *Earth and Planetary Science Letters*, 76 (1–2): 84–92. https://doi.org/10.1016/0012-821X(85)90150-5

Boudier, F. 1995. "Nature of the Moho Transition Zone in the Oman Ophiolite." *Journal of Petrology*, 36 (3): 777–796. https://doi.org/10.1093/petrology/36.3.777

Boudier F., A., Nicolas, and B., Ildefonse. 1996. "Magma chambers in the Oman ophiolite: fed from the top and the bottom." *Earth and Planetary Science Letters*, 144 (1-2): 239-250. https://doi.org/10.1016/0012-821X(96)00167-7

Boudier, F., A., Baronnet, and D., Mainprice. 2010. "Serpentine Mineral Replacements of Natural Olivine and Their Seismic Implications: Oceanic Lizardite versus Subduction-Related Antigorite." *Journal of Petrology*, 51 (1–2): 495–512. https://doi.org/10.1093/petrology/egp049

Bourgault, H., J.-L., Charlou, Y., Fouquet, H. D., Needham, N., Vaslet, P., Appriou, P. J., Baptiste, P. A., Rona, L., Dmitriev, and S., Silantiev. 1993. "Fast and Slow Spreading Ridges: Structure and Hydrothermal Activity, Ultramafic Topographic Highs, and CH_4 Output." *Journal of Geophysical Research*, 98 (B6): 9643. https://doi.org/10.1029/93JB00508

Buck, W. R. 2000. "Can flow of dense cumulate through mushy upper gabbros produce lower gabbros at a fast-spreading center?" In *Ophiolites and Oceanic Crust: New Insights from Field Studies and the Ocean Drilling Program*, edited by Y., Dilek, E., Moores, D., Elthon, and A., Nicolas, 121-128. Geological Society of America. https://doi.org/10.1130/0-8137-2349-3.121

Buck, W. R., L. L., Lavier, and A. N. B., Poliakov. 2005. "Modes of Faulting at Mid-Ocean Ridges." *Nature*, 434: 719–723. https://doi.org/10.1038/nature03358

Canales, J., H., Carton, S. M., Carbotte, J. C., Mutter, M. R., Nedimović, M., Xu, O., Aghaei, M., Marjanović, and K., Newman. 2012. "Network of off-axis melt bodies at the East Pacific Rise." *Nature Geoscience*, 5: 279–283. https://doi.org/10.1038/ngeo1377

Cannat, M.1993. "Emplacement of mantle rocks in the seafloor at mid-oceanic ridges." *Journal of Geophysical Research: Solid Earth*, 98 (B3). https://doi.org/10.1029/92JB02221

Cannat M., M., Mével, M., Maia, C., Deplus, C., Durand, P., Gente, P., Agrinier, A., Belarouchi, G., Dubuisson, E., Humler, and J., Reynolds. 1995. "Thin crust, ultramafic exposures, and rugged faulting patterns at the Mid-Atlantic Ridge (22°–24°N)." *Geology*, 23 (1): 49-52. https://doi.org/10.1130/0091-7613(1995)023<0049:TCUEAR>2.3.CO;2

Cannat, M. 1996. "How Thick Is the Magmatic Crust at Slow Spreading Oceanic Ridges?" *Journal of Geophysical Research: Solid Earth*, 101 (B2): 2847–2857. https://doi.org/10.1029/95JB03116.

Cannat, M., D., Sauter, V., Mendel, E., Ruellan, K., Okino, J., Escartin, V., Combier, and M., Baala. 2006. “Modes of Seafloor Generation at a Melt-Poor Ultraslow-Spreading Ridge.” *Geology*, 34 (7): 605–608. https://doi.org/10.1130/G22486.1

Cannat, M., F., Fontaine, and J., Escartín. 2010. “Serpentinization and Associated Hydrogen and Methane Fluxes at Slow Spreading Ridges.” In *Geophysical Monograph Series, volume 188: Diversity Of Hydrothermal Systems On Slow Spreading Ocean Ridges*, edited by P. A., Rona, C. W., Devey, J., Dyment, and B. J., Murton, 241–264. Washington, D. C.: American Geophysical Union. https://doi.org/10.1029/2008GM000760

Campbell, A. C., M. R., Palmer, G. P., Klinkhammer, T. S., Bowers, J. M., Edmond, J. R., Lawrence, J. F., Casey, G., Thompson, S., Humphris, R. A., Rona, and J. A., Karson. 1988. “Chemistry of hot springs on the Mid-Atlantic Ridge.” *Nature*, 335, 514-519.

Caruso, L. J., and J. V., Chernosky. 1979. “The stability of lizardite.” *Candian Mineralogist*, 17: 757-769.

Chapman D. S., and H. N., Pollack. 1975. “Global heat flow: A new look.” *Earth and Planetary Science Letters*, 28 (1): 23-32. https://doi.org/10.1016/0012-821X(75)90069-2

Charlou, J. L., J. P., Donval, Y., Fouquet, P., Jean-Baptiste, and N., Holm. 2002. “Geochemistry of High H2 and CH4 Vent Fluids Issuing from Ultramafic Rocks at the Rainbow Hydrothermal Field (36°14’N, MAR).” *Chemical Geology*, 15. https://doi.org/10.1016/S0009-2541(02)00134-1

Chen, Y. J. 1992. “Oceanic crustal thickness versus spreading rate.” *Geophysical Research Letters*, 19 (8): 753-756. https://doi.org/10.1029/92GL00161

Cherkaoui, A. S. M., W. S. D., Wilcock, R. A., Dunn, and R., Toomey. 2003. “A numerical model of hydrothermal cooling and crustal accretion at a fast spreading mid-ocean ridge.” *Geochemistry, Geophysics, Geosystems*, 4 (9). https://doi.org/10.1029/2001GC000215

Chollet, M., I., Daniel, K. T., Koga, G., Morard, and B., van de Moortèle. 2011. “Kinetics and mechanism of antigorite dehydration: Implications for subduction zone seismicity.” *Journal of Geophysical Research: Solid Earth*, 116 (B4). https://doi.org/10.1029/2010JB007739

Christensen, N. I. 1972. “The Abundance of serpentinites in the oceanic crust.” *Journal of Geology*, 80, 709–719.

Christensen, N. I., and M. H., Salisbury. 1975. “Structure and Constitution of the Lower Oceanic Crust.” *Reviews of Geophysics*, 13 (1): 57. https://doi.org/10.1029/RG013i001p00057

Connolly, J. A. D., and Y. Y., Podladchikov. 1998. “Compaction-driven fluid flow in viscoelastic rock.” *Geodinamica Acta*, 11 (2-3): 55-84. https://doi.org/10.1080/09853111.1998.1110531

Crawford, W. C., S. C., Webb, and J. A., Hildebrand. 1999. “Constraints on Melt in the Lower Crust and Moho at the East Pacific Rise, 9°48′N, Using Seafloor Compliance Measurements.” *Journal of Geophysical Research: Solid Earth*, 104 (B2): 2923–2939. https://doi.org/10.1029/1998JB900087

Davies, J. H., and D., Davies. 2010. “Earth’s surface heat flux.” *Solid Earth*, 1 (1): 5-24. https://doi.org/10.5194/se-1-5-2010

Debret, B., M., Andreani, M., Godard, C., Nicollet, S., Schwartz, and R., Lafay. 2013. “Trace element behavior during serpentinization/de-serpentinization of an eclogitized oceanic lithosphere: A LA-ICPMS study of the Lanzo ultramafic massif (Western Alps).” *Chemical Geology*, 357: 117-133. https://doi.org/10.1016/j.chemgeo.2013.08.025

DeMartin, B., G., Hirth, and B., Evans. 2004. “Experimental constraints on thermal cracking of peridotite at oceanic spreading centers.” In *Geophysical Monograph Series, volume 148: Mid-Ocean*

Ridges: Hydrothermal Interactions Between the Lithosphere and Oceans, edited by C. R., German, J., Lin, and L. M., Parson, 167-185. Washington, D. C.: American Geophysical Union. https://doi.org/10.1029/148GM07

DeMets, C., R. G., Gordon, D. F., Argus, and S., Stein. 1990. “Current Plate Motions.” *Geophysical Journal International,* 101 (2): 425–478. https://doi.org/10.1111/j.1365-246X.1990.tb06579.x

DeMets, C., R. G., Gordon, D. F., Argus, and S., Stein. 1994. “Effect of Recent Revisions to the Geomagnetic Reversal Time Scale on Estimates of Current Plate Motions.” *Geophysical Research Letters,* 21 (20): 2191–2194. https://doi.org/10.1029/94GL02118

Deschamps, F., S., Guillot, M., Godard, M., Andreani, and K., Hattori. 2011. “Serpentinites Act as Sponges for Fluid-Mobile Elements in Abyssal and Subduction Zone Environments: Serpentinites Act as Sponges for Fluid-Mobile Elements.” *Terra Nova,* 23 (3): 171–178. https://doi.org/10.1111/j.1365-3121.2011.00995.x

Deschamps F., M., Godard, S., Guillot, and K., Hattori. 2013. “Geochemistry of subduction zone serpentinites: A review.” *Lithos,* 178: 96-127. https://doi.org/10.1016/j.lithos.2013.05.019

Dick, H. J. B., J., Lin, and H., Schouten. 2003. “An Ultraslow-Spreading Class of Ocean Ridge.” *Nature,* 426: 405–412. https://doi.org/10.1038/nature02128

Dobson, D. P., P. G., Meredith, and S. A., Boon. 2002. “Simulation of Subduction Zone Seismicity by Dehydration of Serpentine.” *Science,* 298: 1407-1410. https://doi.org/10.1126/science.1075390

Douville E., J. L., Charlou, E H., Oelkers, P., Bienvenu, C. F., Jove Colon, J. P., Donval, Y., Fouquet, D., Prieur, and P., Appriou. 2002. “The rainbow vent fluids (36° 14′ N, MAR): the influence of ultramafic rocks and phase separation on trace metal content in Mid-Atlantic Ridge hydrothermal fluids.” *Chemical Geology,* 184 (1-2): 37-48. https://doi.org/10.1016/S0009-2541(01)00351-5

Dungan, A. D. 1979. “A microscope study of antigorite and some serpentine pseudomorphs.” *Canadian Mineralogist,* 17: 771-784.

Ehlmann, B. L., J. F., Mustard, and S. L., Murchie. 2010. “Geologic setting of serpentine deposits on Mars.” *Geophysical Research Letters,* 37 (6). https://doi.org/10.1029/2010GL042596

Escartin, J., G., Hirth, and B., Evans. 1997. “Effects of serpentinization on the lithospheric strength and the style of normal faulting at slow-spreading ridges.” *Earth and Planetary Science Letters,* 151 (3-4), 181-189. https://doi.org/10.1016/S0012-821X(97)81847-X

Escartin, J., G., Hirth, and B., Evans. 2001. “Strength of Slightly Serpentinized Peridotites: Implications for the Tectonics of Oceanic Lithosphere.” *Geology,* 29 (11): 1023. https://doi.org/10.1130/0091-7613(2001)029<1023:SOSSPI>2.0.CO;2

Evans, B. W. 2004. “The Serpentinite Multisystem Revisited: Chrysotile Is Metastable.” *International Geology Review,* 46 (6): 479–506. https://doi.org/10.2747/0020-6814.46.6.479

Evans, B. W. 2010. “Lizardite versus antigorite serpentinite: Magnetite, hydrogen, and life (?).” *Geology,* 38 (10): 879-882. https://doi.org/10.1130/G31158.1

Evans, B. W., K., Hattori, and A., Baronnet. 2013. “Serpentinite: What, Why, Where?” *Elements,* 9 (2): 99–106. https://doi.org/10.2113/gselements.9.2.99

Faulkner, D. R., C. A. L., Jackson, R. J., Lunn, R. W., Schlische, Z. K., Shipton, C. A. J., Wibberley, and M.O., Withjack. 2010. “A review of recent developments concerning the structure, mechanics and fluid flow properties of fault zones." *Journal of Structural Geology*, 32 (11): 1557-1575. https://doi.org/10.1016/j.jsg.2010.06.009

Feltham, P. 1957. "Grain Growth in Metals." *Acta Metallurgica*, 5 (2): 97–105. https://doi.org/10.1016/0001-6160(57)90136-0

Fliervoet, T. F., M. R., Drury, and P. N., Chopra. 1999. "Crystallographic Preferred Orientations and Misorientations in Some Olivine Rocks Deformed by Diffusion or Dislocation Creep." *Tectonophysics*, 303 (1–4): 1–27. https://doi.org/10.1016/S0040-1951(98)00250-9

Forsyth, D. W., and the MELT Seismic Team. 1998. "Imaging the Deep Seismic Structure Beneath a Mid-Ocean Ridge: The MELT Experiment." *Science*, 280: 1215-1218. https://doi.org/10.1126/science.280.5367.1215

Fouquet Y., U., Von Stackelberg, J. L., Charlou, J. P., Donval, J., Erzinger, J. P., Foucher, P., Herzig, R., Mühe, S., Soakai, M., Wiedicke, and H., Whitechurch. 1991. "Hydrothermal activity and metallogenesis in the Lau back-arc basin." *Nature*, 349: 778-781. https://doi.org/10.1038/349778a0

Fouquet Y., J.-M., Auzende, V., Ballu, R., Batiza, D., Bideau, M., Cormier, P., Geistdoerfer, Y., Lagabrielle, J., Sinton, and P., Spadea. 1994. "Variabilité des manifestations hydrothermales actuelles le long d'une dorsale ultra rapide. Dorsale Est Pacifique entre 17° et 19° S (campagne NAUDUR)." *Compte Rendus de l'Académie des Sciences Série II*, 319 (11): 1399-1406.

Fouquet, Y. 1997. "Where are the large hydrothermal sulphide deposits in the oceans?" *Philosophical Transactions of the Royal Society of London. Series A: Mathematical, Physical and Engineering Sciences*, 355 (1723): 427-441. https://doi.org/10.1098/rsta.1997.0015

Früh-Green, G. L., A., Plas, and L. N., Dell'Angelo. 1996. "Mineralogic and stable isotope record of polyphase alteration of upper crustal gabbros of the East Pacific Rise (Hess Deep, Site 894)." *Proceedings of the Ocean Drilling Program, Scientific Results*, 147: 235-254.

Früh-Green, G. L., J. A. D., Connolly, and A., Plas. 2004. "Serpentinization of Oceanic Peridotites: Implications for Geochemical Cycles and Biological Activity." In *Geophysical Monograph Series, volume 144: The Subseafloor Biosphere at Mid-Ocean Ridges*, edited by W. S. D. Wilcock, E. F. Delong, D. S. Kelley, J. A. Baross, and S. C. Cary, 119-136. Washington, D. C.: American Geophysical Union. https://doi.org/10.1029/144GM08

Gahlan, H. A., S., Arai, A. H., Ahmed, Y., Ishida, Y. M., Abdel-Aziz, and A., Rahimi. 2006. "Origin of Magnetite Veins in Serpentinite from the Late Proterozoic Bou-Azzer Ophiolite, Anti-Atlas, Morocco: An Implication for Mobility of Iron during Serpentinization." *Journal of African Earth Sciences*, 46 (4): 318–330. https://doi.org/10.1016/j.jafrearsci.2006.06.003

Gill, R. 2010. "Igneous Rocks and Processes: A Practical Guide." Wiley Publication.

Gorczyk, W., S., Guillot, T. V., Gerya, and K., Hattori. 2007. "Asthenospheric upwelling, oceanic slab retreat, and exhumation of UHP mantle rocks: Insights from Greater Antilles." *Geophysical Research Letters*, 34 (21). https://doi.org/10.1029/2007GL031059

Grevemeyer, I., T. J., Reston, and S., Moeller. 2013. "Microseismicity of the Mid-Atlantic Ridge at 7°S-8°15′S and at the Logatchev Massif Oceanic Core Complex at 14°40′N-14°50′N: Seismicity of the Mid-Atlantic Ridge." *Geochemistry, Geophysics, Geosystems*, 14 (9): 3532–3554. https://doi.org/10.1002/ggge.20197

Grevemeyer, I., N. W., Hayman, D., Lange, C., Peirce, C., Papenberg, H. J.A., Van Avendonk, F., Schmid, L. G., de La Peña, and A., Dannowski. 2019. "Constraining the Maximum Depth of Brittle Deformation at Slow- and Ultraslow-Spreading Ridges Using Microseismicity." *Geology*, 47 (11): 1069–1073. https://doi.org/10.1130/G46577.1

Guillot, S., K., Hattori, P., Agard, S., Schwartz, and O., Vidal. 2009. “Exhumation processes in oceanic and continental subduction contexts: a review.” In *Subduction Zone Dynamics*, edited by S., Lallemand, and F., Funiciello, 175-204. Berlin: Springer. https://doi.org/10.1007/978-3-540-87974-9_10

Guillot, S., and K., Hattori. 2013. “Serpentinites: Essential Roles in Geodynamics, Arc Volcanism, Sustainable Development, and the Origin of Life.” *Elements,* 9 (2): 95–98. https://doi.org/10.2113/gselements.9.2.95

Hansen, L. N., M. J., Cheadle, B. E., John, S. M., Swapp, H. J. B., Dick, B. E., Tucholke, and M. A., Tivey. 2013. “Mylonitic Deformation at the Kane Oceanic Core Complex: Implications for the Rheological Behavior of Oceanic Detachment Faults: Rheology of Kane Oceanic Core Complex.” *Geochemistry, Geophysics, Geosystems*, 14 (8): 3085–3108. https://doi.org/10.1002/ggge.20184

Hattori, K. H., and S., Guillot. 2003. “Volcanic fronts form as a consequence of serpentinite dehydration in the forearc mantle wedge.” *Geology*, 31 (6): 525-528. https://doi.org/10.1130/0091-7613(2003)031<0525:VFFAAC>2.0.CO;2

Hattori, K. H., and S., Guillot. 2007. “Geochemical character of serpentinites associated with high‐ to ultrahigh‐pressure metamorphic rocks in the Alps, Cuba, and the Himalayas: Recycling of elements in subduction zones.” *Geochemistry, Geophysics, Geosystems,* 8 (9). https://doi.org/10.1029/2007GC001594

Haymon, R. M., D. J., Fornari, M. H., Edwards, S., Carbotte, D., Wright, and K. C., MacDonald. 1991. “Hydrothermal vent distribution along the East Pacific Rise crest (9° 09′ –54′ N) and its relationship to magmatic and tectonic processes on fast-spreading mid-ocean ridges.” *Earth and Planetary Science Letters*, 104 (2-4): 513-534. https://doi.org/10.1016/0012-821X(91)90226-8

Hess, H. H. 1962. “History of ocean basins.” *Petrologic studies: a volume to honor A. F. Buddington*, 599-620.

Hirth, G., and S., Guillot. 2013. “Rheology and Tectonic Significance of Serpentinite.” *Elements*, 9 (2): 107-113. https://doi.org/10.2113/gselements.9.2.107

Hirth, G., and J., Tullis. 1992. “Dislocation creep regimes in quartz aggregates.” *Journal of Structural Geology*, 14 (2): 145-159. https://doi.org/10.1016/0191-8141(92)90053-Y

Holm, N. G., and J. L., Charlou. 2001. “Initial Indications of Abiotic Formation of Hydrocarbons in the Rainbow Ultramafic Hydrothermal System, Mid-Atlantic Ridge.” *Earth and Planetary Science Letters*, 191 (1): 1–8. https://doi.org/10.1016/S0012-821X(01)00397-1

Horning, G., R. A., Sohn, J. P., Canales, and R. A., Dunn. 2018. “Local Seismicity of the Rainbow Massif on the Mid-Atlantic Ridge.” *Journal of Geophysical Research: Solid Earth*, 123 (2): 1615–1630. https://doi.org/10.1002/2017JB015288

Hövelmann, J., H., Austrheim, and B., Jamtveit. 2012. “Microstructure and Porosity Evolution during Experimental Carbonation of a Natural Peridotite.” *Chemical Geology,* 334 (December): 254–265. https://doi.org/10.1016/j.chemgeo.2012.10.025

Huang, P. Y., and S. C., Solomon. 1987. “Centroid Depths and Mechanisms of Mid-Ocean Ridge Earthquakes in the Indian Ocean. Gulf of Aden, and Red Sea.” *Journal of Geophysical Research*, 92 (B2): 1361-1382. https://doi.org/10.1029/JB092iB02p01361

Ildefonse, B., D. K., Blackman, B. E., Jhon, Y., Ohara, D. J., Miller, C. J., MacLeod, and the Integrated Ocean Drilling Program Expeditions 304/305 Science Party. 2007. “Oceanic core complexes and crustal accretion at slow-spreading ridges.” *Geology,* 35 (7): 623-626. https://doi.org/10.1130/G23531A.1

Iyer, K., B., Jamtveit, J., Mathiesen, A., Malthe-Sørenssen, and J., Feder. 2008. "Reaction-Assisted Hierarchical Fracturing during Serpentinization." *Earth and Planetary Science Letters*, 267 (3–4): 503–516. https://doi.org/10.1016/j.epsl.2007.11.060

Iyer, K., L. H., Rüpke, and J. P., Morgan. 2010. "Feedbacks between Mantle Hydration and Hydrothermal Convection at Ocean Spreading Centers." *Earth and Planetary Science Letters*, 296 (1–2): 34–44. https://doi.org/10.1016/j.epsl.2010.04.037

Iyer, K., L. H., Rüpke, J. P., Morgan, and I., Grevemeyer. 2012. "Controls of Faulting and Reaction Kinetics on Serpentinization and Double Benioff Zones." *Geochemistry Geophysics Geosystems*, 13 (September): Q09010. https://doi.org/10.1029/2012GC004304

Jamtveit, B., H., Austrheim, and A., Malthe-Sørenssen. 2000. "Accelerated Hydration of the Earth's Deep Crust Induced by Stress Perturbations." *Nature*, 408: 75–78. https://doi.org/10.1038/35040537

Jamtveit, B., A., Malthe-Sørenssen, and O., Kostenko. 2008. "Reaction enhanced permeability during retrogressive metamorphism." *Earth and Planetary Science Letters*, 267 (3-4): 620-627. https://doi.org/10.1016/j.epsl.2007.12.016

Jamtveit, B., H., Austrheim, and A., Putnis. 2016. "Disequilibrium Metamorphism of Stressed Lithosphere." *Earth-Science Reviews*, 154 (March): 1–13. https://doi.org/10.1016/j.earscirev.2015.12.002

Jamtveit, B., Y., Ben-Zion, F., Renard, and H., Austrheim. 2018. "Earthquake-Induced Transformation of the Lower Crust." *Nature*, 556: 487–491. https://doi.org/10.1038/s41586-018-0045-y

Jung, H. 2001. "Water-Induced Fabric Transitions in Olivine." *Science*, 293: 1460–1463. https://doi.org/10.1126/science.1062235

Jung, H., and S. I., Karato. 2001. "Effects of Water on Dynamically Recrystallized Grain-Size of Olivine." *Journal of Structural Geology*, 23 (9): 1337–1344. https://doi.org/10.1016/S0191-8141(01)00005-0

Kelemen, P. B., N., Shimizu, and V. J. M., Salters. 1995. "Extraction of mid-ocean-ridge basalt from the upwelling mantle by focused flow of melt in dunite channels." *Nature*, 375, 747-753. https://doi.org/10.1038/375747a0

Kelemen, P. B., K., Koga, and N., Shimizu. 1997. "Geochemistry of gabbro sills in the crust-mantle transition zone of the Oman ophiolite: implications for the origin of the oceanic lower crust." *Earth and Planetary Science Letters*, 146 (3-4): 475-488. https://doi.org/10.1016/S0012-821X(96)00235-X

Kelemen, P. B., J., Matter, E. E., Streit, J. F., Rudge, W. B., Curry, and J., Blusztajn. 2011. "Rates and Mechanisms of Mineral Carbonation in Peridotite: Natural Processes and Recipes for Enhanced, in Situ CO_2 Capture and Storage." *Annual Review of Earth and Planetary Sciences*, 39 (1): 545–576. https://doi.org/10.1146/annurev-earth-092010-152509

Kelley, D. S., J. A., Karson, D. K., Blackman, G. L., Früh-Green, D. A., Butterfield, M. D., Lilley, E. J., Olson, M. O., Schrenk, K. K., Roe, G. T., Lebon, P., Rivizzigno, and the AT3-60 Shipboard Party. 2001. "An off-axis hydrothermal vent field near the Mid-Atlantic Ridge at 30° N." *Nature*, 412: 145-149. https://doi.org/10.1038/35084000

Kile, D. E., D. D., Eberl, A. R., Hoch, and M. M., Reddy. 2000. "An Assessment of Calcite Crystal Growth Mechanisms Based on Crystal Size Distributions." *Geochimica et Cosmochimica Acta*, 64 (17): 2937–2950. https://doi.org/10.1016/S0016-7037(00)00394-X

Kita, S., and T. P., Ferrand. 2018. “Physical mechanisms of oceanic mantle earthquakes: Comparison of natural and experimental events.” *Scientific Reports*, 8: 17049. https://doi.org/10.1038/s41598-018-35290-x

Klein, F., W., Bach, N., Jöns, T., McCollom, B., Moskowitz, and T., Berquó. 2009. “Iron Partitioning and Hydrogen Generation during Serpentinization of Abyssal Peridotites from 15°N on the Mid-Atlantic Ridge.” *Geochimica et Cosmochimica Acta*, 73 (22): 6868–6893. https://doi.org/10.1016/j.gca.2009.08.021

Klein, F., W., Bach, and T. M., McCollom. 2013. “Compositional controls on hydrogen generation during serpentinization of ultramafic rocks.” *Lithos*, 178: 55-69. https://doi.org/10.1016/j.lithos.2013.03.008

Klein, F., W., Bach, S. E., Humphris, W.-A., Kahl, N., Jöns, B., Moskowitz, and T. S., Berquó. 2014. “Magnetite in seafloor serpentinite—Some like it hot.” *Geology*, 42 (2): 135-138. https://doi.org/10.1130/G35068.1

Klein, F., and V., Le Roux. 2020. “Quantifying the volume increase and chemical exchange during serpentinization.” *Geology*, 48 (6): 552-556. https://doi.org/10.1130/G47289.1

Kodolányi, J., and T., Pettke. 2011. “Loss of trace elements from serpentinites during fluid-assisted transformation of chrysotile to antigorite — An example from Guatemala.” *Chemical Geology*, 284 (3-4): 351-362. https://doi.org/10.1016/j.chemgeo.2011.03.016

Kodolányi, J., T., Pettke, C., Spandler, B. S., Kamber, and K., Gméling. 2012. “Geochemistry of Ocean Floor and Fore-arc Serpentinites: Constraints on the Ultramafic Input to Subduction Zones.” *Journal of Petrology*, 53 (2): 235-270. https://doi.org/10.1093/petrology/egr058

Kong, L., S., Solomon, and G., Purdy. 1992. “Microearthquake Characteristics of a Midocean Ridge Along-Axis High.” *Journal of Geophysical Research: Solid Earth*, 97 (B2): 1659–1685. https://doi.org/10.1029/91JB02566

Lefeldt, M., C. R., Ranero, and I., Grevemeyer. 2012. “Seismic Evidence of Tectonic Control on the Depth of Water Influx into Incoming Oceanic Plates at Subduction Trenches.” *Geochemistry Geophysics Geosystems*, 13 (May). https://doi.org/10.1029/2012GC004043

Lowell, R. P., and P. A., Rona. 2002. “Seafloor Hydrothermal Systems Driven by the Serpentinization of Peridotite.” *Geophysical Research Letters,* 29 (11). https://doi.org/10.1029/2001GL014411

Lundin, E. R., and A. G., Doré. 2011. “Hyperextension, serpentinization, and weakening: A new paradigm for rifted margin compressional deformation.” *Geology*, 39 (4): 347-350. https://doi.org/10.1130/G31499.1

Maaløe, S., and R., Steel. 1980. “Mantle composition derived from the composition of lherzolites.” *Nature*, 285: 321–322. https://doi.org/10.1038/285321a0

MacLeod, C. J., and G., Yaouancq. 2000. “A fossil melt lens in the Oman ophiolite: Implications for magma chamber processes at fast spreading ridges.” *Earth and Planetary Science Letters*, 176 (3-4): 357-373. https://doi.org/10.1016/S0012-821X(00)00020-0

Malvoisin, B. 2015. “Mass Transfer in the Oceanic Lithosphere: Serpentinization Is Not Isochemical.” *Earth and Planetary Science Letters*, 430 (November): 75–85. https://doi.org/10.1016/j.epsl.2015.07.043

Malvoisin, B., F., Brunet, J., Carlut, S., Rouméjon, and M., Cannat. 2012. “Serpentinization of Oceanic Peridotites: 2. Kinetics and Processes of San Carlos Olivine Hydrothermal Alteration: Kinetics of Serpentinization.” *Journal of Geophysical Research: Solid Earth*, 117 (B4). https://doi.org/10.1029/2011JB008842

Marjanovic, M., S. M., Carbotte, H., Carton, M. R., Nedimović, J. C., Mutter, and J. P., Canales. 2014. “A multi-sill magma plumbing system beneath the axis of the East Pacific Rise.” *Nature Geoscience*, 7: 825-829. https://doi.org/10.1038/ngeo2272

Martin, B., and W. S., Fyfe. 1970. “Some Experimental and Theoretical Observations on the Kinetics of Hydration Reactions with Particular Reference to Serpentinization.” *Chemical Geology*, 6 (January): 185–202. https://doi.org/10.1016/0009-2541(70)90018-5

Mattey, D., D., Lowry, and C., Macpherson. 1994. “Oxygen Isotope Composition of Mantle Peridotite.” *Earth and Planetary Science Letters*, 128 (3–4): 231–41. https://doi.org/10.1016/0012-821X(94)90147-3

McCollom, T. M., F., Klein, M., Robbins, B., Moskowitz, T. S., Berquó, N., Jöns, W., Bach, and A., Templeton. 2016. “Temperature Trends for Reaction Rates, Hydrogen Generation, and Partitioning of Iron during Experimental Serpentinization of Olivine.” *Geochimica et Cosmochimica Acta*, 181 (May): 175–200. https://doi.org/10.1016/j.gca.2016.03.002

McCollom, T. M., and J. S., Seewald. 2007. “Abiotic Synthesis of Organic Compounds in Deep-Sea Hydrothermal Environments.” *Chemical Reviews*, 107 (2): 382–401. https://doi.org/10.1021/cr0503660

McCollom, T. M., and W., Bach. 2009. “Thermodynamic constraints on hydrogen generation during serpentinization of ultramafic rocks.” *Geochimica et Cosmochimica Acta*, 73 (3): 856-875. https://doi.org/10.1016/j.gca.2008.10.032

McCollom, T. M. 2013. “Laboratory Simulations of Abiotic Hydrocarbon Formation in Earth’s Deep Subsurface.” *Reviews in Mineralogy and Geochemistry*, 75 (1): 467-494. https://doi.org/10.2138/rmg.2013.75.15

McCollom, T. M., and J. S., Seewald. 2013. “Serpentinites, Hydrogen, and Life.” *Elements*, 9 (2): 129-134. https://doi.org/10.2113/gselements.9.2.129

Mével, C. 2003. “Serpentinization of Abyssal Peridotites at Mid-Ocean Ridges.” *Comptes Rendus Geoscience*, 335 (10): 825–52. https://doi.org/10.1016/j.crte.2003.08.006

Michibayashi, K., Y., Harigane, Y., Ohara, J., Muto, and A., Okamoto. 2014. “Rheological Properties of the Detachment Shear Zone of an Oceanic Core Complex Inferred by Plagioclase Flow Law: Godzilla Megamullion, Parece Vela Back-Arc Basin, Philippine Sea.” *Earth and Planetary Science Letters*, 408 (December): 16–23. https://doi.org/10.1016/j.epsl.2014.10.005

Middleton, A. P., and E. J. W., Whittaker. 1976. “The structure of Povlen-type chrysotile.” *Canadian Mineralogist*, 14: 301-306.

Miller, D. J., and N. I., Christensen. 1997. “Seismic velocities of lower crustal and upper mantle rocks from the slow-spreading Mid-Atlantic Ridge, South of the Kane Transform Fault zone (MARK).” *Proceedings of the Ocean Drilling Program, Scientific Results*, 437-456.

Miranda, E. A., and Y., Dilek. 2010. “Oceanic Core Complex Development in Modern and Ancient Oceanic Lithosphere: Gabbro-Localized versus Peridotite-Localized Detachment Models.” *The Journal of Geology*, 118 (1): 95–109. https://doi.org/10.1086/648460

Miura, M., S., Arai, and T., Mizukami. 2011. “Raman Spectroscopy of Hydrous Inclusions in Olivine and Orthopyroxene in Ophiolitic Harzburgite: Implications for Elementary Processes in Serpentinization.” *Journal of Mineralogical and Petrological Sciences*, 106 (2): 91–96. https://doi.org/10.2465/jmps.101021d

Momoh, E., M., Cannat, L., Watremez, S., Leroy, and S. C., Singh. 2017. "Quasi-3D seismic reflection imaging and wide-angle velocity structure of nearly amagmatic oceanic lithosphere at the ultraslow-spreading southwest Indian ridge." *Journal of Geophysical research: Solid Earth*, 122 (12): 9511-9533. https://doi.org/10.1002/2017JB014754

Morandi, N., and G., Felice. 1979. "Serpentine minerals from veins in serpentinites rocks." *Mineralogical Magazine*, 43 (325): 135-140. https://doi.org/10.1180/minmag.1979.043.325.13

Morgan, J. P., E. M., Parmentier, and J., Lin. 1987. "Mechanisms for the origin of mid-ocean ridge axial topography: Implications for the thermal and mechanical structure of accreting plate boundaries." *Journal of Geophysical Research*, 92 (B12): 12823-12836. https://doi.org/10.1029/JB092iB12p12823

Murata, K., H., Maekawa, H., Yokose, K., Yamamoto, K., Fujioka, T., Ishii, H., Chiba, and Y., Wada. 2009. "Significance of serpentinization of wedge mantle peridotites beneath Mariana forearc, western Pacific." *Geosphere*, 5 (2): 90-104. https://doi.org/10.1130/GES00213.1

Mutter, C. Z., and J. C., Mutter. 1993. "Variations in Thickness of Layer 3 Dominate Oceanic Crustal Structure." *Earth and Planetary Science Letters*, 117 (1–2): 295–317. https://doi.org/10.1016/0012-821X(93)90134-U

Mutter, J. C., and J. A., Karson. 1992. "Structural Processes at Slow-Spreading Ridges." *Science*, 257: 627–634. https://doi.org/10.1126/science.257.5070.627

Normand, C., A. E., Williams-Jones, R. F., Martin, and H., Vali. 2002. "Hydrothermal alteration of olivine in a flow-through autoclave: Nucleation and growth of serpentine phases." *American Mineralogist*, 87 (11-12): 1699–1709. https://doi.org/10.2138/am-2002-11-1220

O'Hanley, D. S. 1992. "Solution to the Volume Problem in Serpentinization." *Geology*, 20 (8): 705–708. https://doi.org/10.1130/0091-7613(1992)020<0705:STTVPI>2.3.CO;2

Ohara, Y., M. K., Reagan, K., Fujikura, H., Watanabe, K., Michibayashi, T., Ishii, R. J., Stern, I., Pujana, F. Martinez, G., Guirard, J., Ribeiro, M., Brounce, N., Komori, and M., Kino. 2012. "A serpentinite-hosted ecosystem in the Southern Mariana Forearc." *Proceedings of the National Academy of Sciences of the United States of America*, 109 (8): 2831-2835. https://doi.org/10.1073/pnas.1112005109

Olive, J.-A., and J., Escartin. 2016. "Dependence of seismic coupling on normal fault style along the Northern Mid-Atlantic Ridge." *Geochemistry, Geophysics, Geosystems*, 17 (10): 4128-4152. https://doi.org/10.1002/2016GC006460

Oufi, O., M., Cannat, and H., Horen. 2002. "Magnetic Properties of Variably Serpentinized Abyssal Peridotites." *Journal of Geophysical Research*, 107 (B5). https://doi.org/10.1029/2001JB000549

Parson, B., and J. G., Sclater, 1977. "An analysis of the variation of ocean floor bathymetry and heat flow with age." *Journal of Geophysical Research*, 82 (5): 803-827.

Pens, M., M., Andreani, I., Daniel, J.-P., Perrillat, and H., Cardon. 2016. "Contrasted Effect of Aluminum on the Serpentinization Rate of Olivine and Orthopyroxene under Hydrothermal Conditions." *Chemical Geology*, 441 (November): 256–264. https://doi.org/10.1016/j.chemgeo.2016.08.007

Pérez-Gussinyé, M., and T. J., Reston. 2001. "Rheological evolution during extension at nonvolcanic rifted margins: Onset of serpentinization and development of detachments leading to continental breakup." *Journal of Geophysical Research: Solid Earth*, 106 (B3): 3961-3975. https://doi.org/10.1029/2000JB900325

Perk, N. W., L. A., Coogan, J. A., Karson, E. M., Klein, and H. D., Hanna. 2007. “Petrology and geochemistry of primitive lower oceanic crust from Pito Deep: implications for the accretion of the lower crust at the Southern East Pacific Rise.” *Contributions to Mineralogy and Petrology,* 154: 575-590. https://doi.org/10.1007/s00410-007-0210-z

Peters, D., T., Pettke, T., John, and M., Scambelluri. 2017. “The role of brucite in water and element cycling during serpentinite subduction – Insights from Erro Tobbio (Liguria, Italy).” *Lithos,* 360-361: 105431. https://doi.org/10.1016/j.lithos.2020.105431

Petley-Ragan, A., K. G., Dunkel, H., Austrheim, B., Ildefonse, and B., Jamtveit. 2018. “Microstructural Records of Earthquakes in the Lower Crust and Associated Fluid-Driven Metamorphism in Plagioclase-Rich Granulites.” *Journal of Geophysical Research: Solid Earth,* 123 (5): 3729–3746. https://doi.org/10.1029/2017JB015348

Plumper, O., A., Royne, A., Magraso, and B., Jamtveit. 2012. “The Interface-Scale Mechanism of Reaction-Induced Fracturing during Serpentinization.” *Geology,* 40 (12): 1103–1106. https://doi.org/10.1130/G33390.1

Quick, J. E., and R. P., Denlinger. 1993. “Ductile deformation and the origin of layered gabbro in ophiolites.” *Journal of Geophysical Research: Solid Earth,* 98 (B6): 14015-14027. https://doi.org/10.1029/93JB00698

Raleigh, C. B., and M. S., Paterson. 1965. “Experimental Deformation of Serpentinite and Its Tectonic Implications.” *Journal of Geophysical Research,* 70 (16): 3965–3985. https://doi.org/10.1029/JZ070i016p03965

Ramsay, J. G. 1980. “The crack-seal mechanism of rock deformation.” *Nature,* 284: 135-139.

Ranero, C. R., J. P., Morgan, K., McIntosh, and C., Reichert. 2003. “Bending-Related Faulting and Mantle Serpentinization at the Middle America Trench.” *Nature,* 425: 367–373. https://doi.org/10.1038/nature01961

Richardson, W. P., S., Stein, C. A., Stein, and M. T., Zuber. 1995. “Geoid Data and Thermal Structure of the Oceanic Lithosphere.” *Geophysical Research Letters,* 22 (14): 1913–1916. https://doi.org/10.1029/95GL01595

Rouméjon, S., and M., Cannat. 2014. “Serpentinization of Mantle-Derived Peridotites at Mid-Ocean Ridges: Mesh Texture Development in the Context of Tectonic Exhumation.” *Geochemistry, Geophysics, Geosystems,* 15 (6): 2354–2379. https://doi.org/10.1002/2013GC005148

Rouméjon, S., M., Cannat, P., Agrinier, M., Godard, and M., Andreani. 2015. “Serpentinization and Fluid Pathways in Tectonically Exhumed Peridotites from the Southwest Indian Ridge (62-65 E).” *Journal of Petrology,* 56 (4): 703–734. https://doi.org/10.1093/petrology/egv014

Rouméjon, S., G. L., Früh-Green, B. N., Orcutt, and the IODP Expedition 357 Science Party. 2018a. “Alteration Heterogeneities in Peridotites Exhumed on the Southern Wall of the Atlantis Massif (IODP Expedition 357).” *Journal of Petrology,* 59 (7): 1329–58. https://doi.org/10.1093/petrology/egy065.

Rouméjon, S., M. J., Williams, and G. L., Früh-Green. 2018b. “In-Situ Oxygen Isotope Analyses in Serpentine Minerals: Constraints on Serpentinization during Tectonic Exhumation at Slow- and Ultraslow-Spreading Ridges.” *Lithos,* 323 (December): 156–73. https://doi.org/10.1016/j.lithos.2018.09.021

Rouméjon, S., M., Andreani, and G. L., Früh-Green. 2019. “Antigorite crystallization during oceanic retrograde serpentinization of abyssal peridotites.” *Contributions to Mineralogy and Petrology,* 174: 60. https://doi.org/10.1007/s00410-019-1595-1

Rumori, C., M., Mellini, and C., Viti. 2004. “Oriented, Non-Topotactic Olivine Serpentine Replacement in Mesh-Textured, Serpentinized Peridotites.” *European Journal of Mineralogy*, 16 (5): 731–741. https://doi.org/10.1127/0935-1221/2004/0016-0731

Rüpke, L. H., and J., Hansclever. 2017. “Global rates of mantle serpentinization and H_2 production at oceanic transform faults in 3-D geodynamic models.” *Geophysical Research Letters*, 44 (13): 6726-6734. https://doi.org/10.1002/2017GL072893

Saccocia, P. J., J. S., Seewald, and W. C., Shanks. 2009. “Oxygen and hydrogen isotope fractionation in serpentine–water and talc–water systems from 250 to 450 °C, 50 MPa.” *Geochimica et Cosmochimica Acta*, 73 (22), 6789-6804. https://doi.org/10.1016/j.gca.2009.07.036

Sammis, C., G., King, and R., Biegel. 1987. “The Kinematics of Gouge Deformation.” *Pure and Applied Geophysics*, 125 (5): 777–812. https://doi.org/10.1007/BF00878033

Sauter, D., V., Mendel, C., Rommevaux-Jestin, L. M., Parson, H., Fujimoto, C., Mével, M., Cannat, and K., Tamaki. 2004. “Focused magmatism versus amagmatic spreading along the ultra-slow spreading southwest Indian ridge: Evidence from TOBI side scan sonar imagery.” *Geochemistry, Geophysics, Geosystems*, 5 (10). https://doi.org/10.1029/2004GC000738

Sauter, D., and M., Cannat. 2010. “The Ultraslow Spreading Southwest Indian Ridge.” In *Geophysical Monograph Series, volume 188: Diversity Of Hydrothermal Systems On Slow Spreading Ocean Ridges*, edited by Peter A. Rona, Colin W. Devey, Jérôme Dyment, and Bramley J. Murton, 153–173. Washington, D. C.: American Geophysical Union. https://doi.org/10.1029/2008GM000843

Sauter, D., M., Cannat, S., Rouméjon, M., Andreani, D., Birot, A., Bronner, D., Brunelli, J., Carlut, A., Delacour, V., Guyader, C. J., MacLeod, G., Manatschal, V., Mendel, B., Ménez, V., Pasini, E., Ruellan, and R., Searle. 2013. “Continuous Exhumation of Mantle-Derived Rocks at the Southwest Indian Ridge for 11 Million Years.” *Nature Geoscience*, 6 (4): 314–320. https://doi.org/10.1038/ngeo1771

Schlindwein, V., and F., Schmid. 2016. “Mid-Ocean-Ridge Seismicity Reveals Extreme Types of Ocean Lithosphere.” *Nature*, 535: 276-279. https://doi.org/10.1038/nature18277

Schmid, F., and V., Schlindwein. 2016. “Microearthquake Activity, Lithospheric Structure, and Deformation Modes at an Amagmatic Ultraslow Spreading Southwest Indian Ridge Segment.” *Geochemistry, Geophysics, Geosystems*, 17 (7): 2905–2921. https://doi.org/10.1002/2016GC006271

Schmid, F., V., Schlindwein, I., Koulakov, A., Plötz, and J.-R., Scholz. 2017. “Magma Plumbing System and Seismicity of an Active Mid-Ocean Ridge Volcano.” *Scientific Reports*, 7 (February): 42949. https://doi.org/10.1038/srep42949

Schmidt, M. W., and S., Poli. 2003. “Generation of Mobile Components during Subduction of Oceanic Crust.” *Treatise on Geochemistry*, 3: 567-591. https://doi.org/10.1016/B0-08-043751-6/03034-6

Schrenk, M. O., W. J., Brazelton, and S. Q., Lang. 2013. “Serpentinization, Carbon, and Deep Life.” *Reviews in Mineralogy and Geochemistry*, 75 (1): 575–606. https://doi.org/10.2138/rmg.2013.75.18

Schulte, M., D., Blake, T., Hoehler, and T., McCollom. 2006. “Serpentinization and Its Implications for Life on the Early Earth and Mars.” *Astrobiology*, 6 (2): 364-376. https://doi.org/10.1089/ast.2006.6.364

Sclater, J. G., C., Jaupart, and D., Galson. 1980. “The heat flow through oceanic and continental crust and the heat loss of the Earth.” *Reviews of Geophysics*, 18 (1): 269-311. https://doi.org/10.1029/RG018i001p00269

Sempéré, J.-C., and J. R., Cochran. 1997. “The Southeast Indian Ridge between 88°E and 118°E: Variations in Crustal Accretion at Constant Spreading Rate.” *Journal of Geophysical Research: Solid Earth*, 102 (B7): 15489–15505. https://doi.org/10.1029/97JB00171

Seyfried, W. E., D. I., Foustoukos, and Q., Fu. 2007. “Redox Evolution and Mass Transfer during Serpentinization: An Experimental and Theoretical Study at 200°C, 500bar with Implications for Ultramafic-Hosted Hydrothermal Systems at Mid-Ocean Ridges.” *Geochimica et Cosmochimica Acta*, 71 (15): 3872–86. https://doi.org/10.1016/j.gca.2007.05.015

Seyfried, W. E., N. J., Pester, B. M., Tutolo, K., Ding. 2015. “The Lost City hydrothermal system: Constraints imposed by vent fluid chemistry and reaction path models on subseafloor heat and mass transfer processes.” *Geochimica et Cosmochimica Acta*, 163: 59-79. https://doi.org/10.1016/j.gca.2015.04.040

Shillington, D., A., Bécel, M., Nedimović, H., Kuehn, S. C., Webb, G.A., Abers, K. M., Keranen, J., Li, M., Delescluse, and G. A., Mattei-Salicrup. 2015. “Link between plate fabric, hydration and subduction zone seismicity in Alaska.” *Nature Geoscience,* 8: 961–964. https://doi.org/10.1038/ngeo2586

Sibson, R. H. 2000. “Fluid Involvement in Normal Faulting.” *Journal of Geodynamics*, 29 (3–5): 469–499. https://doi.org/10.1016/S0264-3707(99)00042-3

Singh, S. C., G. M., Kent, J. S., Collier, A. J., Harding, and J. A., Orcutt. 1998. “Melt to Mush Variations in Crustal Magma Properties along the Ridge Crest at the Southern East Pacific Rise.” *Nature*, 394: 874–878. https://doi.org/10.1038/29740

Smith, D. 2010. “Antigorite Peridotite, Metaserpentinite, and other Inclusions within Diatremes on the Colorado Plateau, SW USA: Implications for the Mantle Wedge during Low-angle Subduction.” *Journal of Petrology,* 51 (6): 1355-1379. https://doi.org/10.1093/petrology/egq022

Snow, J., and H., Edmonds. 2007. “Ultraslow-Spreading Ridges: Rapid Paradigm Changes.” *Oceanography*, 20 (1): 90–101. https://doi.org/10.5670/oceanog.2007.83

Solomon, S.C. 1989. “Just how do ocean ridges vary?: Characteristic and population statistics of ocean ridges”. In: *Drilling the Oceanic Crust and Upper Mantle: JOI/USSAC Workshop Report*, WHOI-89-39: 73-74. Woods Hole, Massachusetts: Woods Hole Oceanographic Institution.

Steacy, S. J., and C. G., Sammis. 1991. “An Automaton for Fractal Patterns of Fragmentation.” *Nature*, 353: 250-252.

Stein, C. A., and S., Stein. 1992. “A model for the global variation in oceanic depth and heat flow with lithospheric age.” *Nature*, 359: 123-129. https://doi.org/10.1038/359123a0

Stein, C. A., and S., Stein. 1994. “Constraints on hydrothermal heat flux through the oceanic lithosphere from global heat flow.” *Journal of Geophysical Research: Solid Earth*, 99 (2B):3081-3095.

Stein, S., and D. F., Woods. 1989. “Seismicity: mid-ocean ridge.” In *The Encyclopedia of Solid Earth Geophysics*, edited by D. E. James, 1050-1054.Van Nostrand Reinhold, New York.

Stipp, M., H., Stünitz, R., Heilbronner, and S. M., Schmid. 2002. “Dynamic Recrystallization of Quartz: Correlation between Natural and Experimental Conditions.” *Geological Society, London, Special Publications*, 200 (1): 171–190. https://doi.org/10.1144/GSL.SP.2001.200.01.11

Talwani, M., C. C., Windisch, and M. G., Langseth. 1971. “Reykjanes Ridge Crest: A Detailed Geophysical Study.” *Journal of Geophysical Research*, 76 (2): 473–517. https://doi.org/10.1029/JB076i002p00473

Toomey, D. R., D., Jousselin, R. A., Dunn, W. S. D., Wilcock, and R. S., Detrick. 2007. “Skew of Mantle Upwelling beneath the East Pacific Rise Governs Segmentation.” *Nature*, 446 (7134): 409–414. https://doi.org/10.1038/nature05679

Tucholke, B. E., J., Lin, and M. C., Kleinrock. 1998. “Megamullions and Mullion Structure Defining Oceanic Metamorphic Core Complexes on the Mid-Atlantic Ridge.” *Journal of Geophysical Research: Solid Earth*, 103 (B5): 9857–9866. https://doi.org/10.1029/98JB00167

Tucholke, B. E., M. D., Behn, W. R., Buck, and J., Lin. 2008. “Role of Melt Supply in Oceanic Detachment Faulting and Formation of Megamullions.” *Geology*, 36 (6): 455–458. https://doi.org/10.1130/G24639A.1

Tutolo, B. M., D. F. R., Mildner, C. V. L., Gagnon, M. O., Saar, and W. E., Seyfried. 2016. “Nanoscale Constraints on Porosity Generation and Fluid Flow during Serpentinization.” *Geology*, 44 (2): 103–106. https://doi.org/10.1130/G37349.1

VanTongeren, J. A., G., Hirth, and P. B., Kelemen. 2015. “Constraints on the accretion of the gabbroic lower oceanic crust from plagioclase lattice preferred orientation in the Samail ophiolite.” *Earth and Planetary Science Letters*, 427: 249-261. https://doi.org/10.1016/j.epsl.2015.07.001

Viti, C., and M., Mellini. 1998. “Mesh Textures and Bastites in the Elba Retrograde Serpentinites.” *European Journal of Mineralogy*, 10 (6): 1341–1360. https://doi.org/10.1127/ejm/10/6/1341

Wegner, W. W., W. G., Ernst. 1983. “Experimentally determined hydration and dehydration reaction rates in the system MgO-SiO_2-H_2O.” *Journal of Science*, 283-A: 151-180.

Wenk, H. R. 1978. “Are Pseudotachylites Products of Fracture or Fusion?” *Geology*, 6 (8): 507. https://doi.org/10.1130/0091-7613(1978)6<507:APPOFO>2.0.CO;2

Wetzel, L. R., and E. L., Shock. 2000. “Distinguishing Ultramafic-from Basalt-Hosted Submarine Hydrothermal Systems by Comparing Calculated Vent Fluid Compositions.” *Journal of Geophysical Research: Solid Earth*, 105 (B4): 8319–8340. https://doi.org/10.1029/1999JB900382

Wicks, F.J., and E. J. W., Whittaker. 1977. “Serpentine textures and serpentinization.” *Canadian Mineralogist*, 15, 459-488.

Yamasaki, T., and T., Seno. 2003. “Double seismic zone and dehydration embrittlement of the subducting slab.” *Journal of Geophysical Research: Solid Earth*, 108 (B4). https://doi.org/10.1029/2002JB001918

Zheng, Y.-F. 1993. “Calculation of oxygen isotope fractionation in hydroxyl-bearing silicates.” *Earth and Planetary Science Letters*, 120 (3-4): 247-263. https://doi.org/10.1016/0012-821X(93)90243-3

Zheng, X., B., Cordonnier, W., Zhu, F., Renard, and B., Jamtveit. 2018. “Effects of Confinement on Reaction-Induced Fracturing During Hydration of Periclase.” *Geochemistry, Geophysics, Geosystems*, 19 (8): 2661-2672. https://doi.org/10.1029/2017GC007322

Zheng, X., B., Cordonnier, J., McBeck, E., Boller, B., Jamtveit, W., Zhu, and F., Renard. 2019. “Mixed-Mode Strain Localization Generated by Hydration Reaction at Crustal Conditions.” *Journal of Geophysical Research: Solid Earth*, 124 (5): 4507-4522. https://doi.org/10.1029/2018JB017008

3 Manuscripts summaries

3.1 Manuscript 1: Olivine grain size distributions in faults and shear zones: Evidence for nonsteady state deformation

This first manuscript has been published in the *Journal of Geophysical Research: Solid Earth*, in August 2018. It contains a microstructural study on mantle rocks deformation. It focuses particularly on the use of grain size distribution for deformation characterization.

3.1.1 Summary

This study characterizes deformation of peridotite based on grain size distributions mainly from olivine-rich rocks deformed under a wide range of stress and strain rate conditions. Samples are both from experiments and natural settings. Convincing lognormal distributions across all scales were only observed for samples experimentally deformed at high temperature (1200 °C) and for some mantle-deformed natural samples. Other samples were better fitted by power-law grain size distributions. Single power law distributions were observed for natural samples deformed by brittle mechanisms and by samples deformed experimentally in the regime of low-temperature plasticity. Most natural samples could be fitted by a combination of two power laws with a crossover near the median grain size from a steep slope for the larger grain fraction to a gentler slope for the smaller grains. The common departure from lognormal distributions suggests that naturally deformed samples often have a deformation history that is far from a steady state scenario and probably reflects deformation under highly variable stress and strain rates. All small grain fractions of the grain size distributions, except for the brittle samples, showed a surprising alignment following a power law of -1 indicative of a common grain size controlling process. A model is proposed to explain this behavior based on the competition between the rate of the dislocation dynamics and the imposed strain rates.

3.1.2 Work and techniques involved

This work started with only a few samples for which we had extracted the grain sizes from the EBSD data. Their grain size area distributions curiously aligned along a ca. -1 slope in a loglog plot for small grain sizes. We started to try adding more samples for which we had data available in our group, to see if this curious behavior was only a coincidence or a more general law. When we became convinced that this behavior was not an artefact, we started to think that there may be an important finding behind this, and we needed to understand how such a thing could occur.

To do so, we first did a selection within the samples we had EBSD data available, only keeping unaltered samples, composed of only one mineral, most of the time olivine, and belonging to deformation zones. We had a group of samples associated with pseudotachylytes, and a group of samples from the Leka ophiolite, associated with shear zones of various sizes and intensities. To be able to cover a larger range of strain rates and deformation conditions, we asked other researchers if we could use their data: G. Falus for slow mantle deformation (Falus et al., 2011), J. A. Padrón-Navarta for brittle deformation (Padrón-Navarta et al., 2010), M. Tasaka for steady-state deformation experiments (Tasaka et al., 2016), and C. Trepmann for her kick-and-cook experiments simulating recrystallization after a coseismic deformation (Druiventak et al., 2012; Trepmann et al., 2013). We were looking for studies with deformed samples, mostly composed of olivine for which EBSD analysis had been done. That is how we ended up with a large selection of samples of quite diverse origins.

For all samples except the kick-and-cook experiments (for which C. Trepmann gave us directly the grain sizes) we worked from the EBSD data to extract the grain sizes. This was done using the MatLab toolbox MTEX (http://mtex-toolbox.github.io). As we were manipulating all the grain size distributions, it started to appear that they had shapes varying from power law to lognormal, with a full range of intermediate shapes. The power law samples being associated with brittle deformation and lognormal shapes with steady-state deformation. We decided to create a MatLab code to find the best curve fitting the grain size area distribution of each sample between lognormal, power law or intermediate. We first had to find a way to fit the intermediate shapes. A combination of two power laws seemed to be a good compromise as a lognormal curve can be locally approximated by two power laws.

In practice, the MatLab code that we designed provides the best lognormal fit as well as the best power law fit for each sample. The code only decides whether a single power law or a two power law fit is better, but not if the lognormal fit is best over the power law fit and vice-versa. This interpretation is left to the observer as the differences can be very subtle. An indicator of the goodness of fit of the lognormal fit, *S*, was added to help with this decision; the least good the lognormal fit, the more likely it is that the power law fit is more representative of the distribution. The MatLab code returns figures showing the different fits, and an Excel file with some statistical parameters (number of grains in the distribution, mean grain size area, standard deviation, etc.) and all the fitting parameters. This makes it easier for the user to compare samples in his/her dataset.

Finally, we designed a model to explain the -1 power law slope along which grain size distribution of all samples aligned except those best fitted by a single power law. This model is based on stochastic physics to explain the movements of the crystal lattice dislocations that define the grain boundaries.

3.1.3 Impact on current research

Many researchers work on grain size deformation, either through experiments (e.g. Druiventak et al., 2012; Heilbronner & Keulen, 2006; Jung & Karato, 2001; Tasaka et al, 2016; Trepmann et al., 2013), numerical modelling (e.g. Cross et al., 2015), or studying natural rocks (e.g. Austrheim et al., 2017; Falus et al., 2011; Padrón-Navarta et al., 2010). While eye observations are of prime importance, they may differ from one observer to another. It is in consequence of crucial importance that we develop criteria to help describe microstructures in an objective way that anyone can refer to. Criteria most commonly used are crystallographic orientations, grain shapes, and grain sizes. If the use of distributions of the crystallographic and shape orientations is common through the use of Crystallographic Preferred Orientation (CPO) and Shape Preferred Orientation (SPO) respectively, the use of grains size orientations to characterize deformation at mantle depths is too rare. The use of the mean grain size to characterize the samples is in general preferred. However, more and more studies start to get interested in grain size distributions (e.g. Austin & Evan, 2007; Ricard & Bercovici, 2009; Rozel et al., 2011) and realize that characterizing the grain size of a sample by a single number may not always be appropriate, and that grain size distributions also contain precious information. The coupling of grain size distributions studies with CPO and SPO would be an extremely powerful tool for the description of deformation processes. The increasingly common use EBSD analyses should favor this kind studies, too rare today.

The main results in this first article are that steady state may not be as common as previously thought in natural rocks, and that a common process controlling grain sizes exists that lead to an alignment of grain size distributions along a -1 power law slope. The rare occurrence of steady-state deformation in natural rocks has a major impact on our understanding of deformation in natural settings. We propose that the absence of steady-state is caused by a succession of brittle-recovery processes, and that the duration of the deformation is not always sufficient for steady-state to be reached. Deformation is composed of a multitude of individual, short-life events among which those that develop enough, are reactivated, or sustained long-enough to reach steady-state are rare. Another consequence concerns the use of paleopiezometry. This method uses the mean grain size of a rock to estimate the stress it experienced and implies that steady-state deformation is reached. We need in consequence to be more careful with our stress estimates based on grain sizes, either coupling it with other independent methods of stress estimation, or making a thorough study of the grain size distribution to check if steady-state is indeed reached.

We propose a stochastic model to explain the occurrence of the common -1 power law slope followed by small grains of most of the distributions. The stochastic approach consists in adding a noise term that represents variations around an equilibrium state. The equilibrium state is the continuous, steady-state deformation. The addition of noise leads to the creation of new steady-states. The further these are from the equilibrium deformation, the more discontinuous the deformation is and the most short-lived the steady-states are because the conditions to obtain large amplitude noise are far from an equilibrium state. The new steady-state that is obtained for the largest noise amplitudes is a -1 power law slope. It is obtained when the movements of dislocations are fast compared to the strain rate. Meaning that during this state healing processes are favored, corresponding to our observations. The fact that dislocations move fast implies their concentration is high, explaining why this behavior is always observed for small grain sizes.

This kind of approach is very interesting as it reveals new states of deformation that would normally be overlook. It also introduces imperfections in the model through the addition of the noise and considering the movements of the dislocations are not continuous. The use of such a model makes sense as it deals with dislocations, thus atomic scale, that is known to integrate such discontinuous processes. The comparison between the rate of dislocation movements and strain rate and the importance of their role in determining the grain size distribution is also interesting as it is not considered very often. There is no doubt that this model can be improved and that it would benefit from experimental work to confirm or infirm its results, but it constitutes a good lead for future research on the subject.

The MatLab code that was used for the grain size distribution fits is available on the OSF platform: https://osf.io/6hkyu/ and can be used by anyone. This fitting method is a useful tool that we believe could be of great use for other studies working with grain size distributions. It can be used as it is, as it has been used in Jamtveit et al. (2019) or in the third article manuscript included in this thesis, but can also be the base for modifications and improvements. The two-power law fit is only a proposition of fit for the intermediate states between lognormal and power fits. It does not mean that it is the most accurate representation of these intermediate stages. Other fitting curves could be proposed. More studies are required to better understand the processes controlling grain size distributions. The indicator for the best fitting curve could also be improved. Currently it only indicates how good the lognormal fit is but there may be ways to include a comparison with the power law fits. But again, to be really reliable, this would require a better understanding of the processes behind the grain size distribution curve for intermediate stages.

References

Austin, N.J., and B., Evans. 2007. “Paleowattmeters: A scaling relation for dynamically recrystallized grain size.” *Geology*, 35 (4): 343–346. https://doi.org/10.1130/G23244A.1

Austrheim, H., K.G., Dunkel, O., Plümper, B., Ildefonse, Y., Liu, and B., Jamtveit. 2017. “Fragmentation of wall rock garnets during deep crustal earthquakes.” *Science Advances*, 3 (2): e1602067. https://doi.org/10.1126/sciadv.1602067

Cross, A.J., S., Ellis, and D.J., Prior. 2015. “A phenomenological numerical approach for investigating grain size evolution in ductiley deforming rocks.” *Journal of Structural Geology*, 76: 22–34. https://doi.org/10.1016/j.jsg.2015.04.001

Druiventak, A., A., Matysiak, J., Renner, and C.A. Trepmann. 2012. “Kick-and-cook experiments on peridotite: simulating coseismic deformation and post-seismic creep.” *Terra Nova*, 24 (1): 62–69. https://doi.org/10.1111/j.1365-3121.2011.01038.x

Falus, G., A., Tommasi, and V., Soustelle. 2011. “The effect of dynamic recrystallization on olivine crystal preferred orientations in mantle xenoliths deformed under varied stress conditions.” *Journal of Structural Geology*, 33 (11): 1528–1540. https://doi.org/10.1016/j.jsg.2011.09.010

Heilbronner, R., and N., Keulen. 2006. Grain size and grain shape analysis of fault rocks. *Tectonophysics*, 427(1-4): 199-216. https://doi.org/10.1016/j.tecto.2006.05.020

Jamtveit, B., A., Petley-Ragan, S., Incel, K. G., Dunkel, C., Aupart, H., Autrheim, F., Corfu, L., Menegon, and F., Renard. 2019. “The Effects of Earthquakes and Fluids on the Metamorphism of the Lower Continental Crust.” *Journal of Geophysical Research: Solid Earth*, 124 (8): 7725-7755. https://doi.org/10.1029/2018JB016461

Jung, H., and S.I., Karato. 2001. “Effects of water on dynamically recrystallized grain-size of olivine.” *Journal of Structural Geology*, 23 (9): 1337–1344. https://doi.org/10.1016/S0191-8141(01)00005-0

Padrón-Navarta, J.A., A., Tommasi, C.J., Garrido, V.L., Sánchez-Vizcaíno, M.T., Gómez-Pugnaire, A., Jabaloy, and A., Vauchez. 2010. “Fluid transfer into the wedge controlled by high-pressure hydrofracturing in the cold top-slab mantle.” *Earth and Planetary Science Letters*, 297 (1-2): 271–286. https://doi.org/10.1016/j.epsl.2010.06.029

Ricard, Y., and D., Bercovici. 2009. “A continuum theory of grain size evolution and damage.” *Journal of Geophysical Research: Solid Earth*, 114: B01204. https://doi.org/10.1029/2007JB005491

Rozel, A., Y., Ricard, and D., Bercovici. 2011. “A thermodynamically self-consistent damage equation for grain size evolution during dynamic recrystallization.” *Geophysical Journal International*, 184 (2): 719–728. https://doi.org/10.1111/j.1365-246X.2010.04875.x

Tasaka, M., M.E., Zimmerman, and D. L., Kohlstedt. 2016. “Evolution of the rheological and microstructural properties of olivine aggregates during dislocation creep under hydrous conditions.” *Journal of Geophysical Research: Solid Earth*, 121 (1): 92-113. https://doi.org/10.1002/2015JB012134

Trepmann, C.A., J., Renner, and A., Druiventak. 2013. “Experimental deformation and recrystallization of olivine - processes and timescales of damage healing during postseismic relaxation at mantle depths.” *Solid Earth*, 4 (2): 423–450. https://doi.org/10.5194/se-4-423-2013

3.2 Manuscript 2: Seismic controls on the progress of serpentinization at ultra-slow spreading ridges

This second manuscript is in preparation to be send to the *Journal of Geophysical Research: Solid Earth*. It is a study based on the application of a damaged rock volume calculation presented in Jamtveit et al. (2018) using seismic data from the ultra-slow South-West Indian Ridge (SWIR). Consequences for serpentinization in mid-oceanic ridge settings are discussed.

3.2.1 Summary

This study explores how seismic faulting controls the progress of serpentinization. It is based on seismic data from two ultra-slow sections of the SWIR. Three types of ultra-slow ridge segments with significant differences in seismic activity were identified. The amagmatic type is characterized by scarce basaltic crust and deep seismic activity. The magmatic type is characterized by a thin basaltic crust and intermediate depth seismic activity. The volcanic type is characterized by a thick basaltic crust and shallow seismic activity. At amagmatic and magmatic ridge types, aseismic zones are identified above the seismic zone. The lower limit of the aseismic zone along amagmatic sections is thermally controlled and follows an isotherm around 400-500°C. This observation suggests that the aseismic zone is extensively serpentinized, and the temperature control of its lower limit suggests ample supply of water to the peridotite-serpentine interface. We calculated the volume of lithosphere affected by brittle damage based on the seismic activity at each segment type. The results show that the permeability created along both amagmatic and magmatic ridge types is sufficient to sustain extensive serpentinization. The damaged volume is much more limited in the case of the volcanic ridge type only allowing for localized serpentinization.

3.2.2 Work and techniques involved

This article is based on seismic data from the SWIR acquired within 11 months in 2012-2013 by Ocean Bottom Seismometers (OBS). This dataset was thus acquired well before the beginning of this PhD thesis and three papers had already been published (Schlindwein & Schmid, 2016; Schmid & Schlindwein, 2016; Schmid et al., 2017) when we started working on this article. It is composed of two ridge segments: one located in the south of the SWIR, in a mostly amagmatic zone (divided into a magmatic and an amagmatic portion based on differences in seismic depth), the other one located in the north of the SWIR, around a volcanic center. The element that started this project is the fact that Schlindwein & Schmid (2016) observed a shallow aseismic zone along the south segment. As the seafloor along this segment is mostly composed of serpentinized peridotite (Schlindwein & Schmid, 2016) and since serpentinization has the effect of weakening the rock (Escartin et al., 1997; Escartin et al., 2001), Schlindwein & Schmid (2016) proposed that this aseismic zone could mark a serpentinized zone. Our aim in this work was to check if this hypothesis is possible based on the data we had available: the seismicity.

The core of this project relies on an application of a calculation presented in Jamtveit et al. (2018). This calculation estimates the volume of rock that is damaged by a certain seismic activity defined by the *a*- and *b*-values of the Gutenberg-Richter law (Figure 3.2.1). To be able to use this formula we consequently had to estimate the *a*- and *b*-values from the SWIR earthquake catalogues. For this task, we used lists of all the earthquakes reliably identified during a localization procedure made on the raw seismic data. These lists contain the spatial position, and estimated magnitude of all events, as well as their time and date of occurrence. From the relative position of the earthquakes, in particular from variations in the depth of the seismic zone, we defined the limits of three ultra-slow ridge types: amagmatic, magmatic and volcanic. We wrote a MatLab code to estimate the *a*- and *b*-values based the cumulative distributions of the earthquake magnitudes for each ridge type (amagmatic, magmatic and volcanic). The method has been designed to obtain *a*- and *b*-values as precise and reliable as possible. It relies on the determination of two magnitudes, M_c and M_{co} in the manuscript, between which the Gutenberg-Richter law is valid (Figure 3.2.1). The determination of M_c is done by combining already existing methods, while the determination of M_{co} is done combining new methods, adapted from existing ones. The *a*- and *b*-values are then obtained from a simple linear regression between M_c and M_{co}. The damage volume calculation was implemented on the same MatLab code as the *a*- and *b*- values determination. One value of damage volume was calculated for each ridge type. To make results easier to read and interpret, the damage volumes obtained were normalized with the size of the seismic zone to obtain percentages.

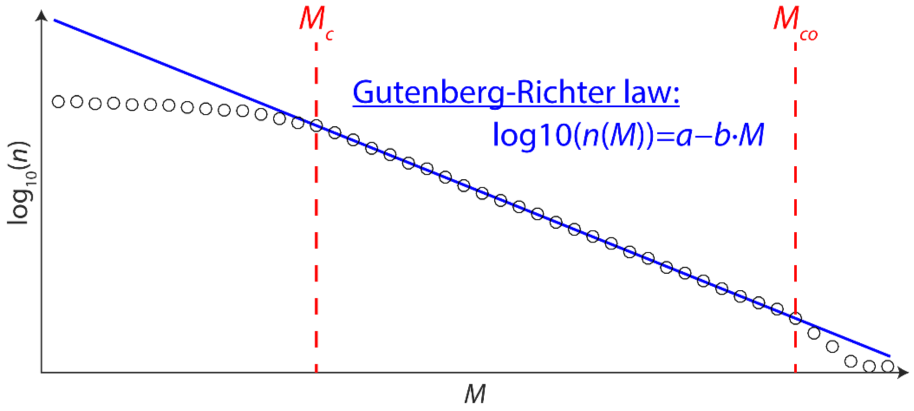

Figure 3.2.1: *Representation of the Gutenberg-Richter Law. The black circles represent a cumulative distribution of earthquake magnitudes. They follow the Gutenberg-Richter law (in blue) between two magnitudes noted* M_c *and* M_{co}*. M represents the magnitudes; n represents the cumulative number of earthquakes of a certain magnitude.*

A first version of the work presented in this manuscript has already been submitted and rejected by the journals *Earth and Planetary Science Letters* and *Geochemistry, Geophysics, Geosystems*. The main reason for these rejections is a controversy on the localization of the seismic data along the southern most segment we studied. In this first version, we had used the same localization presented in the two 2016 papers (Schlindwein & Schmid, 2016; Schmid & Schlindwein, 2016) that displayed large errors on the localization of the seismic depths. These large errors are due to the presence of unusual soft sediments under four of the eight OBS stations used during the acquisition. This makes this dataset particularly difficult to localize with accuracy. One of the reviewers suggested that we should propose an improved localization of the seismic dataset that would make our work more robust. We decided to follow this advice, and the last version of this article in this PhD thesis manuscript includes a relocation of the seismic catalogue. Consequently, the *a*- and *b*- values as well as the volumes of damaged rock have all been recalculated according to the new catalogue.

Meanwhile, another localization of the same earthquake catalogue from the south of the SWIR had been made by Grevemeyer et al. (2019). We contacted I. Grevemeyer to propose to make a comparative study between the two datasets in the discussion part of our paper. He accepted and sent us his own location of the seismicity. Unfortunately, as his group had not calculated the earthquakes' magnitudes, we could not calculate the corresponding *a*- and *b*-values. We, in consequence, compare and discuss the two datasets only based on the earthquakes repartition in space. Repartition plots used were made using MatLab.

3.2.3 Impact on current research

The processes that are active during serpentinization at depth along mid-oceanic ridges are still poorly understood. Thanks to numerous geophysical and sampling campaigns, we know that serpentinization occurs up to several kilometers depth (e.g. Momoh et al., 2017; Canales et al., 2008), at least in specific locations. The processes active during serpentinization at depth along mid-oceanic ridges are difficult to constrain as samples are limited. It is thus crucial to be innovative and use at best the data we have available. In this work, we present an application of the calculation of the volume of seismically damaged rocks presented in Jamtveit et al. (2018). Using data from the SWIR seemed a good starting point as it has ultra-slow ridge sections that are more seismically active than faster mid-oceanic ridges.

Because this work uses the sensitive seismic dataset from the SWIR first published in Schlindwein & Schmid (2016), it has been included into the controversy associated with the delicate localization of the seismic events of this dataset. It forced us to propose a new localization of the seismicity and consequently, to participate to this controversy. This even though, as we show in our discussion with the comparison with Grevemeyer et al.'s (2019) localization, that the exact position of the seismic zone, thus the controversy itself, does not have any major impact on our main result. The discussion over this particular dataset is still ongoing (Grevemeyer et al., 2019; Schlindwein, 2020; Grevemeyer & Lange, 2020).

Our study highlights the major impact that has the tectonic activity along mid-oceanic ridges on permeability of the crust and consequently on its hydration. We show that, among mid-oceanic ridge portions that we study, those which extension is dominated by tectonics (i.e. the amagmatic and magmatic ultra-slow ridge types) produce a significant proportion of damaged rocks, enabling deep seawater penetration. These portions also exhibit thinned magmatic crust or exposed peridotite. This implies that all the conditions for extensive serpentinization to occur are gathered, with seismic activity as the driving process. As the ridge segments we study represent typical ultra-ridge sections, we assume this result is valid for other ultra-slow ridges. A comparison between the *b*-values we obtain from our datasets and *b*-values obtained by other studies along mid-oceanic ridges seem to indicate that this result could extend to other ridge types, the amagmatic ridge type being represented only along ultra-slow ridges, the slow ridges by a combination of magmatic and volcanic ridges types, and the fast ridges being composed only of the volcanic ridge type. However, this extrapolation of our result should be verified, in particular because differences on the *a*-values, that could not be compared, could lead to significant differences on the damaged rock volume result. This result is nonetheless significant as tectonic faulting has often been observed as controlling the localization of serpentinization (e.g. Bayrakci et al., 2016; Bourgault et al., 1993) but is rarely recognized as a mean of pervasive serpentinization by microscale studies. This highlights that intermediate scale tectonic activity, not only the largest faults, contribute to the hydration of the oceanic lithosphere.

Based on this main result, we propose a conceptual model for serpentinization along ultra-slow spreading ridges. In this model, we distinguish three ridge types according to the ones we identify based on our seismic data. These different ridge types are only there to be used as illustration of how, for similar spreading rates, variations in thermal regime of the ridge controls the depth and intensity of seismicity and consequently the serpentinization depth. According to our result that colder and most tectonically active portions of ridge produce sufficient fracturing for deep water penetration to occur, the amagmatic and magmatic ridge types both are represented with a seismic zone, mostly located in fresh peridotite, below a shallow serpentinized zone. The two zones overlap in a transition zone thermally controlled corresponding to the onset of serpentinization. In these cases, the serpentinization depth is not limited by the availability of water. In the case of the volcanic segment, however, the seismic activity is not sufficient for water to pervasively penetrate the rock and serpentinization occurs only locally. The seismic zones' depths used for illustration in the conceptual model are based on the depths observed in our relocation. It thus must be specified that this study has been made along one of the slowest ultra-slow ridge sections on Earth. In this context, there is very limited heat coming from the oceanic ridge and the maximum depth of seismicity is deeper than along any other ridge. This means that the depths we use to illustrate our model are maximum depths and should not be considered as absolute depths.

We finally propose an estimate of the serpentinized volume produced along mid-oceanic ridges. This estimate is admittedly rather rough, as is often the case with this kind of estimate. The results it returns are nonetheless reasonable, in the same order of magnitude and slightly larger than Cannat et al.

(2010), and supports the likeliness of our model. It also suggests that tectonic activity is the driving force for most of the serpentinization along mid-oceanic ridges.

The damage calculation (Jamtveit et al., 2018) that we use in this study is a versatile tool that can be use in various tectonic contexts. Concerning its application in relation with serpentinization along mid-oceanic ridges, it would be interesting to conduct similar studies as this one along other mid-oceanic ridge portions. It would both help confirm the result and proposed model of this study, and provide better constraints on serpentinization along faster spreading ridges. Still in relation with serpentinization, an application along subduction zones could also be of interest to study the impact of factors such as the age or orientation of the subducting plate on the intensity of the seismic activity, permeability creation and consequently on the repartition of serpentinization.

A few points of the damaged rock volume calculation should be considered for further application. One of the hypotheses we make to establish the formula of the damaged rock volume calculation is that the shape of the damage zone is circular. This approximation is likely close to the reality for small magnitude earthquakes, but a closer approximation for large magnitude earthquakes would be an ellipsoidal shape. This point may not have a big impact in studies along mid-oceanic ridges, such as our study, but it may be of importance for applications along subduction zones or other zones with a significant proportion of large magnitude earthquakes. In addition to the *a*- and *b*-values that are determined directly from the dataset, the damaged rock volume calculation depends on two other parameters, the *e*- and *d*-values characterizing the earthquake potency (Ben-Zion & Zhu, 2002), not directly dependent on the dataset, but that could vary depending on the geological context. There is currently no estimate of these parameters in an oceanic context, thus the *e*- and *d*-values we use in this study were obtained in South California (Ben-Zion & Zhu, 2002). If a more systematic use of the damaged rock calculation formula were to be done along mid-oceanic ridges or subduction zones, it would be beneficial to have estimate of the *e*- and *d*-values in corresponding settings available.

For any study using the damaged volume calculation, we suggest the use of the method of *a*- and *b*- values determination we designed. The MatLab code is available on the the OSF platform: https://osf.io/zt23n/. It has the advantage to provide similar *a*- and *b*-values than most commonly used methods (Utsu, 1965; Shi & Bolt, 1982), but with a higher precision. This helps to limit the error generated during the damaged volume calculation that was in our study only estimated based on the *a*- and *b*-values variations as they were the only variables varying from one zone of study to the other. Despite this, the overall error in our case stayed relatively large. This is due to the fact that the magnitude range over which we calculate the damaged rock volume is larger than the one over which we determined the *a*- and *b*-values. There is a higher incertitude on the Gutenberg-Richter law the further the magnitudes are from the range of *a*- and *b*-values estimate. The incertitude on the amount of large magnitude earthquakes, that produce the most damage, leads to large errors on the damaged rock volumes. This problem cannot be solved by excluding earthquakes of magnitudes above the *a*- and *b*-values determination range, as they produce important damage to the rock that should be accounted for. The ideal way to deal with this problem would be to have an extensive dataset including the largest possible range of magnitudes for the *a*- and *b*-values estimate. Another way to deal with it would be to combine datasets recorded at different scales. This, however, would raise a magnitude conversion problem between the different datasets. Conversions exist (e.g. Das et al., 2011; Edwards et al., 2010; Kanamori, 1977), but their exactitude and reliability are debatable, and they may actually create erroneous results. The resolution of this scaling problem would surely be a major improvement for the error estimate of the damaged volume calculation.

Finally, the estimate of the damage overlapping would be a major addition to the damage volume calculation. It would require some knowledge in statistics and mathematics, but it should be possible to provide a probability curve of the most likely amount of damage overlapping considering a certain density of damage. Another way would be to model the localization of all the earthquakes with their associated damage zone and calculate the cumulative intersection of all the damage zones. The result would then be highly dependent on the quality of the localization of the seismic data. The damage overlap estimate could represent a first step towards a proper estimate of the permeability from the seismic activity. The results we obtained in our study were sufficiently extreme to assume with confidence a pervasive permeability or limited permeability. However, future studies may not obtain such extreme results and need an estimate of the permeability to interpret their results.

References

Bayrakci, G., T. A., Minshull, D. S., Sawyer, T. J., Reston, D., Klaeschen, C., Papenberg, C., Ranero, J. M., Bull, R. G., Davy, D. J., Shillington, M., Pérez-Gussinyé, and J. K., Morgan. 2016. "Fault-Controlled Hydration of the Upper Mantle during Continental Rifting." *Nature Geoscience*, 9 (5): 384–388. https://doi.org/10.1038/ngeo2671

Ben-Zion, Y., and L., Zhu. 2002. "Potency-magnitude scaling relations for southern California earthquakes with 1.0<ML<7.0." *Geophysical Journal International*, 148 (3): F1–F5. https://doi.org/10.1046/j.1365-246X.2002.01637.x¨

Bourgault, H., J.-L. Charlou, Y. Fouquet, H. D. Needham, N. Vaslet, P. Appriou, P. J. Baptiste, P. A. Rona, L. Dmitriev, and S. Silantiev. 1993. "Fast and Slow Spreading Ridges: Structure and Hydrothermal Activity, Ultramafic Topographic Highs, and CH $_4$ Output." *Journal of Geophysical Research*, 98 (B6): 9643. https://doi.org/10.1029/93JB00508

Canales, J. P., B. E., Tucholke, M., Xu, J. A., Collins, and D. L., DuBois. 2008. "Seismic evidence for large-scale compositional heterogeneity of oceanic core complexes." *Geochemistry, Geophysics, Geosystems*, 9 (8). https://doi.org/10.1029/2008GC002009

Cannat, M., F. Fontaine, and J. Escartín. 2010. "Serpentinization and Associated Hydrogen and Methane Fluxes at Slow Spreading Ridges." In *Geophysical Monograph Series, volume 188: Diversity Of Hydrothermal Systems On Slow Spreading Ocean Ridges*, edited by P. A. Rona, C. W. Devey, J. Dyment, and B. J. Murton, 241–264. Washington, D. C.: American Geophysical Union. https://doi.org/10.1029/2008GM000760

Das, R., H. R. Wason, and M. L., Sharma. 2011. “Global regression relations for conversion of surface wave and body wave magnitudes to moment magnitude.” *Natural Hazards*, 59: 801–810. https://doi.org/10.1007/s11069-011-9796-6

Edwards, B., B., Allmann, D., Fäh, and J., Clinton. 2010. “Automatic computation of moment magnitudes for small earthquakes and the scaling of local to moment magnitude.” *Geophysical Journal International*, 183 (1): 407–420.

Escartin, J., G. Hirth, and B. Evans. 1997. “Effects of serpentinization on the lithospheric strength and the style of normal faulting at slow-spreading ridges.” *Earth and Planetary Science Letters*, 151 (3-4), 181-189. https://doi.org/10.1016/S0012-821X(97)81847-X

Escartin, J., G. Hirth, and B. Evans. 2001. “Strength of Slightly Serpentinized Peridotites: Implications for the Tectonics of Oceanic Lithosphere.” *Geology*, 29 (11): 1023-1026. https://doi.org/10.1130/0091-7613(2001)029<1023:SOSSPI>2.0.CO;2

Grevemeyer, I., N. W. Hayman, D. Lange, C. Peirce, C. Papenberg, H. J.A. Van Avendonk, F. Schmid, L. G. de La Peña, and A. Dannowski. 2019. “Constraining the Maximum Depth of Brittle Deformation at Slow- and Ultraslow-Spreading Ridges Using Microseismicity.” *Geology*, 47 (11): 1069–1073. https://doi.org/10.1130/G46577.1

Grevemeyer, I., and D., Lange. 2020. “Constraining the Maximum Depth of Brittle Deformation at Slow- and Ultraslow-Spreading Ridges Using Microseismicity: REPLY.” *Geology*, 48 (5): 502. https://doi.org/10.1130/G47542Y.1

Jamtveit, B., Y. Ben-Zion, F. Renard, and H. Austrheim. 2018. “Earthquake-Induced Transformation of the Lower Crust.” *Nature*, 556: 487–491. https://doi.org/10.1038/s41586-018-0045-y

Kanamori, H. 1977. “The energy release in great earthquakes.” *Journal of geophysical research*, 82 (20): 2981-2987. https://doi.org/10.1029/JB082i020p02981

Momoh, E., M., Cannat, L., Watremez, S., Leroy, and S. C., Singh. 2017. “Quasi-3D seismic reflection imaging and wide-angle velocity structure of nearly amagmatic oceanic lithosphere at the ultraslow-spreading southwest Indian ridge.” *Journal of Geophysical research: Solid Earth*, 122 (12): 9511-9533. https://doi.org/10.1002/2017JB014754

Schlindwein, V., and F. Schmid. 2016. “Mid-Ocean-Ridge Seismicity Reveals Extreme Types of Ocean Lithosphere.” *Nature*, 535: 276-279. https://doi.org/10.1038/nature18277

Schlindwein, V. 2020. “Constraining the Maximum Depth of Brittle Deformation at Slow- and Ultraslow-Spreading Ridges Using Microseismicity: COMMENT.” *Geology*, 48 (5): 501. https://doi.org/10.1130/G47444C.1

Schmid, F., and V. Schlindwein. 2016. “Microearthquake Activity, Lithospheric Structure, and Deformation Modes at an Amagmatic Ultraslow Spreading Southwest Indian Ridge Segment.” *Geochemistry, Geophysics, Geosystems*, 17 (7): 2905–2921. https://doi.org/10.1002/2016GC006271

Schmid, F., V. Schlindwein, I. Koulakov, A. Plötz, and J.-R. Scholz. 2017. “Magma Plumbing System and Seismicity of an Active Mid-Ocean Ridge Volcano.” *Scientific Reports*, 7 (February): 42949. https://doi.org/10.1038/srep42949

Shi, Y., and B. A., Bolt. 1982. “The standard error of the magnitude-frequency *b* value.” *Bulletin of the Seismological Society of America*, 72 (5): 1677–1687.

Utsu, T. 1965. “A Method for Determining the Value of b in a formula $\log n = a\text{-}b\mathrm{M}$ showing the Magnitude-Frequency Relation for Earthquakes.” *Geophysical Bulletin of Hokkaido University*, 13: 99-103.

3.3 Manuscript 3: Mass-transfer during early stage faulting and cataclasis of peridotites from the Samail Ophiolite, Oman

This third manuscript is a work in progress. It is a multiscale, microstructural and chemical study based on samples obtained during the Oman Drilling Project. It focuses on a family of faults and cataclasites associated with the early stages of serpentinization.

3.3.1 Summary

This third manuscript is focused on the role of faulting during the early stages of serpentinization. It is based on the study of rock samples from cores recovered during the Oman Drilling Project. These cores are crosscut by a series of ubiquitous dark and highly localized faults. We investigated their timing and role with respect to the formation of the main serpentinization event represented by mesh-textured serpentinites using a combination of microstructural observations and chemical analysis. Asymmetric wall-rock damage, weakening of crystal preferred orientation (CPO) in small fault clasts, and intense fragmentation within the fault zones even with very small displacements suggest that the early stage faults represents seismic events and predate mesh formation. Hydration and mesh texture formation follows in the wake of this faulting. Moderate enrichments in fluid mobile elements indicate mesh texture formation occurred under relatively low water-rock ratios. This is consistent with a scenario where serpentinization took place below a thick magmatic crust following an earthquake induced permeability increase. The oxygen isotope compositions of mesh serpentine are consistent with high temperature serpentinization (up to ~350˚C) by a hydrothermally evolved fluid composition.

3.3.2 Work and techniques involved

Samples used in this study have been obtained through the Oman Drilling Project (https://www.omandrilling.ac.uk/). The drilling within the Samail ophiolite in Oman occurred in two phases: one in winter 2016-2017, the other one in winter 2017-2018. One of the axes of study of the whole project was active serpentinization. One site, the BA site, was dedicated to it. Seven holes were drilled at this site, including one 400 m long and two 300 m long cores recovered with 100% recovery. The major part of the drilling at the BA site occurred during winter 2017-2018, in particular the drilling of the recovered cores. We were involved in this whole project and went on the drilling site to help recover the cores. The cores were drilled by sections of 3 meters. Each 3-meter section was thoughtfully reassembled if broken and precisely measured. It was then divided into sections of less than one meter to be put into boxes. All the pieces of the cores were counted, curated, scanned (if the core was not too fragile) and labelled. Fragments that were too small were put into bags. They were then quickly drawn and described before a picture of each box was taken and the box was closed. Every ca. ten meters a sample, preferably representative of the background composition, was collected for thin sections and X-ray analyses. A team of biologist also collected a sample every ca. ten meters to study the populations of microorganism present (if any) and their contribution to the rock alteration.

Once in their boxes, the cores were transferred to the research drilling vessel Chikyu were they were thoroughly described in august 2018. Again, we participated to this description phase. The study of the cores was divided in five groups. Three groups were describing ca. 60 meters of cores every day, one group describing the original (pre-alteration) composition of the cores and estimating the amount and minerals of alteration, a second group dedicated to the veins description and a last group giving a structural description of the cores. Thin sections and X-ray analyses could be done on-board to help with the descriptions. The two last groups were conducting physical and chemical analyses, respectively. All of the observations and results obtained during this month are grouped in an International Ocean Drilling Program Report (soon available at http://publications.iodp.org/other/Oman/OmanDP.html). Before the description started, the Chikyu scientific crew had cut in halves all the cores. One half of the cores was used for sampling and manipulations (especially by the structural description team). The second halves are kept as an archive, no sampling should be done on them. They were used for the core background and veins descriptions and were scanned by the Chikyu scientific crew.

During autumn 2018, we received the 143 samples we had requested from the cores and could start working on them. We had 15 thin sections made in January 2019. All of them were microscopically described. Among other interesting features present in these samples, we decided to focus on a family of fault that seemed to occur rather early in the history of the rock and tried to understand their place in this history. Macroscopic observations were made directly on the samples we received and on the core scans made on the Chikyu and on the drilling site. The few thin sections we had containing these faults were studied under the Scanning Electronic Microscope (SEM). We choose a thin section that did not contain any dyke or chemical source other than the fault zone to conduct additional electronic microprobe analyses. We could thus get the chemical signature of the fault. Microscopic and SEM observations as well as electronic microprobe analyses were conducted at the University of Oslo. The thin sections present a relatively high level of serpentinization and olivine relicts are rare. The only mineral that has been left relatively unaltered is clinopyroxene. Luckily, some of our thin sections contain a large grain gabbroic dyke displaced by one of the early faults. We selected one of these to make Electronic Back-Scattered Diffraction (EBSD) maps and access the fault signature in the clinopyroxene crystallographic orientation. These maps were made in Zürich by L. Morales. We selected samples for whole rock trace element analyses: two background samples, as fresh as possible, representative of the core lithology, and two other samples including developed early fault zones. Our aim was to check if there was any signature of the faults in the trace elements. Powders were prepared in Oslo and send in Montpellier to be analyzed in December 2019. Finally, we went to Stockholm for two days in February 2020 to proceed to ion probe analyses (Secondary-Ion Mass Spectrometry; SIMS), focusing on serpentine oxygen isotopes and boron content.

In addition to this work that is included in the article manuscript, we had some Focused Ion Beam section prepared, and supplementary thin sections in preparation. None of them have been analyzed yet.

3.3.3 Impact on current research

The role of fracturing during serpentinization is mostly recognized along large faults where serpentinite has been observed to localize such as detachment faults along mid-oceanic ridges (e.g. Bourgault et al., 1993; Ildefonse et al., 2007), bend-faulting in subduction zones (e.g. Ranero et al., 2003), or large normal faults in passive margin (e.g. Bayrakci et al., 2016). At microscale, the role of tectonic faulting has until now always been described as secondary. The origin of microfractures is most of the time inferred to be thermal cracking (e.g. Boudier et al., 2010; Rouméjon & Cannat, 2014) or self-induced fracturing (e.g. Plümper et al., 2012). There is thus a discrepancy between what happens at the scale of the crust and at microscale. This does not mean that thermal cracking or self-induced fracturing do not occur, but there is a need to reconcile the two scales. This problem partly comes from the methods we can use to obtain data from oceanic lithosphere. While geophysical methods are not able of decerning the details of the microscale processes, dredge or drilled samples only provide a restricted view of the large scale structures associated with serpentinization.

The Oman Drilling Project offered the opportunity to drill within the Samail Ophiolite, an ancient spreading center (Boudier et al., 1997), combining local sampling with the possibility to conduct medium or large scale structural or geophysical studies. Studying an ophiolite is also the opportunity to reach rocks that are normally inaccessible in normal mid-oceanic ridge context such as the lithospheric mantle below a thick magmatic crust. The main advantage of obtaining drilled cores over regular sampling is to be able to obtain continuous sections of the ophiolite, and in the case we are interested in, of the oceanic lithospheric mantle. Due to the easier conditions for drilling, the recovery rates that were obtained (100%) are much higher than those obtained during any oceanic drilling (ca. 40% in general). Another advantage is that the cores reach levels below the weathering front, thus any alteration observed below this front occurred either, while the lithosphere was under the ocean, or during the ophiolite emplacement. For these reasons, the Oman DP cores are pretty unique.

The approach we used with our set of samples groups chemical and microstructural observations from macroscopic to microscopic scale. The main result we obtained is that fracturing has a significant role in the early phases of serpentinization. We could determine that the early faulting occurred before the main stage of serpentinization, represented by mesh texture formation. The deformation associated with the fault has characteristic typical of an energetic, possibly seismic event. Serpentinization occurred at temperatures around 350°C, first in relatively closed system (formation of the mesh veins), opening with time (formation of the mesh cores), likely under a thick magmatic crust. The evolution of the mesh cores with distance to the fault zone indicates a close relation between the fault and the cores formation. Based on these observations, we propose a model for serpentinization.

However, some questions remain. We do not know the origin of the faults, and if our observations suggest that the fault zone controlled the orientation of the mesh veins, we do not have any solid evidence for that. Moreover, if know the relative timing of the structures composing the sample, nothing is certain concerning its timing in the ophiolite history. Some supplementary studies could be made to help answer these questions. Preparing a few more thin sections perpendicular to the ones we already have to reconstruct the 3D orientation of the mesh texture relative to the fault zone would be of great help to better constrain the relation between the fault and the mesh veins. Quantifying the repartition and orientation (when possible) of the early faults and cataclasis in the cores would be a tedious work given their dark aspect, difficult to notice within dark serpentinized peridotites, that can sometimes be confused with magnetite-rich serpentine veins (the distinction is easily made in thin section). Yet, it would be a step further to reconcile scales by increasing the scale of this study and could be key to determine the origin and exact timing of these early deformation features.

The model we propose integrates faulting within the microscale sequence of serpentinization. The fault acts as a permeable pathway leading water inside the peridotite. It is also associated with metasomatism and transport of elements when the system opens in the later stages of serpentinization. This model seems reasonable given the samples we describe. However, the validity of this model elsewhere needs to be assessed. As mentioned above, the role of fracturing during serpentinization is rarely described at microscale. The faults and cataclasis we describe are not particularly rare in the Oman DP cores, but their discreet appearance makes them hard to notice. They could have been easily overlooked previously. The fact that we noticed them in these cores is only thanks to the exceptional recovery rate and quality of core that was obtained during the Oman DP. It would be interesting though to look for them in other ophiolites or in samples obtained in oceanic settings.

References

Bayrakci, G., T. A., Minshull, D. S., Sawyer, T. J., Reston, D., Klaeschen, C., Papenberg, C., Ranero, J. M., Bull, R. G., Davy, D. J., Shillington, M., Pérez-Gussinyé, and J. K., Morgan. 2016. “Fault-Controlled Hydration of the Upper Mantle during Continental Rifting.” *Nature Geoscience,* 9 (5): 384–388. https://doi.org/10.1038/ngeo2671

Boudier, F., A., Nicolas, B., Ildefonse, and D., Jousselin. 1997. “EPR microplates, a model for the Oman ophiolite.” *Terra Nova*, 9 (2): 79-82. https://doi.org/10.1111/j.1365-3121.1997.tb00007.x

Boudier, F., A., Baronnet, and D., Mainprice. 2010. “Serpentine Mineral Replacements of Natural Olivine and Their Seismic Implications: Oceanic Lizardite versus Subduction-Related Antigorite.” *Journal of Petrology,* 51 (1–2): 495–512. https://doi.org/10.1093/petrology/egp049

Bourgault, H., J.-L., Charlou, Y., Fouquet, H. D., Needham, N., Vaslet, P., Appriou, P. J., Baptiste, P. A., Rona, L., Dmitriev, and S., Silantiev. 1993. “Fast and Slow Spreading Ridges: Structure and Hydrothermal Activity, Ultramafic Topographic Highs, and CH_4 Output.” *Journal of Geophysical Research*, 98 (B6): 9643. https://doi.org/10.1029/93JB00508

Ildefonse, B., D. K., Blackman, B. E., Jhon, Y., Ohara, D. J., Miller, C. J., MacLeod, and the Integrated Ocean Drilling Program Expeditions 304/305 Science Party. 2007. “Oceanic core complexes and crustal accretion at slow-spreading ridges.” *Geology*, 35 (7): 623-626. https://doi.org/10.1130/G23531A.1

Plümper, O., A., Røyne, A., Magrasó, and B., Jamtveit. 2012. “The interface-scale mechanism of reaction-induced fracturing during serpentinization.” *Geology*, 40 (12): 1103-1106. https://doi.org/10.1130/G33390.1

Ranero, C. R., J. P., Morgan, K., McIntosh, and C., Reichert. 2003. “Bending-Related Faulting and Mantle Serpentinization at the Middle America Trench.” *Nature*, 425: 367–373. https://doi.org/10.1038/nature01961

Rouméjon, S., and M., Cannat. 2014. “Serpentinization of Mantle-Derived Peridotites at Mid-Ocean Ridges: Mesh Texture Development in the Context of Tectonic Exhumation.” *Geochemistry, Geophysics, Geosystems*, 15 (6): 2354–2379. https://doi.org/10.1002/2013GC005148

Manuscript 1

Olivine Grain Size Distributions in Faults and Shear Zones: Evidence for Nonsteady State Deformation

Claire Aupart, Kristina G. Dunkel, Luiza Angheluta, Håkon Austrheim, Benoit Ildefonse,
Anders Malthe-Sørenssen, and Bjørn Jamtveit.

Journal of Geophysical Research: Solid Earth

My contributions

- Data acquisition:

- Fieldwork and sampling at Leka Island in August 2016 along with supervisors.
- I went to Géosciences Montpellier one week in February 2017 to aquire EBSD data and learn how to process the raw data.
- One of the samples I personally collected (sample LECA16-11) and analysed by EBSD at Montpellier was used in the final paper. All the observations and pictures concerning this sample in the paper were made by me.

- Data processing:

- I processed with MTEX the EBSD maps of samples M02-8a, Cor19-06, ÅF2-4, and LECA16-11, and from Tasaka et al., 2016 presented in the paper to obtain the grain size area. The grain size data for the other samples was obtained from other researchers. I also processed the EBSD data for crystal preferred orientations and misorientations for the samples for which these data are presented in the figures of the paper.
- I created a MatLab code for the curve fitting of the grain size distributions. This code can fit distributions with lognormal, single power law or double power law and creates raw versions of the figures presented in the paper. It also returns an Excel spreadsheet with the fitting parameters, number of grains, mean and median grains area, etc. It is available with the EBSD maps on the OSF platform: https://osf.io/6hkyu/.
- I created another Matlab code to calculate the angle distributions in all samples based on the EBSD maps using MTEX functionalities (done for all samples except the kick-and-cook samples for which I did not have the EBSD maps available). However, I did not prepare a clean, commented version of this code and it is not yet available on the OSF platform.

- Paper:

- I wrote the text in the paper with the help of my main supervisor, B. Jamtveit. The other co-authors participated mostly by proof reading or by helping with the writing of sections they were more involved with.
- I prepared all the tables and figures in the paper and in the supplements.
- Concerning the discussion part, I wrote section 7.2. based on a model developed in collaboration with L. Angheluta, based on her input.

Journal of Geophysical Research: Solid Earth

RESEARCH ARTICLE
10.1029/2018JB015836

Olivine Grain Size Distributions in Faults and Shear Zones: Evidence for Nonsteady State Deformation

Claire Aupart[1], **Kristina G. Dunkel**[1], **Luiza Angheluta**[2], **Håkon Austrheim**[1], **Benoit Ildefonse**[3], **Anders Malthe-Sørenssen**[2], and **Bjørn Jamtveit**[1]

[1]Physics of Geological Processes, The Njord Centre, Department of Geosciences, University of Oslo, Oslo, Norway, [2]Physics of Geological Processes, The Njord Centre, Department of Physics, University of Oslo, Oslo, Norway, [3]Géosciences Montpellier, CNRS, University of Montpellier, Université des Antilles, Montpellier, France

Key Points:

- Olivine grain size distributions from faults and shear zones indicate that steady state deformation is less common than hitherto thought
- Brittle deformation causes power law scaling, while plastic mechanisms lead to lognormal distributions at steady state conditions
- Grain size distributions often show a crossover between two power laws where the smaller grain sizes scale independently of strain rates

Supporting Information:

- Supporting Information S1

Correspondence to:
C. Aupart,
c.o.m.aupart@geo.uio.no

Citation:
Aupart, C., Dunkel, K. G., Angheluta, L., Austrheim, H., Ildefonse, B., Malthe-Sørenssen, A., & Jamtveit, B. (2018). Olivine grain size distributions in faults and shear zones: Evidence for nonsteady state deformation. *Journal of Geophysical Research: Solid Earth*, *123*. https://doi.org/10.1029/2018JB015836

Received 26 MAR 2018
Accepted 1 AUG 2018
Accepted article online 7 AUG 2018

Abstract The grain size distribution of deformed rocks may provide valuable information about their deformation history and the associated mechanisms. Here we present a unique set of olivine grain size distributions from ultramafic rocks deformed under a wide range of stress and strain rate conditions. Both experimentally deformed and naturally deformed samples are included. We observe a surprisingly uniform behavior, and most samples show power law grain size distributions. Convincing lognormal distributions across all scales were only observed for samples experimentally deformed at high temperature (1200 °C) and for some mantle-deformed natural samples. Single power law distributions were observed for natural samples deformed by brittle mechanisms and by samples deformed experimentally in the regime of low-temperature plasticity. Most natural samples show a crossover in power law scaling behavior near the median grain size from a steep slope for the larger grain fraction to a more gentle slope for the smaller grains. The small grain fraction shows a good data collapse when normalized to the crossover length scale. The associated power law slope indicates a common grain size controlling process. We propose a model that explains how such a scaling behavior may arise in the dislocation creep regime from the competition between the rate involved in the dislocation dynamics and the imposed strain rate. The common departure from lognormal distributions suggests that naturally deformed samples often have a deformation history that is far from a steady state scenario and probably reflects deformation under highly variable stress and strain rates.

1. Introduction

Localized deformation, brittle or ductile, is normally associated with a significant reduction in the grain size of the rocks involved. In low-temperature cataclastic fault zones, fragmentation takes place by brittle mechanisms and the fragment size distribution often shows a power law size distribution (e.g., An & Sammis, 1994; Billi, 2005; Heilbronner & Keulen, 2006). Grain growth is in most cases only effective at submicron length scales (Sammis & Ben-Zion, 2008).

At higher temperatures grain size reduction may take place by either brittle or ductile mechanisms depending both on the stress level and a range of other factors, including temperature (De Bresser et al., 2001; Stipp et al., 2002), water content (H. Jung & Karato, 2001), crystal orientation (Linckens et al., 2016), strain rate (Stipp et al., 2002), and the presence or absence of multiple phases (Cross et al., 2015; Doherty et al., 1997; Drury & Urai, 1990). The grain size evolution at elevated temperatures is controlled by a competition between grain size-reducing processes and grain growth (e.g., Cross et al., 2015). It is often assumed that the grain size distribution reaches a steady state during dynamic recrystallization (Tasaka et al., 2016), follows lognormal scaling behavior, and is adequately described by its mean value. The mean grain size is often used as a proxy for past stress levels (paleopiezometry; Stipp et al., 2010; Twiss, 1977; Van der Wal et al., 1993). However, as pointed out by Austin and Evans (2007) and Ricard and Bercovici (2009), the grain size reflects the rate of energy dissipation (the scalar product of stress and strain rate) rather than stress alone and is a paleowattmeter rather than a paleopiezometer. This also implies that the entire grain size distribution (rather than the mean value) needs to be taken into account when relating microstructures to mechanisms (Rozel et al., 2011).

Finally, paleopiezometry and paleowattmetry are based on the assumption that the grain size distribution has reached a steady state. This is not a trivial assumption. Numerous studies suggest that the grain size distribution even in rocks deformed at depth greater than the traditional brittle-ductile transition is often controlled by fragmentation and growth processes that are to some extent separated in time and reflects an initial period of grain size reduction at high stress conditions, followed by recovery and growth at lower stresses (Druiventak et al., 2012; Linckens et al., 2016; Trepmann et al., 2013). Nonsteady state grain size distributions may be more common than hitherto thought and carry valuable information about deformation history beyond the time-independent perspective. In particular, it may contain memory of deformation and growth at very contrasting stress levels.

In this study we present a systematic study of grain size distribution in natural rocks from paleofaults and shear zones and in experimentally sheared rocks. We focus on olivine-rich rocks as representatives of the lithospheric mantle lithologies but include three samples of seismically deformed feldspars and garnets from the lower continental crust for comparison. Our samples, characterized by electron backscattered diffraction (EBSD), show a wide range of grain sizes and microstructures yet a surprisingly consistent grain size scaling behavior. We propose a model for dislocation patterning based on Hähner's (1996a, 1996b) stochastic model to explain the power law behavior observed for the small grain fraction in most of our data set.

2. Acquisition Method

EBSD analyses were made on the CamScan X500FE CrystalProbe at Géosciences Montpellier. Initial processing was made using the CHANNEL5 software suite to remove noise and correct for mineral symmetry. Further processing was done using the MatLab toolbox MTEX (version 4.4.0; http://mtex-toolbox.github.io; Bachmann et al., 2010, 2011; Hielscher & Schaeben, 2008). A misorientation threshold of 10° was applied during grain modeling (a few exceptions are specifically mentioned in the text). Grains smaller than 10 pixels and those with faces on the edges of the orientation map have been excluded for the grain size analysis.

3. Samples

The grain size scaling of deformed rocks will in most cases reflect the influence of both grain fragmentation and grain growth processes. The effects of the growth processes will depend on the relative rates of deformation and growth, and in some situations the growth may have continued long after the fragmentation ceased. We collected data of grain size distributions formed during a wide range of conditions, where the relative influence of fragmentation and growth is different.

Our data can be divided into two subsets. The first one (I) is composed of rocks for which the conditions of deformation are constrained at different levels. These samples come from diverse localities and also include some experimental data. Deformation rates range from seismic faulting to the much slower creep of mantle shear zones. The second set (II) is composed of samples from the Leka Ophiolite Complex (LOC) located in the Central Norwegian Caledonides. This set covers almost the same range of grain sizes as the first set, but the stress and strain rate conditions for the LOC rocks are poorly known. The goal is to use insight gained from the analysis of the first set of data to obtain an increased understanding of the conditions of deformation in a less well understood case, exemplified by the data from the LOC.

3.1. Subset I

3.1.1. Samples From Paleoearthquakes

Paleoearthquakes have been identified through the presence of pseudotachylites, fine-grained rocks believed to have formed during highly energetic events that triggered partial melting of the rocks (e.g., Kirkpatrick & Rowe, 2013; Sibson, 1975). Whereas earthquake slip zones are very narrow, the slip planes are bordered by wider damage zones. In the upper crust this damage zone is usually composed of fault gauge and breccias, often having a power law fragment size distribution (Sammis et al., 1987). However, in the more confined environments at greater depth, fragmentation and recrystallization of wall rocks often seem to take place with very limited shear (e.g., Austrheim et al., 2017; Dunkel, Austrheim, Renard, et al., 2017; Petley-Ragan et al., 2018). We present data on olivine from the Bergen Arcs (Western Norway) and Alpine Corsica ultramafic rocks, as well as on garnet and plagioclase from the Bergen Arcs lower crustal granulites.

One olivine-rich sample (*M02-8a*) comes from a several meters wide lherzolite lens embedded in granulite facies anorthositic rocks and crosscut by pseudotachylite veins on the Holsnøy Island, Bergen Arcs, Norway

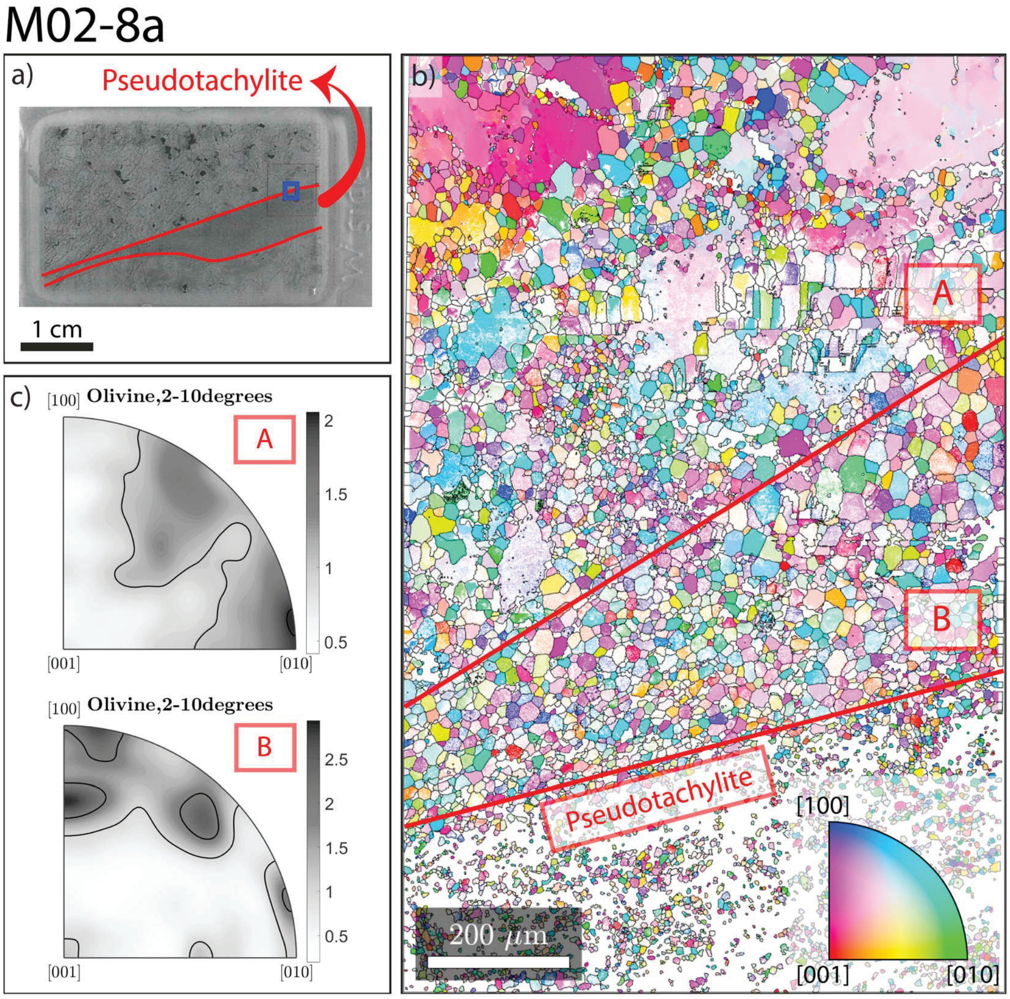

Figure 1. Sample M02-8a. (a) Thin section showing the location of the pseudotachylite in red and the electron backscattered diffraction map (blue square). (b) Olivine orientation map with inverse pole figure color coding. The reference orientation is horizontal. Two zones were defined in the map: Zone B in direct contact with the pseudotachylite and zone A located further from the pseudotachylite and containing olivine porphyroclasts. White areas are clinopyroxenes and orthopyroxenes in the pseudotachylite and mostly orthopyroxenes in zones A and B with some areas of misindexing. These two zones are studied separately and are referred to as M02-8a A and M02-8a B. Horizontal lines drawn by grain boundaries to the left of the zone A label are measurement artifacts. (c) Olivine internal misorientation rotation axes for low angles (2–10°) in zones A and B. Rotation axes are concentrated around [010] in zone A and toward [100] in zone B. Contour lines are drawn for integer multiples of a uniform distribution.

(S. Jung et al., 2014; Kühn et al., 2000). Olivine in this sample is slightly richer in iron than typical mantle olivine (Fo_{80-85}). A second olivine-rich sample from Corsica (*Cor19-06*) represents seismically affected peridotites from a high-pressure-low-temperature (blueschist facies) terrain in the Cima de Gratera ophiolitic nappe (Magott et al., 2016). Coseismic slip is indicated by numerous pseudotachylite-filled faults and injection veins. The geological setting was described by Andersen and Austrheim (2006). For each sample, one EBSD map was made of the wall rock adjacent to pseudotachylite containing faults. Two zones can be identified close to the pseudotachylite: Zone A is the outermost area, collected a few hundred micrometers away from the fault, while zone B is located at the immediate contact with the pseudotachylite. In *M02-8a*, one map in each zone has been done (Figure 1). The map done in *Cor19-06* is located inside zone A (Figure 2). In both cases, zone A is porphyroclastic, with misorientation rotation axes (the crystallographic axes around which the crystal lattices of neighboring subgrains are rotated with respect to each other) concentrated around [010]. This suggests that a process similar to slow, crystal-plastic deformation in the mantle was active. Zone B is composed of more polygonal olivine grains with a complex set of misorientation rotation axes, which we interpret as directly related to the pseudotachylite-generating event.

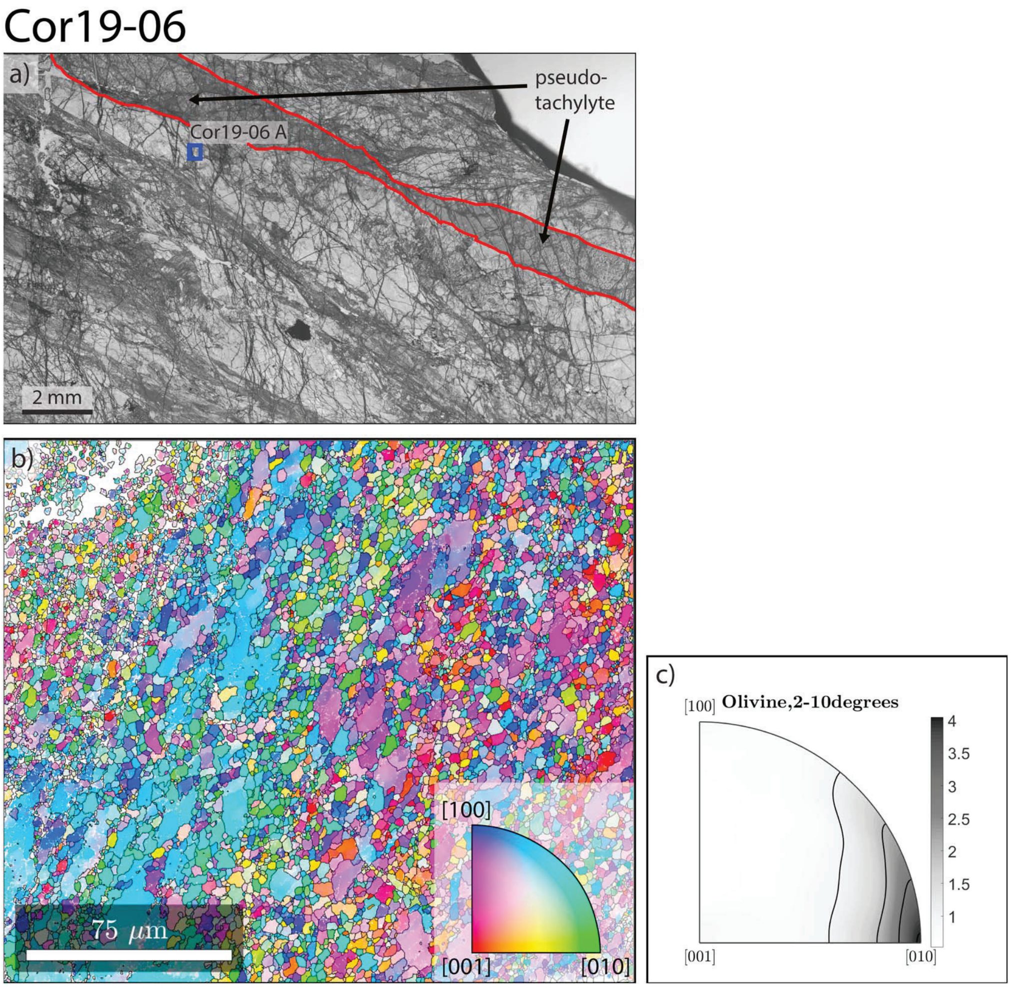

Figure 2. Sample Cor19-06. (a) Image of thin section showing the location of the pseudotachylite in red and the electron backscattered diffraction map (blue square). (b) Olivine orientation map with inverse pole figure color coding. The reference orientation is horizontal. White area in the upper left corner is due to misindexing. The map is located in zone A, that is, not in direct contact with the pseudotachylite and is referred to as Cor19-06 A. The map is rotated 90° clockwise with respect to (a). (c) Olivine internal misorientation rotation axes for low angles (2–10°). Rotation axes are concentrated around [010]. Contour lines are drawn for integer multiples of a uniform distribution.

For comparison with non-olivine silicates, garnet (*ÅF2-4*) and plagioclase (*A16-011 and A16-013A*) samples from wall rocks around pseudotachylite-filled faults through granulite facies anorthosites from Holsnøy, Bergen Arcs, Norway (Austrheim et al., 1996), have also been included. The granulite facies garnets are located within a distance of 2 mm from the pseudotachylite and experienced extensive grain size reduction during earthquakes related to the Caledonian orogeny (Austrheim et al., 2017). Two EBSD maps have been recorded from sample ÅF2-4. Map 1 corresponds to garnet II, and map 2 corresponds to garnet I in Austrheim et al. (2017). Crystal plasticity and possibly also brittle deformation during seismic loading led to an intense fragmentation of the original single crystals, with a smooth transition from subgrains to grains. A 2° threshold has been applied for grain modeling in MTEX to include subgrain data in the analysis. Three EBSD maps were also recorded from fragmented wall rock plagioclase. Two maps (maps 2 and 8) were made from sample A16-011, located approximately 1 mm away from a pseudotachylite, and a third one (map 3) from sample A16-013A, located approximately 10 cm away. These samples are described in more detail by Petley-Ragan et al. (2018; A16-011 map 2 shown in Figure 5a, A16-011 map 8 in Figure 6, and A16-013A map 3 in Figure 7 of the cited reference).

3.1.2. Hydrofractured Samples

To obtain insight into the scaling behavior of a system where growth processes have limited effects on the grain size distribution, we have included a data set that was interpreted to record brittle deformation induced by hydrofracturing (Padrón-Navarta et al., 2010).

Four samples (*Al06-05a*, *-34*, *-35*, and *Al07-07*) from grain size reduction zones in prograde peridotites in the Cerro del Almirez ultramafic massif, Betic Cordillera, Spain, were analyzed. The deformation temperature was estimated to be in the range 680–710 °C. The authors observed features indicating that dislocation creep was not the major deformation process: low dislocation density in grains, few dislocation glide morphologies observed, inherited crystallographic preferred orientation (CPO), high misorientation angles, rotation axis distribution close to random, and remnants of the original crystal shapes. Radial dislocations are indicative of fast fluid assisted growth. More details on the samples are available in Padrón-Navarta et al. (2010).

3.1.3. Samples From *Kick-and-Cook* Experiments

The microstructural effects of deformation at high strain rates (approximately 10^{-4} s^{-1}) followed by an annealing phase at high temperature (between 700 and 1000 °C) were studied in the kick-and-cook experiments of Druiventak et al. (2012) and Trepmann et al. (2013). Their goal was to simulate the effect of recrystallization following coseismic deformation. The samples obtained from these experiments typically show localized grain size reduction zones with a weak CPO independent of the stress field. There are two types of newly formed grains: fragments directly inherited from the porphyroclasts characterized by a high dislocation density, low misorientation angles, and irregular shapes, and recrystallized grains characterized by low dislocation density, nearly random orientation, and concave boundaries (Trepmann et al., 2013).

The samples included in this study (samples *B9006*, *B9010*, *B9014*, *B9028*, *B9029*, *B9036*, and *B9037*) are the products of experiments carried out on natural peridotites from the Almklovdalen peridotite complex in Western Norway. In samples without the annealing step, the authors identify evidences of both brittle and crystal plastic deformation; intragranular microcracks with little offset are the main deformation feature with undulatory extinction concentrated next to shear zones (Druiventak et al., 2011). They observe a larger dispersion of the CPO with increasing annealing temperature (Druiventak et al., 2012; Trepmann et al., 2013). Detailed descriptions of the experimental settings and samples are available in Druiventak et al. (2012) and Trepmann et al. (2013).

An additional sample included here, *Am23b 01*, was described as a natural equivalent to kick-and-cook experimental samples. It is a peridotite from a shear zone in the Balmuccia and Baldissero complexes previously described by Druiventak et al. (2012).

3.1.4. Samples From Torsion Experiments

Paleopiezometry is based on the assumption that the rates of grain size reduction and growth have reached a steady state. The torsion experiments by Tasaka et al. (2016) simulate the effects of steady state shearing without any postdeformational annealing process.

Tasaka et al. (2016) conducted experiments to test the effects of high strain rate torsion (approximately 10^{-4} s^{-1}) on hydrated olivine aggregates at temperatures of 1200 °C. Hydrated conditions were believed to be representative of the lithospheric mantle conditions. Samples were made from a mix of synthetic fayalite power and San Carlos olivine power (Fa_{10}; details on the preparation techniques are given in Zhao et al., 2009). The olivine used during the experiments had a composition near Fo_{50} to facilitate effective deformation since this composition has lower strength compared to natural Fo-rich mantle olivine. The deformed samples show the activity of the [100]{0kl} sliding system expected in mantle rocks plastically deformed at temperatures higher than 1000 °C (e.g., Falus et al., 2011; Hansen et al., 2011; Nicolas & Christensen, 1987; Tommasi et al., 2000). Data from 12 samples (*PT-889*, *PT-892*, *PT-916*, *PT-930*, *PT-933*, *PT-938*, *PT-939*, *PT-952*, *PT-954*, *PT-966*, *PT-973*, and *PT-976*) including two dry (*PT-916* and *PT-930*) and two initial undeformed (*PT-916* and *PT-933*) samples from Tasaka et al. (2016) are presented below.

3.1.5. Mantle-Deformed Samples

All natural and laboratory deformed samples described above, except for the torsion experiment samples, have an initial fabric controlled by plastic deformation in the mantle.

Ten samples (*BC05-101*, *-123*, *NV05-123*, *-128*, *-129*, *-161*, *-162*, *-165*, *-168*, and *-171*) from Falus et al. (2011) consisting of dynamically recrystallized olivine in spinel peridotite xenoliths from Persani Mountains, Southeastern Carpathians, Romania, are included below as representatives of microstructures believed to

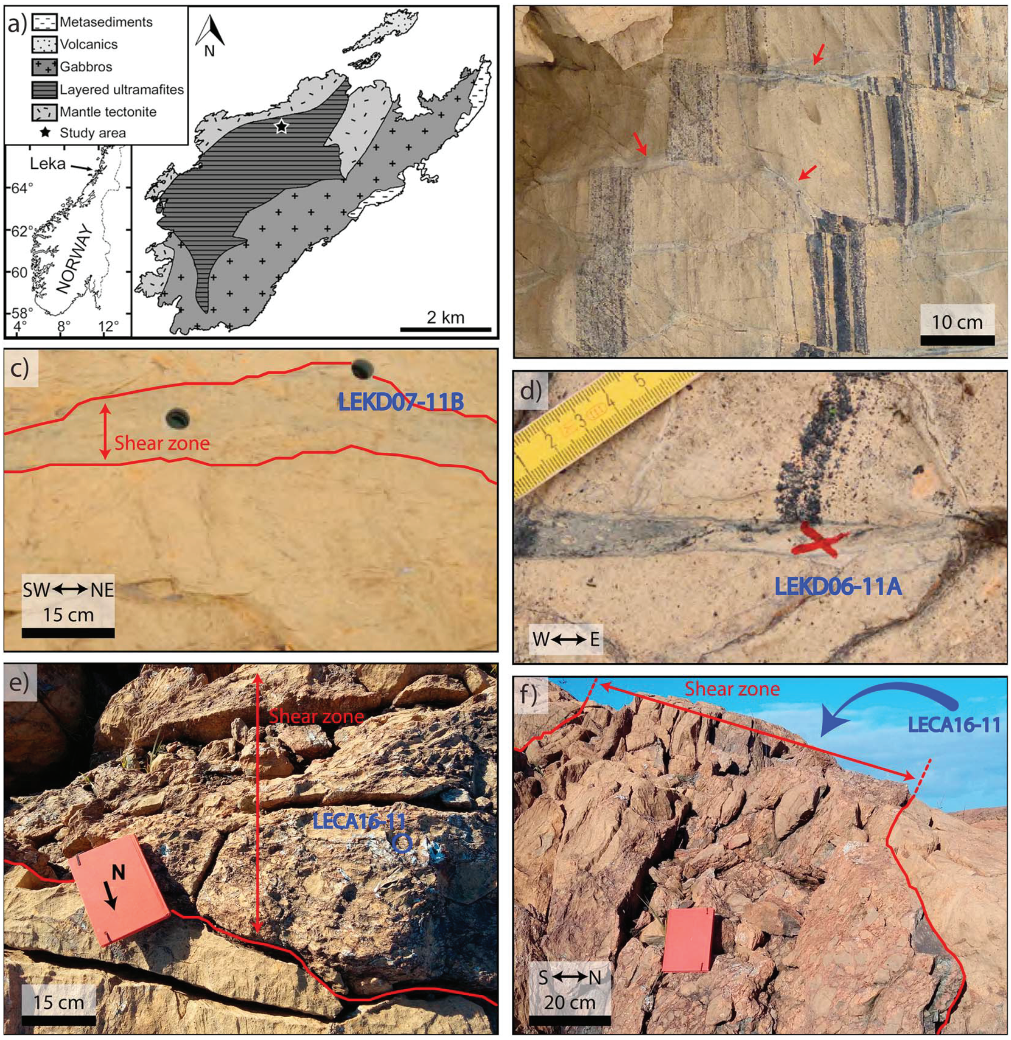

Figure 3. (a) Geological map of the Leka Ophiolite Complex (reprinted from Dunkel, Austrheim, Renard, et al., 2017, with permission from Elsevier), showing the study area of samples from Subset II. (b) Field images showing chromite layers offset by localized faults (red arrows). The fragmented wall rocks of these faults are referred to as zone C by Dunkel, Austrheim, Renard, et al. (2017) and Dunkel, Austrheim, Ildefonse, and Jamtveit (2017). (c) Location of sample LEKD07-11B along a narrow shear zone. (d) Location of sample LEKD06-11A at the tip of a narrow shear zone. (e) Location of sample LECA16-11 in a large shear zone. (f) Side view of the shear zone where LECA16-11 was sampled.

have formed at mantle conditions. Subgrain rotation was the main recrystallization mechanism, and dislocation glide occurred mainly on [100]{0kl} systems.

3.2. Subset II: The LOC

The LOC is part of the Uppermost Allochthon of the Scandinavian Caledonides which has been emplaced during the collision between Laurentia and Baltica during closure of the Iapetus Ocean (Roberts et al., 2007). It is located on the Leka Island around 65°N (Nord-Trøndelag) on the Norwegian west coast and is one of the best exposed and preserved ophiolites in the Scandinavian Caledonides. The LOC has been dated at 497 Ma ± 2 Ma (Dunning & Pedersen, 1988) and comprises a complete ophiolite section (Furnes et al., 1988). Basalts and volcanic rocks have geochemical signatures ranging from mid-ocean ridge basalt to island arc tholeiite, making the LOC a supra-subduction zone-type ophiolite (Furnes et al., 1988). It is situated in a sinistral extensional pull-apart structure, which permitted its preservation (Titus et al., 2002).

Samples from shear zones and faults come from the northwestern part of the island (Figure 3a). The layered ultramafic unit of the LOC consists of alternating layers of harzburgite, dunite, and websterite showing

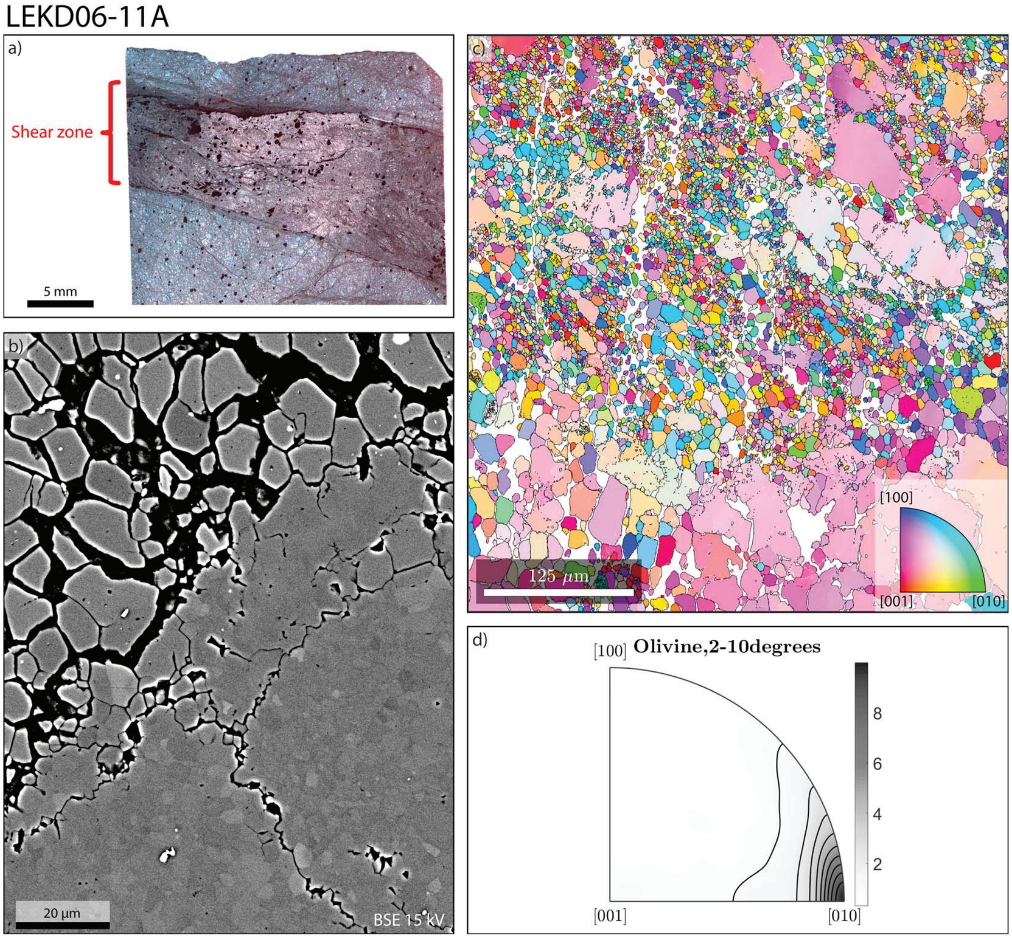

Figure 4. Sample LEKD06-11A. (a) Image of thin section showing the location of the pseudotachylite in red and the electron backscattered diffraction map (blue square). (b) Backscattered electron image showing characteristic microstructures of olivine recrystallization and fragmentation inside the shear band. Bricky olivine is visible near the upper left corner, while subgrains are visible in the lower right corner. The black network is serpentine. (c) Olivine orientation map with inverse pole figure color coding. The reference orientation is horizontal. The white network is serpentine. (d) Olivine internal misorientation rotation axes for low angles (2–10°). Rotation axes are concentrated around [010]. Contour lines are drawn for integer multiples of a uniform distribution.

various degrees of serpentinization. All analyzed rocks are dunites. Faults and shear zones are mostly oriented E-W, vertical, and with offsets ranging from millimeters to tens of meters.

Background (mantle-deformed) samples (*LE04-14 areas 2 and 6*) have been sampled outside the shear zones. They show dynamically recrystallized olivine with dislocation glide on the [100]{0kl} systems (zone A from Dunkel, Austrheim, Ildefonse, & Jamtveit, 2017; Dunkel, Austrheim, Renard, et al., 2017).

Samples *LE05-14 areas 1 and 3* represent damage zones around highly localized faults (Figure 3b) believed to have formed by dehydration embrittlement during dehydration of former serpentine veins (zone C from Dunkel, Austrheim, Ildefonse, & Jamtveit, 2017; Dunkel, Austrheim, Renard, et al., 2017). These samples show brittle fragmentation with very little shear strain, and microstructures predating the deformation can still be identified.

The remaining samples come from shear zones of various widths (Figures 3c–3f). *LEKD06-11A* and *LEKD07-11B* are located close to each other at the tip and the border of approximately 20-cm-wide shear zones, respectively (Figures 3c and 3d). Deformation is restricted to a centimeter-wide shear band with a sharp transition to the host rock in LEKD06-11A (Figure 4a), while it affects most of the thin section in LEKD07-11B with a gradual transition to the host rock. In both samples relatively undeformed olivine with straight boundaries coexist with interlobate grains subdivided into smaller fragments. The microstructures look very similar on

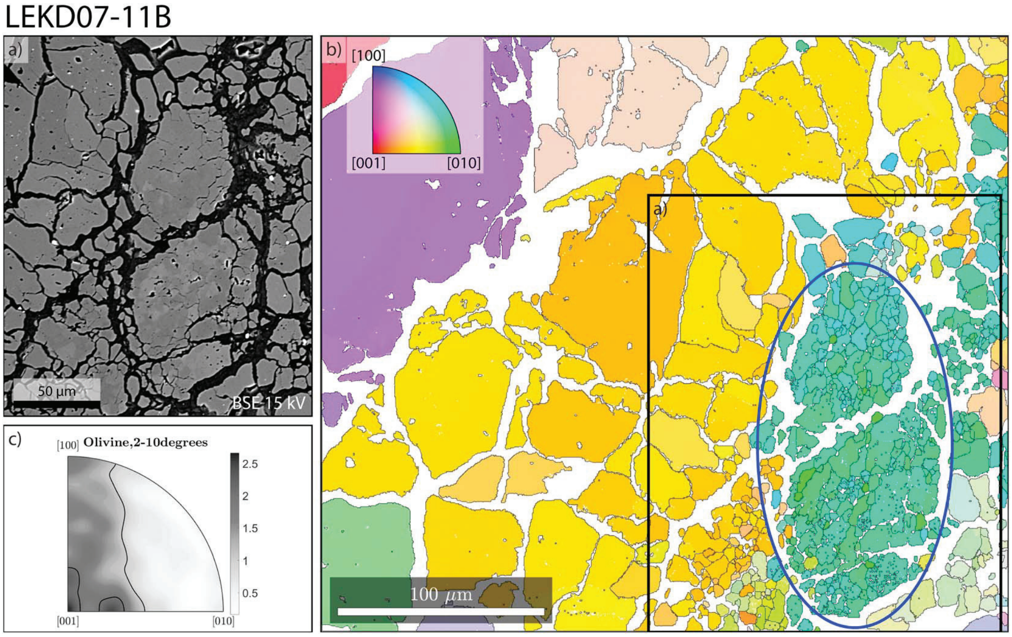

Figure 5. Sample LEKD07-11B. (a) Backscattered electron image of the mapped area. Different shades of gray indicate the presence of subgrains. The black network is serpentine. (b) Olivine orientation map with inverse pole figure color coding. The reference orientation is horizontal. The blue ellipse indicates the area used for grain size distribution analysis. The white network is serpentine. (c) Olivine internal misorientation rotation axes in the blue ellipse for low angles (2–10°). Contour lines are drawn for integer multiples of a uniform distribution.

scanning electron microscopy micrographs (Figure 4b and 5a), but orientation maps show that the grain fragments are subgrains in LEKD07-11B (Figure 5b; a 2° threshold has been used for grain modeling in MTEX), while they are grains in LEKD06-11A (Figure 4c). The low-angle (2–10°) misorientation axes are concentrated around [010] for LEDK06-11A (Figure 4d). In LEKD07-11B, the low-angle misorientation axes are distributed in the plane described by the [100] and [001] axes of the olivine crystals suggesting that the sliding system [010]{h0l} was active during deformation (Figure 5c).

LECA16-11 areas 1 and 2 (Figure 6) come from an approximately 1-m-wide shear zone (Figures 3e and 3f). The two areas display two kinds of domains of newly formed grains (Figures 6a and 6b). The first domain type is composed of rounded to angular domains inside original relatively undeformed grains (such as grains 1 and 2 in Figure 6a). They display angular and often elongated grains, which have undergone little shearing and largely kept the orientation of the host grain (Figures 6a–6d). The second type of domain is composed of equigranular grains with more varied crystal orientations compared to the original crystals (Figures 6a–6d). They are visible in significantly sheared domains between the original relatively undeformed grains. We call the first type fragmented domains and the second type sheared domains. The fragmented domains include both grains and subgrains; thus, grain modeling by MTEX has been done while considering 2° as the minimal misorientation angle between two grains. The misorientation axes distributions for low angles (2–10°) are close to random (Figure 6e). The grains from the two types of domains are identified in the figures as fragments and sheared grains or by the letters f (fragmented) and s (sheared) following the sample number.

4. Grain Size Distributions

In the following, grain size distributions are defined by the probability density functions (pdfs) of the grain cross-section areas. The pdf $f(X) = \frac{dC(x<X)}{dX}$ is related to the cumulative distribution function $C(x < X)$, which includes the grain areas smaller than a given size X. The probability that a grain area is between X and $X + dX$ is given by $f(X)dX$.

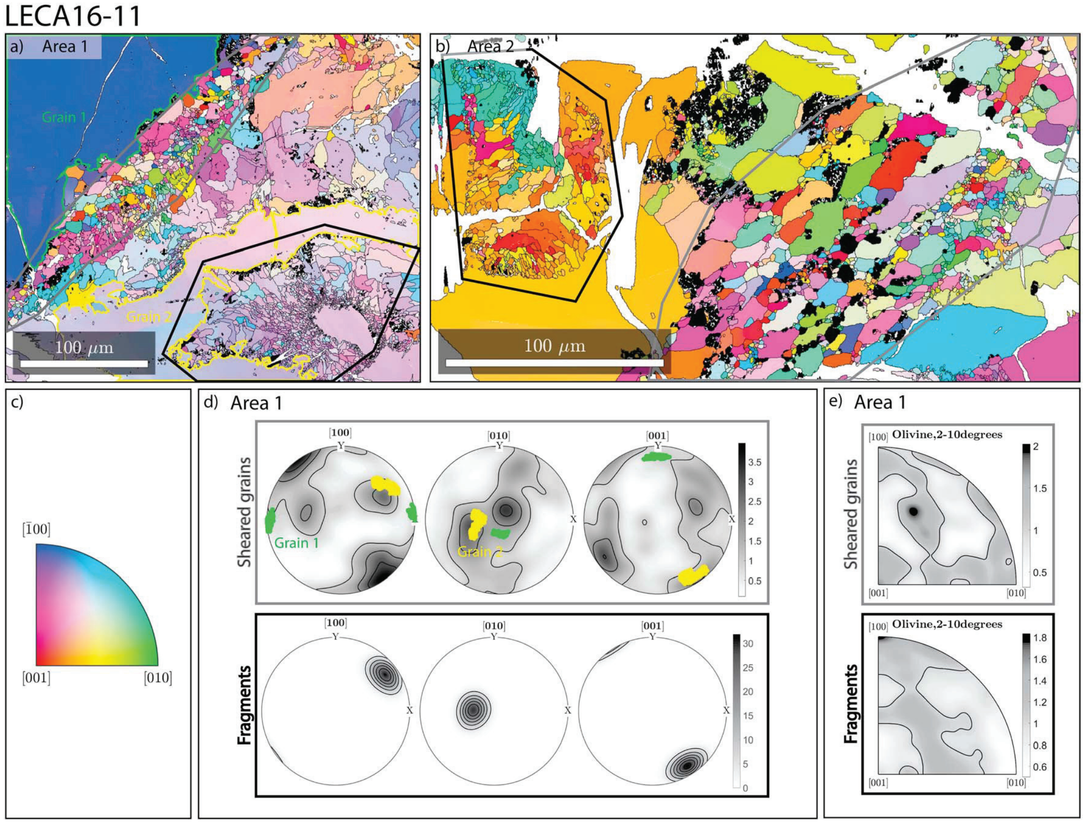

Figure 6. Two electron backscattered diffraction maps were done in sample LECA16-11. (a and b) Olivine orientation map with inverse pole figure color coding of areas 1 and 2, respectively. White areas are serpentine veins and antigorite crystals. Black areas are mostly clinopyroxene grains and a few orthopyroxene and magnetite grains. The domains being used for grain size distributions analysis are marked with black (fragments) and gray (sheared grains) lines. (c) Inverse pole figure color coding for olivine. The reference orientation is horizontal. (d) CPO of the rounded grains and of the fragments. The green and yellow dots in the diagram for sheared grains are the CPO of the two large relatively undeformed grains identified in (a). (e) Olivine internal misorientation rotation axes for low angles (2–10°) for sheared grains and fragments in area 1. Both show almost random rotation axis orientation. Contour lines are drawn for integer multiples of a uniform distribution.

4.1. Curve Fitting

Most attempts to model grain size coarsening or fragmentation have assumed that the entire distribution can be obtained from the mean grain size (Austin & Evans, 2007; De Bresser et al., 2001). This requires that the distributions are self-similar and show similar scaling behavior. It is usually assumed that the distribution is lognormal as suggested by experimental studies of nucleation and growth processes (Feltham, 1957; Kile et al., 2000). However, analyses of our extensive set of data show significant deviations from such a distribution. Samples deformed by brittle processes and by low-temperature plasticity tend to show simple power law scaling behavior reflecting a scale-independent fragmentation mechanism (Figure 7a). Other data sets show a pdf with lower slope for small grains than for large grains. While this is the case for a lognormal distribution (Figure 7b), some of the data sets reveal a much better fit to a combination of two power law segments intersecting at some crossover length than to a continuously curving lognormal function (Figure 7c). A combination of two power laws may arise if two different physical processes operate at different length and time scales. One possibility that will be discussed below is that the steeper distribution of large grains is mainly controlled by fragmentation processes, while the more gentle slopes of the smaller grains are influenced by healing processes operating at shorter length scales.

Fitting laws are described by the parameters given in Figure 7b. For a lognormal distribution, these parameters are μ and σ. The μ is closely linked to the median value of the distribution, and σ is related to the spread of the distribution. The goodness of the lognormal fit is evaluated by the standard error of the regression (*S*; see the supporting information for the definition of *S*). *S* values less than approximately 0.1

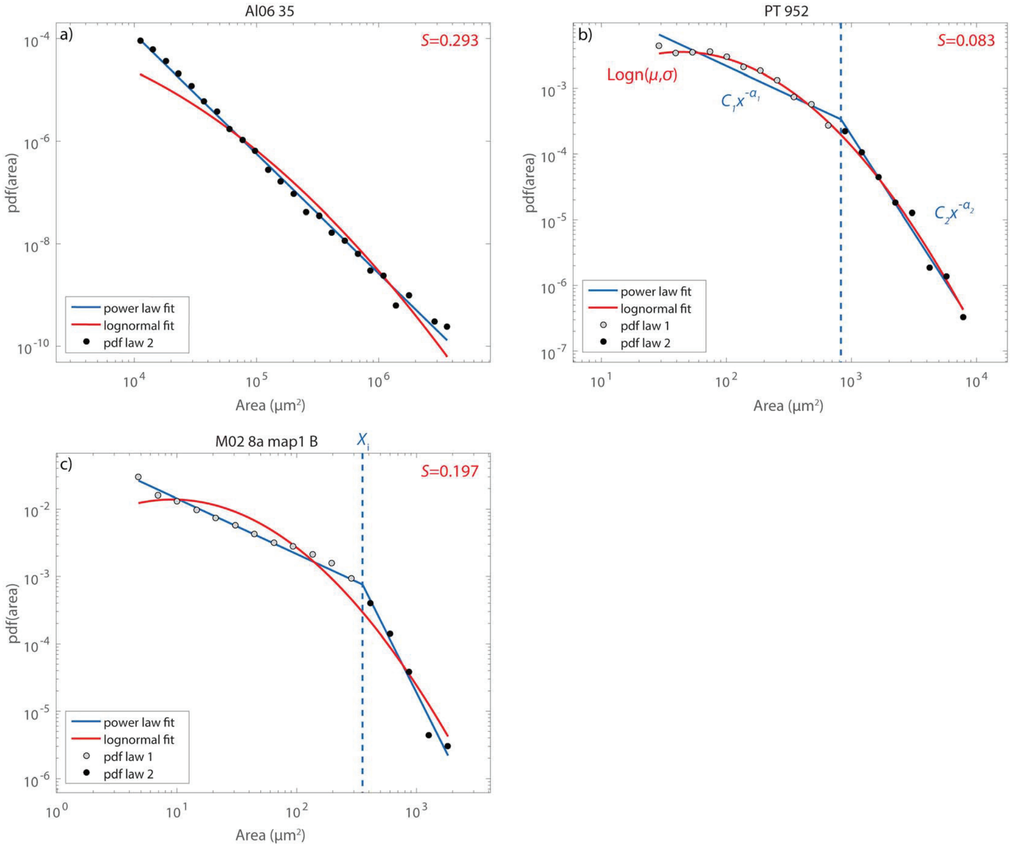

Figure 7. Representative examples of grain size distributions. (a) Probability density function (pdf) of one of the brittle samples from Padrón-Navarta et al. (2010) fitted by both a power law (blue line) and a lognormal law (red line). In this case the simple power law fit is unambiguously the best. (b) pdf of one of the samples deformed by steady state torsion from Tasaka et al. (2016). The distribution is fitted both by a lognormal distribution and two power laws. In this case the fit to a lognormal distribution is best. This figure also shows the parameters describing the lognormal and the power law fits. (c) pdf of one of the samples from the damaged wall rock adjacent to a pseudotachylite. It has been fitted both by a lognormal distribution and a combination of two power laws. In this case the two power laws fit is clearly the best.

are taken to indicate a good fit to a lognormal distribution (e.g., Figure 7). For a perfect fit, *S* is 0. Power laws are also described by two parameters: their slope α and a coefficient *C*. For clarity, we only present the slope values of the power laws. In the case of the two power laws fit, we also add the crossover area at which the power laws intersect. We call this parameter X_i. The steepest power law slope is termed α_2, while the less steep one is termed α_1. In the case of a single power law fit, the slope is referred to as α_2 if the slope is close to 2 or larger, or α_1 if the slope is closer to 1.

Details on the fitting method, including the identification of the range in which a power law is applicable (following Clauset et al., 2009), are given in the supporting information (Text S1).

4.2. Individual Fits

Data from each sample have been fitted both to power law and lognormal distributions (Figure 7 and Figure S1). All fits and associated distribution parameters can be found in Table 1. Median grain areas vary over 5 orders of magnitude, from 1.16 to 7.04×10^4 μm^2. The mean values of α_1 and α_2 over the whole data set are 1.05 ± 0.31 and 2.51 ± 0.48, respectively (errors are given by the standard deviation). The intersect value of the two power laws is approximately 3.0 times the median grain area (Figure 8).

The use of median area rather than the mean area of each sample is preferred because it is more robust with respect to extreme values, which could be caused by measurement uncertainties. The conversion from

Table 1
Properties of EBSD Maps and Fitting Parameters

Sample	Number of grains	Resolution (μm)	Median equivalent diameter (μm)	Mean area (μm^2)	Median area (μm^2)	μ	σ	S	α_1	α_2	X_i (μm^2)
Subset I											
Cor19 06 map 3 A	5,404	0.2	1.93E+00	5.96E+00	2.92E+00	0.79	1.31	0.306	1.02	2.46	7.63E+00
M02 8a map 1 A	2,493	0.5	8.24E+00	1.43E+02	5.33E+01	3.56	1.54	0.343	0.96	2.26	1.55E+02
M02 8a map 1 B	1,451	0.5	1.06E+01	1.49E+02	8.89E+01	3.95	1.32	0.197	0.82	3.56	3.54E+02
AF2 4 map 1 gt	3,291	0.35	2.43E+00	8.74E+00	4.66E+00	1.36	1.20	0.232	1.27	2.58	1.21E+01
AF2 4 map 2 gt	7,357	0.4	5.05E+00	4.04E+01	2.00E+01	2.76	1.24	0.149	1.05	3.51	1.23E+02
A16 011 map 2 pl	2,198	0.2	1.22E+00	1.73E+00	1.16E+00	0.05	0.96	0.110	1.39	2.73	2.55E+00
A16 011 map 8 pl	3,087	0.2	1.40E+00	2.14E+00	1.54E+00	0.37	0.79	0.186	1.12	3.35	2.94E+00
A16 013A map 3 pl	1,991	0.2	1.48E+00	3.29E+00	1.72E+00	0.51	1.10	0.128	1.08	2.31	3.85E+00
Al06 05a	3,733	Between 30 and 35	1.35E+02	2.14E+04	1.44E+04	9.03	1.20	0.382		2.63	
Al06 34	363		1.68E+02	3.38E+04	2.21E+04	9.95	0.90	0.209		2.49	
Al06 35	4,756		1.48E+02	3.24E+04	1.71E+04	8.82	1.69	0.293		2.33	
Al07 07	6,236		1.53E+02	2.35E+04	1.84E+04	9.39	0.93	0.308		3.35	
Am23b 01	3,118	3.2	1.69E+01	6.06E+02	2.25E+02	4.18	2.05	0.354		2.08	
B9006	3,285	1	4.92E+00	8.62E+01	1.90E+01	1.40	2.42	0.422		1.89	
B9010	5,070	1	5.17E+00	6.06E+01	2.10E+01	2.98	1.45	0.287		2.12	
B9014	5,830	0.7	3.53E+00	4.33E+01	9.80E+00	−0.34	2.79	0.499		1.86	
B9028	383	0.7	4.67E+00	9.49E+01	1.72E+01	2.87	1.95	0.227	1.42	2.07	2.35E+02
B9029	1,840	0.7	4.87E+00	3.95E+01	1.86E+01	2.88	1.22	0.128	1.40	3.24	1.31E+02
B9036	5,599	1	5.97E+00	9.93E+01	2.80E+01	3.23	1.62	0.308	1.58	2.26	1.81E+02
B9037	4,452	0.7	3.95E+00	5.28E+01	1.23E+01	1.76	1.84	0.704		1.97	
PT 889	1,053	Between 0.7 and 3	8.96E+00	1.01E+02	6.30E+01	4.11	1.09	0.101	0.84	2.92	1.65E+02
PT 892	640		1.26E+01	1.92E+02	1.25E+02	4.53	1.14	0.173	1.17	2.58	2.07E+02
PT 916 initial dry	527		2.79E+01	1.13E+03	6.12E+02	6.33	1.15	0.114	0.80	2.34	1.32E+03
PT 930 dry	1,692		1.38E+01	3.12E+02	1.49E+02	4.94	1.28	0.111	1.17	3.07	8.60E+02
PT 933 initial	585		3.17E+01	1.82E+03	7.90E+02	6.65	1.36	0.121	1.45		
PT 938 partial slip	673		2.58E+01	1.16E+03	5.22E+02	6.20	1.37	0.069	1.01	2.17	1.46E+03
PT 939	1,793		1.17E+01	1.99E+02	1.08E+02	4.68	1.10	0.184	0.98	2.98	3.76E+02
PT 952	1,238		1.63E+01	4.22E+02	2.08E+02	5.26	1.22	0.083	0.89	2.96	8.24E+02
PT 954	2,052		1.18E+01	2.09E+02	1.09E+02	4.58	1.26	0.111	0.95	2.97	4.01E+02
PT 966	1,258		7.87E+00	8.17E+01	4.86E+01	3.78	1.09	0.059	0.74	2.87	1.18E+02
PT 973	1,715		9.03E+00	1.34E+02	6.40E+01	4.06	1.28	0.132	0.78	2.40	1.27E+02
PT 976	643		1.67E+01	3.86E+02	2.18E+02	5.28	1.20	0.071	0.35	2.20	3.04E+02
NV05 123	2,051	>1/5 of mean diameter (between 10 and 100)	1.69E+02	5.11E+04	2.25E+04	9.49	1.59	0.250	1.71	2.23	4.27E+04
NV05 128	2,122		2.03E+02	8.27E+04	3.25E+04	10.23	1.44	0.214	1.21	2.45	1.32E+
NV05 129	3,526		1.43E+02	3.99E+04	1.60E+04	9.32	1.59	0.194	1.37	2.28	5.30E+04
NV05 161	1,579		2.99E+02	1.50E+05	7.04E+04	11.09	1.29	0.096	1.27	2.54	3.06E+05
NV05 162	1,477		2.59E+02	9.31E+04	5.25E+04	10.47	1.35	0.228		2.38	
NV05 165	2,886		2.26E+02	7.52E+04	4.00E+04	10.27	1.33	0.201	1.62	2.47	8.80E+04
NV05 168	1,803		1.64E+02	4.30E+04	2.13E+04	9.67	1.39	0.167	1.32	2.41	5.40E+04
NV05 171	1,843		2.63E+02	1.21E+05	5.44E+04	10.59	1.53	0.170	1.45	2.27	1.64E+05
BC05 101	1,458		1.39E+02	4.65E+04	1.52E+04	9.41	1.61	0.214	1.35	2.09	4.35E+04
BC05 123	1,122		2.49E+02	1.16E+05	4.86E+04	10.74	1.34	0.151	1.37	2.79	3.66E+05
Subset II											
LE04 14 map 2 A	1,851	1.5	1.86E+01	9.99E+02	2.71E+02	5.45	1.75	0.189	0.97	2.18	1.21E+03
LE04 14 map 6 A	4,670	5	3.97E+01	2.60E+03	1.24E+03	7.06	1.18	0.534	1.28	2.47	3.42E+03
LE05 14 map 1 C	2,922	10	5.05E+01	5.72E+03	2.00E+03	6.79	1.91	0.290		2.03	
LE05 14 map 3 C	2,851	1	7.41E+00	7.25E+01	4.32E+01	2.97	1.52	0.297	0.44	2.47	4.83E+01
LEKD06 11A map 2	3,308	0.4	4.69E+00	5.02E+01	1.73E+01	1.84	2.03	0.283		2.05	
LEKD07 11B map 1	480	0.5	4.43E+00	3.46E+01	1.54E+01	2.62	1.42	0.148	1.02	2.19	4.04E+01
LECA16 11 map 1 f	1,318	0.2	1.53E+00	6.94E+00	1.85E+00	0.34	1.81	0.162	1.34	1.90	6.24E+00
LECA16 11 map 2 f	624	0.2	1.60E+00	7.42E+00	2.02E+00	0.54	1.76	0.140	1.29	1.84	6.22E+00
LECA16 11 map 1 s	899	0.2	2.04E+00	8.31E+00	3.28E+00	1.08	1.52	0.080	0.89	2.05	8.06E+00
LECA16 11 map 2 s	1,038	0.2	1.72E+00	1.32E+01	2.32E+00	0.73	1.97	0.145		1.70	

Note. Error due to binning is given in supporting information Table S1. EBSD = electron backscattered diffraction.

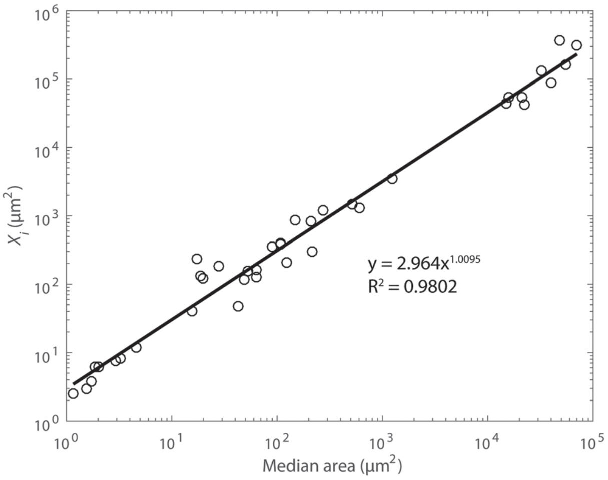

Figure 8. Median area versus intersection scale for the two power law parts. A similar figure can be obtained for mean area.

equivalent diameter to area is direct with the median ($D_{eq} = \sqrt{4A/\pi}$) but not with the mean. Finally, the median is a scaling parameter for lognormal distributions.

In the following, we present data from each subset of samples by groups. The fitting parameters associated with these groups are obtained from the mean value of the individual parameters. Errors are estimated based on maximum and minimum values as the number of sample in each group is too small for the standard deviation to be representative.

As samples are spread over several orders of magnitude in size, distributions are normalized to enable comparison. Two types of normalization are used: normalization to the median grain area (preferred if samples have a best fit to lognormal distributions) and normalization to the intersect value X_i (preferred if samples are best fitted by two power laws). In the case of fits using a single power law, the normalization is done using either median value normalization or normalization to 3.0 times the median grain size if samples are plotted with distributions normalized to X_i according to Figure 8. Plots representing all samples depending on their scaling behavior (two power laws, one power law, or lognormal) are given in Figures S2–S4 of the supporting information.

4.2.1. Subset I

Figure 9 shows the grain size distributions of the samples of subset I separated into the five groups defined in section 3.1. For each group a mean fit has been determined.

Samples undergoing grain size reduction during intermediate depth earthquakes display two power law parts with a mean α_1 of 1.1 $\pm^{0.3}_{0.3}$ (Figure 9a). Values of α_2 cluster around 2.5 $\pm^{0.3}_{0.2}$ but for three samples (M02-8a B, ÅF-4 map 2 and A16-011 map 8) collected in the immediate vicinity of the earthquake slip plane (represented by the pseudotachylites), for which the values are in the range 3.4–3.6.

All the hydrofractured samples (Padrón-Navarta et al., 2010) can be described by a single power law with a mean α_2 of 2.7 $\pm^{0.6}_{0.4}$ (Figure 9b).

Most of the kick-and-cook experiments and the natural equivalent (Druiventak et al., 2012; Trepmann et al., 2013) can be fitted by one power law with a mean value of α_2 of 2.0 $\pm^{0.2}_{0.2}$ (Figure 9c). Three kick-and-cook samples are better fitted to two power laws (B9028, B9029, and B9036). These three samples correspond to the ones that have undergone either the longest annealing times (144 hr for B9028 and B9029) or highest annealing temperatures (1100 °C for B9036). Their first power law part has a mean value of α_1 of 1.5 $\pm^{0.1}_{0.1}$, while their second parts follow the same power law as other samples.

Steady state torsion experiments from Tasaka et al. (2016) show a good fit to lognormal distribution with a value of σ close to 1.2 $\pm^{0.1}_{0.1}$ (Figure 9d). There is no clear difference in the distribution between wet and dry samples.

The case of mantle-deformed samples (Falus et al., 2011) is intermediate. A lognormal distribution with a σ value around 1.5 $\pm^{0.2}_{0.2}$ can fit all of the data except NV05-123, -162, and -165 with almost perfect data collapse when normalized to the median grain size (Figure 9e). However, a combination of two power laws fits all distributions well, including NV05-123, -162, and -165 with a mean α_1 of 1.3 $\pm^{0.1}_{0.1}$ and a mean α_2 of 2.4 $\pm^{0.4}_{0.3}$ (Figure 9f).

4.2.2. Subset II

Figure 10 shows the grain size distributions of the samples of subset II. Samples have been separated in three groups: mantle-deformed samples (zone A) from Dunkel, Austrheim, Renard, et al. (2017) and Dunkel, Austrheim, Ildefonse, and Jamtveit (2017); samples which can be fitted with a single power law comprising zone C samples from Dunkel, Austrheim, Renard, et al. (2017) and Dunkel, Austrheim, Ildefonse, and Jamtveit (2017; these were interpreted to have been deformed by brittle mechanisms during seismic slip) and sample LEKD06-11A; and the rest of the samples coming from two shear zones of variable width (LECA16-11 and LEKD07-11B).

Grain size distributions of mantle-deformed samples have been normalized to their median grain size area and can be fitted by lognormal distributions (Figure 10a). LE04-14 area 6 can be fitted with a σ value

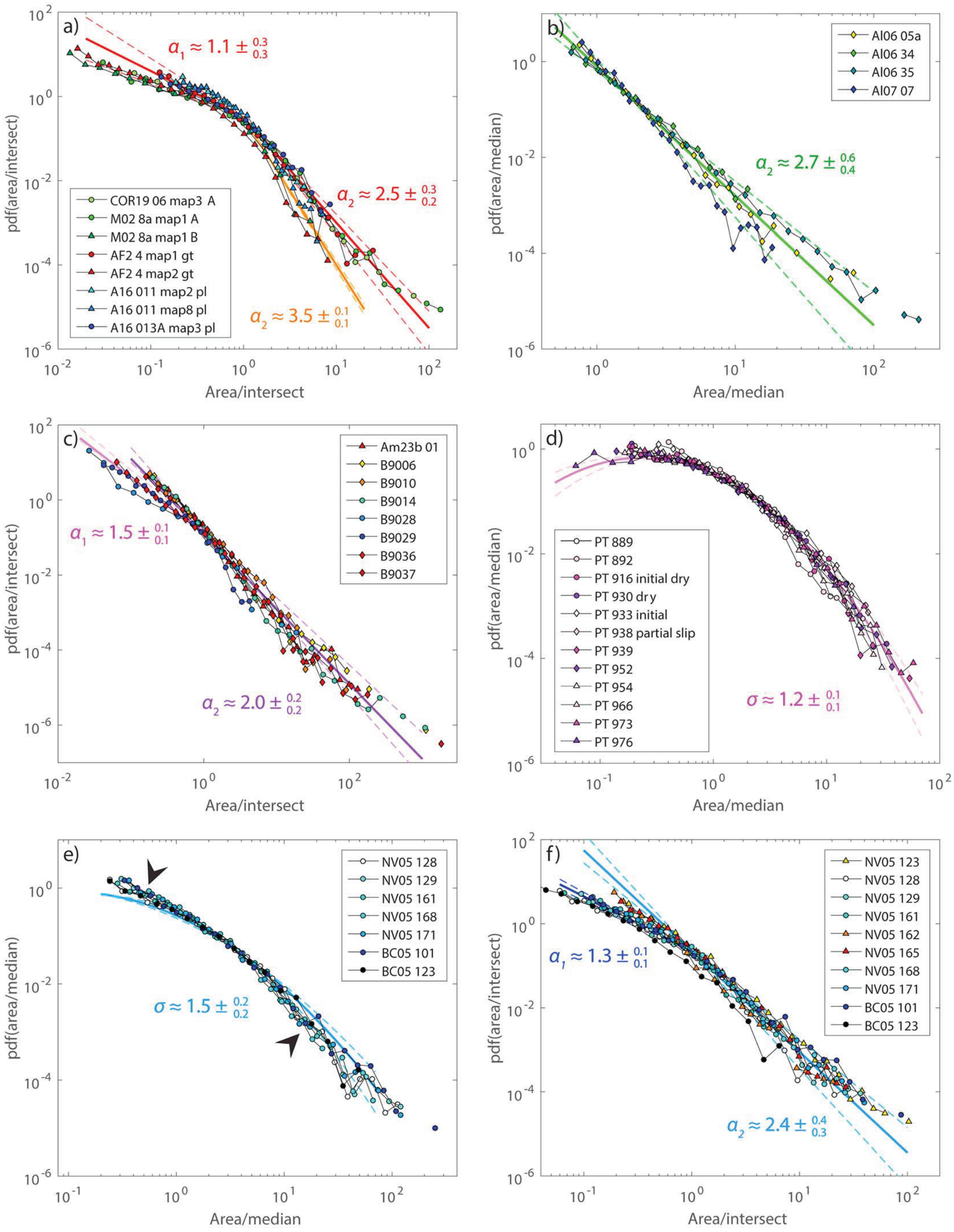

Figure 9. Grain size distributions of samples from Subset I. Mean values of α_1, α_2, or σ and their errors are indicated. Dashed lines indicate the error on the fitted slopes and σ. (a) Probability density functions (pdfs) of samples from intermediate depth earthquakes (Austrheim et al., 2017; Petley-Ragan et al., 2018) normalized to the intersection area of the two power laws. (b) pdf of samples from kick-and-cook experiments and a natural equivalent (Druiventak et al., 2012; Trepmann et al., 2013) normalized to the intersection area of the two power laws or 3.0 times their median grain size area when samples are fitted by only one power law. (c) pdf of hydrofractured samples (Padrón-Navarta et al., 2010) normalized to the median grain size area. (d) pdf of samples from steady state torsion experiments (Tasaka et al., 2016) normalized to the median area. (e and f) pdf of mantle-deformed samples (Falus et al., 2011) normalized to the median grain size area (e) and to the intersection area of the two power laws or 3.0 times their median grain size area when samples are fitted by a single power law (f). Black arrows in (e) indicate systematic deviations of the distributions from the lognormal law.

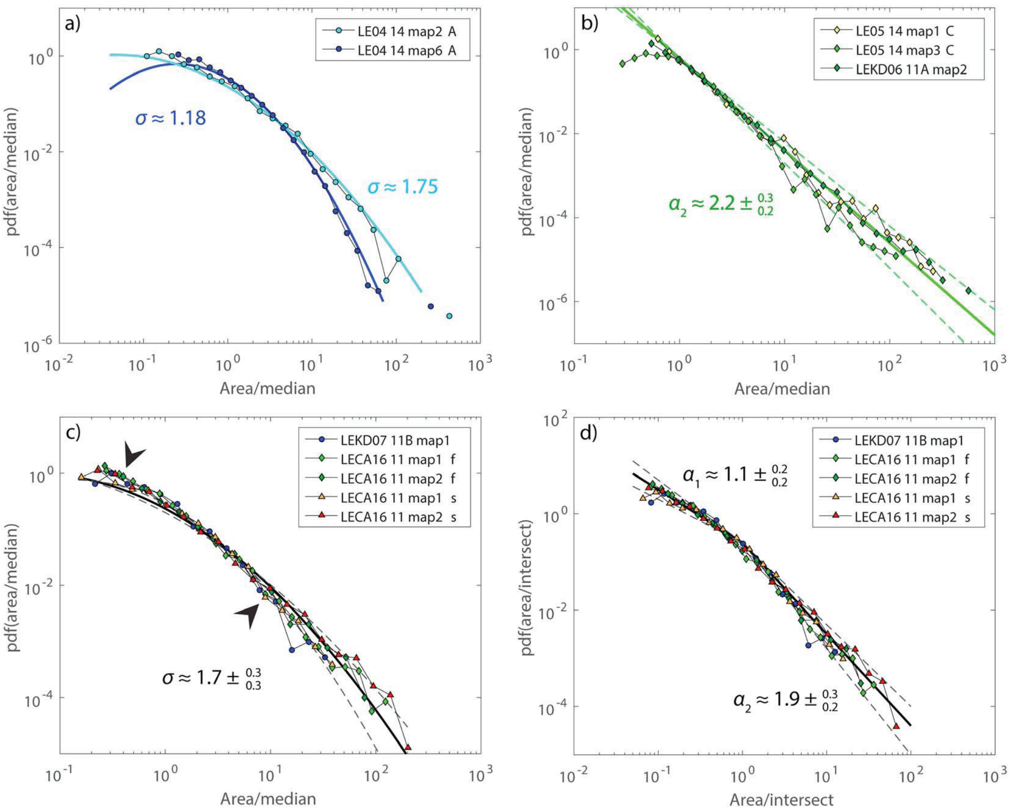

Figure 10. Grain size distributions of samples from Subset II. Dashed lines indicate the error of the fitted slopes and σ. (a) Mantle-deformed samples. (b) Fragmented wall rocks deformed by brittle deformation. (c) Samples from shear zones normalized to the median. (d) Samples from shear zones normalized to the scale where the two power laws intersect. Black arrows indicate systematic deviations of the distributions from the lognormal law.

around 1.2 similar to steady state torsion experiment values (Tasaka et al., 2016). LE04-14 area 2 is fitted by a higher σ value around 1.8.

Samples fitted by a single power law display α_2 values around 2.2 $\pm^{0.3}_{0.2}$ (Figure 10b). Two power laws have been identified for LE05-14 area 3, but the one identified for small grain sizes spreads over less than an order of magnitude (Figure S1), and its slope is low (Table 1), indicating that this power law most probably corresponds to a lack of small grains due to measurement limitations. This sample is thus considered to be well represented by a single power law.

The remaining samples are presented normalized to their median grain size area (Figure 10c) and normalized by the intersect area obtained from fits with two power laws (Figure 10d). As for mantle-deformed samples from Falus et al., 2011, the normalization to the median grain size provides a very good data collapse. The grain size distributions obtained from samples LECA16-11 and LEKD07-11B display distributions close to lognormal distributions with sigma values around 1.7 $\pm^{0.3}_{0.3}$. Normalization to the intersect value X_i returns a fairly good collapse, which fits a combination of two power laws with a mean α_1 of 1.1 $\pm^{0.2}_{0.2}$ and a mean α_2 of 1.9 $\pm^{0.3}_{0.2}$. There is no clear difference between fragmented (f) and sheared (s) domains in LECA16-11.

5. Grain Junctions

An analysis of the grain boundary angles at grain junctions reveals a very dominant peak around 120° for all the samples (Figure 11). This result is independent of grain size and indicates that grain boundary angles are highly influenced by surface energy reducing processes (such as growth) with no clear evidence for junctions controlled by hierarchical or conjugate fracture sets (cf. Iyer et al., 2008). However, the method used to determine angles may introduce some bias in the angle distributions as it leads to a finite smoothening of grain boundaries calculated from EBSD data.

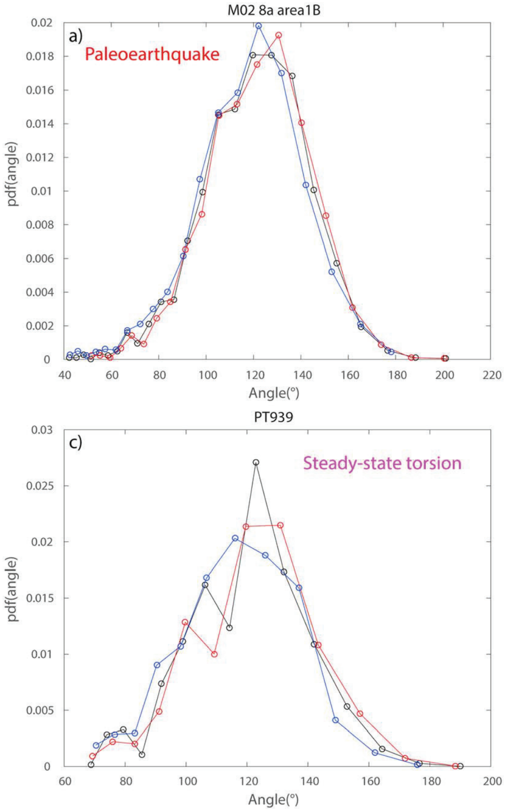

Figure 11. (a–c) Examples of angle distributions obtained from electron backscattered diffraction maps. The black curve is the distribution considering all the grains. The blue curve is the distribution obtained for grains smaller than the median grain size, and the red curve is the distribution obtained from grains bigger than the median grain size. In all cases, there is a maximum at around 120°, indicating a strong influence of surface energy reducing processes.

6. Stress and Strain Rates

Figure 12a shows all the data plotted in one diagram. Most data for grains smaller than the median value align along a single curve with a slope given by the first power law exponent. It can be approximated by $\mathrm{pdf}(A) = 10^{-0.5}A^{-1}$. Exceptions include samples undergoing brittle fragmentation (the hydrofractured samples and zone C from Leka) and some samples from the kick-and-cook experiments of Trepmann et al. (2013), which follow a unique power law scaling at all scales. The grain sizes along this power law range from the resolution limit of the images (pixel size approximately 0.25 $\mu\mathrm{m}^2$) to approximately 10^5 $\mu\mathrm{m}^2$.

The largest grain populations, with median grain sizes around 10^5 $\mu\mathrm{m}^2$, have been inferred to form at mantle conditions with expected strain rates on the order of 10^{-13}–10^{-15} s^{-1} (Pfiffner & Ramsay, 1982). Samples deformed experimentally at strain rates of 10^{-4}–10^{-5} s^{-1} show a median grain size variation in the range 10–800 $\mu\mathrm{m}^2$, depending on the temperature and hence the stress level of the experiment, while seismically deformed samples are characterized by mean grain sizes below 10 $\mu\mathrm{m}^2$. Figure 12b indicates that the strain rate roughly correlates with the median area to a power of -3.5 to -4.

7. Discussion

7.1. Distributions and Deformation Mechanics

The experiments of Tasaka et al. (2016) suggest that during dislocation creep, a steady state grain size distribution approaches lognormal scaling behavior, in agreement with previous assumptions. However, the fact that we find few lognormal distributions in the remaining natural samples indicates that steady state distributions are often not achieved during natural deformation.

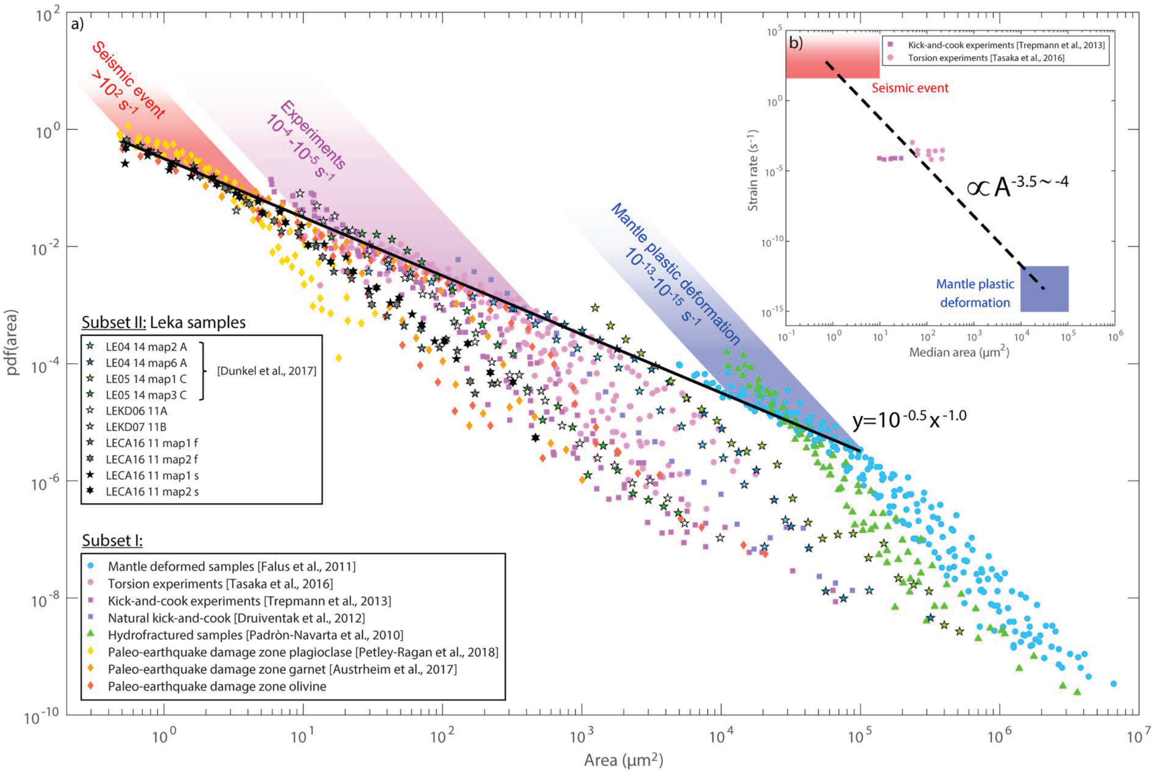

Figure 12. (a) Plot of the grain size distributions for all the studied samples. An envelope with a slope exponent of −1.0 can be identified. (b) Mantle-deformed samples (Falus et al., 2011), experimentally deformed samples (Tasaka et al., 2016; Trepmann et al., 2013), and samples from intermediate depth earthquakes (Austrheim et al., 2017; Petley-Ragan et al., 2018) allow constraints to be put on the negative correlation between strain rate and grain size. Note that the median grain size for samples from the kick-and-cook experiments are approximately 1 order of magnitude smaller than those from the steady state torsion experiments which were conducted at similar strain rates (10^{-4}–10^{-5} s^{-1}). This is due to the higher stress required to achieve a given strain rate for the lower-temperature (kick-and-cook) experiments.

Brittle fragmentation processes clearly lead to a power law grain size scaling, even in situations where there is very little shear deformation such as for the LE05 14 C sample from Leka (Dunkel, Austrheim, Ildefonse, & Jamtveit, 2017; Dunkel, Austrheim, Renard, et al., 2017). This also seems to hold in situations where the fragmentation takes place by low-temperature plasticity such as during the experiments of Druiventak et al. (2012) and Trepmann et al. (2013). Interestingly, kick-and-cook experiments carried out at high annealing temperature (1100 °C) or with long annealing times show a crossover to lower power law slopes for small grain sizes. This may suggest that the change from a large power law exponent to a smaller exponent is related to grain growth and recovery processes. This is also consistent with the scaling behavior observed for the seismically deformed garnets from the Bergen Arcs where growth of strain-free grains was reported to occur at the expense of dislocation-rich grains and subgrains (Austrheim et al., 2017). In that case the initial fragmentation process probably occurred by a combination of brittle mechanisms and low-temperature plasticity. We thus infer that the common situation observed in our data, where the grain size distribution fits a combination of two power laws, reflects the combination of a fragmentation process responsible for the steep slopes (given by α_2) and a recovery process that breaks the scaling toward more gentle slopes (α_1). In many situations, the fragmentation process precedes a later recovery and growth process, and thus, the final microstructure does not represent a steady state situation.

The use of a median grain size as a representative of the size distribution may still be useful as indicated by the close relation between the median and the power laws intersection (Figure 8), but one needs to be careful if using it to estimate paleostress.

The samples from the LOC show a wide range of grain size distributions, with median values in the range 1–10^3 μm^2. According to Figure 12b, this may reflect more than 10 orders of magnitude range in strain rates. As mentioned above, the fragmented wall rock olivine next to what was interpreted as a seismic fault by Dunkel, Austrheim, Renard, et al. (2017) and Dunkel, Austrheim, Ildefonse, and Jamtveit (2017) shows a single power law. The mean grain size is approximately 7 μm^2, approaching the mean values for seismically deformed wall rock garnets and olivines from the Bergen Arcs and Corsica (1–8 μm^2). The initial mantle fabric shows a mostly lognormal distribution as expected, with mean grain sizes around 10^3 μm^2, which is 1–2 orders of magnitude smaller than the data from Falus et al. (2011) for mantle samples. The remaining data from Leka mainly show combination of two power laws, and the grain sizes are in most cases even smaller than for the wall rock olivines described by Dunkel, Austrheim, Renard, et al. (2017) and Dunkel, Austrheim, Ildefonse, and Jamtveit (2017), suggesting deformation at high stresses and strain rates. By comparison with the other data, it is reasonable to conclude that the microstructures in most of the studied samples of dunites from shear zones in the LOC reflect deformation at near-seismic strain rates. Since the sampling was biased to avoid samples rich in serpentine where fluids clearly played a key role during deformation, this does not imply that all deformation was related to earthquakes. It seems likely, however, that earthquakes were an important ingredient in the structural and metamorphic evolution of this ophiolite complex and perhaps even a key factor in introducing fluids into the system (cf. Jamtveit et al., 2018).

7.2. Model: Dislocation Patterning and Density Distributions

During crystal plastic deformation, the formation and size evolution of grains and subgrains at macroscopic scale are controlled at the microscopic scale by formation, movements, and annihilation of dislocations in the crystal lattice. Under stress, crystalline materials often develop a network of dislocations, which self-organize into cellular structures where dislocation-poor regions are bounded by cell walls with high dislocation densities. It has been observed experimentally (Raj & Pharr, 1986) that the average grain size of these cellular patterns (λ) is inversely proportional to the applied stress, similarly to what Twiss (1977) observed with grain and subgrain sizes. This is known as the *principle of similitude* (i.e., Gómez-García et al., 2006; Hähner, 1996a, 1996b; Hansen et al., 2001):

$$\frac{\sigma}{\mu} = K\frac{b}{\lambda}, \tag{1}$$

where σ is the applied stress, μ the shear modulus, b the magnitude of the Burgers vector, and K is an empirical constant. A phenomenological explanation of this experimental observation originates from Taylor's theory of plastic flow (Taylor, 1938). It defines the flow stress (σ_{plast}) as being proportional to the square root of the average density of dislocations:

$$\frac{\sigma_{\mathrm{plast}}}{\mu} = \alpha b\sqrt{\rho}, \tag{2}$$

where ρ represents the number of dislocations intersecting a slip plane per unit area (2-D dislocation density) and α is a constant. Thus, from equations (1) and (2) the dislocations density ρ determines a typical length scale λ associated with the average size of the dislocation depleted regions. Hence, we can also interpret this length scale as a 1-D measure of the typical grain size, which means that the typical grain areas scale like the area of dislocation cells $A{\sim}\lambda^2$ which is inversely proportional to the dislocation density:

$$\lambda{\sim}\rho^{-1/2} \text{ or } A{\sim}\rho^{-1} \tag{3}$$

Dislocation formation, migration, and annihilation are adequately described by semiempirical equations. Using relation (3), we can connect the statistics of dislocation density fluctuations with the statistics of grain or subgrain sizes.

The main factors contributing to the time evolution of the mean dislocation density are the effective energy dissipation associated with plastic flow, $\frac{dE}{dt}$, and the driving force to stable dislocation configuration that minimize the interaction energy, $-\frac{dU}{d\rho}$ (Appendix A). This can be expressed by the following equation:

$$\dot{\rho} = -C_1\ln(\rho) - C_1 + C_2\left(\sigma_{\mathrm{ext}} - \alpha b\mu\sqrt{\rho}\right)\dot{\varepsilon}, \tag{4}$$

where C_2 is a constant and $\dot{\varepsilon}$ is the strain rate. The term $-C_1\ln(\rho) - C_1 = -C_1\frac{d}{d\rho}(\rho\log\rho) = -\frac{dU}{d\rho}$ is the driving force associated with an average interaction potential $\rho\log\rho$ (Foreman, 1955; Appendix A), where C_1 is a constant depending on the elastic constants, for example, shear modulus and the Poisson ratio of the medium. The effective energy dissipation term is $\frac{dE}{dt} = \sigma_{\text{eff}}\dot{\varepsilon} \approx \left(\sigma_{\text{ext}} - \alpha b\mu\sqrt{\rho}\right)\dot{\varepsilon}$ and has two sources: the external stress term and the plastic flow from the internal stress. The external stress component is related to the overall tectonic stress and considered as the unique source for dislocation generation, while plastic flow stress is related to the internal stress variations generated by the heterogeneous distribution of dislocations. Plastic flow stress and interactions between dislocations act to order and reduce dislocation density.

To study the distribution of the fluctuations in grain sizes that we observe in our samples, we propose a stochastic approach to equation (4) based on a modified version of the stochastic model by Hähner (1996a, 1996b). The basic idea is that collective interactions between dislocations lead to a fractal patterning and a power law distribution of grain sizes. In our case the global strain rate $\dot{\varepsilon}$ is expressed as the sum of an average deterministic value $\langle\dot{\varepsilon}\rangle$ representing an equilibrium value and a randomly fluctuating value η corresponding to fluctuations around the stationary average strain rate:

$$\dot{\varepsilon} = \langle\dot{\varepsilon}\rangle + \eta, \tag{5}$$

The noise term η originates from microscopic spatial heterogeneities of the strain rate and the evolving, complex dislocation structure. For simplicity, we assume that it has zero mean and is δ correlated with an autocorrelation function given by the following:

$$\langle\eta(t_1)\eta(t_2)\rangle = 2\zeta^2\delta(t_1 - t_2), \tag{6}$$

This means that the noise at different instants is uncorrelated and that the noise magnitude ζ increases with the occurrence of far from equilibrium strain rate values over the studied time interval.

The introduction of a stochastic strain rate into equation (4) leads to the following expression (Langevin equation) for the dislocation density variations:

$$\dot{\rho} = -C_1 \ln(\rho) - C_1 + C_2\sigma_{\text{ext}}\langle\dot{\varepsilon}\rangle - C_2\alpha b\mu\sqrt{\rho}(\langle\dot{\varepsilon}\rangle + \eta) \tag{7}$$

The elastic energy stored in the presence of external stress couples with the average strain rate; hence, its dissipation rate gives the term $\sigma_{\text{ext}}\langle\dot{\varepsilon}\rangle$ in the time evolution of dislocation density. Noise stems solely from the stress component associated with plastic flow and thus internal deformation dynamics. This multiplicative noise term has a variance that increases linearly with ρ. The interpretation of this type of noise is nonunique, and a choice has to be made regarding which computation method to adopt. In our case, we use the Ito calculus (LeBlanc et al., 2013; Morita, 1981). We will not enter into the computational details of this method but simply discuss the consequences relevant to our model.

The evolution of the pdf of ρ, $P(\rho)$, is governed by the Fokker-Plank equation corresponding to equation (7) using Ito calculus for the multiplicative noise (Morita, 1981):

$$\frac{\partial P}{\partial t} = -\frac{\partial}{\partial\rho}\left[\left(a - C_1 \ln(\rho) - C_3\sqrt{\rho}\right)P\right] + {C_3}^2\zeta^2\frac{\partial^2}{\partial\rho^2}[\rho P], \tag{8}$$

where $C_3 = C_2\alpha b\mu$ and a regroups all the constant terms affecting the variable ρ in (7). The steady state solution is given by the following (see Appendix B):

$$P(\rho) \sim \exp\left[-\frac{C_1}{2{C_3}^2\zeta^2}\left(\ln(\rho) + \frac{{C_3}^2\zeta^2}{C_1} - \frac{a}{C_1}\right)^2\right] \tag{9}$$

After a change of variable from dislocation density to grain size area using relation (3), that is, $P_A(A)dA = P(\rho)\,d\rho$, the distribution of grain areas $P_A(A)$ approaches a power law with a slope of -1 for large noise amplitude (large ζ^2) and a lognormal distribution for small noise amplitude (small ζ^2; Figure 13; see Appendix B).

The Ito calculus applies when we interpret the multiplicative noise as a punctuated process, which is a superposition of discrete events of a given magnitude that occur at random points in time (LeBlanc et al., 2013). When plastic motion is driven by dislocation motion, that is, when the global strain rate is determined

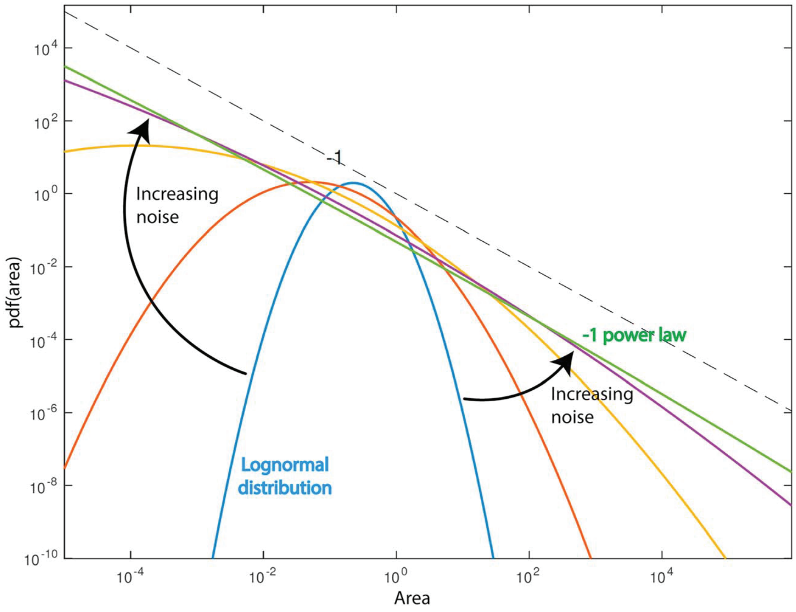

Figure 13. Area distribution for different values of the noise parameter $C_3{}^2\zeta^2$, showing that with increasing noise, the distribution changes from lognormal to power law.

by the dislocation dynamics (rate of dislocation formation, storage, annihilation, etc.), the global strain rate can be approximated by a superposition of nonoverlapping *slip avalanches*:

$$\dot{\varepsilon} = \Sigma_i \widehat{\varepsilon}_i G(t - t_i), \tag{10}$$

$\widehat{\varepsilon}_i$ is the strain accumulated during the slip event *i* happening within a short time interval (*T*) centered at t_i, and G ($t - t_i$) is a sharply peaked function (or time kernel). The average time lag between slip events and the average strain increment are denoted by τ and $\widehat{\varepsilon}$, respectively. The noise arises from variations of $\widehat{\varepsilon}_i$ and t_i relative to values $\widehat{\varepsilon}$, τ, and T. The mean ($\langle\dot{\varepsilon}\rangle$) and standard deviation (noise amplitude, ζ^2) of the strain rate can be determined from the parameters $\widehat{\varepsilon}$, τ, and T (Hähner, 1996b):

$$\langle\dot{\varepsilon}\rangle = \frac{\widehat{\varepsilon}}{\tau} \tag{11}$$

$$\zeta^2 = \frac{\widehat{\varepsilon}^2}{\sqrt{2\pi}} \frac{1}{\tau T} \tag{12}$$

For small noise amplitude ($\zeta^2 \ll \langle\dot{\varepsilon}\rangle^2$), relations (11) and (12) lead to $\tau \ll T$, meaning that dislocations are almost constantly slipping to accommodate the strain. Since we assume steady state, the rate of dislocation reactions reducing the dislocation density is of the same order as the rate of dislocation multiplication. In this case the steady state solution to equation (8) indicates the grain size distribution will be lognormal (Figure 13).

In the case of large noise amplitude, $\tau \gg T$. This means that slips happen during very short time steps compared to the overall deformation. Deformation is happening discontinuously and dislocation self-organization is very efficient compared to strain rate. In this case the steady state solution to equation (8) indicates that the grain size distribution is a power law of slope −1 (Figure 13). As the variance of the noise is positively correlated with the dislocation density, this case implies high dislocation densities in the limits of our model.

During deformation, noise can have various origins, including heterogeneities already present in the rock (occurrence of different phases, grain sizes, modifying locally the strength of the rock), but the main controlling parameter is the rate of dislocation storage and healing compared to strain rate. If the self-organization of dislocations is fast compared to deformation strain rate, leading to discontinuous strain accommodation by the dislocations, a distribution of grain areas is expected to follow a power law with a slope of -1. If the self-organization of dislocations is fast enough to control the deformation strain rate but of the same order of magnitude as the deformation rate, a lognormal distribution is expected for grain size area distribution. The model presented above assumes dislocation controlled deformation. Hence, it does not describe the situation where the strain rate is too fast to be accommodated by dislocation motion. Based on our data and previous studies of grain size distributions of samples fragmented by brittle mechanisms (e.g., An & Sammis, 1994; Billi, 2005; Heilbronner & Keulen, 2006), a power law distribution with a slope around -2 would then be expected.

For a given rate of dislocation self-organization, the -1 power law case would be expected for very slow strain rates eventually down to 0 (healing) and high dislocation density (which could be the normal situation after a seismic event), while the lognormal case would be expected for strain rates of the same order of magnitude as the dislocation dynamics with efficient organization of the dislocations and thus lower dislocation density in bulk. Power laws with larger slopes are expected for high strain rates. The lognormal distribution, as we observe in steady state torsion experiments and some mantle-deformed samples, could be considered as the *equilibrium* one which can be used for paleostress estimates as it is expected when the dislocation dynamics operate at rates comparable to the strain rate.

The steady state leading to the -1 slope is not a long-lived steady state as it requires a high dislocation density, which may not last long under conditions where strain rate is slow and recovery processes active. In between events leading to these high dislocation densities and discontinuous deformation, the regime may progressively tend toward a regime of more continuous deformation and thus lognormal distribution. This could explain the intermediate distribution of most of our samples.

The envelope (line with -1 slope) shown in Figure 12a may reflect the equilibrium lognormal shape towards which all the distributions eventually should converge. Indeed, the envelope created by lognormal distributions of similar σ but spread over a large range of μ values follows a relation proportional to a power law of slope -1. In the case of σ close to 1.2, the proportionality coefficient is close to $10^{-0.5}$, as observed.

The strain rate is externally imposed by tectonic stress, but it is interesting to identify what controls how fast dislocations can organize themselves. Dislocation slip events are often considered as equivalent to chemical reactions, which means that the two main parameters controlling their rates are temperature and dislocation concentration. Higher temperatures and concentrations lead to higher reaction rates. For a deforming polycrystalline rock, the temperature is the same for all grain sizes; thus, dislocation density is controlling the *reaction rates* of the dislocations. The dislocation self-organization will be faster in small grains than in large grains, and different noise conditions may apply depending on grain size.

8. Summary

In this paper we presented a unique set of grain size distributions of olivine-dominated rocks deformed over a wide range of strain rates from slow mantle flow to seismic fragmentation. We observe a surprisingly coherent behavior for most natural samples, with a power law probability distribution function of areas near -1 for the smallest grain fraction, and a steeper slope (in most cases in the range -2 to -2.5) for the larger grain fraction. Convincing lognormal distributions across scales were only observed for samples experimentally deformed at high temperatures (and designed to achieve steady state distributions) and some mantle-deformed natural samples. Simple power law distribution with a single exponent was only observed for natural samples deformed by brittle mechanisms and experimentally deformed samples interpreted to have deformed by low-temperature plasticity.

Most natural samples show a clear cross over in scaling behavior near the median grain size and show a good data collapse for small grains when normalized to the crossover scale. The associated power law slope of approximately -1 indicates that a common process controls grain size behavior. We present a model that explains how such scaling behavior may arise in the dislocation creep regime from the competition between the rates involved in the dislocation dynamics and the strain rate.

The common departure from lognormal distributions suggests that naturally deformed samples often display a grain size distribution that reflects a deformation history far from a steady state scenario and probably arises due to deformation under changing stress and strain rates as previously proposed by Trepmann and Stöckhert (2003) and Trepmann et al. (2007).

Appendix A: Interaction Energy Contribution to Dislocation Density Variations

The average energy of dislocation due to the interaction with its nearest neighbor is (Foreman, 1955) as follows:

$$u(\lambda)\sim-\mu b^2\frac{1-{}^{\nu}/_{2}}{4\pi(1-\nu)}\ln\left(\frac{\lambda}{b}\right) \tag{A1}$$

Assuming that all the dislocations have approximately the same interaction energy u and using relation (3), the total interaction energy for a configuration of dislocations with density ρ is given as follows:

$$U(\rho)\sim\rho u\left(\rho^{-1/2}\right)\sim-\mu b^2\frac{1-{}^{\nu}/_{2}}{4\pi(1-\nu)}\rho\ln\left(\frac{1}{b\sqrt{\rho}}\right), \tag{A2}$$

The driving force obtained from minimizing dislocation interactions energy is then

$$-\frac{\mathrm{d}U}{\mathrm{d}\rho}=-C_1\ln(\rho)-C_1,\ \text{where}\ 2C_1=\mu b^2\frac{1-{}^{\nu}/_{2}}{4\pi(1-\nu)} \tag{A3}$$

Appendix B: Solution to Fokker-Plank Equation for Dislocation Density

The probability density $P(\rho,t)$ for the dislocation density is obtained by writing the Fokker-Plank equation related to equation (7) in its Ito form (Morita, 1981):

$$\frac{\partial P}{\partial t}=-\frac{\partial}{\partial\rho}\left[\left(a-C_1\ln(\rho)-C_3\sqrt{\rho}\right)P\right]+{C_3}^2\zeta^2\frac{\partial^2}{\partial\rho^2}[\rho P] \tag{B1}$$

The stationary solution satisfies the following:

$$\frac{\partial P}{\partial\rho}+P=\frac{1}{{C_3}^2\zeta^2}\left(a-C_1\ln(\rho)-C_3\sqrt{\rho}\right)P \tag{B2}$$

$$\frac{\mathrm{d}P}{P}=\left(-1+\frac{a}{{C_3}^2\zeta^2}\right)\frac{\mathrm{d}\rho}{\rho}-\frac{C_1}{{C_3}^2\zeta^2}\ln(\rho)\frac{\mathrm{d}\rho}{\rho}-\frac{1}{C_3\zeta^2}\sqrt{\rho}\frac{\mathrm{d}\rho}{\rho} \tag{B3}$$

$$P(\rho)\sim\exp\left[\left(-1+\frac{a}{{C_3}^2\zeta^2}\right)\ln(\rho)-\frac{C_1}{{C_3}^2\zeta^2}\ln^2(\rho)\right] \tag{B4}$$

$$P(\rho)\sim\exp\left[-\left(\sqrt{\frac{C_1}{2{C_3}^2\zeta^2}}\ln(\rho)-\sqrt{\frac{{C_3}^2\zeta^2}{2C_1}}\left(-1+\frac{a}{{C_3}^2\zeta^2}\right)\right)^2\right] \tag{B5}$$

$$P(\rho)\sim\exp\left[-\frac{C_1}{2{C_3}^2\zeta^2}\left(\ln(\rho)-\frac{{C_3}^2\zeta^2}{C_1}\left(-1+\frac{a}{{C_3}^2\zeta^2}\right)\right)^2\right] \tag{B6}$$

$$P(\rho)\sim\exp\left[-\frac{C_1}{2{C_3}^2\zeta^2}\left(\ln(\rho)+\frac{{C_3}^2\zeta^2}{C_1}-\frac{a}{C_1}\right)^2\right] \tag{B7}$$

Or with the change of variable from dislocation density to area $P_A(A)dA = P(\rho)d\rho = A^{-2}P(A^{-1})$,

$$P_A(A)\sim A^{-2}\exp\left[-\frac{C_1}{2{C_3}^2\zeta^2}\left(-\ln(A)+\frac{{C_3}^2\zeta^2}{C_1}-\frac{a}{C_1}\right)^2\right] \tag{B8}$$

In the case of large noise amplitude ${C_3}^2\zeta^2\gg C_1$,

$$P_A(A)\sim A^{-1} \tag{B9}$$

In the case of small noise amplitude ${C_3}^2\zeta^2\ll C_1$,

$$P_A(A)\sim A^{-2}\exp\left[-\frac{C_1}{2{C_3}^2\zeta^2}\left(\ln(A)+\frac{a}{C_1}\right)^2\right] \tag{B10}$$

For illustration of the solution with various noise values see Figure 13.

Acknowledgments
This project was supported by the European Union's Horizon 2020 Research and Innovation Programme under the ERC Advanced Grant Agreement 669972, *Disequilibrium Metamorphism* (*DIME*) to B. J. We thank the EBSD (Fabrice Barou) and thin sections preparation (Christophe Nevado and Doriane Delmas) teams at Géosciences Montpellier for their help and warm welcome in their premises. We also thank György Falus, José Alberto Padrón-Navarta, Miki Tasaka, and Claudia Trepmann for their kind sharing of data, Kerstin Drivdal for pictures and sampling of some of the Leka samples, and François Renard for suggestions regarding the statistical analysis. John Platt and an anonymous reviewer are thanked for their valuable comments that improved the manuscript. All data used in this article are presented in the figures. Rock thin sections used to estimate the grain size distributions are available by contacting the corresponding author. Used EBSD maps can be downloaded here: https://osf.io/6hkyu/.

References

An, L.-J., & Sammis, C. G. (1994). Particle size distribution of cataclastic fault materials from Southern California: A 3-D study. *Pure and Applied Geophysics*, *143*(1–3), 203–227. https://doi.org/10.1007/BF00874329

Andersen, T. B., & Austrheim, H. (2006). Fossil earthquakes recorded by pseudotachylytes in mantle peridotite from the Alpine subduction complex of Corsica. *Earth and Planetary Science Letters*, *242*(1–2), 58–72. https://doi.org/10.1016/j.epsl.2005.11.058

Austin, N. J., & Evans, B. (2007). Paleowattmeters: A scaling relation for dynamically recrystallized grain size. *Geology*, *35*(4), 343–346. https://doi.org/10.1130/G23244A.1

Austrheim, H., Dunkel, K. G., Plümper, O., Ildefonse, B., Liu, Y., & Jamtveit, B. (2017). Fragmentation of wall rock garnets during deep crustal earthquakes. *Science Advances*, *3*(2), e1602067. https://doi.org/10.1126/sciadv.1602067

Austrheim, H., Erambert, M., & Boundy, T. M. (1996). Garnets recording deep crustal earthquakes. *Earth and Planetary Science Letters*, *139*(1–2), 223–238. https://doi.org/10.1016/0012-821X(95)00232-2

Bachmann, F., Hielscher, R., & Schaeben, H. (2010). Texture analysis with MTEX—Free and open source software toolbox. *Solid State Phenomena*, *160*, 63–68. https://doi.org/10.4028/www.scientific.net/SSP.160.63

Bachmann, F., Hielscher, R., & Schaeben, H. (2011). Grain detection from 2d and 3d EBSD data—Specification of the MTEX algorithm. *Ultramicroscopy*, *111*(12), 1720–1733. https://doi.org/10.1016/j.ultramic.2011.08.002

Billi, A. (2005). Grain size distribution and thickness of breccia and gouge zones from thin (<1 m) strike-slip fault cores in limestone. *Journal of Structural Geology*, *27*(10), 1823–1837. https://doi.org/10.1016/j.jsg.2005.05.013

Clauset, A., Shalizi, C., & Newman, M. (2009). Power-law distributions in empirical data. *SIAM Review*, *51*(4), 661–703. https://doi.org/10.1137/070710111

Cross, A. J., Ellis, S., & Prior, D. J. (2015). A phenomenological numerical approach for investigating grain size evolution in ductiley deforming rocks. *Journal of Structural Geology*, *76*, 22–34. https://doi.org/10.1016/j.jsg.2015.04.001

De Bresser, J. H. P., Ter Heege, J. H., & Spiers, C. J. (2001). Grain size reduction by dynamic recrystallization: Can it result in major theological weakening? *International Journal of Earth Sciences*, *90*(1), 28–45. https://doi.org/10.1007/s005310000149

Doherty, R. D., Hughes, D. A., Humphreys, F. J., Jonas, J. J., Jensen, D. J., Kassner, M. E., et al. (1997). Current issues in recrystallization: A review. *Materials Science and Engineering A*, *238*(2), 219–274. https://doi.org/10.1016/S0921-5093(97)00424-3

Druiventak, A., Matysiak, A., Renner, J., & Trepmann, C. A. (2012). Kick-and-cook experiments on peridotite: Simulating coseismic deformation and post-seismic creep. *Terra Nova*, *24*(1), 62–69. https://doi.org/10.1111/j.1365-3121.2011.01038.x

Druiventak, A., Trepmann, C. A., Renner, J., & Hanke, K. (2011). Low-temperature plasticity of olivine during high stress deformation of peridotite at lithospheric conditions—An experimental study. *Earth and Planetary Science Letters*, *311*(3–4), 199–211. https://doi.org/10.1016/j.epsl.2011.09.022

Drury, M., & Urai, J. (1990). Deformation-related recrystallization processes. *Tectonophysics*, *172*(3–4), 235–253. https://doi.org/10.1016/0040-1951(90)90033-5

Dunkel, K. G., Austrheim, H., Ildefonse, B., & Jamtveit, B. (2017). Transfer of olivine crystallographic orientation through a cycle of serpentinisation and dehydration. *Contributions to Mineralogy and Petrology*, *172*(8), 64. https://doi.org/10.1007/s00410-017-1378-5

Dunkel, K. G., Austrheim, H., Renard, F., Cordonnier, B., & Jamtveit, B. (2017). Localized slip controlled by dehydration embrittlement of partly serpentinized dunites, Leka Ophiolite Complex, Norway. *Earth and Planetary Science Letters*, *463*, 277–285. https://doi.org/10.1016/j.epsl.2017.01.047

Dunning, G. R., & Pedersen, R. B. (1988). U/Pb ages of ophiolites and arc-related plutons of the Norwegian Caledonides: Implications for the development of Iapetus. *Contributions to Mineralogy and Petrology*, *98*(1), 13–23. https://doi.org/10.1007/BF00371904

Falus, G., Tommasi, A., & Soustelle, V. (2011). The effect of dynamic recrystallization on olivine crystal preferred orientations in mantle xenoliths deformed under varied stress conditions. *Journal of Structural Geology*, *33*(11), 1528–1540. https://doi.org/10.1016/j.jsg.2011.09.010

Feltham, P. (1957). Grain growth in metals. *Acta Metallurgica*, *5*(2), 97–105. https://doi.org/10.1016/0001-6160(57)90136-0

Foreman, A. J. E. (1955). Dislocation energies in anisotropic crystals. *Acta Metallurgica*, *3*(4), 322–330. https://doi.org/10.1016/0001-6160(55)90036-5

Furnes, H., Pedersen, R. B., & Stillman, C. J. (1988). The Leka Opholite Complex, central Norwegian Caledonides: Field characteristics and geotectonic significance. *Journal of the Geological Society*, *145*(3), 401–412. https://doi.org/10.1144/gsjgs.145.3.0401

Gómez-García, D., Devincre, B., & Kubin, L. P. (2006). Dislocation patterns and the similitude principle: 2.5D mesoscale simulations. *Physical Review Letters*, *96*(12), 12,5503. https://doi.org/10.1103/PhysRevLett.96.125503

Hähner, P. (1996a). A theory of dislocation cell formation based on stochastic dislocation dynamics. *Acta Materialia*, *44*(6), 2345–2352. https://doi.org/10.1016/1359-6454(95)00364-9

Hähner, P. (1996b). On the foundations of stochastic dislocation dynamics. *Applied Physics A*, *62*(5), 473–481. https://doi.org/10.1007/BF01567120

Hansen, L. N., Zimmerman, M. E., & Kohlstedt, D. L. (2011). Grain boundary sliding in San Carlos olivine: Flow law parameters and crystallographic-preferred orientation. *Journal of Geophysical Research*, *116*, B08201. https://doi.org/10.1029/2011JB008220

Hansen, N., Huang, X., & Hughes, D. A. (2001). Microstructural evolution and hardening parameters. *Materials Science and Engineering A*, *317*(1–2), 3–11. https://doi.org/10.1016/S0921-5093(01)01191-1

Heilbronner, R., & Keulen, N. (2006). Grain size and grain shape analysis of fault rocks. *Tectonophysics*, *427*(1–4), 199–216. https://doi.org/10.1016/j.tecto.2006.05.020

Hielscher, R., & Schaeben, H. (2008). A novel pole figure inversion method: Specification of the MTEX algorithm. *Journal of Applied Crystallography*, *41*(6), 1024–1037. https://doi.org/10.1107/S0021889808030112

Iyer, K., Jamtveit, B., Mathiesen, J., Malthe-Sørenssen, A., & Feder, J. (2008). Reaction-assisted hierarchical fracturing during serpentinization. *Earth and Planetary Science Letters*, *267*(3–4), 503–516. https://doi.org/10.1016/j.epsl.2007.11.060

Jamtveit, B., Ben-Zion, Y., Renard, F., & Austrheim, H. (2018). Earthquake-induced transformation of the lower crust. *Nature*, *556*(7702), 487–491. https://doi.org/10.1038/s41586-018-0045-y

Jung, H., & Karato, S. I. (2001). Effects of water on dynamically recrystallized grain-size of olivine. *Journal of Structural Geology*, *23*(9), 1337–1344. https://doi.org/10.1016/S0191-8141(01)00005-0

Jung, S., Jung, H., & Austrheim, H. (2014). Characterization of olivine fabrics and mylonite in the presence of fluid and implications for seismic anisotropy and shear localization. *Earth, Planets and Space*, *66*(1), 46. https://doi.org/10.1186/1880-5981-66-46

Kile, D. E., Eberl, D. D., Hoch, A. R., & Reddy, M. M. (2000). An assessment of calcite growth mechanisms based on crystal size distributions. *Geochimica et Cosmochimica Acta*, *64*(17), 2937–2950. https://doi.org/10.1016/S0016-7037(00)00394-X

Kirkpatrick, J. D., & Rowe, C. D. (2013). Disappearing ink: How pseudotachylytes are lost from the rock record. *Journal of Structural Geology*, *52*, 183–198. https://doi.org/10.1016/j.jsg.2013.03.003

Kühn, A., Glodny, J., Iden, K., & Austrheim, H. (2000). Retention of Precambrian Rb/Sr phlogopite ages through Caledonian eclogite facies metamorphism, Bergen Arc Complex, W-Norway. *Lithos*, *51*(4), 305–330. https://doi.org/10.1016/S0024-4937(99)00067-5

Leblanc, M., Angheluta, L., Dahmen, K., & Goldenfeld, N. (2013). Universal fluctuations and extreme statistics of avalanches near the depinning transition. *Physical Review E*, *87*(2), 022126. https://doi.org/10.1103/PhysRevE.87.022126

Linckens, J., Zulauf, G., & Hammer, J. (2016). Experimental deformation of coarse-grained rock salt to high strain. *Journal of Geophysical Research: Solid Earth*, *121*, 6150–6171. https://doi.org/10.1002/2016JB012890

Magott, R., Fabbri, O., & Fournier, M. (2016). Subduction zone intermediate-depth seismicity: Insights from the structural analysis of Alpine high-pressure ophiolite-hosted pseudotachylyte (Corsica, France). *Journal of Structural Geology*, *87*, 95–114. https://doi.org/10.1016/j.jsg.2016.04.002

Morita, T. (1981). On the interpretation of multiplicative white noise. *Physics Letters A*, *82*(5), 215–217. https://doi.org/10.1016/0375-9601(81)90187-0

Nicolas, A., & Christensen, N. I. (1987). Formation of anisotropy in upper mantle peridotites—A review. In K. Fuchs & C. Froidevaux (Eds.), *Composition, structure and dynamics of the lithosphere-asthenosphere system* (pp. 111–123). Washington, DC: American Geophysical Union. https://doi.org/10.1029/GD016p0111

Padrón-Navarta, J. A., Tommasi, A., Garrido, C. J., Sánchez-Vizcaíno, V. L., Gómez-Pugnaire, M. T., Jabaloy, A., & Vauchez, A. (2010). Fluid transfer into the wedge controlled by high-pressure hydrofracturing in the cold top-slab mantle. *Earth and Planetary Science Letters*, *297*(1–2), 271–286. https://doi.org/10.1016/j.epsl.2010.06.029

Petley-Ragan, A., Dunkel, K. G., Austrheim, H., Ildefonse, B., & Jamtveit, B. (2018). Microstructural records of intermediate-depth earthquakes and associated fluid-driven metamorphism of plagioclase-rich granulites. *Journal of Geophysical Research: Solid Earth*, *123*, 3729–3746. https://doi.org/10.1029/2017JB015348

Pfiffner, O. A., & Ramsay, J. G. (1982). Constraints on geological strain rates: Arguments from finite strain states of naturally deformed rocks. *Journal of Geophysical Research*, *87*, 311–321. https://doi.org/10.1029/JB087iB01p00311

Raj, S. V., & Pharr, G. M. (1986). A compilation and analysis of data for the stress dependence of the subgrain size. *Materials Science and Engineering*, *81*, 217–237. https://doi.org/10.1016/0025-5416(86)90265-X

Ricard, Y., & Bercovici, D. (2009). A continuum theory of grain size evolution and damage. *Journal of Geophysical Research*, *114*, B01204. https://doi.org/10.1029/2007JB005491

Roberts, D., Nordgulen, Ø., & Melezhik, V. (2007), The uppermost allochthon in the Scandinavian Caledonides: From a Laurentian ancestry through Taconian orogeny to Scandian crustal growth on Baltica. In R. D. Hatcher, Jr., M. P. Carlson, J. H. McBride, & J. R. Martínez Catalán (Eds.), *4-D framework of continental crust* (mem. 200, pp. 357–377). Boulder, Colorado: Geological Society of America. https://doi.org/10.1130/2007.1200(18)

Rozel, A., Ricard, Y., & Bercovici, D. (2011). A thermodynamically self-consistent damage equation for grain size evolution during dynamic recrystallization. *Geophysical Journal International*, *184*(2), 719–728. https://doi.org/10.1111/j.1365-246X.2010.04875.x

Sammis, C., King, G., & Biegel, R. (1987). The kinematics of gouge deformation. *Pure and Applied Geophysics*, *125*(5), 777–812. https://doi.org/10.1007/BF00878033

Sammis, C. G., & Ben-Zion, Y. (2008). Mechanics of grain-size reduction in fault zones. *Journal of Geophysical Research*, *113*, B02306. https://doi.org/10.1029/2006JB004892

Sibson, R. H. (1975). Generation of pseudotachylyte by ancient seismic faulting. *Geophysical Journal International*, *43*(3), 775–794. https://doi.org/10.1111/j.1365-246X.1975.tb06195.x

Stipp, M., Stunitz, H., Heilbronner, R., & Schmid, S. M. (2002). Dynamic recrystallization of quartz: Correlation between natural and experimental conditions. In S. DeMeer, M. R. Drury, J. H. P. DeBresser, & G. M. Pennock (Eds.), *Deformation mechanisms, rheology and tectonics: Current status and future perspectives* (pp. 171–190). Bath: Geological Soc Publishing House. https://doi.org/10.1144/GSL.SP.2001.200.01.11

Stipp, M., Tullis, J., Scherwath, M., & Behrmann, J. H. (2010). A new perspective on paleopiezometry: Dynamically recrystallized grain size distributions indicate mechanism changes. *Geology*, *38*(8), 759–762. https://doi.org/10.1130/G31162.1

Tasaka, M., Zimmerman, M. E., & Kohlstedt, D. L. (2016). Evolution of the rheological and microstructural properties of olivine aggregates during dislocation creep under hydrous conditions. *Journal of Geophysical Research: Solid Earth*, *121*, 92–113. https://doi.org/10.1002/2015JB012134

Taylor, G. I. (1938). Plastic strain in metals. *Journal of the Institute of Metals*, *62*, 307–324.

Titus, S. J., Fossen, H., Pedersen, R. B., Vigneresse, J. L., & Tikoff, B. (2002). Pull-apart formation and strike-slip partitioning in an obliquely divergent setting, Leka ophiolite, Norway. *Tectonophysics*, *354*(1–2), 101–119. https://doi.org/10.1016/S0040-1951(02)00293-7

Tommasi, A., Mainprice, D., Canova, G., & Chastel, Y. (2000). Viscoplastic self-consistent and equilibrium-based modeling of olivine lattice preferred orientations: Implications for the upper mantle seismic anisotropy. *Journal of Geophysical Research*, *105*, 7893–7908. https://doi.org/10.1029/1999JB900411

Trepmann, C. A., Renner, J., & Druiventak, A. (2013). Experimental deformation and recrystallization of olivine—Processes and timescales of damage healing during postseismic relaxation at mantle depths. *Solid Earth*, *4*(2), 423–450. https://doi.org/10.5194/se-4-423-2013

Trepmann, C. A., & Stöckhert, B. (2003). Quartz microstructures developed during non-steady state plastic flow at rapidly decaying stress and strain rate. *Journal of Structural Geology*, *25*(12), 2035–2051. https://doi.org/10.1016/S0191-8141(03)00073-7

Trepmann, C. A., Stöckhert, B., Dorner, D., Moghadam, R. H., Küster, M., & Röller, K. (2007). Simulating coseismic deformation of quartz in the middle crust and fabric evolution during postseismic stress relaxation—An experimental study. *Tectonophysics*, *442*(1–4), 83–104. https://doi.org/10.1016/j.tecto.2007.05.005

Twiss, R. J. (1977). Theory and applicability of a recrystallized grain size paleopiezometer. In M. Wyss (Ed.), *Stress in the Earth* (pp. 227–244). Birkhäuser, Basel: Contributions to Current Research in Geophysics (CCRG). https://doi.org/10.1007/978-3-0348-5745-1_13

Van der Wal, D., Chopra, P., Drury, M., & Gerald, J. F. (1993). Relationships between dynamically recrystallized grain size and deformation conditions in experimentally deformed olivine rocks. *Geophysical Research Letters*, *20*, 1479–1482. https://doi.org/10.1029/93GL01382

Zhao, Y. H., Zimmerman, M. E., & Kohlstedt, D. L. (2009). Effect of iron content on the creep behavior of olivine: 1. Anhydrous conditions. *Earth and Planetary Science Letters*, *287*(1–2), 229–240. https://doi.org/10.1016/j.epsl.2009.08.006

Journal of Geophysical Research: Solid Earth

Supporting Information for

Evidence for non-steady state deformation in olivine grain size distributions

C. Aupart[1], K. G. Dunkel[1], L. Angheluta[2], H. Austrheim[1], B. Ildefonse[3], A. Malthe-Sørenssen[2], and B. Jamtveit[1]

[1] Physics of Geological Processes (PGP), The Njord Centre, Dept. of Geosciences, University of Oslo, PO Box 1048, N-0316, Oslo, Norway. [2] Physics of Geological Processes (PGP), The Njord Centre, Dept. of Physics, University of Oslo (UiO), PO Box 1048, N-0316, Oslo, Norway. [3] Géosciences Montpellier, CNRS, University of Montpellie, Université des Antilles, Montpellier, France.

Contents of this file

Text S1
Figure S1 to S5
Table S1

Introduction

This supporting information provides details of the fitting method used in the main paper, individual distributions with fits for all samples presented in the main article and a table containing errors on fitting parameters due to binning. Three additional figures present all the samples plotted depending on their scaling behavior (two power laws, one power law, or lognormal).

Text S1: Fitting method

To fit the distributions to a composite function of two power laws, we first used a goodness-of-fit method (Clauset et al., 2009) to identify the scale range of a single power law applicable to the large grain fraction. This method returns a value X_{min} corresponding to the minimum area at which the method finds a power law. The pdf is then plotted in a log-log diagram and the MatLab function polyfit (using a least-square method) is used to determine the exponent of the power laws for both the larger scale (larger than X_{min}) and smaller scale (smaller than X_{min}) ends of the distribution. Some data points (clearly identified on the individual fits in fig. S1) have been excluded at the largest and smallest grain sizes and at the transition between two power laws in order to increase the fitting precision. A power law can be written: $f(x) = Cx^{-\alpha}$ with C a constant and α the slope of the power law. The slope is called α_1 for the first power law (smaller areas) and α_2 for the second power law (larger areas). The intersection of the two power laws X_{i} is calculated after the fitting. The value usually stays close to X_{min} (fig. S5).

Lognormal fits have been obtained by a least square method, using the function fit from the curve fitting MatLab toolbox. This function returns two parameters μ and σ. exp(μ) is the lognormal distribution's median, and $\exp(\sigma)$ its standard deviation. The goodness of the lognormal fit is evaluated using the standard error of the regression, $S = \sqrt{\frac{\sum_{i=1}^{n_{\mathrm{bins}}}(\log(\mathrm{pdf}_{\mathrm{logn}(\mu,\sigma)}(A_i))-\log(\mathrm{pdf}_{\mathrm{data}}(A_i)))}{n_{\mathrm{bins}}-2}}$, where n_{bins} is the number of points in the pdf and A_i are the area values for which the pdf have been calculated.

The calculation of the pdf of each sample requires a fixed number of bins to define the number of points in the final distribution. A robust way of defining the bin size is to use the Freedman–Diaconis rule: bin size $= 2\frac{\mathrm{IQR}(x)}{\sqrt[3]{n}}$ with $\mathrm{IQR}(x)$ the interquartile range of the data and n the number of grains in the sample x. For the clarity of the figures, we restricted the number of bins to be in the range 15 to 25. We then estimated the error induced by the binning by varying the number of bins by one third of its optimal value above and below its optimal value. The fits presented in table 1 and in fig. S1 show results with optimal bin numbers. Errors on the fitting parameters induced by varying the binning are presented in table S1. The influence of the binning on the fitting parameters is negligible (fig. S1).

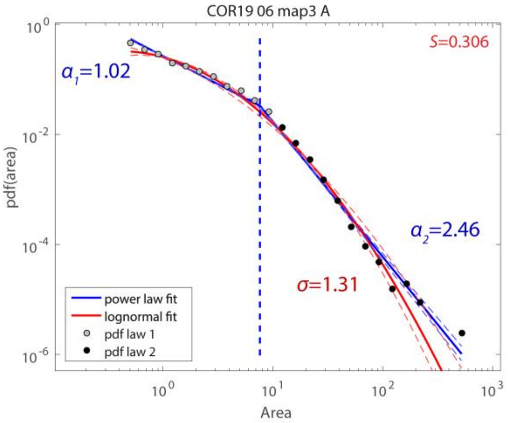
COR19 06 map3 A
S=0.306
α1=1.02
α2=2.46
σ=1.31
pdf(area)
Area
power law fit
lognormal fit
pdf law 1
pdf law 2
10^0
10^-2
10^-4
10^-6
10^0
10^1
10^2
10^3

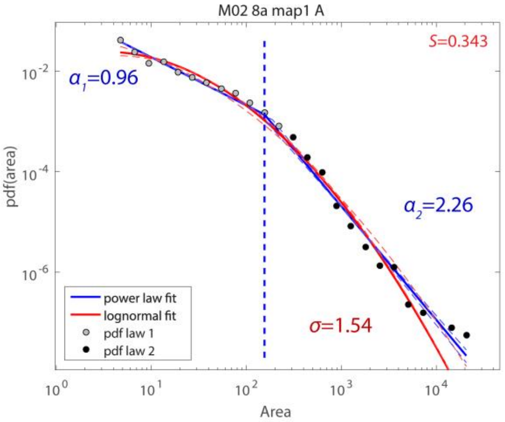
M02 8a map1 A
S=0.343
α1=0.96
α2=2.26
σ=1.54
pdf(area)
Area
power law fit
lognormal fit
pdf law 1
pdf law 2
10^-2
10^-4
10^-6
10^0
10^1
10^2
10^3
10^4

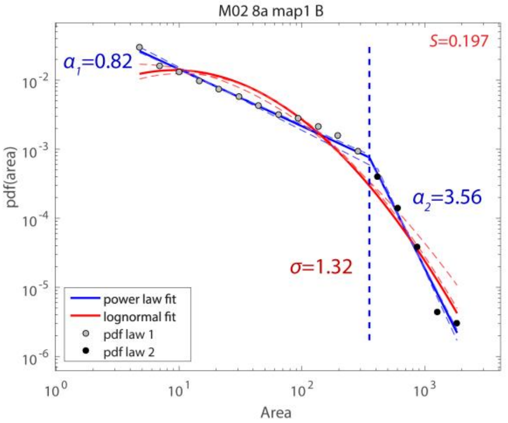
M02 8a map1 B
S=0.197
α1=0.82
α2=3.56
σ=1.32
pdf(area)
Area
power law fit
lognormal fit
pdf law 1
pdf law 2
10^-2
10^-3
10^-4
10^-5
10^-6
10^0
10^1
10^2
10^3

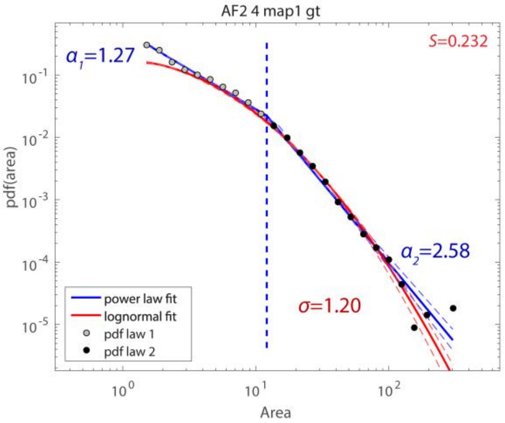
AF2 4 map1 gt
S=0.232
α1=1.27
α2=2.58
σ=1.20
pdf(area)
Area
power law fit
lognormal fit
pdf law 1
pdf law 2
10^-1
10^-2
10^-3
10^-4
10^-5
10^0
10^1
10^2

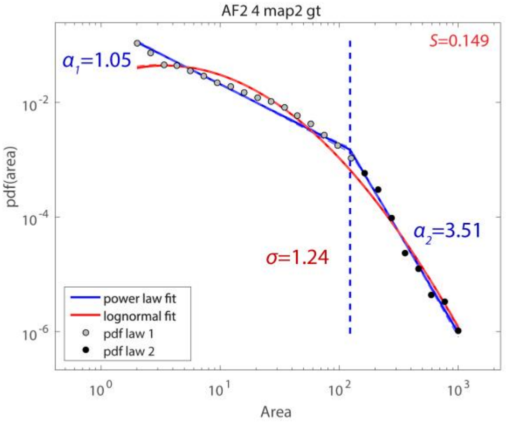
AF2 4 map2 gt
S=0.149
α1=1.05
α2=3.51
σ=1.24
pdf(area)
Area
power law fit
lognormal fit
pdf law 1
pdf law 2
10^-2
10^-4
10^-6
10^0
10^1
10^2
10^3

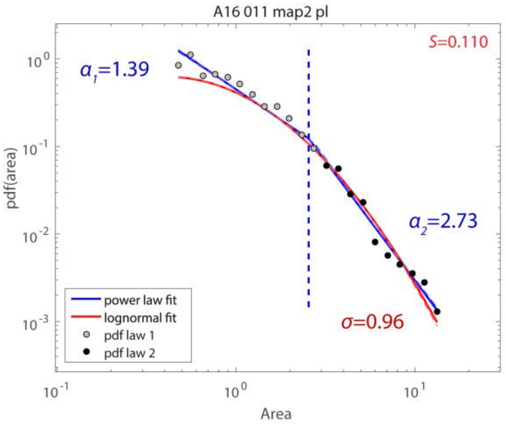
A16 011 map2 pl
S=0.110
α1=1.39
α2=2.73
σ=0.96
pdf(area)
Area
power law fit
lognormal fit
pdf law 1
pdf law 2
10^0
10^-1
10^-2
10^-3
10^-1
10^0
10^1

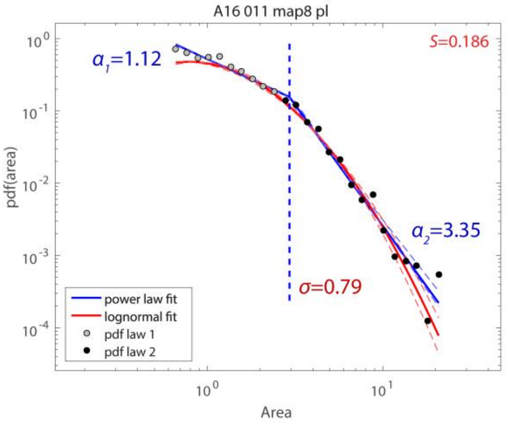
A16 011 map8 pl
S=0.186
α1=1.12
α2=3.35
σ=0.79
pdf(area)
Area
power law fit
lognormal fit
pdf law 1
pdf law 2
10^0
10^-1
10^-2
10^-3
10^-4
10^0
10^1

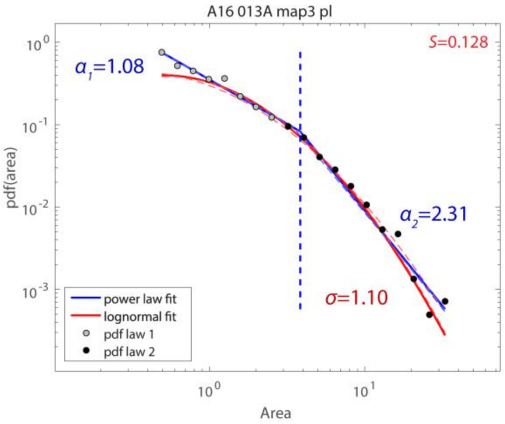
A16 013A map3 pl
S=0.128
α1=1.08
α2=2.31
σ=1.10
pdf(area)
Area
power law fit
lognormal fit
pdf law 1
pdf law 2
10^0
10^-1
10^-2
10^-3
10^0
10^1

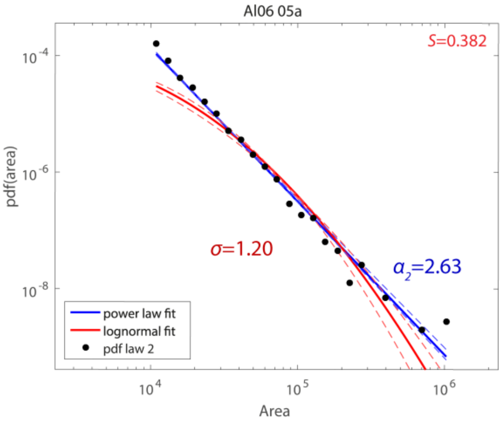
Al06 05a

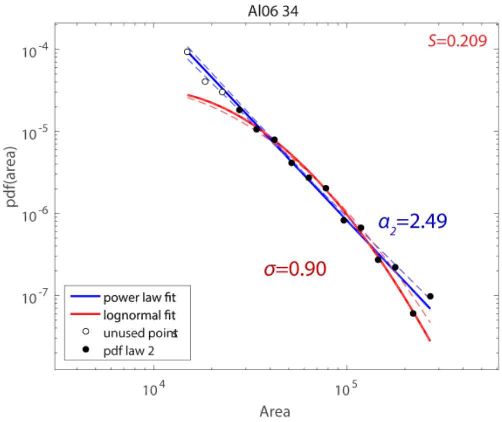
Al06 34

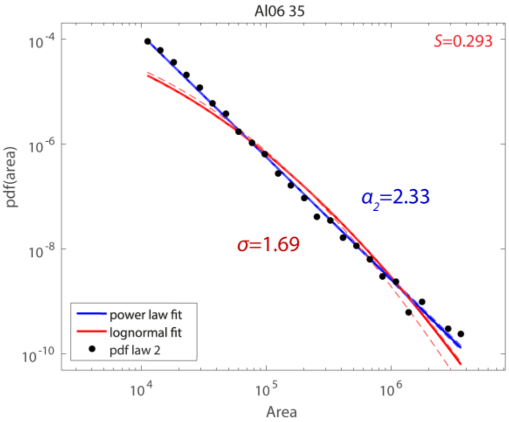
Al06 35

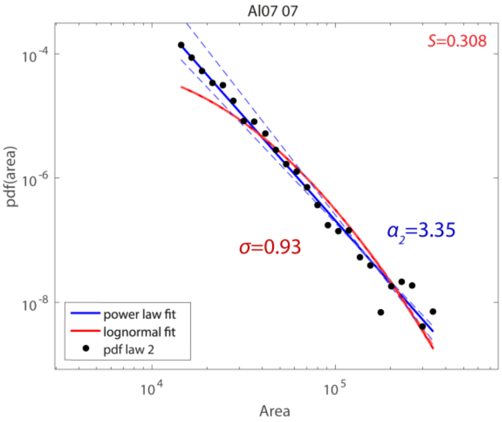
Al07 07

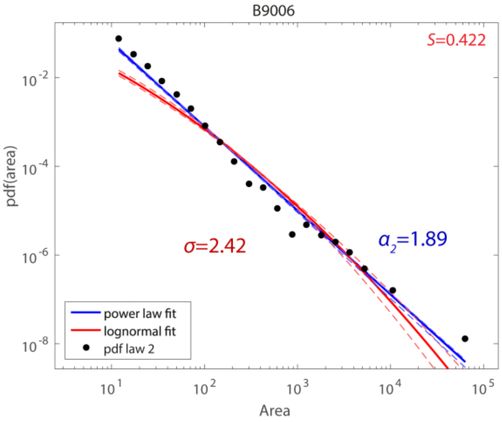
B9006

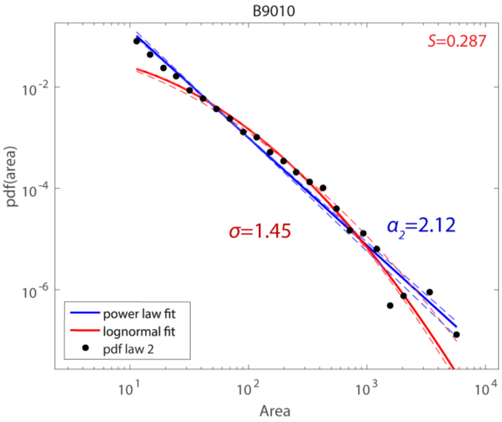
B9010

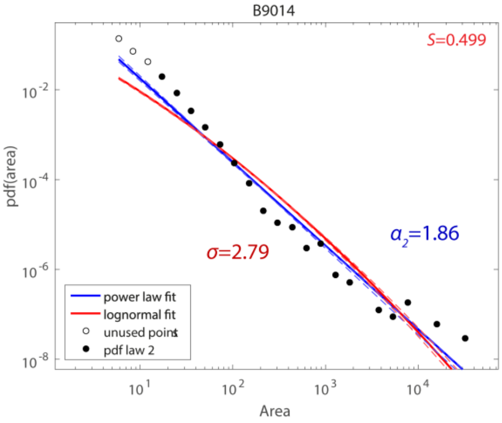
B9014

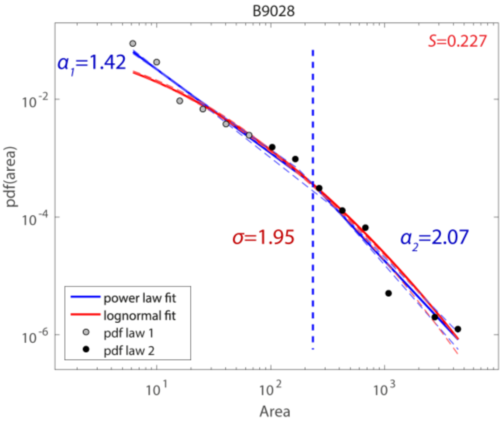
B9028

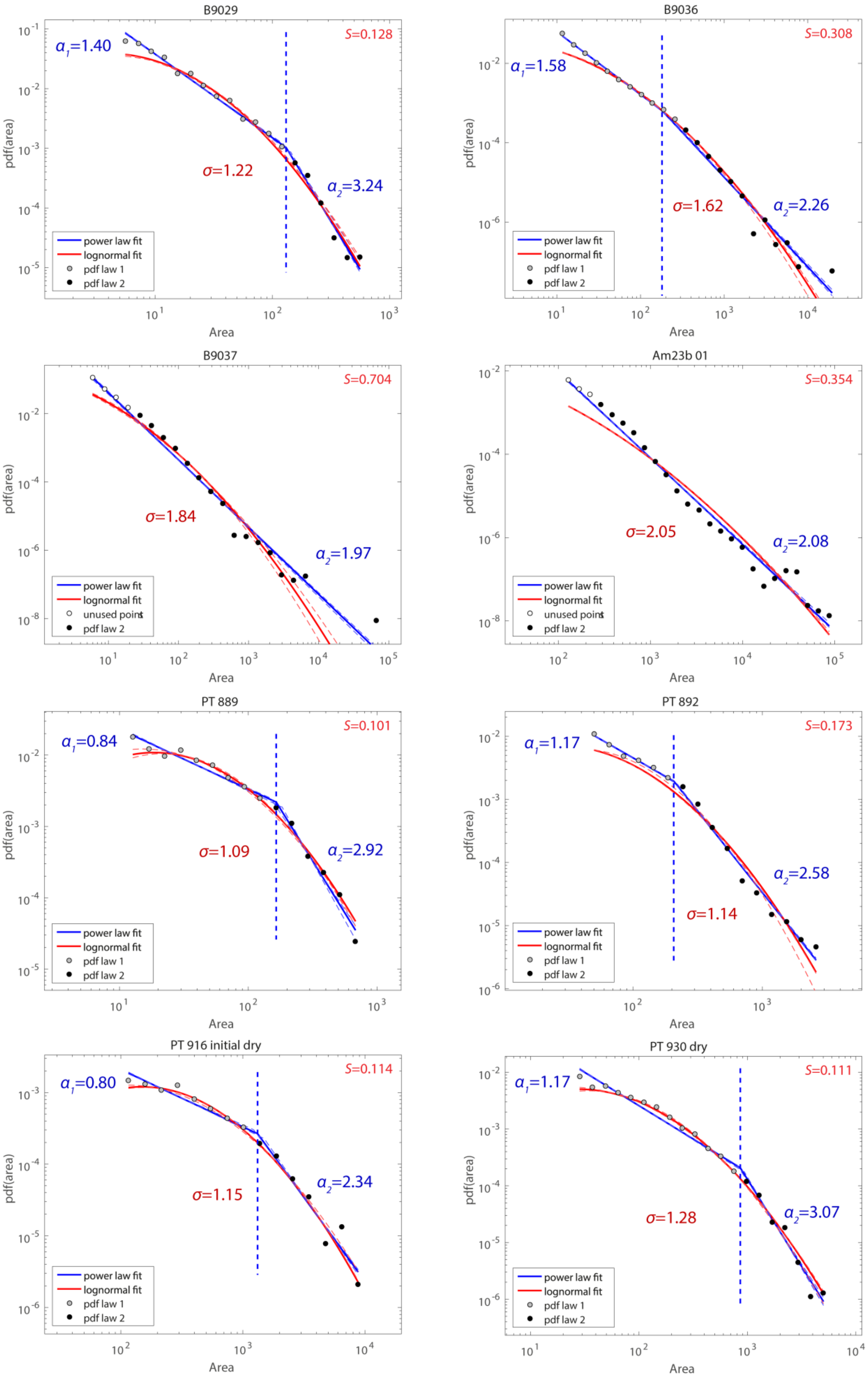
B9029
α1=1.40
S=0.128
σ=1.22
α2=3.24
B9036
α1=1.58
S=0.308
σ=1.62
α2=2.26
B9037
S=0.704
σ=1.84
α2=1.97
Am23b 01
S=0.354
σ=2.05
α2=2.08
PT 889
α1=0.84
S=0.101
σ=1.09
α2=2.92
PT 892
α1=1.17
S=0.173
α2=2.58
σ=1.14
PT 916 initial dry
α1=0.80
S=0.114
α2=2.34
σ=1.15
PT 930 dry
α1=1.17
S=0.111
σ=1.28
α2=3.07
power law fit
lognormal fit
pdf law 1
pdf law 2
unused points
pdf(area)
Area

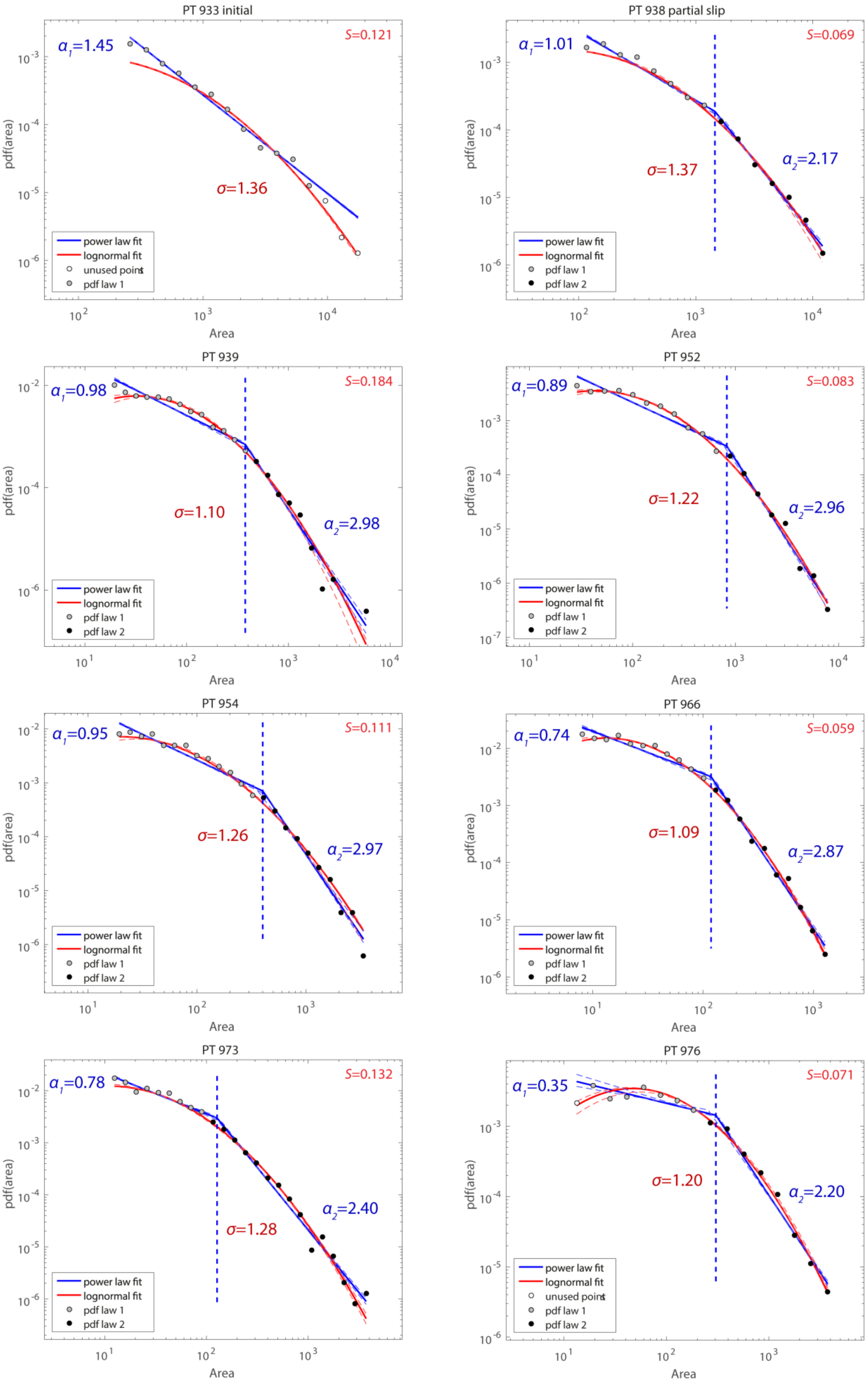
PT 933 initial
α_1=1.45
S=0.121
σ=1.36
PT 938 partial slip
α_1=1.01
S=0.069
σ=1.37
α_2=2.17
PT 939
α_1=0.98
S=0.184
σ=1.10
α_2=2.98
PT 952
α_1=0.89
S=0.083
σ=1.22
α_2=2.96
PT 954
α_1=0.95
S=0.111
σ=1.26
α_2=2.97
PT 966
α_1=0.74
S=0.059
σ=1.09
α_2=2.87
PT 973
α_1=0.78
S=0.132
σ=1.28
α_2=2.40
PT 976
α_1=0.35
S=0.071
σ=1.20
α_2=2.20
power law fit
lognormal fit
unused points
pdf law 1
pdf law 2
pdf(area)
Area
10^{1}
10^{2}
10^{3}
10^{4}
10^{-2}
10^{-3}
10^{-4}
10^{-5}
10^{-6}
10^{-7}

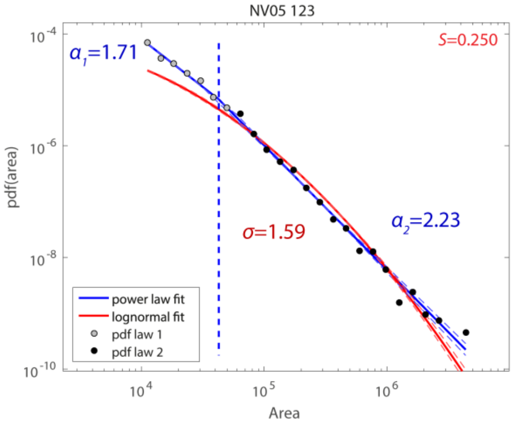
NV05 123
S=0.250
α1=1.71
σ=1.59
α2=2.23
pdf(area)
10-4
10-6
10-8
10-10
10^4
10^5
10^6
Area
power law fit
lognormal fit
pdf law 1
pdf law 2

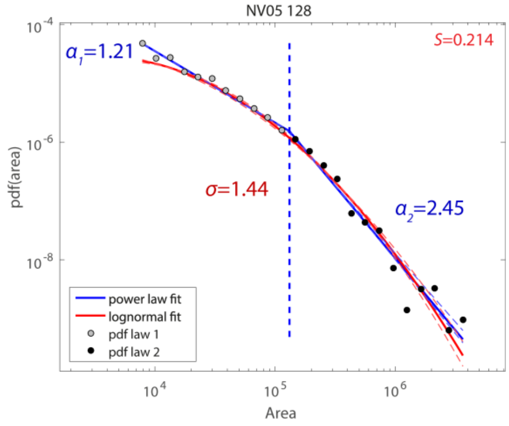
NV05 128
S=0.214
α1=1.21
σ=1.44
α2=2.45
pdf(area)
10-4
10-6
10-8
10^4
10^5
10^6
Area
power law fit
lognormal fit
pdf law 1
pdf law 2

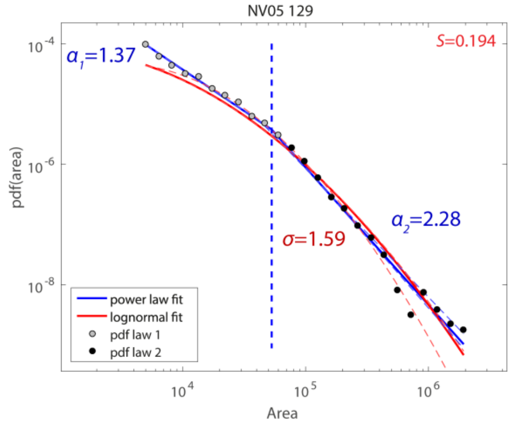
NV05 129
S=0.194
α1=1.37
σ=1.59
α2=2.28
pdf(area)
10-4
10-6
10-8
10^4
10^5
10^6
Area
power law fit
lognormal fit
pdf law 1
pdf law 2

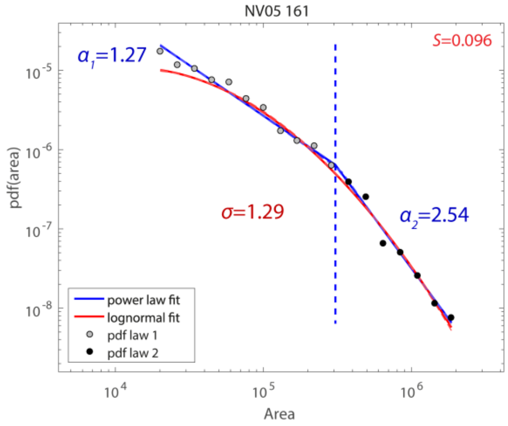
NV05 161
S=0.096
α1=1.27
σ=1.29
α2=2.54
pdf(area)
10-5
10-6
10-7
10-8
10^4
10^5
10^6
Area
power law fit
lognormal fit
pdf law 1
pdf law 2

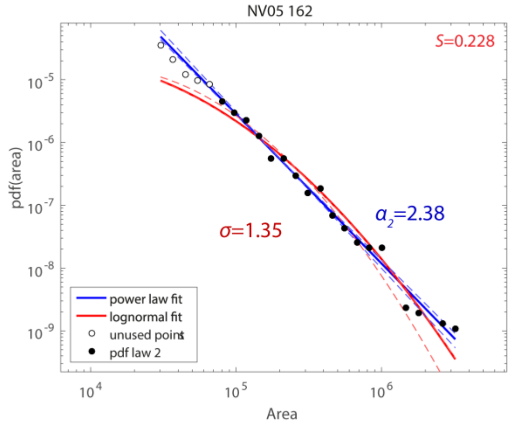
NV05 162
S=0.228
σ=1.35
α2=2.38
pdf(area)
10-5
10-6
10-7
10-8
10-9
10^4
10^5
10^6
Area
power law fit
lognormal fit
unused points
pdf law 2

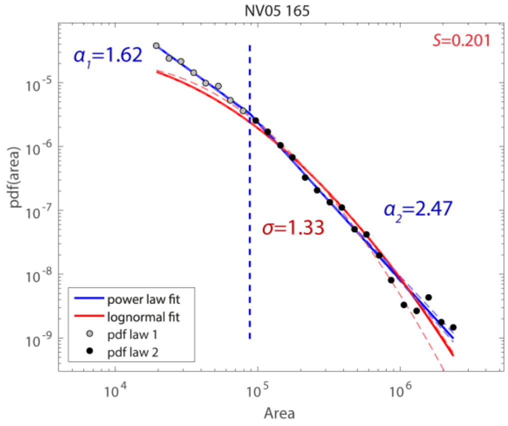
NV05 165
S=0.201
α1=1.62
σ=1.33
α2=2.47
pdf(area)
10-5
10-6
10-7
10-8
10-9
10^4
10^5
10^6
Area
power law fit
lognormal fit
pdf law 1
pdf law 2

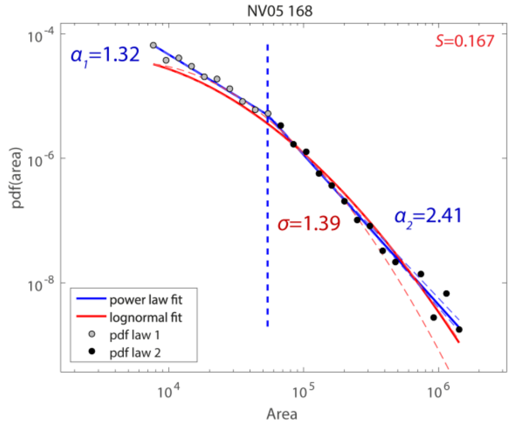
NV05 168
S=0.167
α1=1.32
σ=1.39
α2=2.41
pdf(area)
10-4
10-6
10-8
10^4
10^5
10^6
Area
power law fit
lognormal fit
pdf law 1
pdf law 2

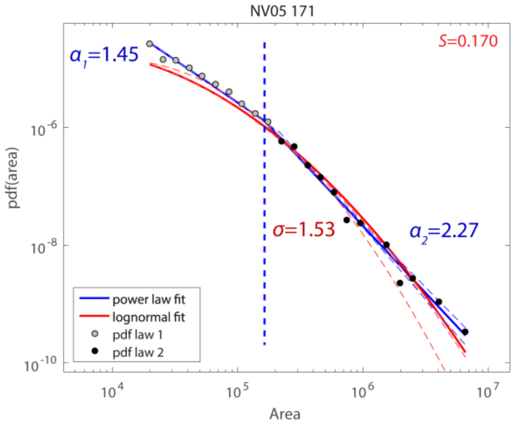
NV05 171
S=0.170
α1=1.45
σ=1.53
α2=2.27
pdf(area)
10-6
10-8
10-10
10^4
10^5
10^6
10^7
Area
power law fit
lognormal fit
pdf law 1
pdf law 2

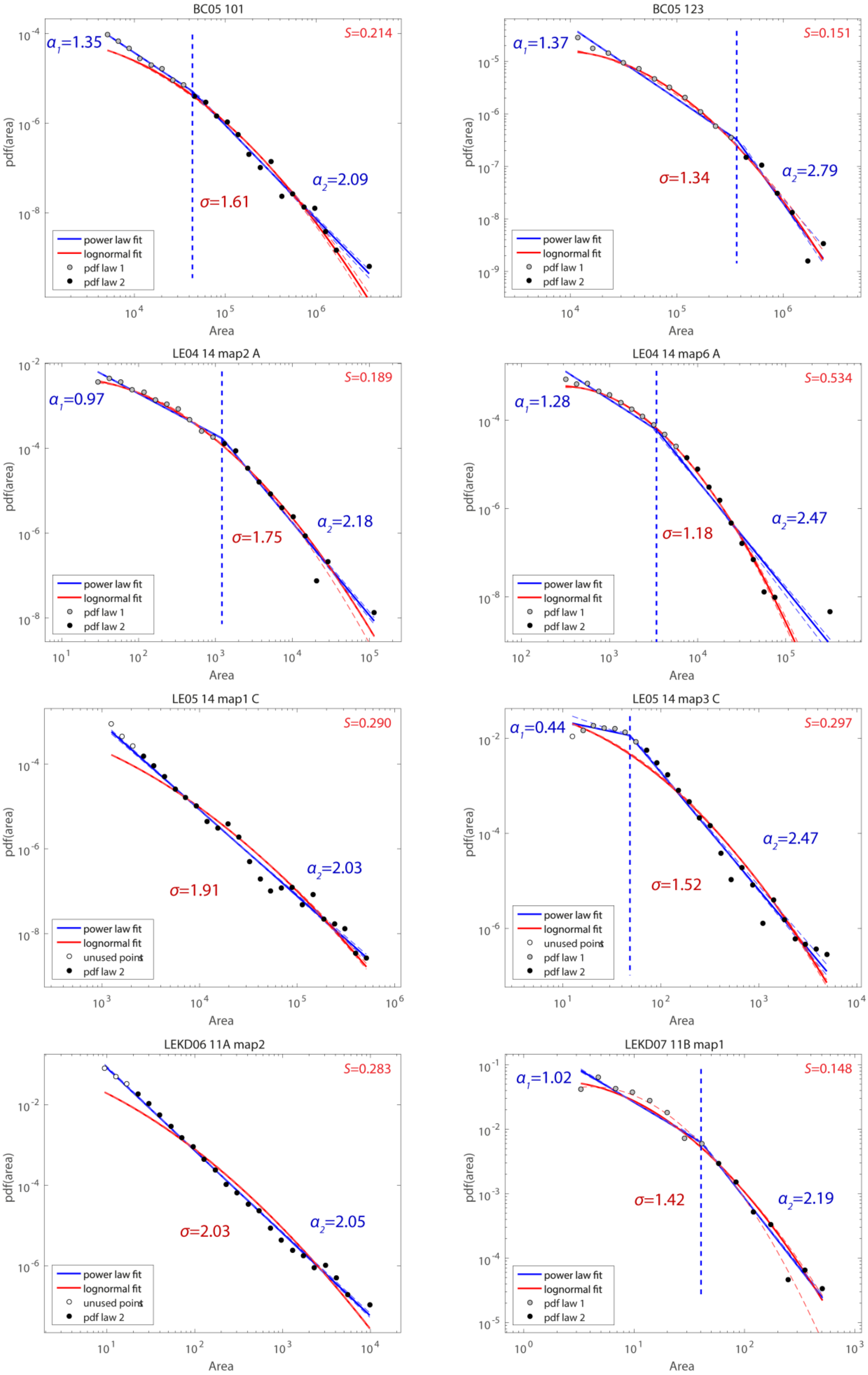
BC05 101
α1=1.35
S=0.214
σ=1.61
α2=2.09
BC05 123
α1=1.37
S=0.151
σ=1.34
α2=2.79
LE04 14 map2 A
α1=0.97
S=0.189
σ=1.75
α2=2.18
LE04 14 map6 A
α1=1.28
S=0.534
σ=1.18
α2=2.47
LE05 14 map1 C
S=0.290
σ=1.91
α2=2.03
LE05 14 map3 C
α1=0.44
S=0.297
σ=1.52
α2=2.47
LEKD06 11A map2
S=0.283
σ=2.03
α2=2.05
LEKD07 11B map1
α1=1.02
S=0.148
σ=1.42
α2=2.19
pdf(area)
Area
power law fit
lognormal fit
unused points
pdf law 1
pdf law 2

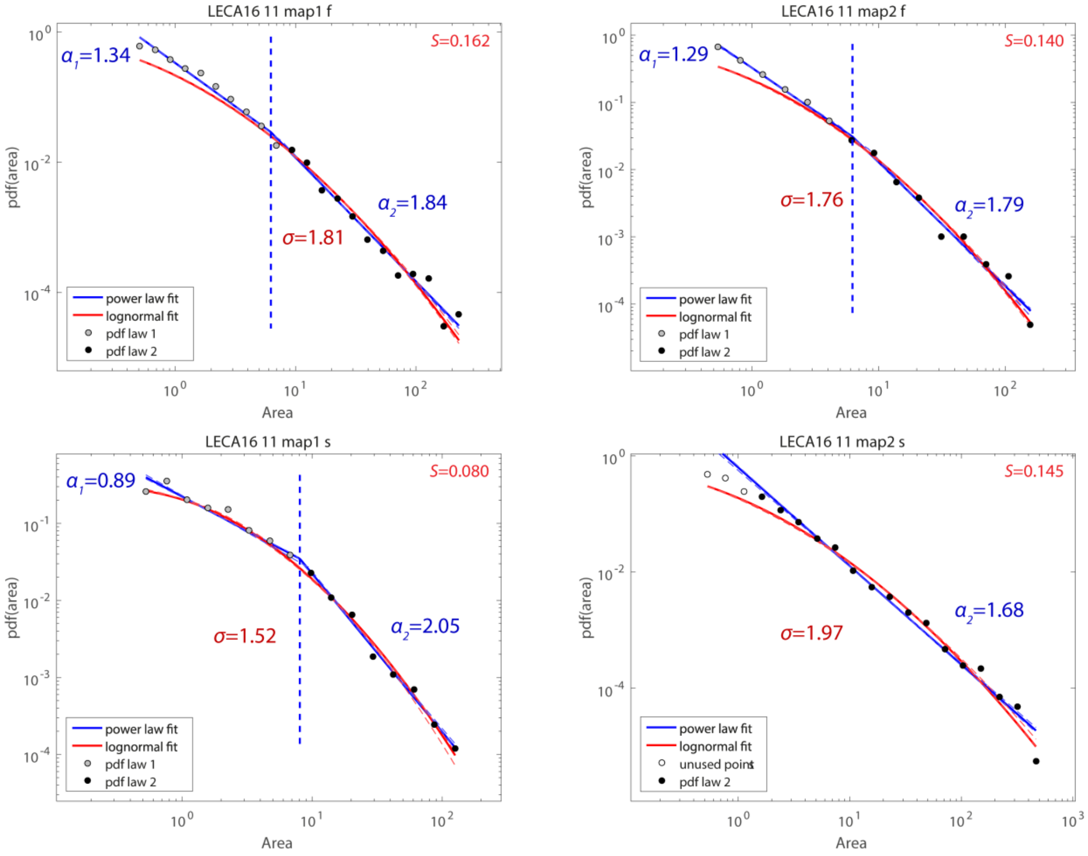

Figure S1. Grain size distributions of all EBSD maps and power law and lognormal fits. Dashed lines indicate the error on the slopes and σ due to binning of the pdf. Precise values of the errors are given in Table S1. Areas are in µm^2. The pdf of each sample is represented by dots. All the points are used for lognormal fit. White dots are point which are not used in the power law fit; grey points are used in the first power law part; black points are used in the second power law part. Vertical blue lines indicate the position of the intersect on the two power law fits.

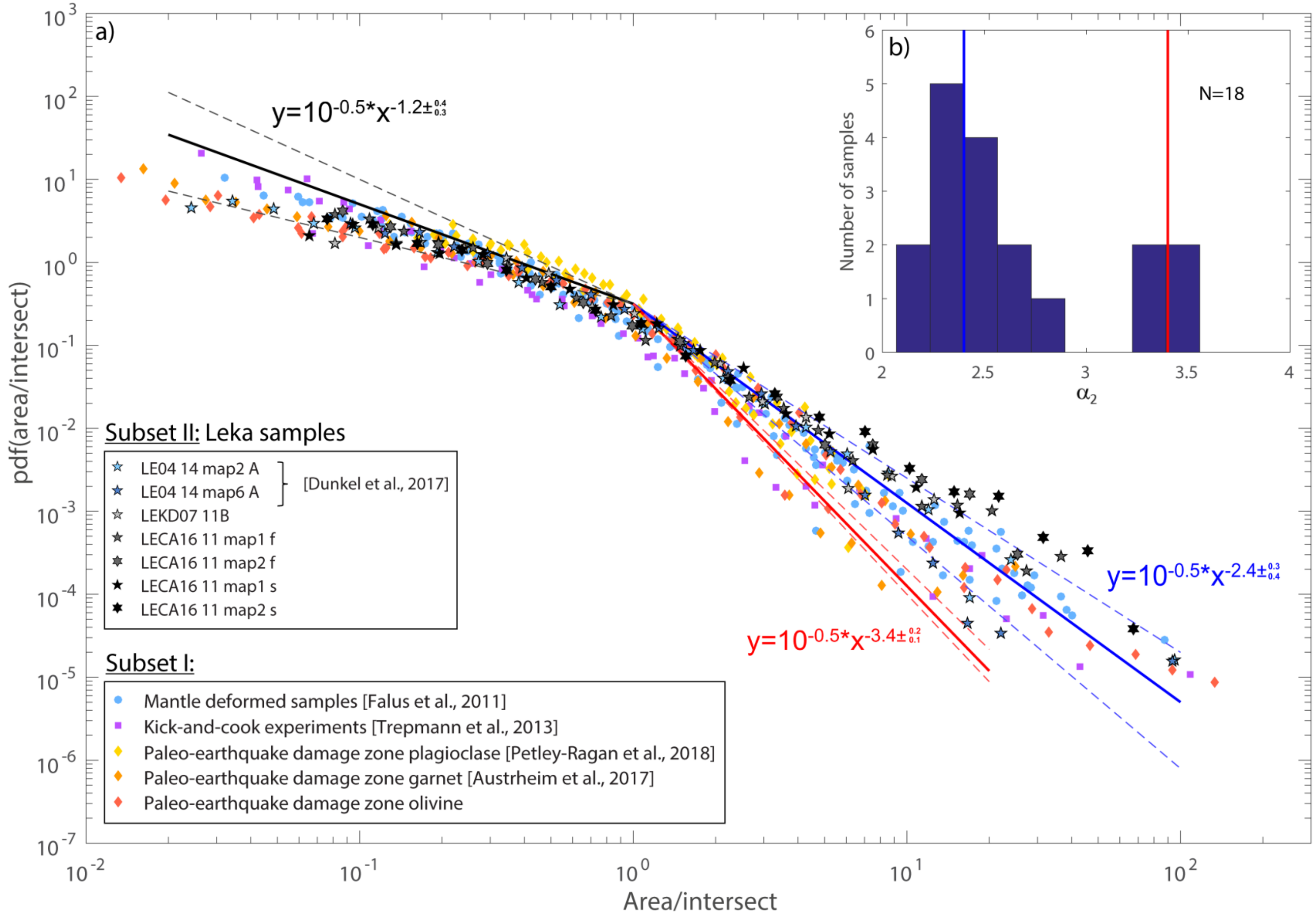
a)
b)
$y=10^{-0.5}*x^{-1.2\pm^{0.4}_{0.3}}$
$y=10^{-0.5}*x^{-2.4\pm^{0.3}_{0.4}}$
$y=10^{-0.5}*x^{-3.4\pm^{0.2}_{0.1}}$
N=18
Number of samples
α_2
0
1
2
3
4
5
6
2
2.5
3
3.5
4
pdf(area/intersect)
Area/intersect
10^{3}
10^{2}
10^{1}
10^{0}
10^{-1}
10^{-2}
10^{-3}
10^{-4}
10^{-5}
10^{-6}
10^{-7}
10^{-2}
10^{-1}
10^{0}
10^{1}
10^{2}
Subset II: Leka samples
LE04 14 map2 A
LE04 14 map6 A
[Dunkel et al., 2017]
LEKD07 11B
LECA16 11 map1 f
LECA16 11 map2 f
LECA16 11 map1 s
LECA16 11 map2 s
Subset I:
Mantle deformed samples [Falus et al., 2011]
Kick-and-cook experiments [Trepmann et al., 2013]
Paleo-earthquake damage zone plagioclase [Petley-Ragan et al., 2018]
Paleo-earthquake damage zone garnet [Austrheim et al., 2017]
Paleo-earthquake damage zone olivine

Figure S2. a) Plot of the grain size distributions of all the studied samples that could be fitted by two power laws from subset I (except NV05-123 and NV05-165) and all samples from subset II except zone C samples from Dunkel et al. (2017) and sample LEKD06-11A. Samples were normalized by the intersect of their fitted power laws or three times their median area if no intersect could be calculated. Dashed lines indicate the error on the fitted slopes. The first parts of the distributions collapse with a mean power law exponent of -1.2. The second parts of the distributions show more variability with two main tendencies with power law exponents around -2.3 and -3.4. b) Histogram of repartition for power law exponents α_2. Two modes can be identified around 2.4 and 3.4, showing two main tendencies for the power law exponents of the second part of the distribution.

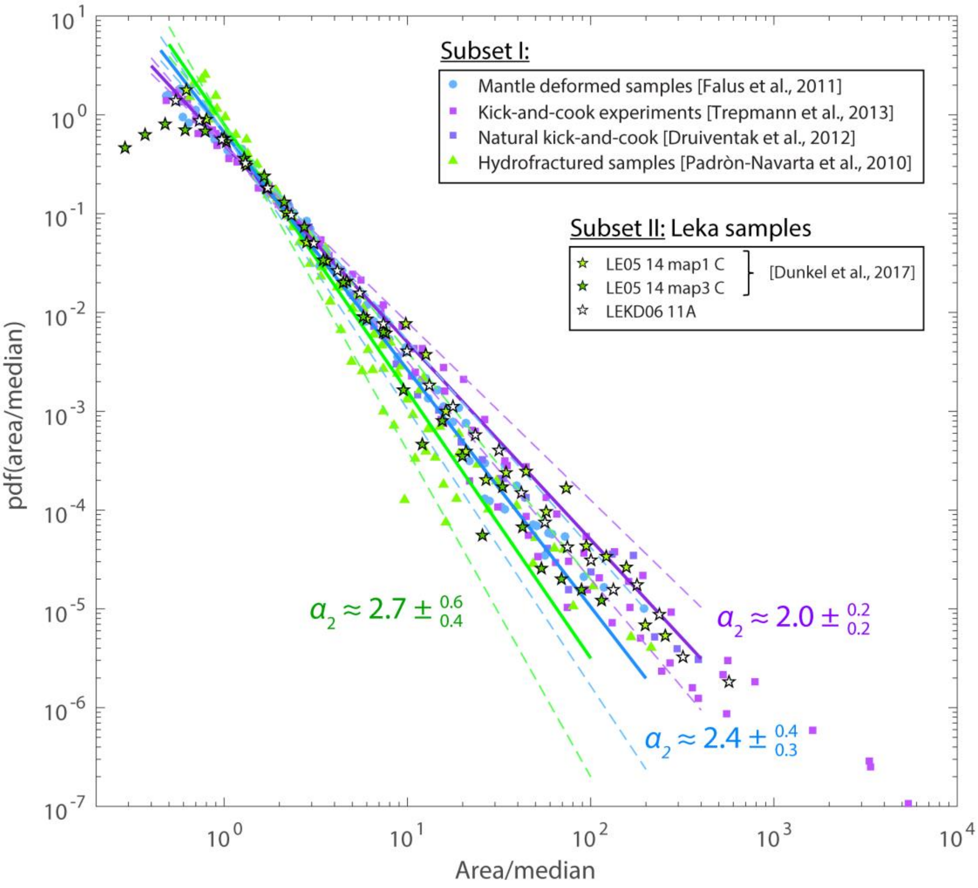

Figure S3. Plot showing all the samples fitted by a single power law and samples NV05-123 and -165, normalized to their median grain size area. Mean α_2 are indicated for the three groups of samples from subset I. Dashed lines indicate the error on the fitted slopes.

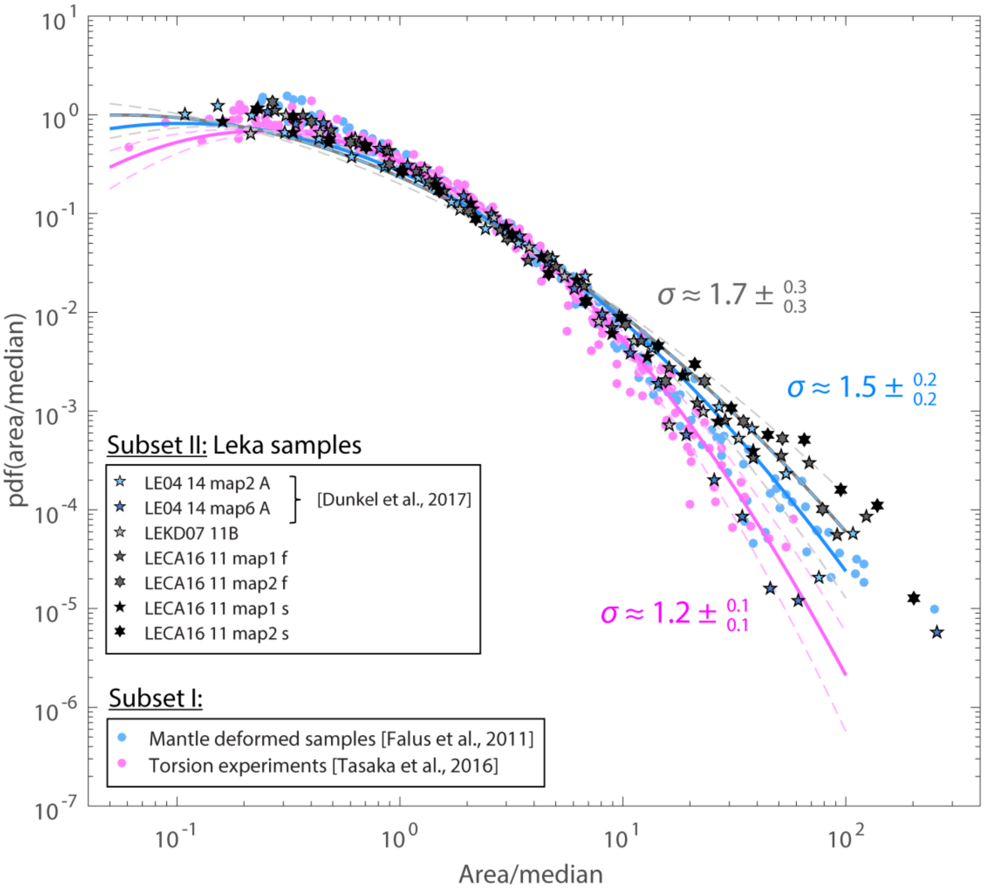

Figure S4. Plot of grain size distributions of steady-state torsion experimental samples (Tasaka et al., 2016), mantle deformed samples (except NV05-123, -162 and -165; Falus et al., 2011) and of all samples from subset II except zone C samples from Dunkel et al. (2017) and sample LEKD06-11A. Samples were normalized to their median grain size area (or three times its median area in the case of LECA16-11 map2 s). They are compared to the lognormal distribution obtained from the steady state torsion experimental samples and from the mantle deformed samples. A third lognormal distribution (corresponding to subset II samples) has been added for comparison. Dashed lines indicate the error on the fitted σ.

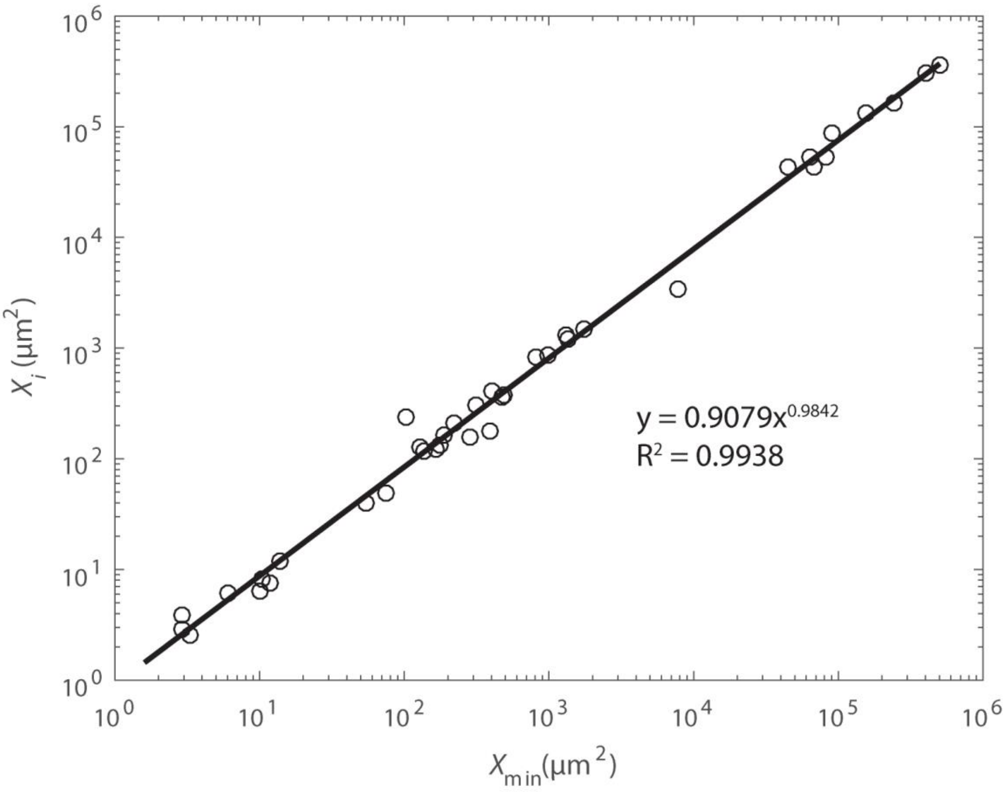

Figure S5. Relation between X_{min} obtained from the goodness-of-fit method (Clauset et al., 2009) and the power-laws intersect X_i.

Sample	μ	-	+	σ	-	+	α_1	-	+	α_2	-	+	X_i (μm^2)	-	+
Cor19 06 map3 A	0.79	0.27	0.12	1.31	0.10	0.25	-1.02	0.04	0.04	-2.46	0.08	0.11	7.63E+00	2.63E-01	1.04E+00
M02 8a map1 A	3.56	0.36	0.15	1.54	0.04	0.30	-0.96	0.02	0.02	-2.26	0.11	0.10	1.55E+02	2.64E+01	3.45E+01
M02 8a map1 B	3.95	0.00	0.11	1.32	0.01	0.26	-0.82	0.09	0.03	-3.56	0.29	0.11	3.54E+02	7.39E+00	3.99E+01
AF2 4 map1 gt	1.36	0.06	0.09	1.20	0.09	0.06	-1.27	0.06	0.02	-2.58	0.18	0.16	1.21E+01	1.87E+00	2.17E+00
AF2 4 map2 gt	2.76	0.03	0.02	1.24	0.01	0.02	-1.05	0.04	0.03	-3.51	0.11	0.09	1.23E+02	6.74E+00	8.99E+00
A16 011 map2 pl	0.05	0.02	0.01	0.96	0.02	0.01	-1.39	0.02	0.04	-2.73	0.09	0.05	2.55E+00	5.50E-02	2.74E-01
A16 011 map8 pl	0.37	0.03	0.04	0.79	0.05	0.06	-1.12	0.03	0.05	-3.35	0.12	0.25	2.94E+00	1.25E-01	2.13E-01
A16 013A map3 pl	0.51	0.04	0.04	1.10	0.00	0.15	-1.08	0.01	0.03	-2.31	0.05	0.06	3.85E+00	5.40E-01	1.65E-02
Al06 05a	9.03	0.28	0.18	1.20	0.14	0.18				-2.63	0.04	0.08			
Al06 34	9.95	0.07	0.00	0.90	0.00	0.10				-2.49	0.06	0.16			
Al06 35	8.82	0.03	0.27	1.69	0.18	0.02				-2.33	0.02	0.03			
Al07 07	9.39	0.02	0.00	0.93	0.00	0.02				-3.35	0.46	0.23			
Am23b 01	4.18	0.05	0.04	2.05	0.01	0.05				-2.08	0.02	0.04			
B9006	1.40	0.32	0.34	2.42	0.25	0.25				-1.89	0.04	0.03			
B9010	2.98	0.26	0.03	1.45	0.04	0.26				-2.12	0.10	0.05			
B9014	-0.34	0.20	0.08	2.79	0.08	0.13				-1.86	0.06	0.02			
B9028	2.87	0.17	0.01	1.95	0.15	0.06	-1.42	0.09	0.07	-2.07	0.15	0.09	2.35E+02	3.96E+01	1.12E+02
B9029	2.88	0.01	0.09	1.22	0.00	0.07	-1.40	0.03	0.03	-3.24	0.18	0.26	1.31E+02	8.75E+00	8.02E+00
B9036	3.23	0.04	0.10	1.62	0.10	0.04	-1.58	0.03	0.02	-2.26	0.07	0.05	1.81E+02	2.65E+01	4.72E+01
B9037	1.76	0.21	0.18	1.84	0.14	0.15				-1.97	0.04	0.03			
PT 889	4.11	0.10	0.03	1.09	0.06	0.05	-0.84	0.05	0.03	-2.92	0.34	0.21	1.65E+02	8.25E+00	2.16E+01
PT 892	4.53	0.05	0.12	1.14	0.14	0.01	-1.17	0.04	0.03	-2.58	0.03	0.04	2.07E+02	1.43E+01	1.15E+01
PT 916 initial dry	6.33	0.01	0.03	1.15	0.00	0.11	-0.80	0.03	0.04	-2.34	0.13	0.06	1.32E+03	1.57E+02	1.10E+02
PT 930 dry	4.94	0.06	0.03	1.28	0.08	0.05	-1.17	0.03	0.01	-3.07	0.15	0.14	8.60E+02	7.94E+01	4.82E+01
PT 933 initial	6.65	0.02	0.02	1.36	0.04	0.01	-1.45	0.01	0.01						
PT 938 partial slip	6.20	0.03	0.01	1.37	0.09	0.04	-1.01	0.06	0.02	-2.17	0.14	0.11	1.46E+03	1.10E+02	3.21E+02
PT 939	4.68	0.06	0.03	1.10	0.09	0.04	-0.98	0.08	0.04	-2.98	0.16	0.12	3.76E+02	2.65E+01	7.21E+01
PT 952	5.26	0.05	0.03	1.22	0.05	0.02	-0.89	0.03	0.03	-2.96	0.16	0.12	8.24E+02	1.36E+02	4.86E+01
PT 954	4.58	0.00	0.06	1.26	0.10	0.01	-0.95	0.05	0.02	-2.97	0.10	0.29	4.01E+02	6.73E+01	2.69E+01
PT 966	3.78	0.04	0.00	1.09	0.01	0.04	-0.74	0.08	0.04	-2.87	0.10	0.11	1.18E+02	7.65E+00	1.15E+01
PT 973	4.06	0.08	0.01	1.28	0.03	0.06	-0.78	0.06	0.04	-2.40	0.07	0.07	1.27E+02	3.39E+00	2.24E+01
PT 976	5.28	0.02	0.11	1.20	0.02	0.03	-0.35	0.09	0.09	-2.20	0.06	0.12	3.04E+02	0.00E+00	6.06E+01
NV05 123	9.49	0.09	0.08	1.59	0.05	0.06	-1.71	0.04	0.04	-2.23	0.08	0.09	4.27E+04	1.55E+04	2.75E+03
NV05 128	10.23	0.13	0.12	1.44	0.09	0.13	-1.21	0.02	0.02	-2.45	0.06	0.13	1.32E+05	7.52E+03	1.61E+04
NV05 129	9.32	0.00	0.30	1.59	0.32	0.03	-1.37	0.03	0.03	-2.28	0.05	0.15	5.30E+04	5.97E+03	5.87E+03
NV05 161	11.09	0.00	0.05	1.29	0.04	0.01	-1.27	0.03	0.02	-2.54	0.06	0.04	3.06E+05	2.00E+02	4.73E+04
NV05 162	10.47	0.04	0.21	1.35	0.22	0.02				-2.38	0.12	0.07			
NV05 165	10.27	0.01	0.20	1.33	0.19	0.02	-1.62	0.06	0.04	-2.47	0.07	0.08	8.80E+04	1.73E+04	6.00E+03
NV05 168	9.67	0.05	0.20	1.39	0.26	0.03	-1.32	0.03	0.02	-2.41	0.06	0.11	5.40E+04	3.80E+03	3.65E+03
NV05 171	10.59	0.09	0.21	1.53	0.31	0.00	-1.45	0.03	0.02	-2.27	0.16	0.10	1.64E+05	2.26E+04	4.08E+04
BC05 101	9.41	0.11	0.07	1.61	0.07	0.09	-1.35	0.01	0.03	-2.09	0.08	0.06	4.35E+04	5.72E+03	8.63E+03
BC05 123	10.74	0.10	0.04	1.34	0.03	0.12	-1.37	0.03	0.01	-2.79	0.22	0.41	3.66E+05	6.49E+04	1.00E+05
LE04 14 map2 A	5.45	0.02	0.07	1.75	0.14	0.00	-0.97	0.02	0.01	-2.18	0.05	0.05	1.21E+03	5.67E+01	1.59E+02
LE04 14 map6 A	7.06	0.05	0.05	1.18	0.04	0.04	-1.28	0.04	0.02	-2.47	0.15	0.09	3.42E+03	6.42E+02	3.59E+02
LE05 14 map1 C	6.79	0.04	0.06	1.91	0.04	0.05				-2.03	0.03	0.05			
LE05 14 map3 C	2.97	0.01	0.12	1.52	0.06	0.02	-0.44	0.29	0.14	-2.47	0.07	0.09	4.83E+01	4.68E-01	3.99E+00
LEKD06 11A map2	1.84	0.04	0.11	2.03	0.04	0.02				-2.05	0.03	0.03			
LEKD07 11B map1	2.62	0.00	0.06	1.42	0.29	0.05	-1.02	0.04	0.05	-2.19	0.04	0.06	4.04E+01	4.12E+00	1.38E+00
LECA16 11 map1 f	0.34	0.04	0.01	1.81	0.03	0.07	-1.34	0.02	0.01	-1.90	0.05	0.02	6.24E+00	1.55E+00	0.00E+00
LECA16 11 map2 f	0.54	0.05	0.04	1.76	0.05	0.09	-1.29	0.03	0.05	-1.84	0.10	0.04	6.22E+00	1.44E+00	1.47E+00
LECA16 11 map1 r	1.08	0.06	0.00	1.52	0.08	0.06	-0.89	0.07	0.03	-2.05	0.03	0.06	8.06E+00	4.14E-01	1.76E+00
LECA16 11 map2 r	0.73	0.07	0.00	1.97	0.00	0.12				-1.70	0.02	0.04			

Table S1. Fitting parameters with errors due to the number of bins in the pdf. A thick line separates subsets I and II.

Manuscript 2

Seismic controls on the progress of serpentinization at ultra-slow spreading ridges

Claire Aupart, Vera Schlindwein, Yehuda Ben-Zion, François Renard and Bjørn Jamtveit.

Under review at Journal of Geophysical Research: Solid Earth

My contributions

- Data processing:

- In this paper, I worked from what we call an “earthquake catalogue”. These are lists of all the earthquakes identified from the raw seismic data. They contain the latitude, longitude, depth, error on depth, and estimated magnitude of each event, as well as its time and date of occurrence. These lists were given to me by V. Schlindwein after she located the data using the method described in the paper.
- I visited V. Schlindwein in her laboratory in Bremerhaven in autumn 2016 so that she could introduce me to the processing of such catalogues.
- I created a MatLab code to automatically estimate the a and b values from these earthquakes lists, using a method I designed, and to calculate the volume of rock damaged following the model in Jamtveit et al., 2018, based on the previously estimated a and b values. This code also allowed construction of most of the figures in the paper, including those showing the distribution and localization of the earthquakes. It is available on the OSF platform: https://osf.io/zt23n/.

- Paper:

- I wrote most of the text in the paper, with the help of B. Jamtveit. The parts I did not write are technical parts on the localization of the data, written by V. Schlindwein. Apart from this contribution, other coauthors assisted in the writing by proof reading.
- I made all the figures and tables included in the paper. Figures S1 to S5 as well as table S1 were prepared by V. Schlindwein. Other figures in the Supplements were made by me.

Manuscript 3

Microstructures and mass-transfer associated with early faults in peridotites from the Samail Ophiolite, Oman

Claire Aupart, Luiz Morales, Marguerite Godard, Bjørn Jamtveit, and the Oman DP science team.

In preparation

My contributions

- Data acquisition:

- Samples come from the international Oman Drilling Project (Oman DP). I participated in the drilling phase in Oman for 3 weeks in January-February 2018, where I mostly helped with the curation and description of the cores. While I was there, the entire BA1B core was been drilled and the drilling of core BA4A started.
- In addition, I spend one month on board the scientific drilling vessel Chikyu in August 2018 to participate in the detailed description of the three BA cores and the writing of the associated ICDP reports. I joined a group who's task it was to describe the protolith of the cores, before serpentinization, also estimating visually the intensity of the alteration and its variations. During the first half of the month I helped to describe the cores BA1B and BA3A. During the second half, I switch to the writing of the ICDP report for our group. It was my job to write the report and summarize the information gathered by my group. I also checked if there were any problems with the description of cores (i.e. that the Excel files used were properly filled and that no core section had been forgotten etc). During that month, I also made the BA core summary logs shown in figures 3, 4 and 11 for the ICDP report (only those for the cores BA1B and BA4A are shown but I also made one for BA3A).
- I made all the observations on the macroscopic/mesoscopic (hand sample, core images) to microscopic (microscope + SEM) scale used in the paper myself. (This excludes the general description of the cores that were of course made by the Oman DP Science Party as a whole)
- I took all the pictures (except for core images that were made on the Chikyu) shown in the paper.
- I prepared the powders for the whole rock analyses with the help of the staff from the University of Oslo.
- I did microprobe analysis in Oslo and went to Stockholm during two days in February 2020 with B. Jamtveit to carry out ion probe (SIMS) analysis.

- Data processing:

- I processed the EBSD maps acquired by L. Morales using MTEX to obtain the crystal preferred orientations, grain size areas, and grain shape preferred orientations.
- I used a lighter version of the code I made for my first manuscript to fit the grain size distributions obtained from the EBSD data.

- Paper:

- I wrote all the text of the manuscript with the help of B. Jamtveit and I prepared all the associated figures.

5 Summary and outlook

The work done during the three projects composing this PhD thesis contributed to the understanding of deformation and hydration of the upper mantle with a special focus on the mid-oceanic ridge context. The first project highlighted the common occurrence of non-steady state deformation in the upper mantle, likely expressed by successions of brittle deformations followed by recovery processes. The second project showed the major role of brittle seismic faulting in permeability formation along tectonically active mid-oceanic ridges. Finally, the third project presents field data from the Oman Drilling Project which corroborate the role of brittle faulting in the early stages of serpentinization. Together, the articles included in this PhD represents a multifaced approach (microstructural, geochemical, and seismic studies, on a variety of scales and locations) to the problem of permeability generation and hydration of the mantle part of the oceanic lithosphere. The results yield a coherent picture of the mechano-chemical interactions within the upper mantle and the preponderance of brittle faulting in the early stages of the process.

In addition to providing new information on the mechano-chemical interactions in the mantle, this PhD work relies on and develops innovative methods. It proposes the use of grain size distributions in combination with Crystal Preferred Orientations (CPO) and Shape Preferred Orientations (SPO), the use of stochastic physics to understand grain size deformation, and the use of multiscale studies. It provides a method to help discern non-steady state deformation based on grain size distributions, a more precise method of determination of the Gutenberg-Richter law parameters from earthquake magnitudes distributions, and applies an innovative calculation based on these Gutenberg-Richter law parameters.

This thesis has shown that brittle faulting within the lithospheric mantle is more common than hitherto thought. Deformation driven by tectonic stress within the mantle will tend to occur though brittle-recovery processes. The recovery processes tend to heal fracture zones and close newly produced porosity. Along mid-oceanic ridges, mantle rocks are brought to shallow depths by tectonic processes. As temperature decreases, recovery processes become less and less active and brittle faulting effectively produces open spaces through which fluids can circulate. The circulation of fluids itself contributes to the cooling of the lithosphere. If the fault network is connected to the surface, seawater can infiltrate and eventually lead to the serpentinization of the peridotite. Of course, supplementary processes such as magmatism can complicate the process and prevent pervasive serpentinization.

A continuation of this work would first be to compare observations made on the Oman samples with results from the South West Indian Ridge (SWIR) to determine if any correspondence can be made between the seismic activity observed along the SWIR and the faulting described in Oman. It should include a thorough comparison of the structures within the serpentinite cores obtained in Oman with serpentinite cores previously obtained from the oceanic floor. Ideally, one would obtain cores from the same area that we studied along the SWIR, but this would require a new drilling campaign. Another interesting point would be to better constrain the inhibiting role of magmatism and volcanism on serpentinization along the mid-oceanic ridges. This could be done by conducting studies similar to the one presented in the second article manuscript included in this thesis on faster mid-oceanic ridge portions. On a similar note, determining the precise timing and source of the serpentinization event associated with the faults and cataclasis we describe in the Oman cores is crucial. The Samail ophiolite is interpreted as a former fast spreading ridge. Today, this type of ridge is not considered to be associated with extensive serpentinization except in the vicinity of transform faults. Yet, the serpentinization we observe in the Oman samples is rather extensive. If the serpentinization observed in Oman occurred before the formation of the ophiolite, either this means the Samail ophiolite may include a former transform fault zone in the vicinity of the Batin dunite, or that we may need to revise our understanding of serpentinization along fast spreading ridges.